Fabrication of Rare-earth Co-doped Cerium Gadolinium Oxide Nanoparticle as Electrolyte Material for Intermediate-temperature Solid Oxide Fuel Cells (IT-SOFCs)

Sri Rahayu

Submitted in accordance with the requirements for the degree of
Doctor of Philosophy

University of Leeds
School of Chemical and Process Engineering

April 2020

Acknowledgements

I would like to express my earnest appreciation to Dr Girish Kale and Prof. Mojtaba Ghadiri for their research expertise, guidance, constant support and motivation over the four years of my PhD, I am truly grateful.

I also wish to thank the Ministry of Research, Technology and Higher Education of the Republic of Indonesia for a scholarship through Riset-Pro (Loan number 8245-ID) and The Agency for Assessment and Application of Technology of Indonesia for the study opportunity.

For helping me, guiding me and ensuring my safety in the laboratory, I express my greatest gratitude to the admirable staff that make up Leeds University; Diane Cochrane, Christopher Bulman, Simon Lloyd, Robert Simpson, John Harrington, Dr Eric Kumi Barimah, Stuart Micklethwaite, Dr Jennifer Forrester, Dr Faye Esat, Karine Alves Throne, Dr Ben Douglas, Dr Zabeada Aslam. Without them, this truly would have not been possible.

Also, I would like to express my appreciation towards my colleagues and group: Suneela Sardar, Mehdrad Pasha, Fabio Fulcini, Lewis Scott, Umair Zafar, Tina, Domenic, James, Alejandro, Pom, Steven Parirenyatawa, Philip Masimba, Lawrance Onyie. Without them, Leeds is not the same place.

I also wanted to express my gratitude to my best supporting system: Indra Oliver Candra Hadyiswanto, Tirto Soenaryo, Jennifer Forrester, Wei Pin Goh, Amimah Nur Sabrina, and Prima. Who are always there for me during ups and downs.

Last but not least, I would like to thank my family for their endless support until the end.

Abstract

In an attempt to solve the energy trilemma, the solid oxide fuel cells (SOFCs) have attracted worldwide interest due to the high efficiency, fuel flexibility, sustainable electricity generation on demand and low pollutant emissions. Conventional SOFCs which operate at high temperatures (700 – 1000°C) and therefore has resulted in several problems, especially with regard to cost, durability and, choice of functional and structural materials. Therefore, reducing the operating temperatures to intermediate temperatures solid oxide fuel cells (IT)-SOFCs (500 – 700°C) is desirable for decreasing operating costs, widening the choice of materials, increasing sustainability, and prolonging durability. However, reducing the operating temperature can limit the oxide ion conductivity of the electrolyte, which can impede the performance of IT-SOFCs. Accordingly, finding the optimum electrolyte materials with high ionic conductivity at intermediate temperatures becomes a factor for the future impact and success of the technology. This research will focus on the development of the electrolyte material for IT-SOFCs with high ionic conductivity.

Two rare-earth substitutional aliovalent cations (co-doped) in MO2 type of fluorite materials are considered as a promising material for use as the solid electrolyte in solid oxide fuel cells because two dissimilar trivalent substitutional cations (co-doping) can be used to reduce the activation energy, increase bulk conductivity and optimise the total conductivity (bulk + grain boundary) at intermediate temperatures. In this research, three different combinations of co-doped materials with four different concentrations using the novel Sodium Alginate (SAL) method also known as Leeds Alginate Process (LAP) in some recent literature have been investigated for IT-SOFCs electrolyte application. A detailed investigation using thermal analysis, scanning and transmission electron microscopy, ambient and high-temperature X-ray diffraction, Raman spectroscopy, and impedance spectroscopy is carried out to optimise the synthesis and characterisation of the new solid electrolyte compositions for future applications.

Firstly, the development of the optimum process to produce nanoparticles is reported in this research. The novel sol-gel sodium alginate bead and granule method are used to prepare the nanoparticle complex metal oxide. Initially, these methods have been successfully applied in this research to produce cubic single-phase nanoparticle of $Ce_{0.8}Gd_{0.2}O_{1.9}$, $Ce_{0.8}Dy_{0.1}Gd_{0.1}O_{1.9}$, $Ce_{0.8}Ho_{0.1}Gd_{0.1}O_{1.9}$ and $Ce_{0.8}Er_{0.1}Gd_{0.1}O_{1.9}$ having homogeneous composition. The calcination temperature at 500°C for 2h showed the optimum temperature to obtain the particles size ~10nm and the sintering temperature at 1500°C for 2h showed the fully dense ceramics with higher relative density (> 96%) obtained.

Subsequently, the alginate method has also been applied in this research to synthesise successfully thirteen co-doped cerium rear-earth oxide solid solution series $Ce_{0.8}RE_xGd_{0.2-x}O_{1.9}$ (RE = Dy, Ho, and Er; $0 \leq x \leq 0.2$). The composition of the solid solution in each series has been varied at an incremental interval of x=0.05. X-ray diffraction (XRD) data shows a single-phase fluorite structure in the entire solid solution series and obey the Vegard’s Law. The crystallite size calculated from XRD using the Rietveld refinement method is in good agreement with those observed from transmission electron microscopy (TEM) (~10nm). The fluorite and defect structure were observed for the entire series by Raman Spectroscopy. The co-doped materials do not change the coefficient of thermal expansion (CTE) significantly.

Co-doping as well as the synthesis method has helped to improve the relative density, which has been confirmed with the microstructure analysis by scanning electron microscopy (SEM) and also leads to an anomalous increase in the ionic conductivity above the critical temperatures in all the three solid solution series. The Ionic conductivity

observed is almost 100 times higher than the single doped at a typical temperature of 500°C from 0.00351 S cm^{-1} for $Ce_{0.8}Gd_{0.2}O_{1.9}$ to 0.3169 S cm^{-1}, 0.2871 S cm^{-1} and 0.3573 S cm^{-1} for $Ce_{0.8}Dy_{0.1}Gd_{0.1}O_{1.9}$, $Ce_{0.8}Ho_{0.1}Gd_{0.1}O_{1.9}$, $Ce_{0.8}Er_{0.15}Gd_{0.05}O_{1.9}$, respectively.

Hence, these novel sol-gel methods are the promising processes to produce nanoparticles of complex metal oxide compounds at low temperatures, and co-doped material can be an alternative solid electrolyte material for future IT-SOFCs due to the high ionic conductivity.

Table of Contents

List of Tables

List of Figures

Nomenclature

ALG	Alginate
CGO	Cerium-gadolinium oxide
CDO	$Ce_{0.8}Dy_{0.2}O_{1.9}$
CEO	$Ce_{0.8}Er_{0.2}O_{1.9}$
CHO	$Ce_{0.8}Ho_{0.2}O_{1.9}$
CTE	Coefficient thermal expansion
DSC	Differential Scanning Calorimetry
Dy5	$Ce_{0.8}Dy_{0.05}Gd_{0.15}O_{1.9}$
Dy10	$Ce_{0.8}Dy_{0.1}Gd_{0.1}O_{1.9}$
Dy15	$Ce_{0.8}Dy_{0.15}Gd_{0.05}O_{1.9}$
EDS	Energy-Dispersive X-ray Spectroscopy
Er5	$Ce_{0.8}Er_{0.05}Gd_{0.15}O_{1.9}$
Er10	$Ce_{0.8}Er_{0.1}Gd_{0.1}O_{1.9}$
Er15	$Ce_{0.8}Er_{0.15}Gd_{0.05}O_{1.9}$
FTIR	Fourier Transform Infrared Spectroscopy
GSAS	General Structure Analysis System
Ho5	$Ce_{0.8}Ho_{0.05}Gd_{0.15}O_{1.9}$
Ho10	$Ce_{0.8}Ho_{0.1}Gd_{0.1}O_{1.9}$
Ho15	$Ce_{0.8}Ho_{0.15}Gd_{0.05}O_{1.9}$
HT-XRD	High Temperature X-ray Diffraction
IT-SOFCs	Intermediate Temperature Solid Oxide Fuel Cells
LAP	Leeds Alginate Process
MIEC	Mixed ionic-electronic conductor
Na-ALG	Sodium Alginate
SAED	Selected Area Electron Diffraction
SEM	Scanning Electron Microscopy
SOFCs	Solid Oxide Fuel Cells
TPB	Triple-phase boundary

TEM	Transmission Electron Microscopy
TGA	Thermogravimetric Analysis
TMO	Transition metal oxide
XRD	X-ray Diffraction
YSZ	Yttria-stabilized zirconia
a	Lattice parameter (Å)
$d_{(hkl)}$	Interplanar spacing (nm) of the plane (hkl)
R_{exp}	Expected residual factor (%)
R_{wp}	Weight residual (%)
σ	Conductivity (Siemens cm^{-1})
θ	Diffraction angle (radiant)
ΔG^o	Standard Gibbs free energy of formation (kJ mol^{-1})
λ	Wavelength (nm)
R	resistance
C	capacitance
f_{max}	maximum frequency in one semi-circle
ρ	solution resistivity
L	thickness of the pellet
A	the area of the pellet

List of Publications / Presentations

Paper

1. Rahayu, S., Forrester, J.S., Kale, G.M., Ghadiri, M. Promising solid electrolyte material for an IT-SOFC: Crystal structure of the cerium gadolinium holmium oxide $Ce_{0.8}Gd_{0.1}Ho_{0.1}O_{1.9}$ between 295 and 1023 K. *Acta Crystallographica Section C: Structural Chemistry*. 2018. **74**.2. 236-239.
2. Barimah, E.K., Rahayu, S., Ziarko, M.W., Bamiedakis, N., White, I.H., Penty, R.V., Kale, G.M., Jose, G. Erbium-Doped Nanoparticle−Polymer Composite Thin Films for Photonic Applications: Structural and Optical Properties. *ACS Omega*, 2020, **5** (16), 9224-9232.

Conference Presentation

1. International Congress Engineering of Advanced Materials (ICEAM2017)
   Erlangen, Germany 10 – 12 October 2017.
   Poster presentation: Synthesis and characterization of co-doped cerium gadolinium oxide nanoparticles employing novel sol-gel method
2. SCaPE Internal Research Exchange Event, University of Leeds, 18th January 2018.
   Poster presentation: Nanoparticle Manufacturing of Co-Doped Cerium Gadolinium Oxide for Electrolyte Intermediate–Temperature Solid–Oxide Fuel Cells (IT–SOFCs)
3. International Congress on Particle Technology (PARTEC) 2019
   Nürnberg, Germany 9 – 11 April 2019.
   Poster presentation: Novel Sol-Gel Method of Co-Doped Cerium Gadolinium Oxide Nanoparticles for Solid Oxide Fuel Cell Electrolyte

Chapter 1 Introduction

1.1 Overview

The current global issue in power generation is the environmental impact. Most of the present electricity generation uses non-renewable energy sources, such as natural gas, coal and other fossil fuels that have high CO_2 emission. To minimise this adverse effect of conventional power generation, renewable energy sources which have highly efficient and low CO_2 emission are necessary. Therefore, research in renewable sources with low or negligible CO_2 emission, e.g. solar cell, wind, battery technology and Fuel Cells, is becoming worldwide interest. Fuel Cells is a technology that generates electricity from a reaction between hydrogen and oxygen with by-product as water and heat. Moreover, fuel cells have higher efficiency than a conventional power generation system, as seen in **Figure 1.1** (1,2).

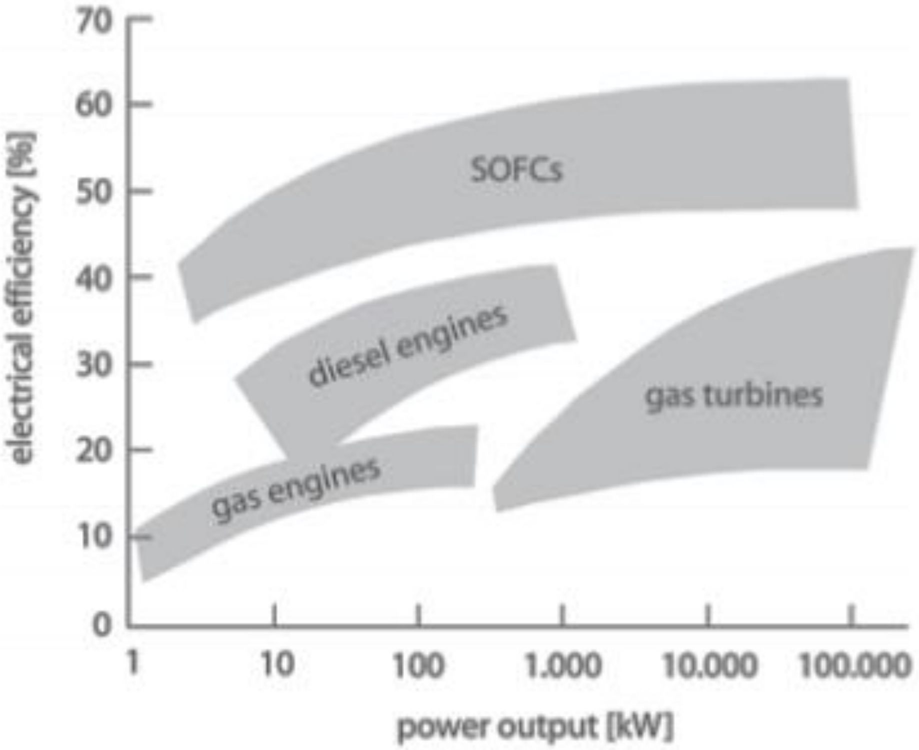

Figure 1.1 Efficiency of different energy technologies as a function of the power output (2).

The classification of fuel cells depends on material characteristic of the electrolyte, for the example Direct Methanol Fuel Cells (DMFCs), Polymer Electrolyte Fuel Cells (PEMFCs), Phosphoric Acid Fuel Cells (PAFCs), Alkaline Fuel Cells (AFCs), Molten Carbonate Fuel Cells (MCFCs) and Solid Oxide Fuel Cells (SOFCs). The highest electrical efficiencies among all other fuel cells that operate in temperature between 800°C – 1000°C is solid oxide fuel cells (SOFCs) (~55 – 60%). This technology also enables to combine with gas/turbines in hybrid power generation systems with improved efficiency up to 80% (1-4). However, high-temperature operation in SOFCs leads several problems such as corrosion in the metal components and needs expensive materials for interconnector and insulation (5, 6).

To achieve long-term performance stability and low affordable operation cost in solid oxide fuel cells (SOFCs), decreasing the temperature of operation below ∼600◦C (intermediate or low-temperature operation) has attracted significant interest worldwide (7-9). Lowering temperature operation in solid oxide fuel cells (SOFCs) requires increased electrolyte conductivity and enhanced electrode overpotential. These challenges lead many researchers to find suitable electrolyte materials with high ionic conductivity and high chemical stability in oxygen potential gradient.

According to literature, two substitutional ions (co-doped) can be used to minimise the activation energy and optimise the conductivity in electrolyte for intermediate-temperature electrolyte solid-oxide fuel cells (IT-SOFCs). Measuring changes in the crystal structure/lattice parameters as a function of dopant concentration is one way to evaluate the minimisation of oxygen vacancy trapping. Lattice simulations have been developed that have led to the recognition of the importance of elastic energy terms due to size mismatch of the dopant cations (9). Kim proposed empirical equations between dopant size and ionic conductivity; the concept of critical ion radius of the dopant was developed. The critical ionic radius for a trivalent dopant in Ceria is 0.1038 nm, close to the ionic radius of Gd^{3+} (10). Kilner suggested that conductivity is affected by ionic size mismatch between the host and the dopant, the smaller ionic size mismatch the higher conductivity will be obtained (9). Dikmen found that co-doped material increased the ionic conductivity more than 300% than single doped ceria for same vacancy concentration (11).

1.2 Research Aim and Objectives

The overall aim of this project is the synthesis and characterisation of ceria-based nanostructured composite materials with the co-doped material through a novel synthesis method that can leads to lowering the temperature operation (IT-SOFCs) and good electrochemical behaviour. The sodium alginate method is used to synthesis the nanoparticle of electrolyte materials. In particular, the objectives of this research are:

a) synthesis the homogeneous nanoparticles of cerium-gadolinium oxide (CGO) using novel synthesis method and optimise the process
b) use the co-doped materials with different rear-earth elements (dysprosium, holmium, and erbium) and control the dopant concentration
c) investigate material characteristic of nanoparticles from the novel synthesis of sodium alginate bead and granule
d) compare the achieved results from cerium-gadolinium oxide (CGO) and cerium-gadolinium oxide (CGO) co-doped with other rear-earth elements
e) propose the optimal sintering temperature of cerium-gadolinium oxide (CGO) and co-doped elements
f) understand the crystallographic features of co-doped materials especially at the operating temperature of SOFCs

g) investigate the electrical properties of electrolytes for Solid Oxide Fuel Cells (SOFCs)

1.3 Outline of the Report

This thesis is organised into six chapters including Introduction, Literature review, Methodology and Instrumentation, Result and discussions, Conclusion and Future Works. Chapter 1 introduction covers a short introduction of fuel cells and solid oxide fuel cells, followed by the research aim and objectives and organisation of this thesis.

Chapter 2 covers a literature review of the theory and current state of the art in electrolyte Intermediate Temperature Solid Oxide Fuel Cells (IT-SOFCs) that are relevant for this project. This chapter also presents the fundamental theories and factors that affected the improvements of the electrolyte ionic conductivity. Furthermore, a detailed study about the novel sodium alginate sol-gel processes, including the mechanism and the chemistry, is also presented.

Chapter 3 Methodology and instrumentation, presents the nanoparticles synthesis using sodium alginate bead and granule as well as the instruments to characterise the phase transformation, crystalline structure, morphologies, chemical composition, microstructure, and electrical properties using simultaneous thermogravimetric analysis and differential scanning calorimetry (TGA/DSC), powder X-ray diffraction (XRD), High-Temperature X-ray Diffraction (HT-XRD), scanning electron microscopy (SEM), transmission electron microscopy (TEM), Raman spectroscopy and AC-impedance spectroscopy, have been investigated in this chapter.

Chapter 4 is results and discussion, which provide the details of the works and analyse the results from the project. These chapters will investigate the electrical property related to the phase transformation, crystalline structure, morphologies, chemical composition, thermal expansion and the microstructure.

Chapter 5 and Chapter 6 discuss the conclusion and recommendation of future work, presents the research plan for the remaining work in this PhD.

Chapter 2 Literature Review

Solid oxide fuel cells (SOFCs) have attracted worldwide research activity due to the high efficiency, fuel flexibility and low pollutant emissions (12, 13, 14). Conventional SOFCs which operate at high temperatures (700 – 1000°C) have resulted in several problems, especially with regard to the cost and durability (9). Therefore, reducing the operating temperatures to intermediate temperatures (IT)-SOFCs (500 – 700°C) is desirable for decreasing operating costs, prolonging durability, and minimising energy usage. In addition, this may allow the reduction of electrode sintering, the diffusion between electrolyte and electrodes, and thermal stress (15, 16, 17). However, reducing the operating temperature can limit the oxide ion conductivity of the electrolyte, which can impede the performance of IT-SOFCs (17). Accordingly, finding the optimum electrolyte materials with high oxide ion conductivity at intermediate temperatures becomes a choice to improve the SOFCs performance. In this chapter, a literature review of SOFCs including the mechanism, each component, and the synthesis methods, is presented.

2.1 Solid Oxide Fuel Cells (SOFCs)

The current global dilemma in the energy system is the environmental impact of greenhouse gasses, which caused increases the global mean temperature (18). The use of fossil fuels resulting in the liberation of huge volumes of carbon dioxide (CO_2). The challenge encourages the scientist to research the another nonfossil sources (18). Nowadays, the renewable energy sources are a vital component in sustainable development as future energy needs. Ehteshami and co-worker (19) found that fuel cells is the most promising renewable energy sources due to the sustainability in energy demand and environmental.

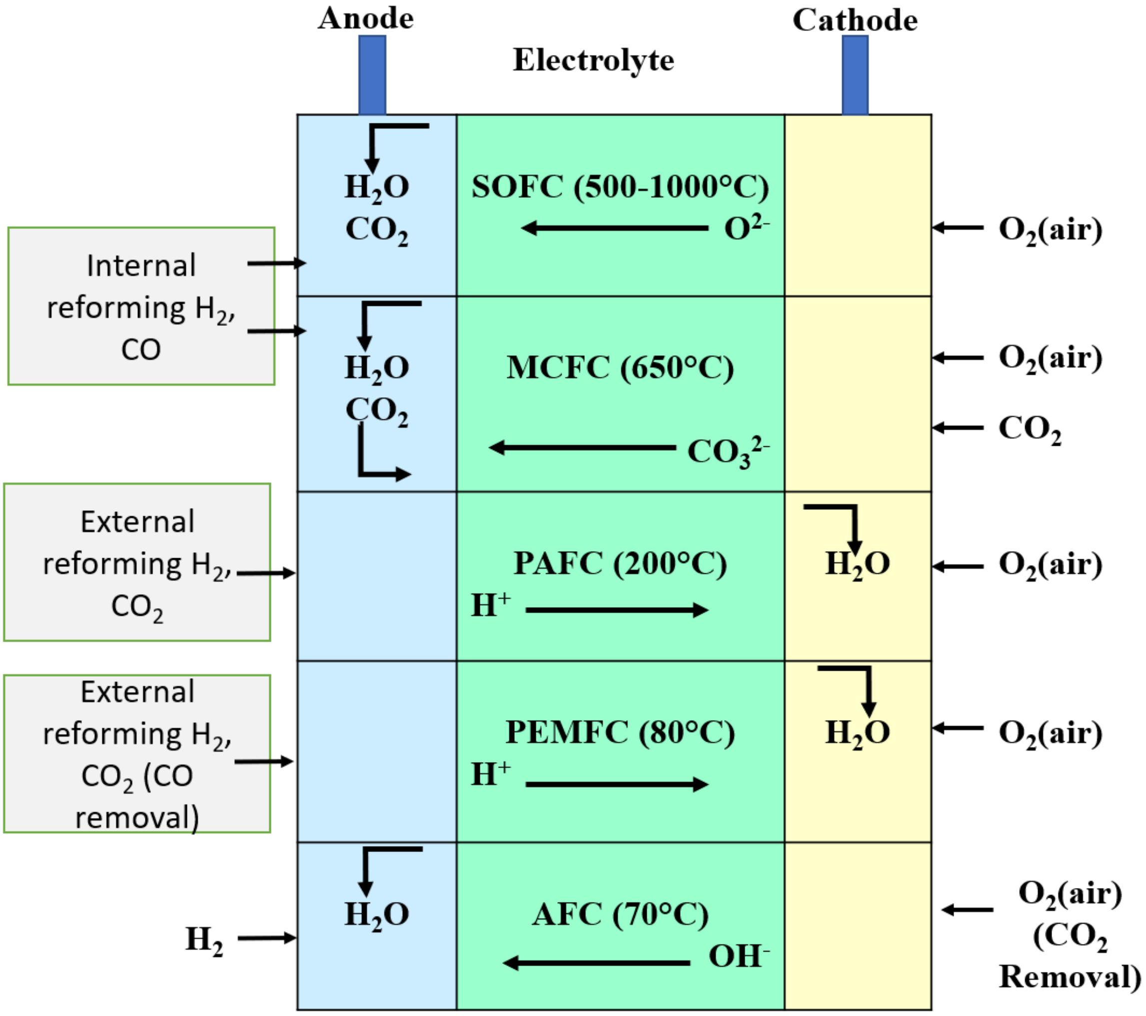

Figure 2.1. Summary of fuel-cell types. The anode is where the oxidation takes place and involves the liberation of electrons. These electrons travel through the external circuit and produce electrical energy and arrive at the cathode to participate in the reduction reaction (Adapted from 23).

Fuel cells do not require recharging, which sets them apart from secondary batteries. However, they are similar in those the main operating principles of fuel cells and batteries are an electrochemical combination of reactants to generate electricity (3, 20-22). **Figure 2.1** shows a summary of the current fuel cells research. Solid-oxide fuel cells (SOFCs) and molten-carbonate fuel cells (MCFCs) operate at a higher temperature which gives the advantage of electrochemical oxidation at the anode from both CO and H_2. In contrast, the phosphoric-acid fuel cell (PAFC), polymeric-electrolyte-membrane fuel cell

(PEMFC), and alkaline fuel cell (AFC) stacks are used at lower temperature but required relatively pure hydrogen to be supplied to the anode. The use of hydrocarbon or alcohol fuels in these systems requires an external fuel processor which not only makes the system more complex and increases the system cost, but also reduces the overall efficiency, as shown in **Figure 2.2** (23).

Having separate reformer compartments that thermally integrated within the stack in high temperature fuel cells (SOFCs and MCFCs) can result in a better thermal management of the stack than when applied directly into the anode compartment. For low-temperature fuel cells, (PAFCs and PEMFCs), an external fuel processor is required. These reformers are needed to maintain the operating temperature. However, this system may result in a significant loss in efficiency because of the impure H_2 fuel (23). Accordingly, this thesis focuses on materials aspects of SOFCs systems especially electrolyte materials, which at present still appear to present opportunities to exploit their potential.

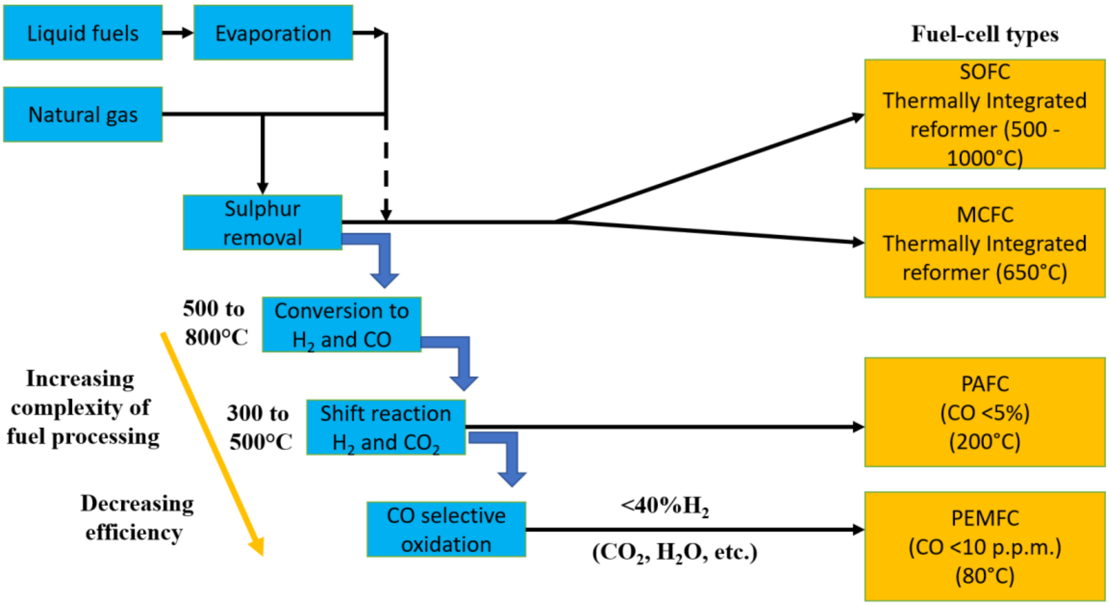

Figure 2.2. Fuel-cell types and fuel processing (Adapted from 23).

Solid oxide fuel cells (SOFCs) are a high-temperature fuel cell technology with high electrical efficiency, environmentally friendliness, and flexibility in the choice of fuel (3, 20-22). The essential components of solid oxide fuel cells (SOFCs) are porous electrodes (cathode and anode) and a dense electrolyte layer sandwiched between the electrodes. SOFCs can use either proton conduction and/or an oxide ion through the electrolyte (**Figure 2.3**). Oxygen (air) is fed into the cathode of the fuel cell, and fuel gas such as hydrogen enters the cell via the anode. The reduction of oxygen at the cathode generates the oxygen ion that transports through a solid electrolyte to the anode; the ion donor from the cathode reacts with fuel as an oxidation reaction and generates electrons. Moreover, the flow of electrons in the external circuit (viz. from anode to the cathode) produces electricity (20, 21, 23).

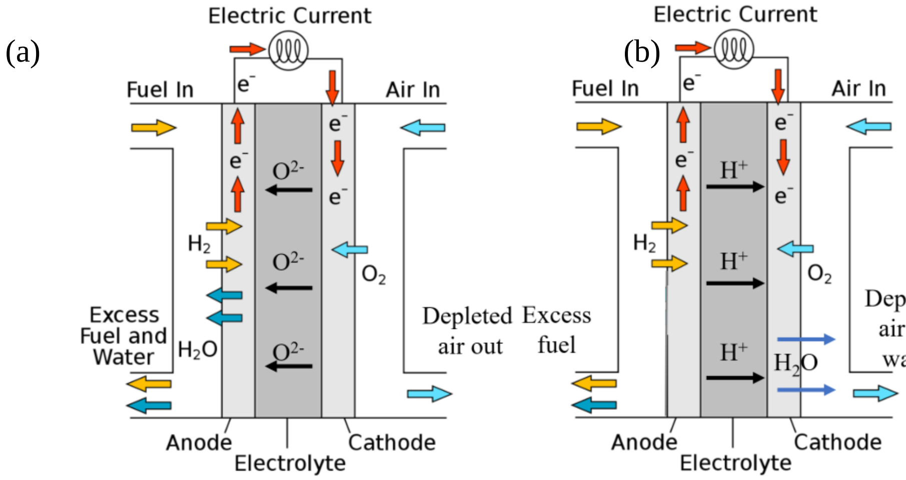

Figure 2.3. Schematic diagram of a solid oxide fuel cell (SOFC): (a) oxide-ion conducting electrolyte, and (b) proton conducting electrolyte during operation (adapted from 21)

As observed in **Figure 2.3**, the reaction at cathode can be represented as (21):

$$O_{2(g)} + 4_{e}^{-} \rightleftharpoons 2O^{2-} \qquad (2.1)$$

The oxygen ions then migrate through the solid electrolyte, furthermore, the oxide ions emerge at the anode and react with fuel (H_2 or CO) as follows:

$$2O^{2-} + H_{2(g)} \rightleftharpoons H_2O_{(g)} + 4e^- \tag{2.2}$$

$$2O^{2-} + CO_{(g)} \rightleftharpoons CO_{2(g)} + 4e^- \tag{2.3}$$

The half-cell reactions at the cathode and anode can be described using Kröger-Vink Notation, where $V_o^{''}$ is the oxygen ion vacancy and O_o^x is the oxygen ion in the electrolyte (3, 24, 25):

Cathode Reaction: $\frac{1}{2}O_{2(g)} + 2e' + V_o^{''} \rightarrow O_o^x$ (2.4)

Anode Reaction: $H_{2(g)} + O_o^x \rightarrow H_2O_{(g)} + V_o^{''} + 2e'$ (2.5)

The overall reaction can be expressed as:

$H_{2(g)} + \frac{1}{2}O_{2(g)} \rightarrow H_2O_{(g)}$ + electricity ($\Delta G = -237 \text{ kJ mol}^{-1}$) (2.6)

The cell voltage corresponds to the Gibbs free energy reaction, can be expressed as (3):

$$\Delta G = nF\Delta U_o \tag{2.7}$$

where n is the number of electrons involved in the reaction, F is Faraday constant and ΔU_o is the theoretical voltage of the cell for thermodynamic equilibrium in the absence of current flow, can be written as (3):

$$\Delta U_o = \frac{\Delta G}{nF} = \frac{-273}{nF} = 1.23\,V \tag{2.8}$$

The power output of SOFCs is affected by the cell and stack design since the cell area is directly proportional to the power output. Over the years, many models of SOFCs have been invented. However, since the 1960s most advancements have focused on the planar and tubular shapes. **Figure 2.4 (a)** shows the planar SOFC design, the cell components are a flat surface, and they are connecting electric series. Many companies are developing this configuration because of the design is well researched and there are advantages in this design. The structure is easily electroded by screen printing, provides short current pathways through interconnect, and can be stacked together with narrow channels to achieve a high-power density. However, this design has significant problems in heat-up and sealing (26).

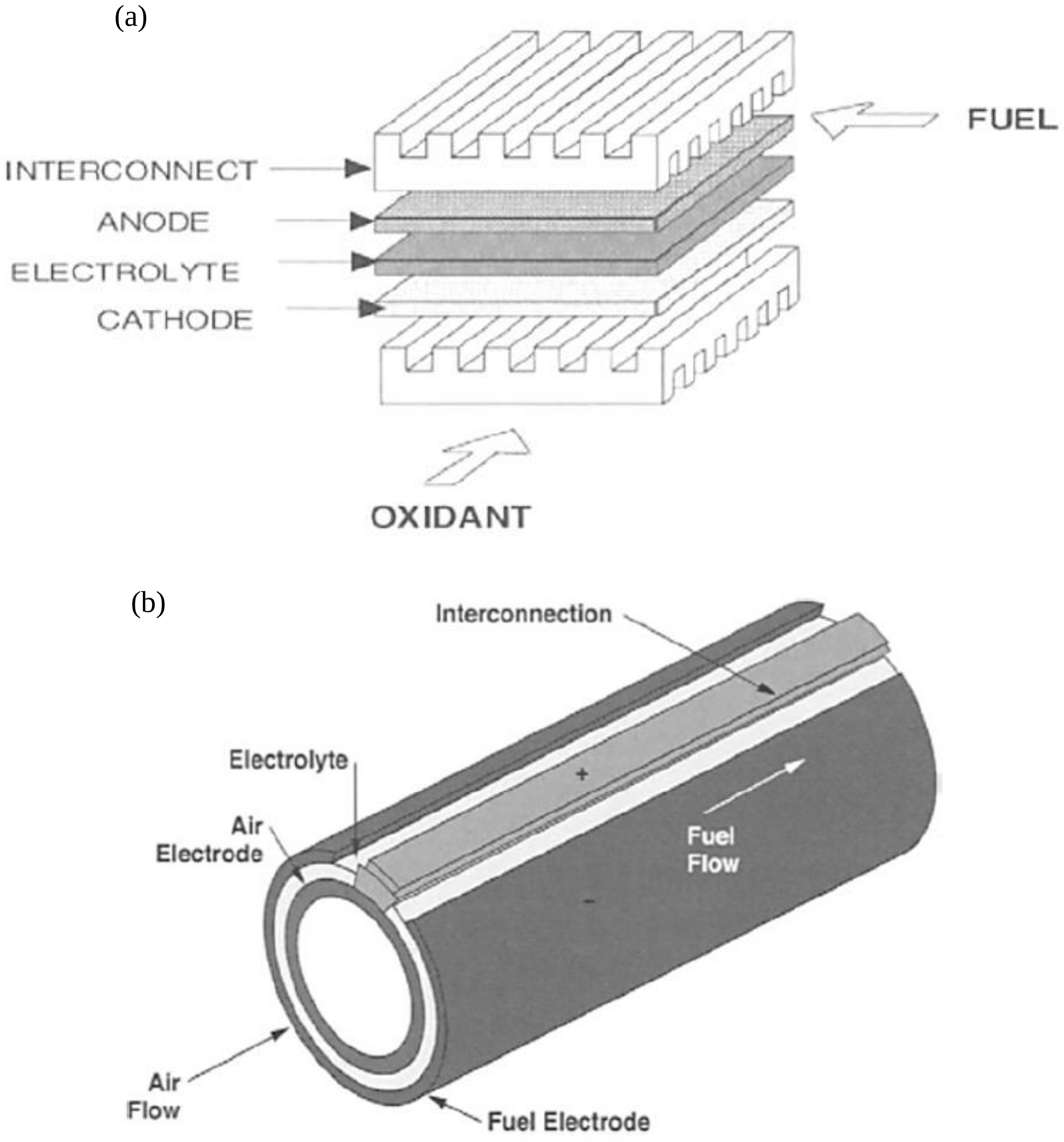

Figure 2.4. (a) Planar SOFC design, **(b)** Siemens Westinghouse tubular SOFC design (26).

The latest design is Siemens Westinghouse tubular cell (**Figure 2.4 (b)**). The electrode tube (lanthanum manganite-based) is produced by extrusion followed by sintering. A 40 µm thick layer of the YSZ (zirconia doped with ~10 mol% yttria) electrolyte is deposited by an electrochemical vapour deposition process. This design can eliminate the sealing problem in the planar design using an air feeder tube down the cell tube. While this design is expensive and large there are some advantages from this technology for the SOFC development: the cells can run for long periods, the efficiency can be maximised, methane can be used as fuel, and the emissions are low (26).

2.2 Electrode Materials

Electrodes are the critical components for the efficiency and operation of commercial SOFC devices. Each electrode (cathode and anode) must have high electro-catalytic activity and electronic conductivity to minimise the effective resistance. Furthermore, both cathode and anode must be mechanically, thermally and chemically compatible with suitable electrolyte (3, 27).

2.2.1 Cathode

Cathode improvement is essential for low-temperature SOFCs. Therefore, many researchers are developing cathodes with the outstanding electrochemical performance. The cathode SOFCs carries out several roles: catalytic activity, reduction of molecular oxygen, high ionic conductivity to transport the ions towards the electrolyte membrane, transport of charged species to the electrolyte and distribution of the electrical current associated with the oxygen reduction reaction (1, 23, 28). There are several requirements for SOFC cathode materials (3, 28).

1) Good electro-catalytic activity for oxygen reduction
2) Stability in oxidising environment
3) Good electronic and ionic conductivity

4) High strength
5) Non-volatility
6) Durability
7) Porous structure and stable at high temperature
8) Coefficient thermal expansion (CTE) matching with other components
9) Fabrication easily at a low cost

The oxygen reduction only occurs at the triple-phase boundary (TPB), where the cathode, electrolyte and air meet. Moreover, the reaction at the interface between SOFC cathode and an O^{2-} conducting electrolyte is (1, 29):

$$O_{2(g)} + 2V_o^{''} + 4e^{-} \leftrightarrow 2O_o^{x} \tag{2.9}$$

A schematic diagram of the triple-phase boundary (TPB) is represented in **figure 2.5**. Usually, the type of SOFC cathode is a p-type semiconductor and can be either an electronic or mixed ionic-electronic conductor (MIEC). When the SOFC cathode is a pure electronic conductor, the oxygen molecule adsorbs on the surface cathode. It diffuses over the surface towards the TPB where it becomes charged and incorporated in the electrolyte, and this cathode acts as an electron supplier. Increasing the TPB area can improve the performance of the cathode due to high current density and low overpotentials (29).

On the other hand, if the SOFC cathode is an MIEC, the oxygen molecules can be easily reduced on the surface and diffuse through the dense electrode. As a consequence, a competition between surface and bulk pathways are not avoided, the fastest one will determine the kinetics of the overall reaction. If the surface pathway is more determining, the electrode will have similar behaviour to a pure electronic conductor. However, if the oxygen migration is more dominantly through the bulk of the cathode, the dense thin layers will produce electrochemical reaction which will enhance the oxygen exchange at both MIEC/gas and MIEC/electrolyte interfaces. The cathode materials should have high oxygen exchange capacity and diffusivity (1, 29).

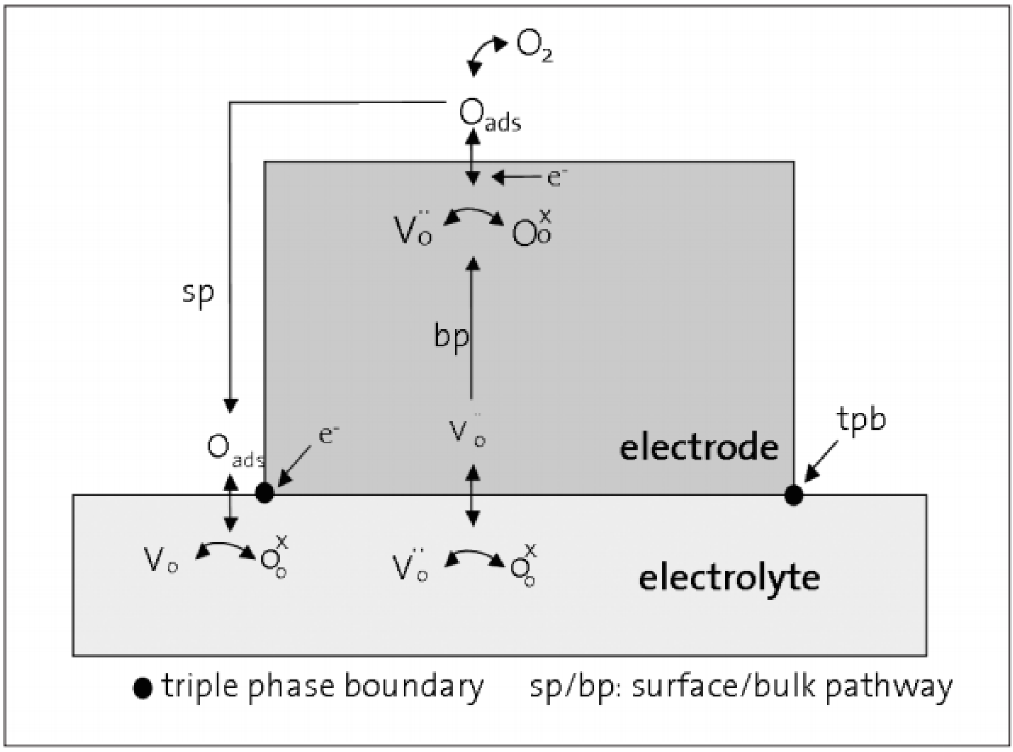

Figure 2.5. Schematic representation of oxygen reduction in a mixed ionic-electronic conductor: Surface and bulk reaction pathways are parallel and in competition. On the surface pathway, charge transfer occurs at the triple phase boundary (29).

Table 2.1 shows the relevant materials properties for state-of-the-art SOFC cathodes. For conventional SOFCs, $La_{1-x}Sr_xMnO_{3-\delta}$ (LSM) is the state-of-the-art of high operation temperature (800 – 1000°C) cathode materials due to the high electrochemical activity, high thermal stability, high electrical conductivity and good compatibility with YSZ, Gd-doped CeO_2 (GDC), and $La_{0.8}Sr_{0.2}Ga_{0.8}Mg_{0.2}O_{2.8}$ (LSGM) at operating conditions. However, this material is not suitable for intermediate-temperature SOFC system, because decreasing the operation temperature makes the polarisation resistance of LSM increases dramatically. A promising cathode material for intermediate temperature is $La_{1-x}Sr_xCoO_{3-\delta}$ (LSC), $La_{0.6}Sr_{0.4}Co_{0.2}Fe_{0.8}O_{3-\delta}$ (LSCF), and $Ba_{0.5}Sr_{0.5}Co_{0.8}Fe_{0.2}O_{3-\delta}$ (BSCF), the other compositions such as $La_{0.8}Sr_{0.2}FeO_{3-\delta}$, $Gd_{1-x}Sr_xCoO_{3-\delta}$,

$Sm_{1-x}Sr_xCoO_{3-\delta}$ (SSC), and $Sm_{0.5}Sr_{0.5}Co_{1-x}Fe_xO_{3-\delta}$ have been proposed to optimise and improve the electrochemical properties of cathode(9).

Table 2.1. Relevant materials properties for the state-of-the-art SOFC cathodes (9).

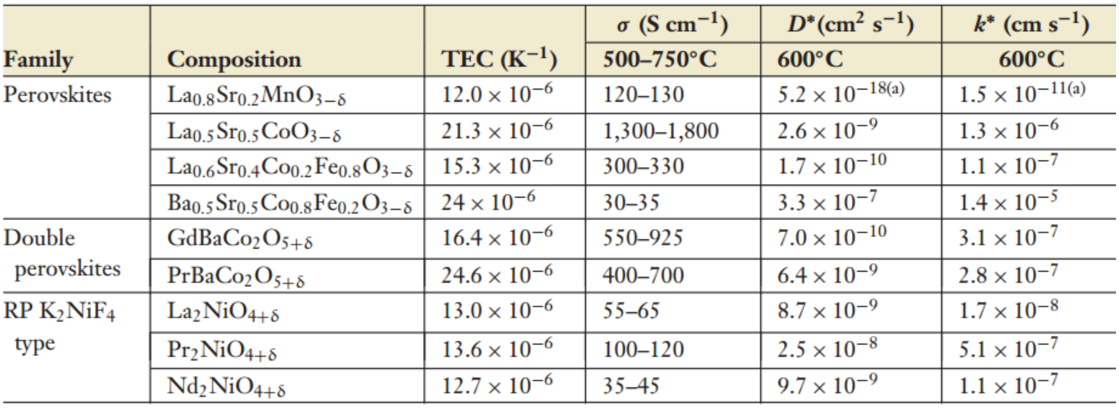

Family	Composition	TEC (K^{-1})	σ ($S\ cm^{-1}$)	D^*($cm^2\ s^{-1}$)	k^* ($cm\ s^{-1}$)
			500–750°C	600°C	600°C
Perovskites	$La_{0.8}Sr_{0.2}MnO_{3-\delta}$	12.0×10^{-6}	120–130	$5.2 \times 10^{-18(a)}$	$1.5 \times 10^{-11(a)}$
	$La_{0.5}Sr_{0.5}CoO_{3-\delta}$	21.3×10^{-6}	1,300–1,800	2.6×10^{-9}	1.3×10^{-6}
	$La_{0.6}Sr_{0.4}Co_{0.2}Fe_{0.8}O_{3-\delta}$	15.3×10^{-6}	300–330	1.7×10^{-10}	1.1×10^{-7}
	$Ba_{0.5}Sr_{0.5}Co_{0.8}Fe_{0.2}O_{3-\delta}$	24×10^{-6}	30–35	3.3×10^{-7}	1.4×10^{-5}
Double perovskites	$GdBaCo_2O_{5+\delta}$	16.4×10^{-6}	550–925	7.0×10^{-10}	3.1×10^{-7}
	$PrBaCo_2O_{5+\delta}$	24.6×10^{-6}	400–700	6.4×10^{-9}	2.8×10^{-7}
RP K_2NiF_4 type	$La_2NiO_{4+\delta}$	13.0×10^{-6}	55–65	8.7×10^{-9}	1.7×10^{-8}
	$Pr_2NiO_{4+\delta}$	13.6×10^{-6}	100–120	2.5×10^{-8}	5.1×10^{-7}
	$Nd_2NiO_{4+\delta}$	12.7×10^{-6}	35–45	9.7×10^{-9}	1.1×10^{-7}

Abbreviations: σ, overall conductivity; D∗, oxygen self-diffusion coefficient; k∗, oxygen surface exchange coefficient; RP, Ruddlesden-Popper; TEC, thermal expansion coefficient

2.2.2 Anode

The anode in SOFCs acts as electro-oxidation of fuel by catalysing the reaction and facilitating fuel access and product removal. Therefore, there are several requirements for SOFC anode materials (3, 24, 29-31):

1) High electronic conductivity
2) High ionic conductivity
3) High porosity
4) High strength
5) Effective oxidation catalyst
6) Chemical stability
7) Mechanical stability
8) Good thermal and chemical compatibility with electrolyte and interconnect materials

9) Durability
10) Low fuel transport resistance
11) Fabrication easily at a low cost

The oxygen ion reaction at the anode is:

$$\mathrm{H}_{2(g)} + O^{2-}\ (electrolyte) \rightarrow \mathrm{H}_2O_{(g)} + 2e^-\ (anode) \qquad (2.10)$$

The anode materials used in early experiments were metals, such as Pt-group or transition metals such as Ni. Nickel anodes were used in the vast majority of SOFCs because the cost is cheaper than other precious metals. However, nickel anodes alone have limitations such as a high thermal expansion coefficient and a tendency to sinter at operation temperature. To minimise these problems, Spacil (9, 32) developed a composite of an electrolyte (YSZ) and Ni, known as a cermet. Although the cermet can solve the nickel anode problem, other problems occur such as coarsening and expansion of the Ni (9, 32).

One of the newer materials examined for anode SOFCs is perovskite and perovskite-related structures. This oxide material has shown promising performance and has demonstrated redox tolerance, but only at high temperatures. In the intermediate temperature range, the catalytic activity reduces considerably with decreasing temperature. **Table 2.2** shows the properties and performance of some anode materials (9).

Table 2.2. Properties and performance of some anode materials (21).

Composition	**Electrolyte/cathode/ current collector**	**Anode performance**	**Cell performance/ maximum power density (mW/cm^2)**
Ni/NiO(/metal)-fluorite cermets 1Ni–YSZ cermet (50 vol.% Ni, 50 vol.% YSZ)2Ni–YSZ	8YSZ/LSM–8YSZ	σ_e ~10^2– 10^3 S/cm (2 x 10^4 S/cm for pure Ni)	1900 (800°C)
Ni-SDC (40–70% Ni)	YSZ/LSM–YSZ	σ_e~1260 – 4000 S/cm	980
Ni –$Sm_{0.2}Ce_{0.8}O_{1.9}$	SDC/SSC-SDC	σ_e~ 837	545
NiO-$Gd_{0.1}Ce_{0.9}O_{1.95}$	GDC/LSCF-GDC		909
Ag–$Ce_{0.8}Gd_{0.2}O_{1.9}$	SDC/LSCF-SDC	σ_e~ 1260	439
$Fe_{0.1}Ni_{0.9}$/YSZ	YSZ/LSM–YSZ	σ_e~ 417–633	~ 960
25% Cu–75% CeO_2; 25% Cu–75% Ni-YSZ			~ 450; ~ 380
$SrTiO_3$ based materials $La_{0.4}Sr_{0.6}TiO_{3-\delta}$ (LST)	Pt as current collector	σ_e~ 220	~ 200
$La_{0.3}Sr_{0.7}TiO_{3-\delta}$	LSGM/SSC	σ_e~ 49	570

2.3 Electrolyte Materials

The electrolyte position is sandwiched between the cathode and anode (illustrated in **Figure 2.3**). This component has an important role in realising ionic conduction. To obtain a good performance of SOFCs, the electrolyte materials should have high ionic conductivity and low electronic conductivity known as Mixed Ionic Electronic Conductivity (MIEC). Dominantly in nature an available electrolyte material is either having purely ionic or MIEC. The main requirements for an electrolyte to work efficiently are (3, 21, 29):

1) High oxygen ion conductivity (~0.1 S/cm at operating temperature)

2) Gas tightness
3) High density
4) High fracture toughness (fracture strength >400 Mpa)
5) Minimum electronic conductivity (less than 1%)
6) High strength
7) Thermodynamic and chemical stability in operational process
8) Negligible volatilisation
9) Durability
10) Coefficient thermal expansion (CTE) matched with other components

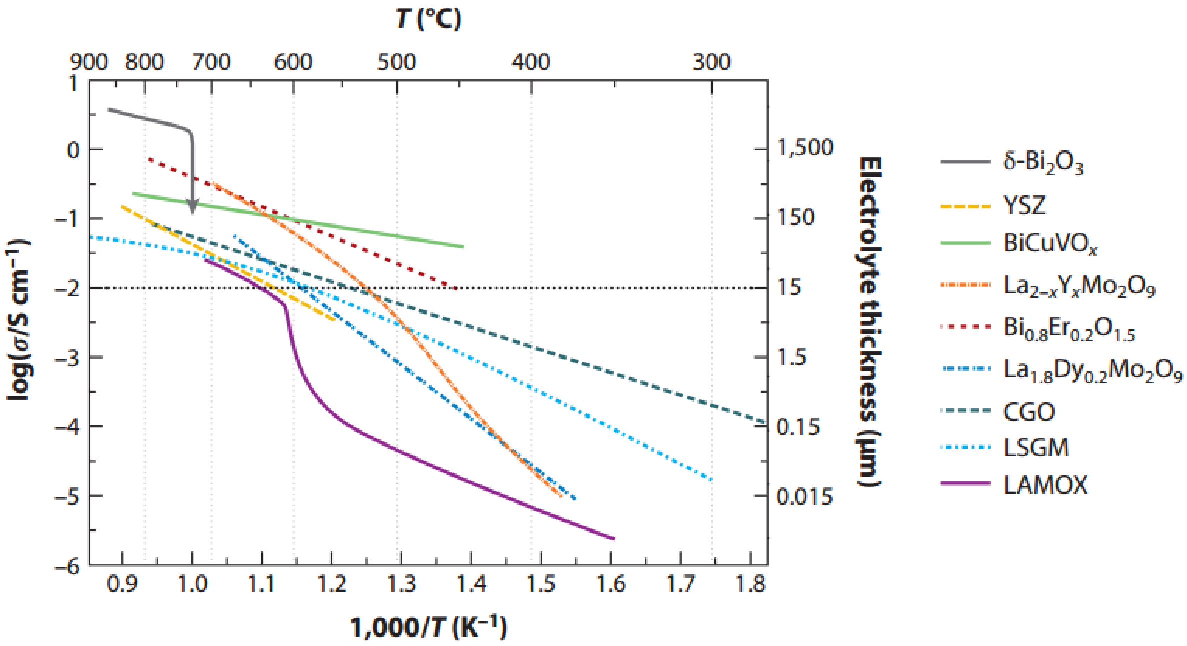

Figure 2.6. The oxygen ion conductivity of state-of-the-art SOFC electrolyte materials (9).

Figure 2.6 shows the ionic conductivity versus temperature of state-of-the-art electrolyte materials. Some of the electrolyte materials in SOFCs are made from fluorite, perovskite and apatite structures (9). However, in recent years many researchers have focused on fluorite structure (AO_2) because this structure is relatively open and exhibits large tolerance for the atomic disorder (33). The most fruitful oxide electrolyte from fluorite structure based on one of the group IVB oxides (i.e. ZrO_2, HfO_2, CeO_2, or ThO_2) with addition of either an alkaline earth oxide (i.e. Sc_2O_2, Y_2O_3) or a rare earth oxide (34, 35).

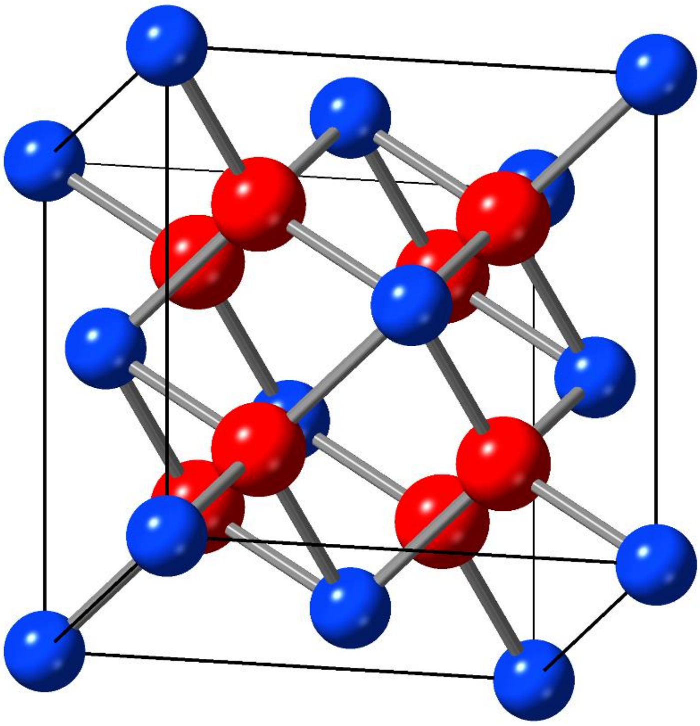

Figure 2.7. The fluorite structure (AO_2) adopted by ZrO_2 and CeO_2. The small blue spheres represent A^{4+} ions and large red spheres O^{2-} ions.

The fluorite crystal structure is illustrated in **Figure 2.7.** The blue spheres represent a tetravalent cation (A^{4+} ions) which occupy the face-centred positions with red anions (O^{2-} ions) in the eight tetrahedral sites between them. A well-known material of this structure is acceptor doped ZrO_2. Since pure zirconia is not a good ion conductor and requires high temperature (above 2300°C) to adopt cubic fluorite symmetry, acceptor dopants at cation sublattice are introduced to stabilise the cubic structure at lower temperatures and to increase the oxygen vacancies concentration (36). This can be described using Kröger–Vink notation:

$$MO + Zr_{Zr}^{\times} + O_O^{\times} \rightarrow M_{Zr}^{''} + V_O^{\bullet\bullet} + ZrO_2 \qquad (2.11)$$

$$R_2O_3 + 2Zr_{Zr}^{\times} + O_O^{\times} \rightarrow 2R_{Zr}' + V_O^{\bullet\bullet} + 2ZrO_2 \tag{2.12}$$

where M is a divalent cation, R is a trivalent cation, and $V_O^{\bullet\bullet}$ is a compensating oxygen vacancy. The substitution ions are using larger cations with a lower valence (37). A typical divalent dopant is Ca^{2+} which produces calcium-stabilized zirconia (CSZ), while a typical trivalent acceptor is Y^{3+} that produces yttria-stabilised zirconia (YSZ) (36).

Yttria-stabilized zirconia (YSZ) has recently been the most widely used of fluorite structure in SOFCs. Although this material has high conductivity, the material requires high operation temperature (~1000°C), which leads to a decrease in efficiency and stability of the cell (33). Moreover, the high-temperature operation makes the technology relatively expensive and can cause long-term degradation problems (38). Lowering the temperature of operation to the intermediate temperature (IT) between 400°–700°C can improve the long-term performance stability, less degradation, faster start-up, lower overall cost and extend the application to portable devices (38, 39, 40).

It is therefore important to locate alternative electrolyte materials for IT-SOFCs with high ionic conductivity. **Figure 2.8** illustrates the main sources of ionic carriers in oxides and their mobilities. The large numbers of carriers generated via deviation from stoichiometry or doping are indicated by broken arrows (8). Among the materials in **Figure 2.8**, δ-phase Bi_2O_3 (fluorite structure) has the highest ionic conductivity for the oxygen in conductors, almost 1-2 orders greater than YSZ (41, 42). However, this material is easily reduced under reductive atmospheres and structurally instable (33, 41). Using $(Bi_2O_3)_{0.8}(Er_2O_3)_{0.2}$ oxide as an electrolyte has a problem with instability under anode conditions in SOFCs (39,43). Thus, ceria-based electrolytes have gained much attention as an alternative electrolyte for solid oxide fuel cell replacing yttria-stabilised zirconia (YSZ).

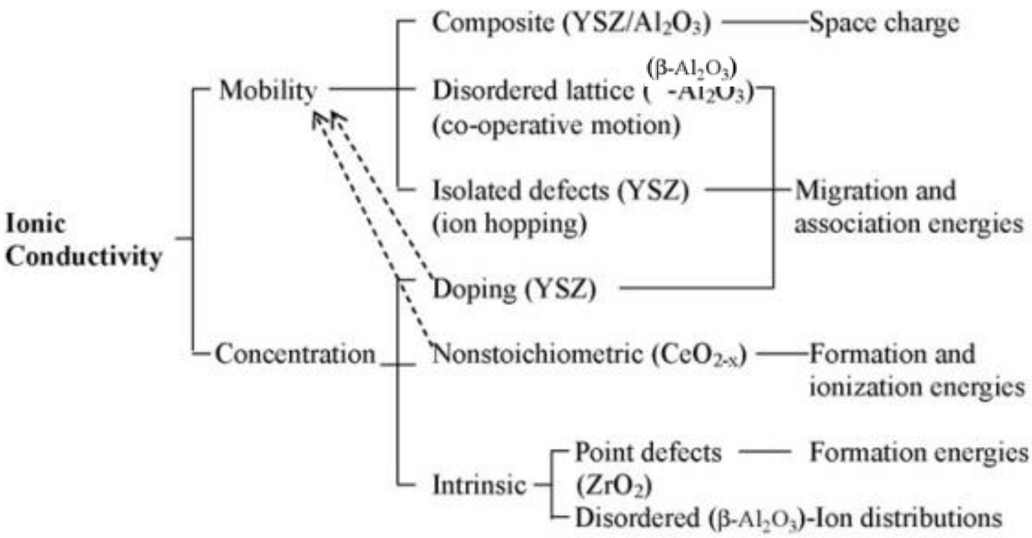

Figure 2.8. The major sources of ionic carriers in oxides (8).

Ceria-based electrolytes have shown an order of magnitude higher ionic conductivity at lower temperatures than yttria stabilised zirconia. A larger ionic radius of cerium ions (Ce^{4+} = 0.97 Å in 8-coordination) than of Zr^{4+} (0.84 Å) make the fluorite structure in this material more open for the migration of oxygen ions (44). Ceria-based oxides have both intrinsic and extrinsic oxygen vacancies to provide the hopping from oxygen ions. The intrinsic vacancies came from a reduction equilibrium of Ce^{3+}/Ce^{4+}, while the extrinsic vacancies are a result from substitution of aliovalent into the ceria lattice (45). Oxygen vacancy defects arise from a reduction of CeO_2 to $CeO_{2-\delta}$, the reduction reaction can be written in Kröger–Vink notation as:

$$2Ce_{Ce} + O_O \rightarrow \frac{1}{2}O_{2(g)} + V_O^{\bullet\bullet} + 2Ce'_{Ce} \qquad (2.13)$$

where Ce'_{Ce} represents Ce^{3+} in Ce^{4+} lattice site. Since pure CeO_2 has very low ionic conductivity, ~3.13×10^{-3} S cm^{-1}, the substitution of aliovalent doping has shown a significantly increase in ionic conductivity (46).

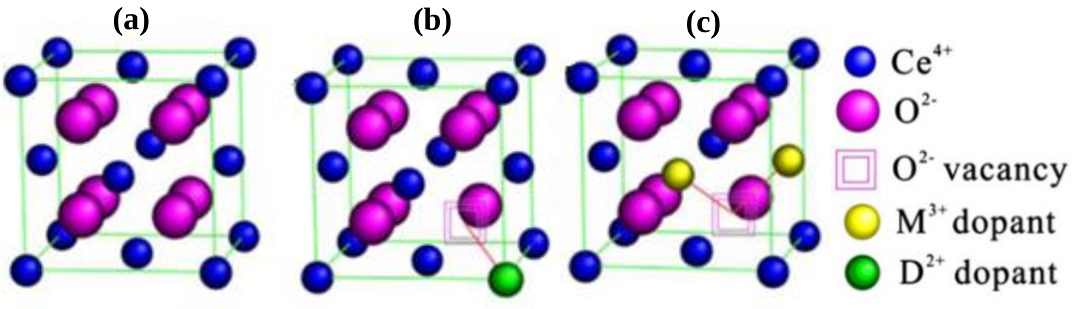

Figure 2.9. (a) A ceria fluorite structure; (b) ceria defect structure with one divalent dopant and corresponding oxygen vacancy; (c) crystalline structure of defect-fluorite ceria with two trivalent dopants and one charge-compensating oxygen vacancy (40).

Figure 2.9 (a) shows a unit cell of ceria fluorite structure, with Ce^{4+} ions forming face-centred-cubic structure and oxygen ions forming a simple cubic sublattice. When the ceria host lattice is doped with lower valance cations, the compensating oxygen vacancies will be introduced to achieve charge neutrality (47). The substitution mechanism of divalent dopant cation doping (DO) into cerium oxide can be described by following defect equation:

$$DO \overset{CeO_2}{\longleftrightarrow} D_{Ce}'' + O_O^x + V_O^{\cdot\cdot} \qquad (2.14)$$

the substitution of divalent dopant cation is accompanied by an oxygen vacancy for only one D^{2+} dopant as shown in **Figure 2.9** (b). Whereas for trivalent dopant cations, the formation of oxygen vacancy is associated with two M^{3+} ions, **Figure 2.9** (c).

$$M_2O_3 \overset{CeO_2}{\longleftrightarrow} 2M_{Ce}' + 3O_O^x + V_O^{\cdot\cdot} \qquad (2.15)$$

The effect of divalent dopant using alkaline earth oxides (CaO, SrO, BaO and MgO) in ceria was studied by Arai et al. (48), and **Figure 2.10** shows the ionic conductivity of these doped oxides. Ca^{2+} (1.12 Å), and Sr^{2+} (1.26 Å), dopants in ceria make a significant improvement of oxide ionic conductivity, while barium and magnesium dopants show slight improvement due to the large size mismatch of Ba^{2+} (1.42 Å), Mg^{2+} (0.89 Å), and the Ce^{4+}(0.97 Å).

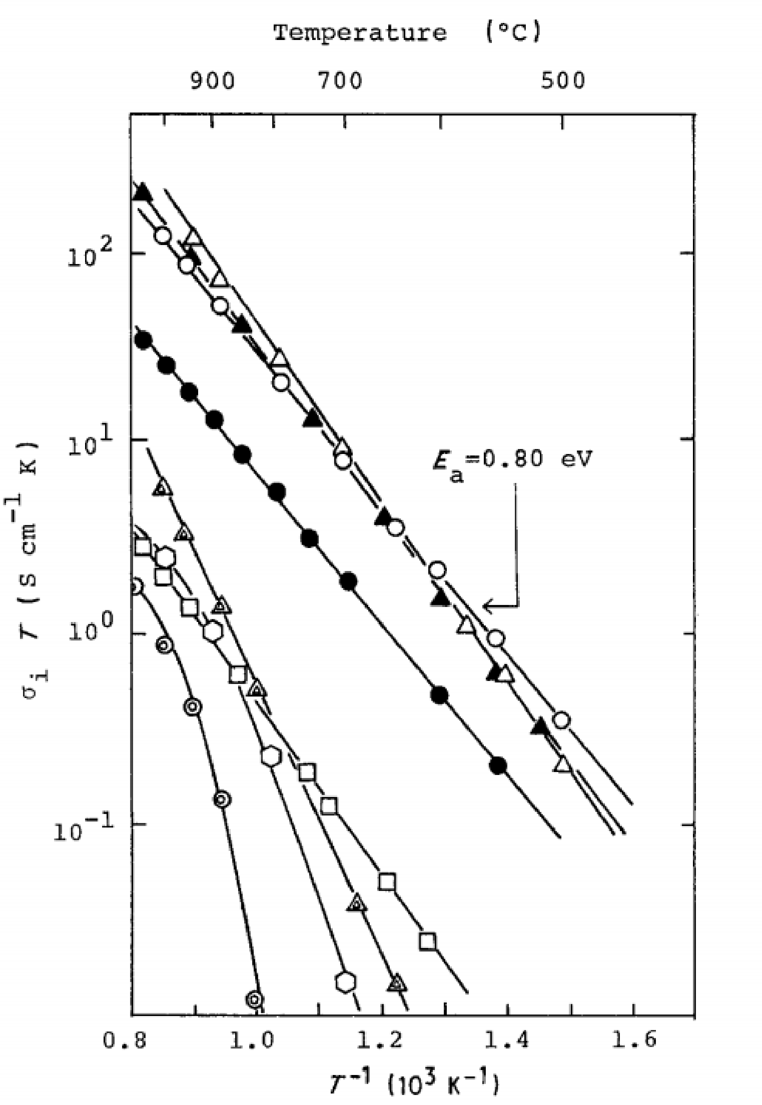

Figure 2.10. Arrhenius plots of ionic conductivity for (Δ) $(CeO_2)_{0.90}(CaO)_{0.10}$, (▲) $(CeO_2)_{0.70}(CaO)_{0.30}$, (○) $(CeO_2)_{0.90}(SrO)_{0.10}$, (●) $(CeO_2)_{0.70}(SrO)_{0.30}$, (□) $(CeO_2)_{0.90}(BaO)_{0.10}$, (⬡) $(CeO_2)_{0.90}(MgO)_{0.10}$, (◬) $(ZrO_2)_{0.85}(CaO)_{0.15}$, (◎) CeO_2 (48).

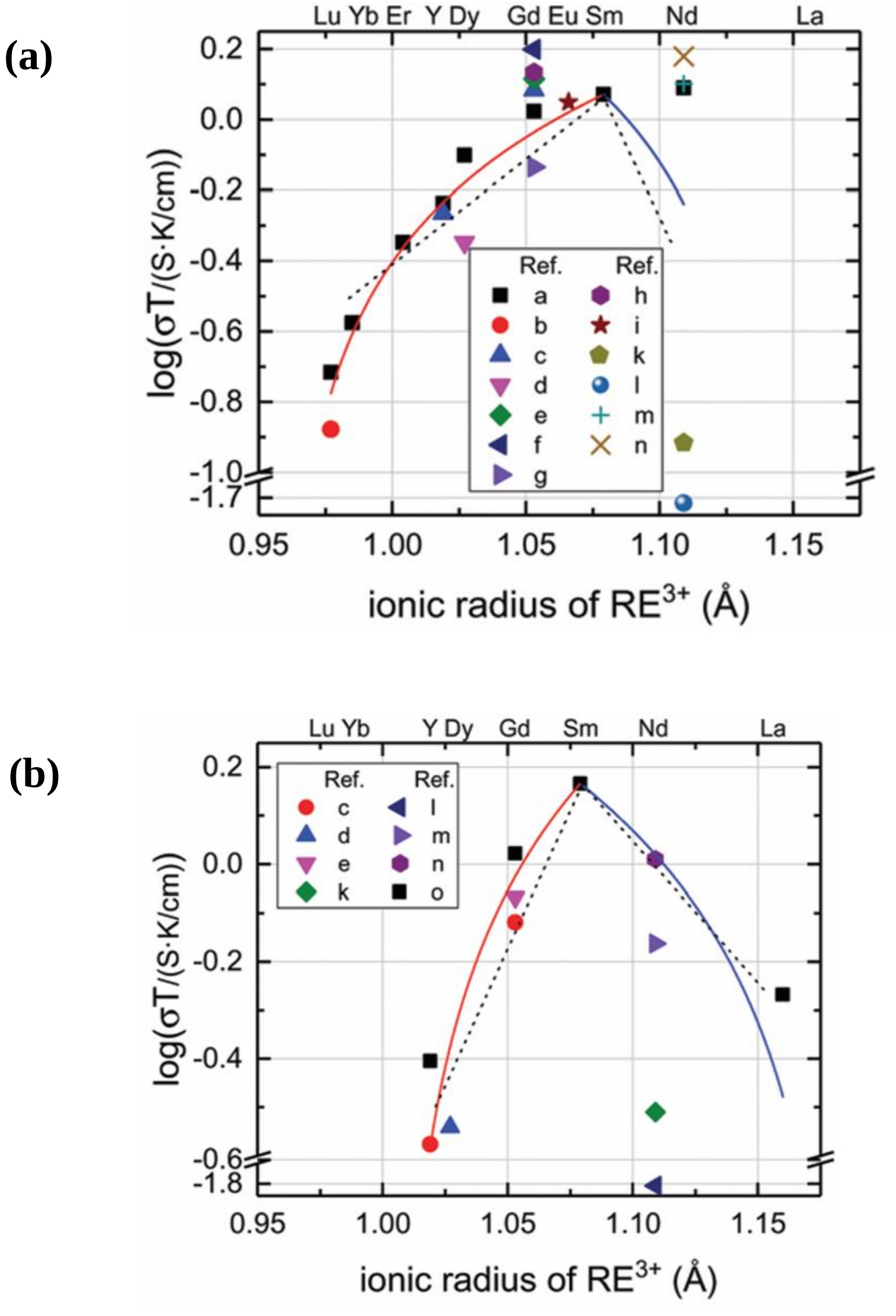

Figure 2.11. Arrhenius plots of ionic conductivity as a function of dopant radius at 400°C. (a) Solid solution series of $Ce_{1-x}Re_{x}O_{2-x/2}$ with x = 0.1; (b) x = 0.2 according to references a(38), b(35), c(49), d(50), e(51), f(52), g(53), h(54), i(55), k(56), l(57), m(58), n(59), o(60). The solid lines show the linear relationship between the ionic radius and the conductivity, while the dashed lines show linear relationship between the ionic radius and the logarithmic conductivity (61).

The trivalent dopants of various rare earth oxides in ceria have been studied by many researchers. **Figure 2.11** shows the bulk conductivity at 400^{o}C from various trivalent dopants. Although the concentration of trivalent dopants is the same, the ionic conductivity among them is different (12). The ionic conductivities of Gd, Eu, Sm and Nd-doped ceria at $x = 0.1$ (**Figure 2.11a**) have similar value. For $x = 0.2$ (**Figure 2.11b**), ceria doped samarium shows the highest conductivity among the other dopants. The dashed lines are the linear relationship between the ionic radius and the logarithmic conductivity, which in this section show a volcano-type (61). Moreover, the conductivity is found at a maximum value around Gd and Sm doped ceria. This result shows that trivalent doped ceria has higher ionic conductivity than divalent cation doped ceria (44).

Kilner and co-workers (9, 62) has suggested evaluating the changes in lattice parameter as a function of the dopant concentration to minimise the oxygen vacancy trapping. Lattice simulation was also developed to recognise the importance of elastic energy terms due to size mismatch of the dopant cations. Kim (8, 10) proposed empirical equations between dopant size and ionic conductivity. The concept of critical ion radius (r_c) for the dopant was developed, and it was shown that the critical ionic radius for trivalent dopant in ceria is 0.1038 nm, close to the ionic radius of Gd^{3+}. Kilner (9, 47) suggested that the conductivity is affected by ionic size mismatch between the host and the dopant, the smaller ionic size mismatch the higher the conductivity will be. **Table 2.3** shows the ionic radius for selected elements.

Table 2.3. Ionic radius for selected elements (63).

Ion	**Ionic radius (Å)**	**Coordination Number**	**Ionic radius (Å)**	**Coordination Number**
Ce^{4+}	0.97	VIII	0.87	VI
Eu^{3+}	1.07	VIII	0.947	VI
Gd^{3+}	1.06	VIII	0.938	VI
Tb^{3+}	1.04	VIII	0.923	VI
Dy^{3+}	1.03	VIII	0.912	VI
Ho^{3+}	1.02	VIII	0.901	VI
Er^{3+}	1.00	VIII	0.89	VI
Tm^{3+}	0.99	VIII	0.88	VI
Yb^{3+}	0.98	VIII	0.868	VI

Ou *et al.* (64) reported that microstructural inhomogeneity has a negative effect on the ionic conductivity of a material due to the interactions between the segregated dopant cations and the oxygen vacancies. Phase homogeneity is a major priority because the oxygen conduction path is mostly aligned along the oxygen vacancies. An inhomogeneous oxygen conduction path can produce isolated oxygen vacancies, which do not contribute to the oxygen conductivity. Non-Vegard behaviour in lattice parameters has been observed in the compounds Ce-Dy, Ce-Ho and Ce-Gd mixed-oxide structures (65, 66).

The main concerns using ceria-based electrolytes is poor densification behaviour. There are two ways to reduce the sintering temperature; the first is to introduce sintering aids, such as a transition metal oxide (TMO) to increase the sintering rate. The second is to decrease the initial particle size because the high surface energy of the nanoparticles can densify at a much lower temperature (39, 67 – 69). TMO can occasionally lead to mixed ionic electronic conductivity which could be undesirable in solid electrolyte. Therefore, it is more appropriate to employ nanoparticles of materials for improving the densification of ceria based solid electrolyte materials.

2.3.1 Local defect and migration of oxide ions in ceria fluorite structure

In many studies, it has been shown that the formation of oxygen vacancies is required for oxygen migration in the ceria fluorite structure (70). The intrinsic defect formation reaction is the Schottky reaction (eqn. 2.16) and Anti-Frenkel reaction (eqn. 2.15) (70).

$$nul \leftrightarrow V_{Ce}^{''''} + 2V_o^{\cdot\cdot} \tag{2.16}$$

$$O_o^x \leftrightarrow O_i^{''} + V_o^{\cdot\cdot} \tag{2.17}$$

Another defect formation mechanism is the interstitial M^{3+} due to the extrinsic mechanism of trivalent dopants.

$$2M_2O_3 \leftrightarrow 3M_{Ce}^{'} + M_i^{\cdot\cdot\cdot} + 6O_o^x \tag{2.18}$$

The relative positions of a substitutional trivalent dopant to oxygen vacancies at first, second and third neighbour sites within the crystal structure is shown in **Figure 2.12** (a). Dopant cations prefer to occupy the nearest neighbour (NN) or next nearest neighbour (NNN) sites. **Figure 2.12** (b) - (g) demonstrate the most stable defect cluster among all possible fluorite crystal structures. The electrostatic interaction between intrinsic or extrinsic oxygen vacancies caused a defect clustering (dimer or trimer type). Dimer ($M_{Ce}^{'}V_o^{\cdot\cdot}$) or the smallest neutralised defect ($2M_{Ce}^{'}1V_o^{\cdot\cdot}$) are randomly distributed through the ceria host matrix. On the other hand, trimer ($M_{Ce}^{'}V_o^{\cdot\cdot}M_{Ce}^{'}$) is more favourable than isolated defects and was recognised as the basic defect associate (17, 40, 71). These defects trap the oxygen vacancies in the cluster and make them immobile (17, 72). Trimer has association energy more than dimer (73). Ohashi et al. (74) reported that the defect complex with two Gd^{3+} and one oxygen vacancy in heavily doped solid solutions leads to a decrease in the ionic conductivity.

$M'_{Ce} + V_O^{\cdot\cdot} \leftrightarrow \{M'_{Ce} + V_O^{\cdot\cdot}\}$ (Dimer defect associate) (2.19)

$M'_{Ce} + V_O^{\cdot\cdot} \leftrightarrow \{M'_{Ce} + V_O^{\cdot\cdot} M'_{Ce}\}$ (Trimer defect associate) (2.20)

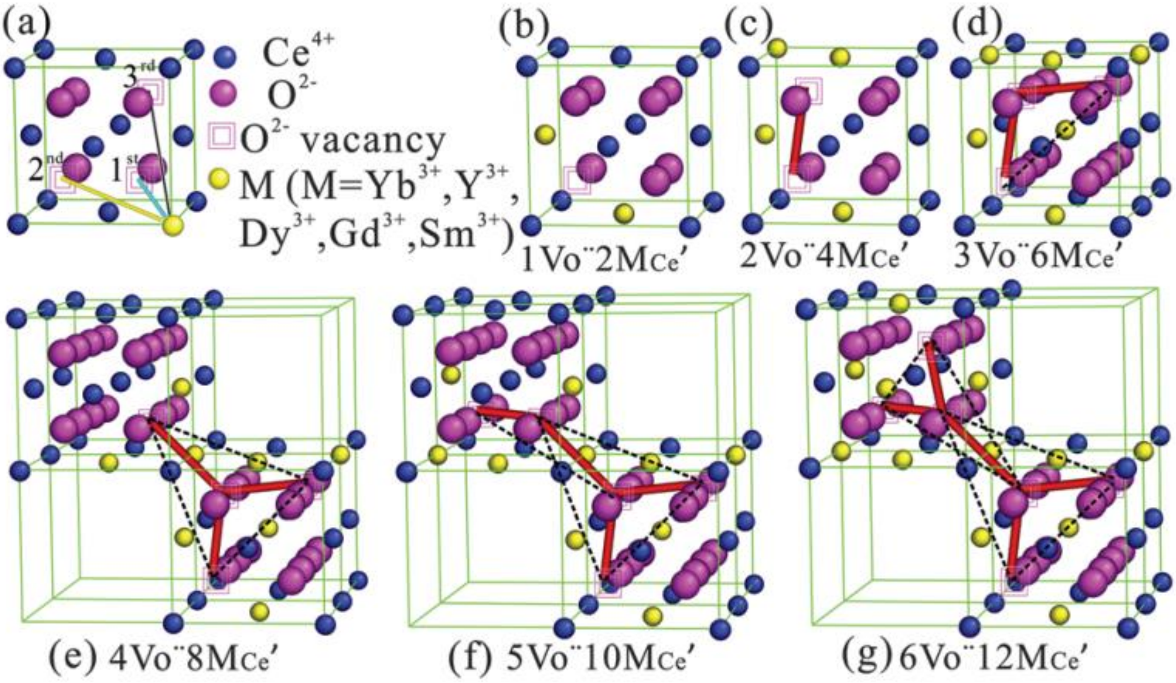

Figure 2.12. (a) Ceria defect fluorite crystal structure with oxygen vacancy located at 1st, 2nd and 3rd neighbour sites. (b) to (g) are oxygen vacancies configuration of defects cluster (ranging from $1V_O^{\cdot\cdot}$ to $6V_O^{\cdot\cdot}$) and associated dopant cations all situated at the 1st neighbour sites (64).

Doping with a trivalent dopant in ceria-based oxide causes the oxide ions to jump. The migration interaction among the ions in the rare-earth-doped ceria is shown in **Figure 2.13.** The oxygen ion migration changes the position during the jump; the interaction can be expanded in the initial, transition, and final state. Since the oxygen vacancies are easier to track, the migration position is labelled based on the defects (61).

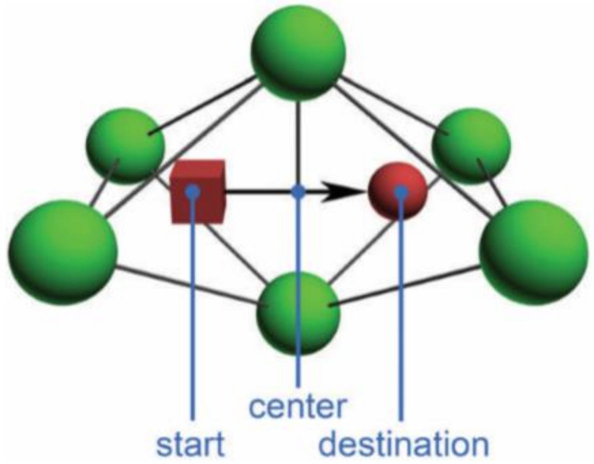

Figure 2.13. The interaction of oxygen migration in rare earth doped ceria. Green spheres are cerium ions, the red box is an oxygen vacancy and the red sphere is an oxygen ion (61).

Using density-functional theory, Nakayama et al. (70) calculated the formation energies of point defects and their migration properties in ceria doped rare-earth oxide. It was found that the ionic radii of the neighbouring dopant cations play an essential role in oxygen vacancy migration energy. It was identified that trapping (or repelling) of an oxygen vacancy at the NN site of the RE^{3+} dopant, and reduction (or enlargement) of the migration barrier by RE^{3+} doping are factors which affect the migration.

Model A

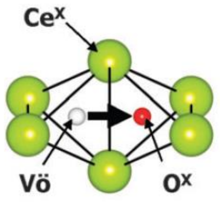

Model B

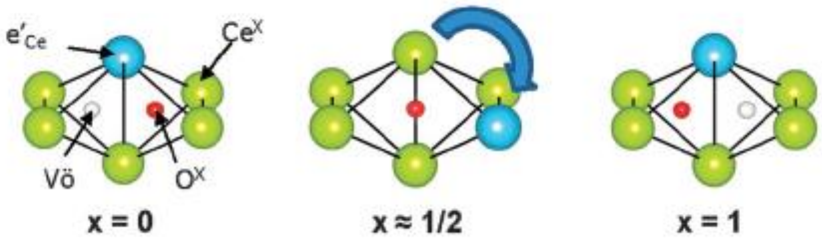

Model C

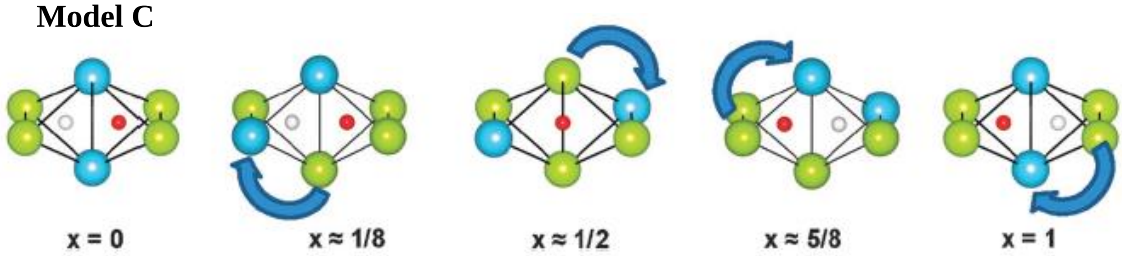

Model D

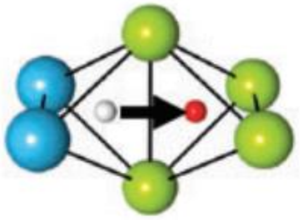

Model E

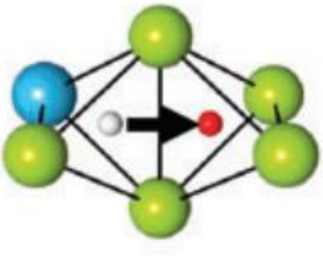

Figure 2.14. Five types of nearest-neighbour (NN) cation configurations for oxygen vacancy migration. Cerium ions (green spheres), rare-earth ions (blue spheres), oxygen ions (red spheres) and oxygen vacancies (white spheres) (70, 75).

The five possible cation configurations in the tetrahedral site were studied by Martin et al. (61, 70, 75) (**Figure 2.14**). The configuration of the oxygen vacancy and the RE^{3+}-dopants in models A, B and C before and after the jump remains unchanged (symmetric cases). Models D and E are asymmetric because the association energy before and after the jump is different (70).

Based on the five possible cation configurations, Kottegen et al. (61) calculated the oxygen-ion conductivity as a function of doping amount using *ab initio* density functional theory (DFT) and Kinetic Monte Carlo (KMC) simulations. If the presence of the dopant changes the migration energy for forward and backward jumps of specific ionic configuration, the energy contribution is referred to as *trapping* (**Figure 2.15**). Meanwhile, if the migration energy is identical, the energy contribution is referred to as *blocking* (**Figure 2.16**).

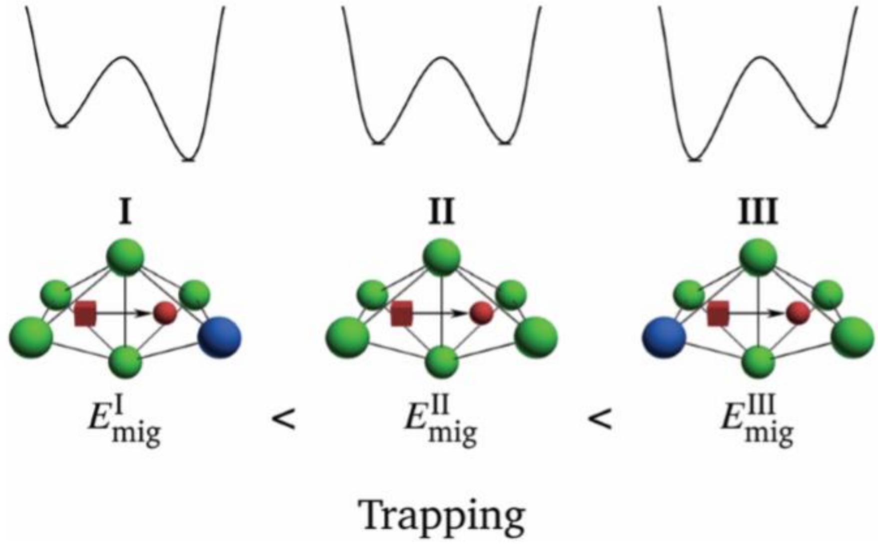

Figure 2.15. The trapping effect in fluorite crystal structure. The upper diagram show energy system as a function of reaction coordinate for migration configurations in rare-earth doped ceria (61).

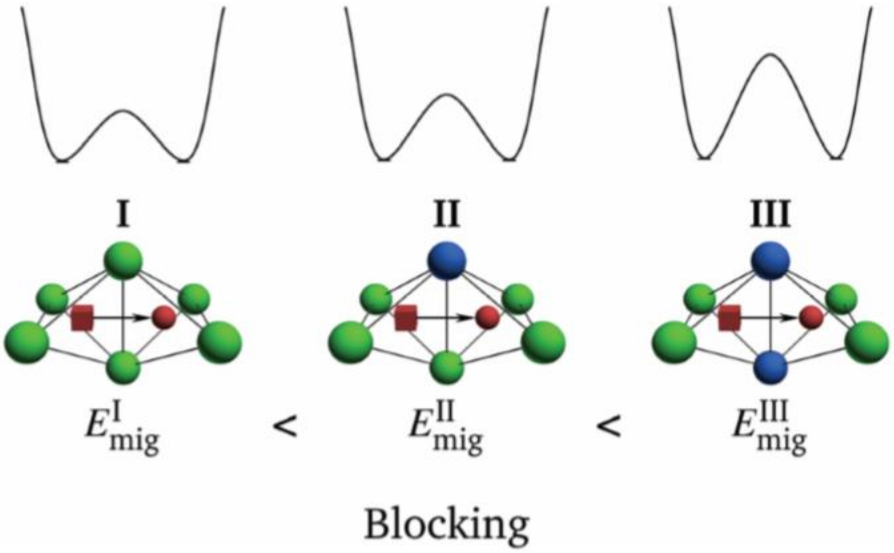

Figure 2.16. The blocking effect in fluorite crystal structure. The upper diagram show energy system as a function of reaction coordinate for migration configurations in rare-earth doped (61).

2.3.2 Co-doped ceria electrolyte

Future improvement of ceria-based electrolyte is using double doping either alkali earth or rare-earth cations. Two substitutional ions (co-doped) are used to minimise the activation energy and optimise the conductivity in electrolyte IT-SOFCs. Herle and co-workers (78) found 10-30% improvement of total ionic conductivity using co-doped material at the same total dopant concentration with singly doped material. Andersson et al. (77) used DFT calculations on the cerium oxide-based materials. It was concluded that the ideal dopant for CeO_2 is between Pm^{3+} and Sm^{3+}. Since Pm^{3+} is radioactive, it was suggested the double substitution electrolyte between larger cation and a smaller cation, either (a) Nd^{3+} and Sm^{3+} or (b) Pr^{3+} and Gd^{3+}. The co-doped materials show improvement in ionic conductivity compared with each element separately.

Mori et al. (78) introduced the concept of effective index (E_i) for ionic conductivity in doped ceria electrolyte using ionic radii and the amount of oxygen vacancies. Effective index can be defined as:

$$\text{Effective index } (E_i) = \frac{\text{avg.r}_\text{c}}{\text{eff.r}_\text{o}} \times \frac{r_d}{r_h} \quad (2.21)$$

where avg.r_c is the average ionic radius of cation, r_d is average ionic radius of dopant and r_h is average ionic radius of host cation (Ce^{4+}). While eff.r_o is the effective oxygen ion radius, which can be given by

$$\text{eff.r}_\text{o} = 1.4 \times \frac{2-\delta}{2} \quad (2.22)$$

where δ is the level of expected oxygen vacancy and 1.4 Å is oxygen ionic radius. The doped cerium oxide achieves the ideal fluorite structure for maximum ionic conductivity when the effective index is close to 1.

Shirbhate and co-workers (17) found that double doping with aliovalent cation in the ceria-based electrolyte system can raise the ionic conductivity more than one order of magnitude than single doped. It was also found that the Arrhenius plot of the conductivity (**Figure 2.17**) of aliovalent (divalent-trivalent) co-dopant pair depicts break in the slope at a temperature between 500 – 600°C. This break slope is mainly because of the change in activation energy. For single doped ($Ce_{0.85}Ca_{0.15}O_{2-\delta}$) and isovalent doped ($Ce_{0.85}Ca_{0.075}Sr_{0.075}O_{2-\delta}$) a single slope in all conductivity curves occurs.

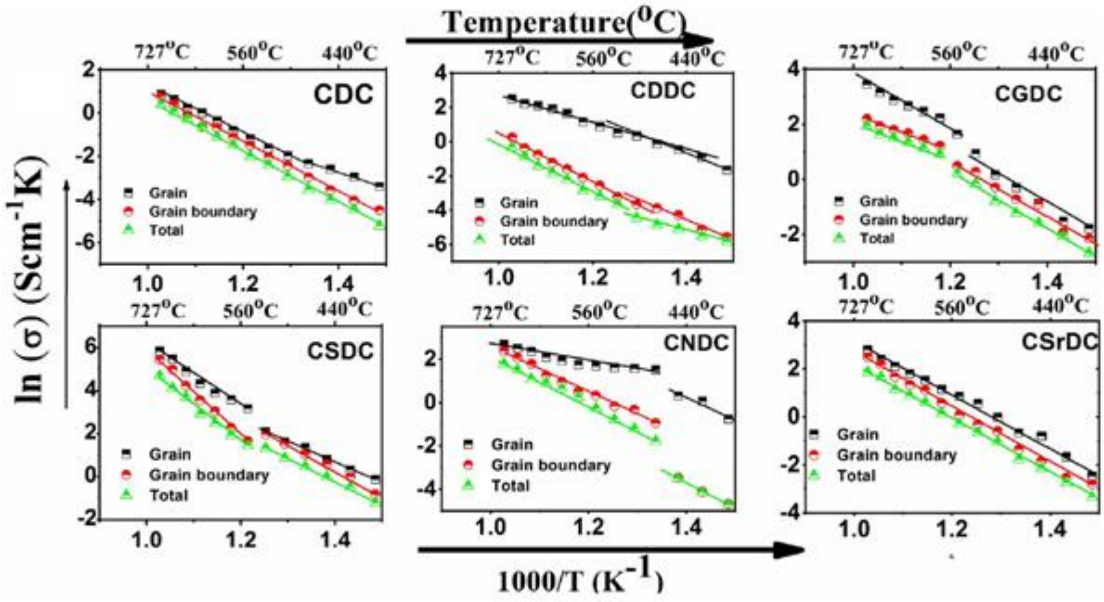

Figure 2.17. Arrhenius plots of doped and co-doped ceria systems: $Ce_{0.85}Ca_{0.15}O_{2-\delta}$ (CDC), $Ce_{0.85}Ca_{0.075}Dy_{0.075}O_{2-\delta}$ (CDDC), $Ce_{0.85}Ca_{0.075}Gd_{0.075}O_{2-\delta}$ (CGDC), $Ce_{0.85}Ca_{0.075}Sm_{0.075}O_{2-\delta}$ (CSDC), $Ce_{0.85}Ca_{0.075}Nd_{0.075}O_{2-\delta}$ (CNDC), and $Ce_{0.85}Ca_{0.075}Sr_{0.075}O_{2-\delta}$ (CSrDC) (17).

Double doped ceria can suppress the ordering of oxygen vacancies and increase the configuration entropy and therefore result in an improvement of total conductivity and reduction of activation energy (79). The configuration entropy of multi doped ceria shows higher than singly doped ceria. Omar et al. (35) found that co-doping can increase the ionic conductivity because the elastic strain in the doubly doped system is negligible compared with the single doped. Venkataramana and co-workers (80) also reported that co-doping enhances the relative density, oxygen vacancy concentration and doubles the total conductivity compare with the single doped. **Table 2.4** shows the summary of co-doping effect on the ionic conductivity of the various SOFC electrolytes.

Table 2.4. Effect of co-doping on the ionic conductivity of various SOFC electrolytes

No	**Compositions**	**Conductivity (S/cm)**	**Operating temperature (°C)**
1.	$Ce_{0.8}Sm_{0.2}Li_{0.05}O_{1.825}$ (13)	1.81×10^{-3}	700
2.	$Ce_{0.8}Sm_{0.12}Gd_{0.08}O_{1.825}$ (14)	5.28×10^{-2}	750
3.	$Ce_{0.8}Sm_{0.1}Gd_{0.1}O_{1.9}$ (15)	1.8×10^{-2}	600
4.	$Ce_{0.85}La_{0.075}Sm_{0.075}O_{2-\delta}$ (16)	2.3×10^{-2}	650
5.	$Ce_{0.85}Ca_{0.15/2}Sm_{0.15/2}O_{2-\delta}$ (17)	1.1×10^{-1}	250–700
6.	$Ce_{0.80}Pr_{0.10}Dy_{0.10}O_{2-\delta}$ (81)	6.8×10^{-3}	500
7.	$Ba_{0.10}Ga_{0.10}Ce_{0.80}O_{3-\delta}$ (82)	7.1×10^{-2}	650
8.	$Ce_{0.84}Gd_{0.15}Cu_{0.01}O$ (83)	7.81×10^{-3}	600
9.	$Ce_{0.83}Dy_{0.14}Ca_{0.03}O_{1.9}$ (84)	1.45×10^{-2}	600
10.	$Ce_{0.78}Sm_{0.2}Ca_{0.01}O_{1.89}$ (85)	2.04×10^{-3}	700
11.	$Ce_{0.8}Sm_{0.1}Gd_{0.1}O_{1.9}$ (86)	0.147×10^{-3}	800
12.	$Li_{0.03}Ce_{0.776}Gd_{0.194}O_{1.858}$ (87)	3.5×10^{-2}	600
13.	$Ce_{0.8}Gd_{0.2}O_{1.9}$ doped Co (0.5 mol%) $Ce_{0.8}Gd_{0.2}O_{1.9}$ doped Li (2 mol%) (88)	9.72×10^{-2} 1.26×10^{-1}	800
14.	$Ce_{0.8}Gd_{0.10}Pr_{0.10}O_{1.90}$ (89)	5.1×10^{-2}	750
15.	$Ce_{0.8}Gd_{0.14}Pr_{0.06}O_{1.90}$ (90)	1.25×10^{-1}	800
16.	$Ce_{0.8}Sm_{0.10}Er_{0.1}O_{1.90}$ (91)	11.2×10^{-3}	600
17.	$Gd_{0.11}Pr_{0.04}Ce_{0.85}O_{2-\delta}$ (92)	Grain interior: $(2.1 \pm 0.05).\ 10^{-4}$ Grain boundary: $(3 \pm 1).10^{-9}$	300 200

18.	$Lu_xNd_yCe_{1-x-y}O_{2-\delta}$ (x+y = 0.05, 0.10, 0.15, and 0.20) (35)	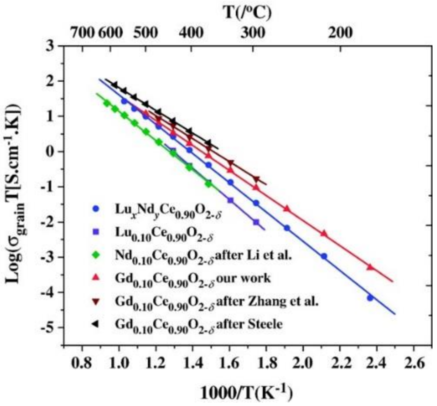	250 – 700 °C
19.	$Ce_{0.8}Gd_{0.2-x}M_xO_{2-\delta}$ (for M: Sm, x = 0, 0.01, 0.02, 0.03, 0.04, 0.05, and 0.1, and for M: Bi, La, and Nd, x = 0.05) (93)	$Ce_{0.8}Gd_{0.1}Sm_{0.1}O_2$-δ: 6.50 x 10^{-2}	700
20.	$Ce_{0.9}(Sm_xNd_{1-x})_{0.1}O_{1.95}$ (x = 0, 0.5, 1) and $Ce_{1-x}(Sm_{0.5}Nd_{0.5})_xO_\delta$ (x = 0.05, 0.10, 0.15, 0.20) (94)	$Ce_{0.9}(Sm_{0.5}Nd_{0.5})_{0.1}O_{1.95}$: 1.0 x 10^{-2}	550
21.	$Sm_{x/2}Nd_{x/2}Ce_{1-x}O_{2-\delta}$ (x= 0.01- 0.20) (5)	$Sm_{0.75}Nd_{0.75}Ce_{0.85}O_2$-δ = 14.0 ± 0.2 x 10^{-3}	550
22.	$Ce_{0.82}Sm_{0.16}Sr_{0.02}O_{1.90}$ and $(Li/Na)_2CO_3$. (95)	SSDC/35LNCO = 7.48 x 10^{-2}	500
23.	$Ce_{0.8}Gd_{0.2-x}M_xO_{2-\delta}$ (for M: Bi, x = 0-0.1, and for M: Sm, La, Nd, x=0.02) (11)	$Ce_{0.8}Gd_{0.1}Bi_{0.1}O_2$-δ = 4.46 x 10^{-2} $Ce_{0.8}Gd_{0.1}Bi_{0.1}O_2$-δ = 1.26 x 10^{-2}	700 500
24.	Mg-doped $Ce_{0.9}Sm_{0.1}O_{1.95}$ and $Ce_{0.9}Gd_{0.1}O_{1.95}$ (containing 0 and 4 mol% MgO), $Ce_{0.9}Nd_{0.1}O_{1.95}$, $Ce_{0.9}(Sm_{0.5}Nd_{0.5})_{0.1}O_{1.95}$, and $Ce_{0.9}(Gd_{0.5}Nd_{0.5})O_{1.95}$ (96)	$Ce_{0.9}(Gd_{0.5}Nd_{0.5})O_{1.95}$ = 1.5 x 10^{-2} $Ce_{0.9}Sm_{0.05}Nd_{0.05}O_{1.95}$ = 1.3 x 10^{-2}	600

25.	$Ce_{0.80}Nd_{0.20-x}Y_xO_{1.90}$ (x = 0.0, 0.02, 0.03, 0.04 and 0.06) (97)	$Ce_{0.80}Nd_{0.18}Y_{0.02}O_{1.90}$ = 1.28 x 10^{-2}	600
26.	$Ce_{0.85}(Sm_{0.6}Nd_{0.4})_{0.15}O_{2-\delta}$ (98)	0.018	550
27.	$Ce_{1-x-y}Gd_xM_yO_{2-\gamma}$, M = Er, Dy, or Nd and 0.0 ≤ x,y ≤ 0.1 (99)	$Ce_{0.85}Gd_{0.1}Er_{0.05}O_{1.925}$ = 15.84 x 10^{-3} $Ce_{0.85}Gd_{0.1}Dy_{0.05}O_{1.925}$ = 17.51 x 10^{-3} $Ce_{0.85}Gd_{0.05}Nd_{0.1}O_{1.925}$ = 29.62 x 10^{-3}	700
28.	$Ce_{0.85}Sm_{0.15-x}R_xO_{1.9}$, R = Y, Gd, Pr, Tb (100)	$Ce_{0.85}Sm_{0.1}Y_{0.05}O_2$ (grain) = 9.84 x 10^{-3} $Ce_{0.85}Sm_{0.1}Y_{0.05}O_2$ (grain boundary) = 6.83 x 10^{-3} $Ce_{0.85}Sm_{0.05}Gd_{0.1}$ O_2 (bulk) = 8.40 x 10^{-3} $Ce_{0.85}Sm_{0.05}Gd_{0.1}$ O_2 (grain boundary) = 6.13 x 10^{-3} $Ce_{0.85}Sm_{0.1}Tb_{0.05}O_{0.2}$ (grain) = 7.81 x 10^{-3} $Ce_{0.85}Sm_{0.1}Tb_{0.05}O_{0.2}$ (grain boundary) = 5.23 x 10^{-3} $Ce_{0.85}$ $Sm_{0.05}Pr_{0.1}O_{0.2}$ (grain) = 1.8 x 10^{-2} $Ce_{0.85}$ $Sm_{0.05}Pr_{0.1}O_{0.2}$ (grain boundary) = 1.1x 10^{-2}	600

2.3.3 Conductivity and activation energy

The ionic conductivity of the electrolyte is affected by various factors, such as grain boundaries, local structure, microdomains, grain size, composition, dopants, impurities, and processing. As shown in **Figure 2.18**, the parameters (composition, processing and microstructure) are correlated to each other (8).

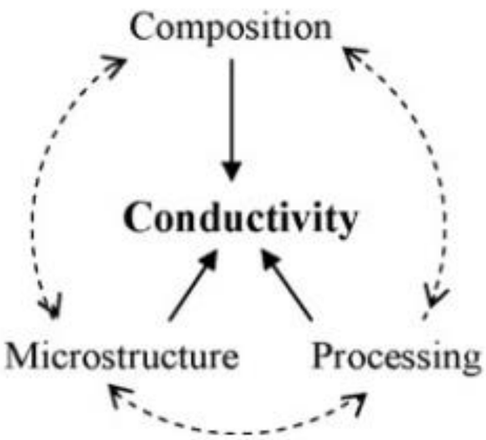

Figure 2.18. The correlation of composition, microstructure, processing, and electrical conductivity in polycrystalline materials under given temperature and surrounding atmosphere (8).

For ceria-based electrolytes the charge carriers are oxygen vacancies. The Arrhenius equation is often applied to oxygen ionic conductors:

$$\sigma T = A \exp\left(\frac{-E_a}{kT}\right) \tag{2.23}$$

where T is the absolute temperature, σ is the ionic conductivity, A is pre-exponential constant, E_a is the activation energy, and k is the Boltzmann constant. Normally, the activation energy includes the energy for formation and migration of oxygen vacancies. In the extrinsic regime, the migration energy is more dominant than formation energy. In this case, the migration energy for the doped oxide ion conductors can be represented as activation energy (8).

At high temperature, the Arrhenius plots in ceria-based electrolyte start to bend due to the different bulk conduction mechanism which associated to dissociation of defect complexes (typically higher than 400°C) (4, 101-104). It is seen from **Figure 2.19** that a critical temperature (T_c) occurs at ~ 410 ^{o}C. The model explained that the oxygen vacancies combine with the dopant cations to form complex defects below T_c, while above T_c, the oxygen vacancies appear to be mobile without any interaction with the dopant cations (49). The conductivity plot breaks mainly because of the temperature regime that caused different operating conduction mechanism and associated with the activation energy.

The total activation energy in the doped ceria system is the sum of the enthalpy of migration (ΔH_m) of oxygen ions and the association enthalpy (ΔH_a) of oxygen vacancies from defect cluster (dimer or trimer type).

$$E_a = \Delta H_m + \Delta H_a \tag{2.24}$$

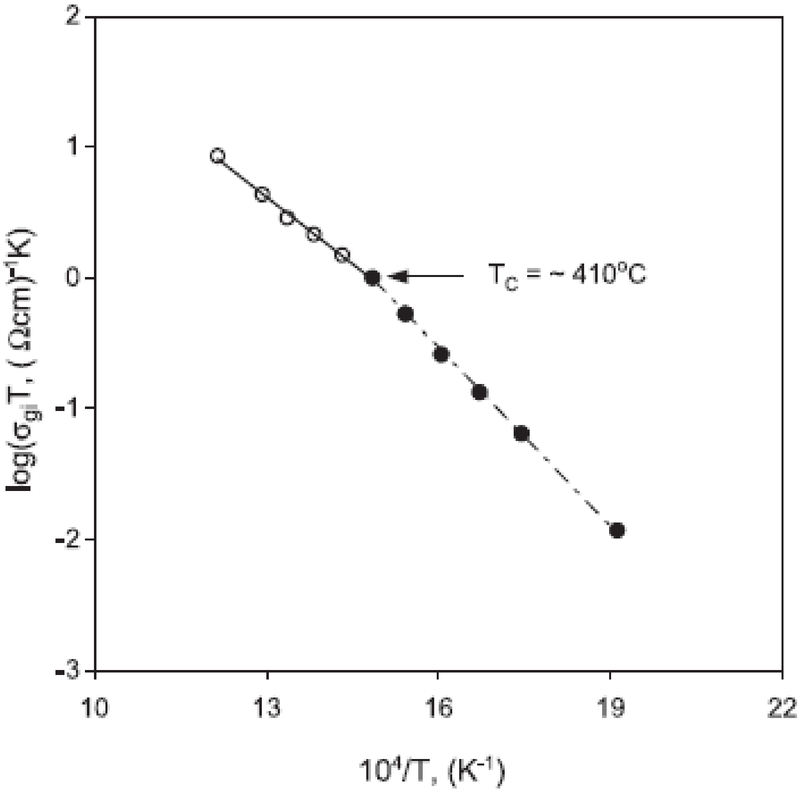

Figure 2.19. Arrhenius plot of grain conductivity for CGO. A critical temperature (TC) is observed at ~ 410°C (49).

The effect of porosity on the grain and grain-boundary conductivity is shown in **Figure 2.20**. In this figure, it can be observed that the bulk conductivity only depends on the porosity throughout the sintering process and increases monotonously with increasing relative density (r.d). The grain boundary conductivity is dependent on both porosity and grain size, which has significant improvement in conductivity on crossing from densification to grain-growth regimes (105). The modified brick-layer model on bulk conductivity as a function of porous ceramics can be expressed as (105):

$$R_b = (f_{por})^{-1}.\rho_B.\frac{L}{A} \tag{2.25}$$

Whereas of the grain boundary resistivity:

$$R_{gb} = (f_{por})^{-1}.\rho_{gb}.\frac{L}{A}.\frac{\delta_{gb}}{d_g} \tag{2.26}$$

where R_b is electrical resistance of bulk, f_{por} is factor of porosity ($0 \leq f_{por} \leq 1$), A is electrode area, L is thickness of sample, ρ_B is resistivity of the bulk process, R_{gb} is grain boundary resistance, ρ_{gB} is resistivity of the grain boundary, d_g is the averaged grain size, and δ_{gb} is average grain-boundary thickness.

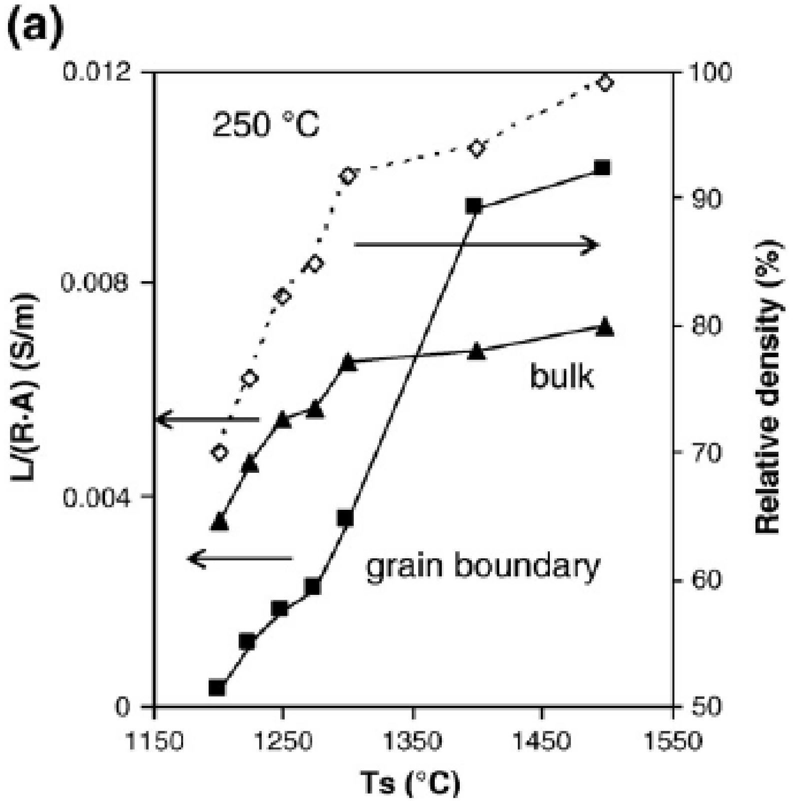

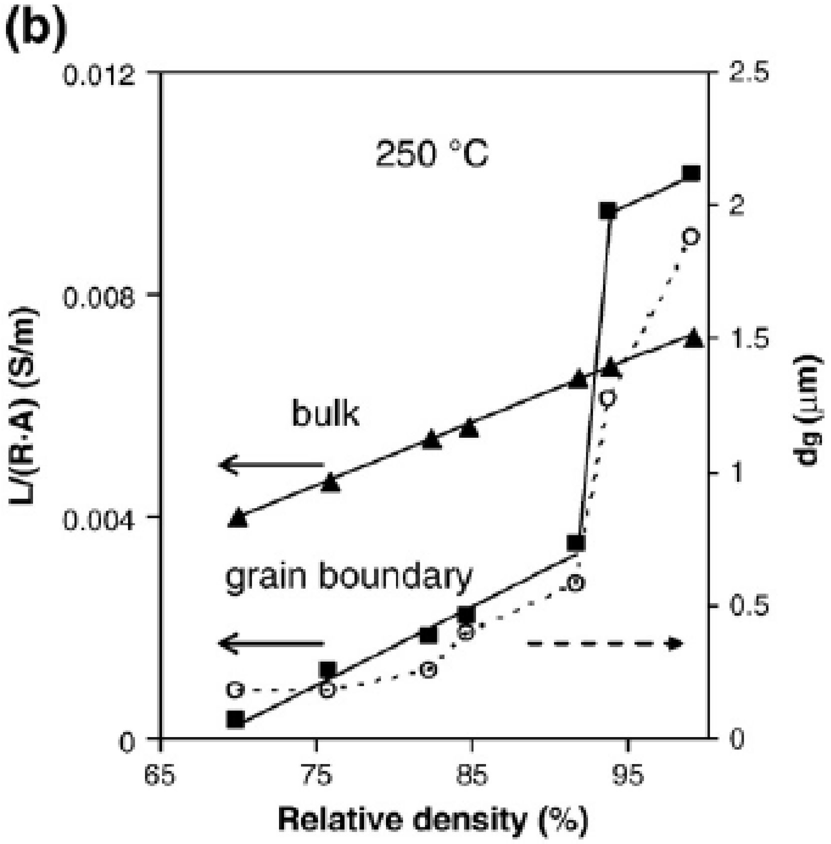

Figure 2.20. (a) Normalised conductance of relative density, bulk and grain-boundary at 250°C as a function of sintering temperature; (b) bulk and grain boundary normalised conductance at 250°C as a function of relative density. The average grain size in open circles as a function of relative density represented in secondary y-axis (105).

Wang et al. (106) found that the bulk conductivity is dependent on the level of densification (**Figures 2.21 and 2.22**). Using an unconventional two-step sintering (TSS) process, the ionic conductivity of dense CGO could be enhanced almost one order of magnitude higher than sintering from a single-step sintering process.

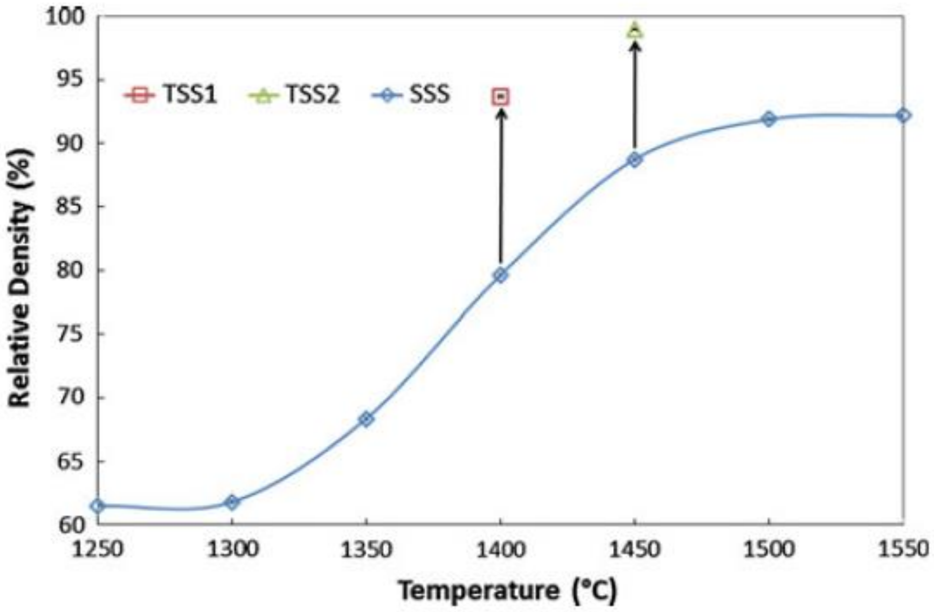

Figure 2.21. Densification curve of CGO samples with single-step sintering (SSS) and two-step sintering (TSS) (106).

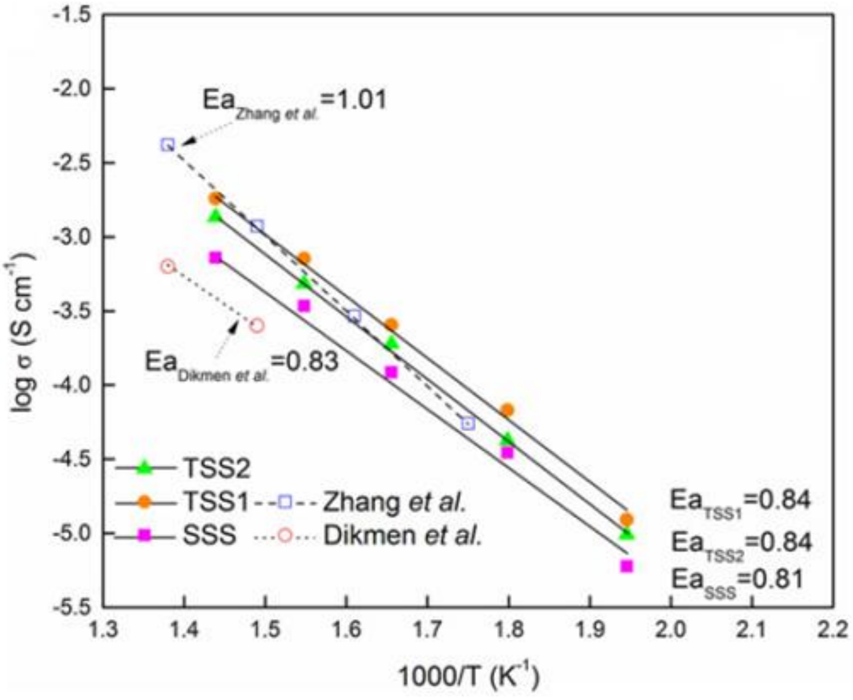

Figure 2.22. Arrhenius plot of ionic conductivity of CGO using a different sintering route (106).

2.4 Powder Synthesis Methods

In general, the synthesis methods can be divided into two categories: mechanical and chemical methods. A mechanical method, which used the mechanical forced to reduce the particle size, is widely used in ceramic processing. While the chemical method generally used to prepare the advanced ceramic powder due to the high purity of a final powder (107).

2.4.1 Mechanical Methods

Mechanical methods are the widely used process in the ceramic industry. The methods are inexpensive and widely used. However, the final products have limited purity and homogeneity and large particle size. The most common process from this method is milling, e.g. high-compression roller mills, jet mills, and ball mills (107).

2.4.2 Chemical Methods

In recent year, the new developments of chemical methods in ceramic processing have been reported. The final powders produced by these methods have high purity, good composition control and chemical homogeneity. The examples of these methods are co-precipitation and sol-gel (107).

In the co-precipitation method, the different salt or alkoxide solutions are mixed together to produce the desired chemical compositions, followed by hydrolysis with water (calcination process). The final powder of this method depends on the controlling of pH, temperature and concentration (107).

The sol-gel method gives a colloidal suspension of solid particles in the liquid phase (sol), and their transformation into a continuous solid skeleton enclosing a continuous liquid (gel). The advantages of the sol-gel method are to avoid generation of dangerous dust, produced at room temperature, potentially homogeneous powders, a wide variety of microstructures possible, and high purity powders. Starting compounds in this process are called precursors, which is surrounded by various ligands (appendages not including another metal atom), i.e. the precursor for aluminium oxide include inorganic salts such as $Al(NO_3)_3$ and organic compounds such as $Al(OC_4H_9)_3$. In the sol-gel process, precursors are surrounded by various ligands. The overview of the sol-gel process is presented in **Figure 2.23**, and in the first stage of this process, a metal alkoxide precursor reacts quickly with water, which is called the hydrolysis process. This reaction can be complete or partial hydrolysis. In a partially hydrolysed reaction, two molecules can link together in a condensation reaction, followed by polymerisation process. Hydrolysis and condensation process are an ongoing reaction so that the length of the polymer chains and viscosity of sol-gel precursor increase concurrently. Moreover, ageing of gels will occur; during this stage, the viscoelasticity of gel is reduced until the rigid gel formed. The rigid gel is dried and fired to result in a fine powder (1, 3, 108).

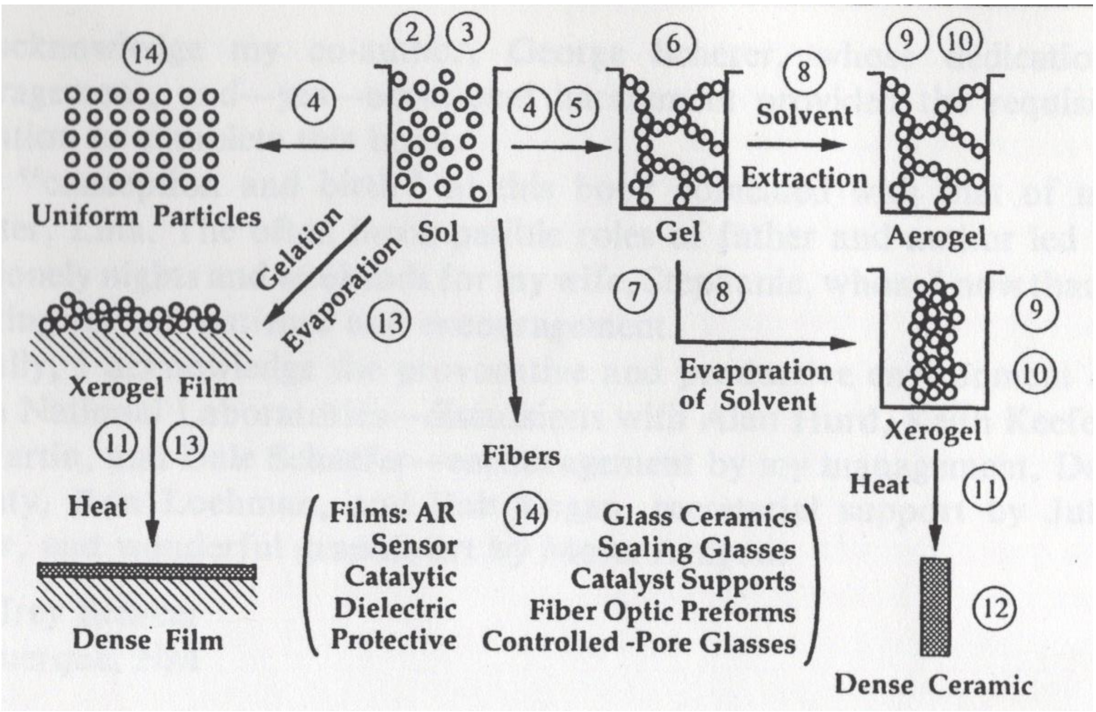

Figure 2.23. Overview of sol-gel process (108).

2.4.2.1 Sodium Alginate Sol-gel Synthesis Method

Alginate is a biopolymer mainly extracted from the cell wall of brown algae and consists of 1,4'-linked β-D-mannuronic acid (M) and its C-5 epimer α-L-guluronic acid (G). The monomer chain can link together in sequences as –GG– or –MM– structures or as –GM– block copolymer (**Figure 2.24**). The alginate can be made from both algae and bacterial sources. Still, the commercial alginate comes from algae, this source will affect the copolymer composition, sequences and molecular weight of alginate. The commercial alginate production in industry is approximately 30,000 units per annum, and this value is estimated less than 10% of the biosynthesised alginate material. A large amount of production is due to the abundance of algae in water bodies. The primary industries that use alginates in their process are food, biomedical and pharmaceutical industries; alginate is used as a thickening, gel-forming, colloidal stabilising, binders and disintegrants agents (109-113).

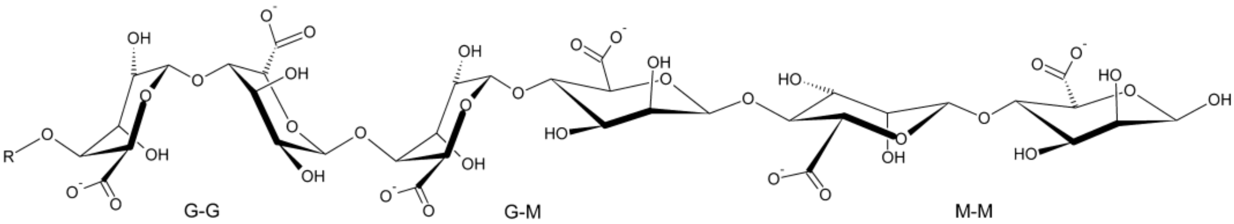

Figure 2.24. A section of alginate polymer (deprotonated) showing the two different G and M monomers and the three different sequential units (114).

Alginate can display gelling when interacting with cations such Na^+ and Ca^{2+}, and this gel formation is linked to specific and strong interactions between the divalent cations and long stretches of G units in the alginate. Moreover, MG block also participates, forming weak junctions. The gelling stage is known to occur via metal-mediated interchain interactions and the areas where this process occurs are commonly referred to 'junction zones' (110, 111, 114).

The egg-box model has been used to describe the gelling of alginate **(Figure 2.25)**. The schematic of egg-box model is associated with G block. When two pairs of two consecutive G blocks are “glued” together through the coordination of a Ca^{2+} cation, the sugar ring of the guluronic acid is in the 1C4 conformation. At the same time, the polymer chain adopts a characteristic zigzag shape (110).

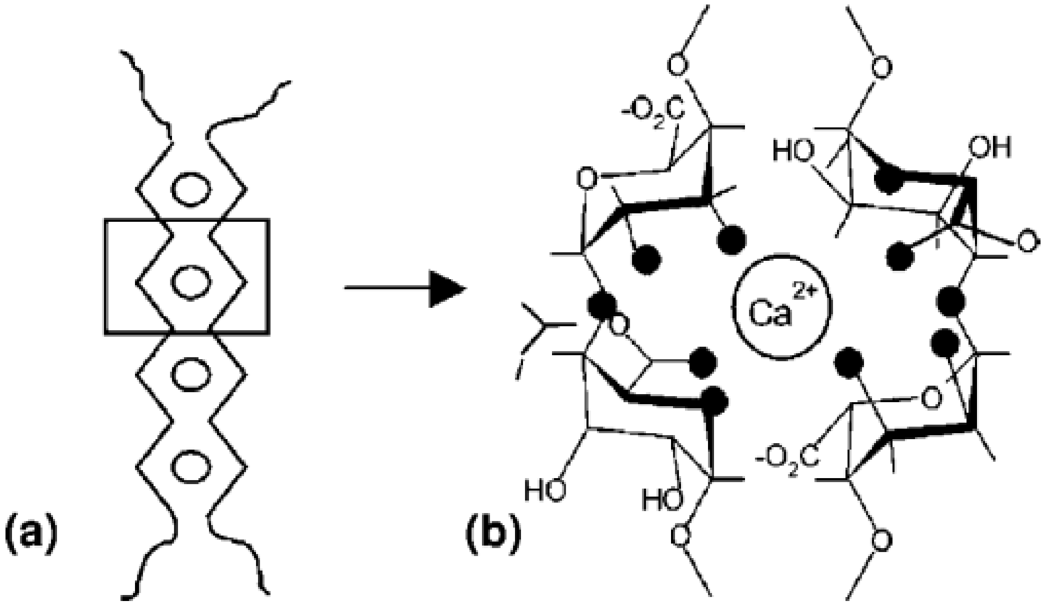

Figure 2.25. Schematic drawing and calcium coordination of the egg-box box model as described for the pair of guluronate chains in calcium alginate junction zones. Dark circles represent the oxygen atoms involved in the coordination of the calcium ion (110).

The crosslinking process between calcium and alginate can be divided by two methods. The first method is “diffusion”, where the crosslinking ions diffuse into the alginate solution from an outside reservoir, this method can yield the gels having different gradient concentration across the thickness. The second method is “internal setting”, wherein the ion source is located within the alginate solution and a controlled trigger (typically pH or solubility of the ion source) sets off the release of crosslinking ions into solution, this method gives gels with homogeneous ion concentrations(103, 105).

Sodium alginate (SAL) is a natural polysaccharide extracted from marine brown algae and composed of 1,4-linked – d-mannuronic acid (M) and –l-guluronic acid (G) residues, this raw material has been used to formulate matrix tablets of various drugs. However, sodium alginate (SAL) has some limitations to become an ideal matrix material such as easy solubility in water, substantial swelling and rapid erosion. To minimise these limitations, the crosslinking of sodium alginate (SAL) with Ca^{2+} ions is reacted through an ionotropic gelation process. Further investigation shows that when alginate matrix tablets containing a calcium salt such as calcium gluconate (CG) come in contact with acidic aqueous solution, in situ gelation takes place between SAL and Ca^{2+} ions generated from the calcium salt, and as a result formation of calcium alginate gel matrix(115).

Rajkumar and co-workers (116) developed a new method in order to produce a nanostructured composite by varying the composition of sodium alginate. They found that increasing in the concentration of sodium alginate up to 1.5 weight percent can increase in crystallite size and degree of crystallinity. However, beyond this concentration the crystallite size and degree of crystallinity will decrease. Similar with the crystallinity, microhardness and density in nanostructured composites show an increasing trend with an increase in the concentration of sodium alginate from 1.5 to 3.0 weight percent. The increasing amount of sodium alginate can increase the mechanical properties of composite (117, 118).

Wang et al. (3) synthesised cerium gadolinium oxide using sodium alginate (SAL) mediated novel ion-exchange processes. The result indicated that the final particle size after calcination is ~7 nm. From Fourier-transform infrared spectroscopy (FTIR) patterns, they found that the peak width becomes more pronounced in CGO-ALG spectra because of increase in the charge density. Moreover, the radius and atomic weight of trivalent Ce^{3+} and Gd^{3+} cations higher than monovalent Na^{+}. Based on charge balance, one trivalent

Ce^{3+}/Gd^{3+} requires three Na^{+} ions for bonding. This situation would lead to formation of cage-like structure during the ion exchange process and instantaneous gelling of alginate. The method, which is low cost, environmentally friendly and non-toxic route, produces single phase nanoparticle with a high purity concentration. Thus, this method is a promising synthesis route for advanced ceramic powder.

2.5 Scope of Project

The focus on this project is to develop a novel sol-gel synthesis route that is environmentally friendly and cost effective of high purity nanoparticles at low temperature. From literature review, it can be surmised that an ultrafine particle size can reduce the sintering temperature of cerium-based electrolyte, which may lead to improved ionic conductivity of the material. Moreover, double doped cerium oxide can enhance the ionic conductivity and reduce the activation energy. Therefore, multiple doped cerium oxide with trivalent rare-earth (Dy^{3+}, Ho^{3+}, Er^{3+} and Gd^{3+}) and different concentration variations will be investigated. The experimental process of manufacturing nanoparticles using sodium alginate bead and granule is described in Chapter 3. The optimum calcination temperature will be obtained by thermal analysis. The nanoparticles were analysed by X-ray diffraction (XRD). Raman measurements were also carried out to investigate the structural arrangement of doped and co-doped cerium gadolinium nanoparticles.

The morphology, size and chemical composition of nanoparticles were examined under high resolution transmission electron microscope (HRTEM). The microstructure and chemical composition of dense pellets were examined by scanning electron microscope (SEM) and energy dispersive spectrum (EDS). The density of dense ceramics was measured by the Archimedes principle.

Dense pellets were coated on both sides with silver coating to obtain a conductive layer. The alternating current (ac) conductivity measurements of co-doped CGO pellets were performed by impedance analyser. The data will be analysed, and suitable conclusion will be drawn for answering the suitability of co-doped ceria as solid electrolyte for IT-SOFCs.

Chapter 3 Methodology and Instrumentation

Metal complex nanoparticles have been prepared using the sodium alginate bead and granule method. The phase transformations, crystalline structure, morphologies, chemical composition, microstructure, and electrical properties have been investigated using a variety of techniques. These include thermogravimetric analysis (TGA), powder X-ray diffraction (XRD), High Temperature X-ray Diffraction (HT-XRD), scanning electron microscopy (SEM), transmission electron microscopy (TEM), Raman spectroscopy, and AC-impedance spectroscopy.

3.1 Metal Complex Nanoparticle Production Using the Sodium Alginate Bead Method

In this study, nanoparticles were synthesised using sodium alginate (SAL) beads. **Figure 3.1** shows the flow diagram for this process. Sodium alginate and the metal complex solutions were prepared by this method. The sodium alginate solution was prepared by dissolving appropriate amounts of sodium alginate powder in distilled water using a magnetic stirrer and a 500-rpm stirring rate. The metal complex solution was produced by adding appropriate amounts of metal nitrates to 500 ml distilled water when stirred (500 rpm) with the magnetic stirrer. Sodium alginate solution was dripped into the metal solution, with an instantaneous formation of the gel beads. The alginate beads were maintained in the gelling phase for several hours with gentle magnetic stirring in the nitrate solution to facilitate an ion exchange reaction between Na^+ and the metal atom in the solution. This process is illustrated in **Figure 3.1**. Following the ion exchange process, the wet metal-alginate beads were separated from the solution using a stainless-steel sieve, followed by washing with distilled water and overnight drying (T = 90°C). Clean wet metal-alginate beads and dried metal-alginate beads are shown in **Figure 3.2**.

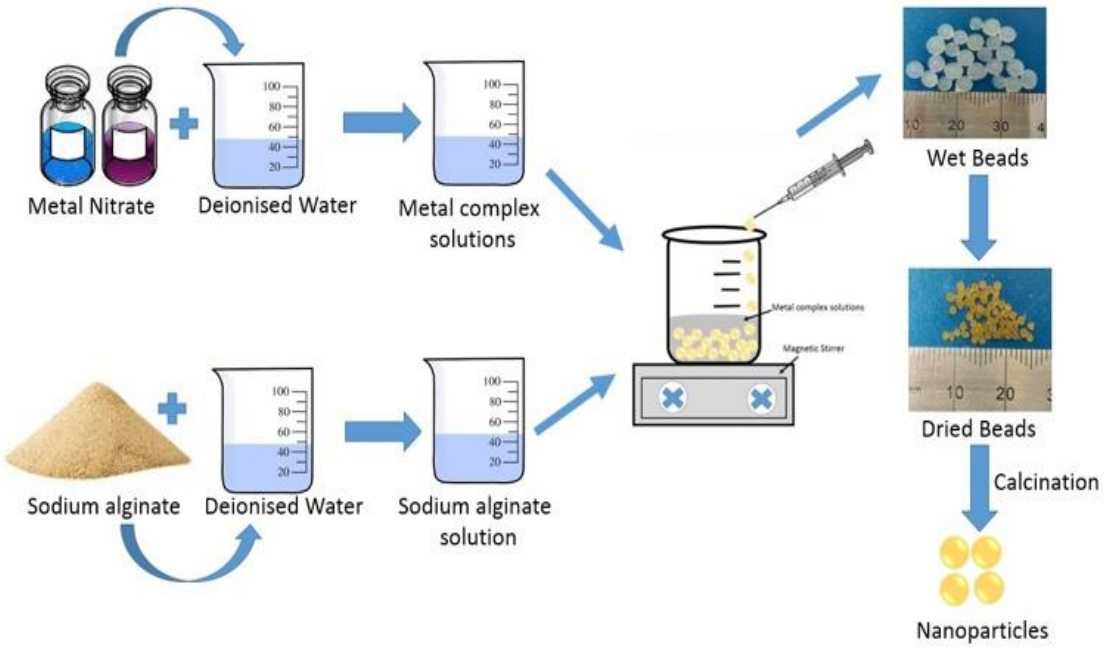

Figure 3.1. Flow diagram of sodium alginate bead method.

CGO wet beads	CGO dry beads
	

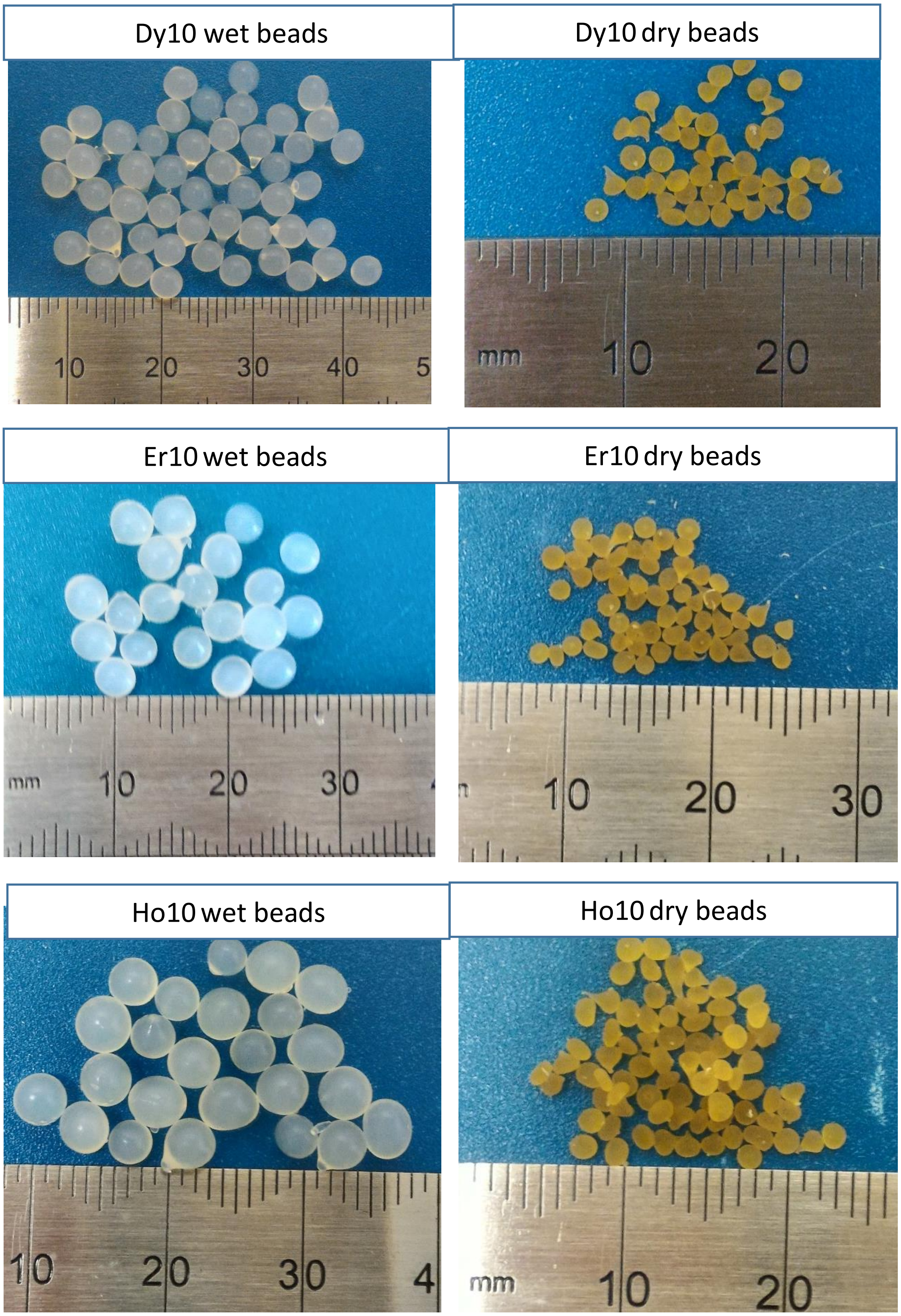

Dy10 wet beads

Dy10 dry beads

Er10 wet beads

Er10 dry beads

Ho10 wet beads

Ho10 dry beads

Figure 3.2. Metals-alginate wet and dry beads.

3.2 Metal Complex Nanoparticle Production using the Sodium Alginate Granules Method

Sodium alginate granules were prepared with a mechanical rotary pan device (**Figure 3.3**). The sodium alginate powders were placed in a rotating pan and distilled water was sprayed onto the powders during the pan spinning, and then granules can be formed. **Figure 3.4** shows the sodium alginate granules made using the mechanical rotary pan device have different sizes. The granules were sieved to obtain homogeneously sized granules through the sieves of different aperture sizes.

Figure 3.3. The mechanical rotary pan device

Figure 3.4. Sodium alginate granules.

Figure 3.5 shows a flow diagram of the sodium alginate granule method used in this study; Firstly, a sodium alginate granule and metal complex solution were prepared. The metal complex solution is 500 ml of distilled water with appropriate amounts of cerium (III) nitrate hexahydrate, gadolinium (III) nitrate hexahydrate co-doped with dysprosium (III) nitrate pentahydrate, erbium (III) nitrate hydrate and holmium (III) nitrate pentahydrate under a stirring rate of 500 rpm with a magnetic stirrer. Then 10 g of sodium alginate granules with a similar size (~2 mm) were added to the metal complex solution to form gel granules. The stirring rate for this process has been decreased to prevent the gel dissolve into solution and this ion exchange reaction has been set for one hour. After the ion-exchange reaction, wet granules were separated from the solution using a sieve, followed by washing the wet granules with distilled water, and drying the wet granules in an oven (T = 90^{o}C) overnight. Dried metal-alginate granules were placed in a furnace for the calcination process. During the calcination process, dried metal-alginate granules decompose and oxidise into metal-oxide nanoparticles.

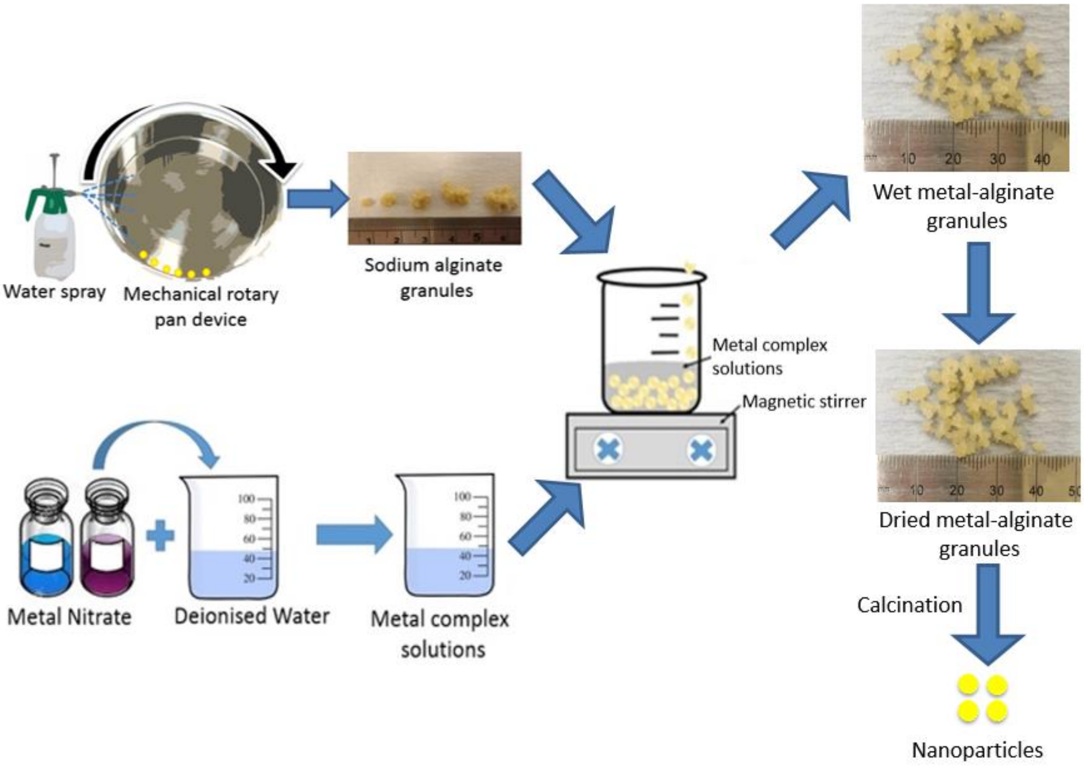

Figure 3.5. Flow diagram of sodium alginate granules method.

3.3 Thermogravimetric Analysis (TGA) / Differential Scanning Calorimetry (DSC)

Thermogravimetric analysis (TGA) is an experimental testing technique which determines changes in weight as a function of sample temperature or time. This technique has two temperature program types based on the information required from a sample, i.e. constant heating rate and non-linear temperature program. Various factors influence the result of TGA measurements, such as method parameters, sample preparation (homogeneity, purity, etc.), choice of the crucible, instrument effects, humidity control, and furnace atmosphere. The resulting TGA curve from the measurement may be plotted as a change in per cent mass against temperature or time. In addition to the TGA curve, other temperature experiments can be used in the analysis, e.g. a Differential Scanning Calorimetry (DSC) curve to show the exothermic and endothermic reaction (119).

Differential Scanning Calorimetry (DSC) is a thermal analysis technique which measures the heat flow as a function of temperature. This technique is widely used because it is fast and easy without complicated sample preparation required. Moreover, much information about the material can be obtained from this technique, including transition temperatures, melting processes, glass transition temperature, and a range of complex events. The basic principle of DSC is maintaining the same temperature for both sample and reference when the sample undergoes phase transitions. A schematic diagram of power compensation DSC is shown in **Figure 3.6**. To maintain the same heating rate while transitions occur in the sample, a power compensation circuit reduces or increases the power. This power compensation circuit therefore reflects the heat flow directly from the system. Display of the heat flux curve is a result of DSC experiment, and is plotted as energy changes versus temperature or time (120).

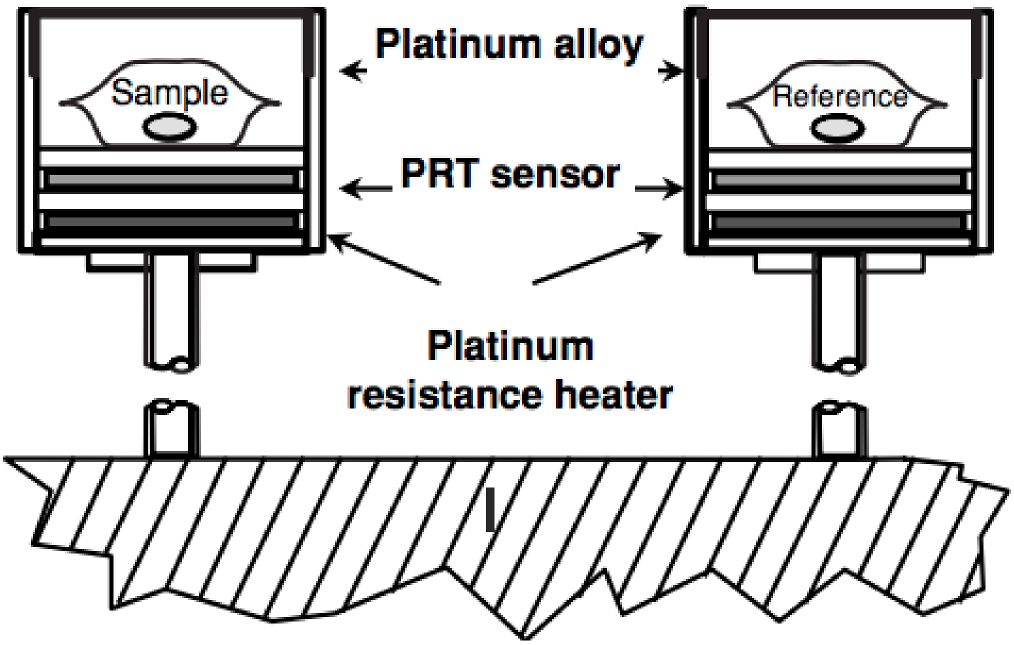

Figure 3.6. Diagram of power compensation DSC

In the current research, a Mettler Toledo STAR$^{@}$ System was used for simultaneous thermogravimetric analysis (TGA) and differential scanning calorimetry (DSC). The thermal analysis (TGA/DSC) of dried metal complex-ALG beads and granules experiments were conducted in a controlled atmosphere of air at a flow rate of 50cc/min from ambient temperature until 700^{o}C with a heating rate 10°C/min without dwell times.

3.4 X-Ray Diffraction (XRD)

X-ray diffraction is a prevalent method to analyse characteristics of powders because this technique is cost efficient and a non-destructive test. An important use of this technique is to determination of crystal structure examine the phases present, and to determine phase purity. X-rays are electromagnetic radiation with a shorter wavelength (range 0.5 – 2.5 Å) than visible light (6000 Å), which occur in part of the electromagnetic spectrum between gamma and ultraviolet rays. X-rays are produced when high speed electrons decelerate when they strike a metal target (copper in many cases) (121-123).

Figure 3.7 shows two parallel planes of atoms A–A' and B–B', which have similar Miller indices (h, k, and l). Plane A and B are separated by an interplanar spacing d_{hkl}. Assuming that a parallel, monochromatic beam, and coherent X-rays of wavelength λ incident on these two planes at an angle θ, called the Bragg angle, where θ is measured between the particular atom planes and the incident beam under consideration, two rays in this beam, labelled 1 and 2, are scattered by atoms P and Q. These scattered rays labelled 1' and 2', make an exit angle θ with respect to the diffraction planes which have a similar value with the incidence angle. If the path length difference between 1 – P – 1' and 2 – Q – 2' (i.e., $\overline{SQ}$ + $\overline{QT}$) is equal to a whole number, n, of wavelength λ (123- 125).

$$n\lambda = \overline{SQ} + \overline{QT} \tag{3.1}$$

$$n\lambda = d_{hkl}\sin\theta + d_{hkl}\sin\theta \tag{3.2}$$

$$= 2\,d_{hkl}\sin\theta \tag{3.3}$$

Equation 3.3 is known as Bragg's Law, where n is the order of diffraction, which may be any integer (1, 2, 3. . . .) consist with sin θ not exceeding unity and is equal to the exit angle θ. The magnitude of interplanar spacing d_{hkl} is a function of the Miller indices (h, k, and l) as well as the lattice parameter(s). Equation 3.4 shows the cubic crystal structure formulation to calculate the interplanar spacing, a in this equation is the lattice parameter (unit cell edge length).

$$d_{hkl} = \frac{a}{\sqrt{h^2 + k^2 + l^2}} \tag{3.4}$$

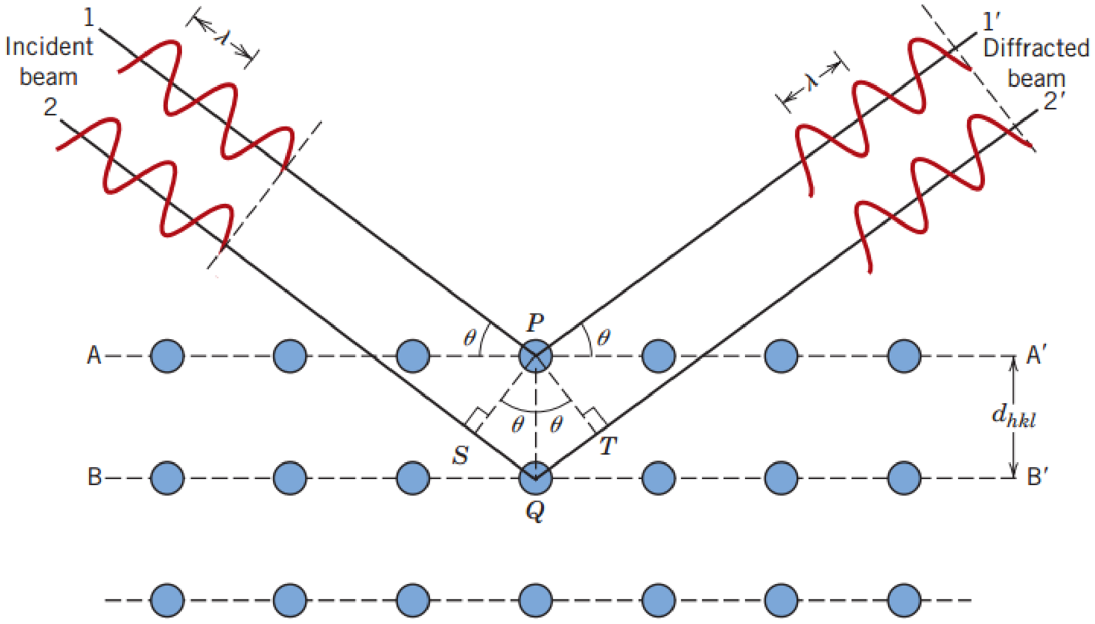

Figure 3.7. Diffraction of X-rays by a plane of atoms (A–A' and B–B') (123).

Scherrer's formula in equation 3.5 is used to estimate crystallite size (< 0.2 μm). The equation has certain assumption regarding strain broadening and instrumental broadening effect. This equation is formulated from measuring a peak width of the diffraction curve, which assumes all reflections along the reflection plane are equal. The width B is usually measured at an intensity equal to half the maximum intensity also known as full-width at half maximum (FWHM) (122, 124, 125).

$$t = \frac{K\,\lambda}{B\cos\theta_B} \tag{3.5}$$

where:

- t is crystallite size
- K is correction factor
- λ is the X-ray wavelength
- B is broadening line at full-width at half maximum (FWHM), in radians
- θ_B is the angle which exactly satisfies Bragg's Law

Equation 3.6 is the mean crystallite size calculated using the modified Debye-Scherrerr equation from the General Structure Analysis System (GSAS).

$$D = \frac{18000K\,\lambda}{\pi LX} \tag{3.6}$$

where LX is the Lorentzian profile shape width, K is Scherrer constant (0.9) and λ is the X-ray wavelength in Angstroms (Cu = 1.5408 Å).

In this study, nanoparticles were analysed using X-Ray diffraction (XRD), using a PANalytical X'Pert MPD, The Netherlands diffractometer and scanned using Cu Kα radiation (λ = 0.15406 nm) from 20 – 100°2θ with a step size of ca. 0.033°/s at room temperature.

Rietveld refinements were carried out on the XRD patterns using the General Structure Analysis System (GSAS) software program (125). The patterns were modelled using peak shape profile 4 and background parameters in the Shifted Chebyschev function. To determine the shape profiles, GSAS offers 5 different Constant Wavelength (CW) X-ray profile functions. Every profile function uses different functions and parameters. CW profile function 4 uses convolution of pseudo-Voigt, asymmetry and function, and microstrain broadening. Moreover, there are 10 different background functions offered by GSAS, with different number of terms and complex shape. However, for these materials, background fitting with Shifted Chebyschev function is preferable (125). The refinement of the crystallographic parameters has been done to get a better fitting result. Refined crystallographic parameters included scale factors, lattice parameters, general atomic positions, isotropic displacement parameters, and atomic site occupancies have been done.

Phase transformation of samples were investigated using High Temperature X-ray Diffraction (HT-XRD). The nanoparticles were analysed by XRD using a PANalytical X'Pert XRD diffractometer equipped with an Anton Paar HTK heating attachment. The XRD patterns were recorded in the 2θ 10-100˚ over the temperature range $300°C \leq T \leq 700°C$ in 50 °C intervals. The samples were heated in air using a heating rate of 5 °C /min and held at each temperature for 30 min to record the diffraction data.

3.5 Scanning Electron Microscopy (SEM)

Scanning electron microscopy (SEM) is a technique which captures sample surface images by using an electron beam. The electron beam is reflected to produce images of the surface. Optical microscopy, which has limited magnification (approximately 1000 times) is a major reason for the development of electron microscopy (~ 50,000 times or more). The limitation is because optical microscopy uses visible light as an energy source, which has a relatively long wavelength. SEM uses an electron beam with a much shorter wavelength than visible light (~0.02 nm), and the shorter wavelength allows a higher image resolution to the nanometer scale. SEM is suitable for a wide variety of materials that are stable in electron beam and in vacuum. However, sample preparation is needed before analysis, such as sample surface polishing and sample coating for non-metallic materials. **Figure 3.8** shows a schematic diagram of scanning electron microscopy (123, 126-128).

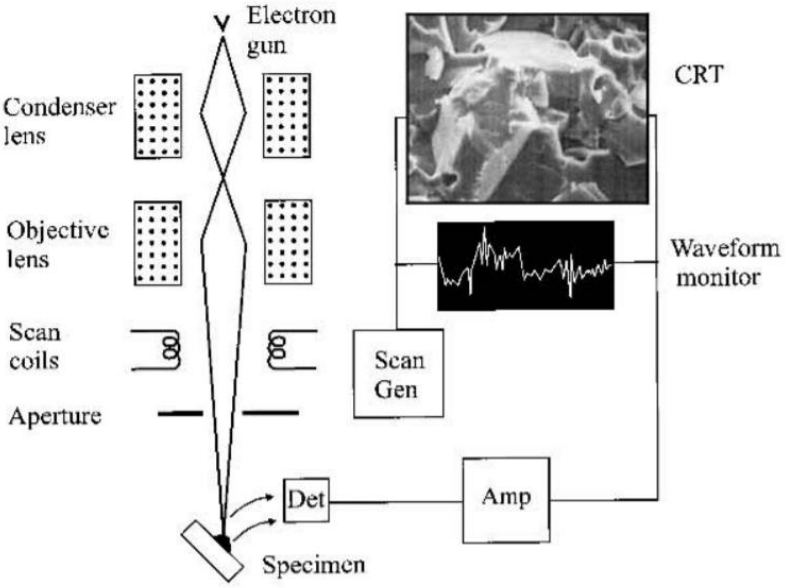

Figure 3.8. Schematic diagram of scanning electron microscope (SEM) (128).

Energy dispersive X-ray spectroscopy (EDS) is a non-destructive technique for the characterisation of chemical composition. This instrumentation is usually integrated with SEM or TEM in order to measure the sample composition concurrently. When an electron hits the material, various signals are produced, one of which is X-rays, and these signals interact with the sample to determine the elemental composition. Because each element has a unique atomic structure, the emitted X-ray represents the characteristic of each element. However, the lighter elements ($Z \leq 11$) are often below the detection limit (129).

In this study, the microstructure and chemical composition were examined by scanning electron microscope (SEM) and energy dispersive spectrum (EDS) (Hitachi SU8230 and Oxford instruments 80 mm^2). The synthesised nanoparticles were mounted on a carbon sticker and attached on an aluminium metal stub. The samples were coated with a carbon to make the surface conductive. The dense pellets were polished using silicon carbide paper and 3 µm diamond paste until there was a mirror finish, followed by thermal etching at 1350^{o}C for1.5h. Energy dispersive X-ray spectroscopy (EDS) analysis and mapping were performed with Oxford Instruments EDS X-ray Microanalysis Systems coupled to the SEM microscope.

3.6 Transmission Electron Microscopy (TEM)

Transmission electron microscopy (TEM) is a technique which produces an image by using an electron beam that passes through the specimen. This microscope has similar features to SEM, such as the electron gun, condenser lenses and vacuum system. However, the ways in which the images are produced and magnified are different. TEM uses an electron beam that passes through the specimen to analyse the internal structure, while SEM mainly uses the electron beam to analyse the surface of materials. The magnification from TEM may be approximately 1,000,000X, which is utilised in the study of defects and lattice imaging. In this technique, there is no metallic coating required during sample preparation. However, an electron transparent sample is needed for TEM studies, and this is difficult for a bulk sample (3, 121-123, 128, 129).

Diffraction patterns can also be viewed using TEM by changing the strength of the intermediate lens. The diffraction pattern is called a selected area electron diffraction (SAED) because the contributing area is limited by the aperture. This technique is used to identify lattice parameters of objects visualised in TEM (129).

For TEM sample preparation, a small number of nanoparticles are diluted in acetone solution then vibrated with an ultrasonic bath for 20 mins. A droplet of solution is then deposited on a copper grid with amorphous holey carbon film from Agar scientific, followed by drying under a UV light.

In this research, high resolution transmission electron microscopy (HRTEM) (FEI Tecnai TF20 operated at 200 kV fitted with a Gatan Orius CCD camera and Oxford instruments 80 mm^2) has been used to analyse the particle size and distribution of nanoparticle metal oxide powder. Dark-field image and electron diffraction pattern were used to obtain the interplanar spacing. Moreover, energy dispersive X-ray spectroscopy in TEM (EDS: Oxford Instruments) was used to calculate the chemical composition from the sample.

3.7 Raman Spectroscopy

Raman spectroscopy is a powerful non-destructive analytical technique which can detect vibrations in chemical bonds and provide information on chemical structure and physical forms. This technique is easy to use and does not require special sample preparation; samples can be examined in a range of physical states; e.g. as solids, liquids or vapours, in hot or cold state, in bulk, as microscopic particles, or as surface layers. Raman spectroscopy is less utilised than infrared absorption spectroscopy because of fundamental and technical issues, including weak intensity, sample degradation, fluorescence interference, and inefficient light collection and detection. However, modern Raman spectroscopy has reduced the problems substantially and simplified the instrumentation (131-133).

Raman spectroscopy uses a single wavelength to irradiate a sample and the radiation scattered from the molecules. **Figure 3.9** shows a schematic diagram of the Rayleigh and Raman scattering process which occurs at one vibration level. The virtual states are not a real state of the molecule, the light interacts with molecules and polarises the electron cloud to form these states, the energy of the states determined by the frequency of the light source used. The Rayleigh scattering process is an elastic scattering and is a dominant process because most photons scatter this way. In this scattering process, there is no energy change so that the light will return to the same energy level (131-132).

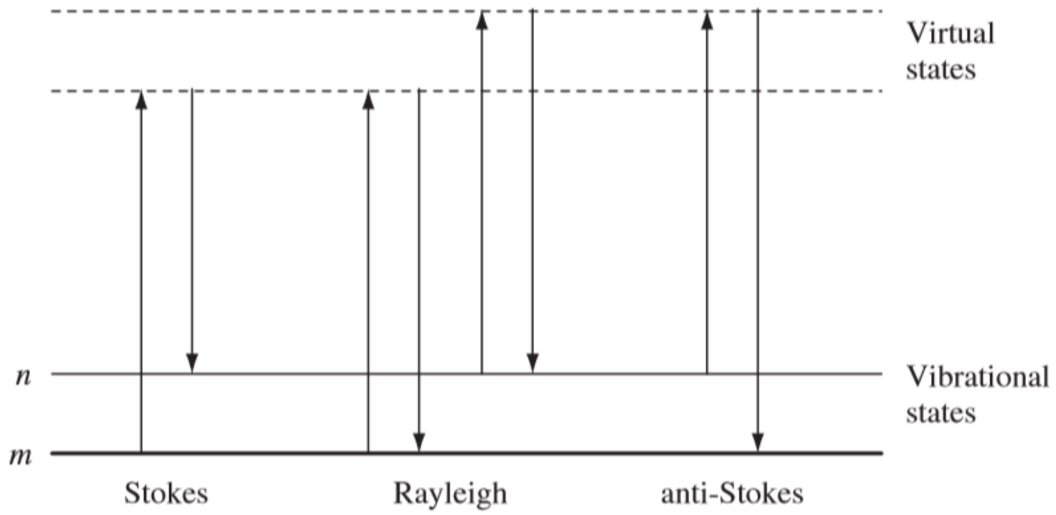

Figure 3.9. Schematic diagram of the Rayleigh and Raman scattering processes (Stokes and anti-Stokes). The lowest energy vibrational state m is shown at the bottom with states of increasing energy above it. Both the low energy (upward arrows) and the scattered energy (downward arrows) have much larger energies than the energy of a vibration (131).

In contrast, the Raman scattering process is an inelastic process, and the energy of the scattered photon is different from the incident photon since the nuclear motion is induced during the scattering process so the energy will be transferred either from molecule to the photon or vice versa. The scattering process called Stokes scattering when the molecule absorbs the energy, and it promotes a higher energy vibration state *n*. While in the anti-Stokes scattering the molecule transfers the energy to the scattered photon and scattering from *n* state to the ground state *m* (lower energy level). Usually, Raman scattering recorded at low energy (Stokes scattering) because the anti-Stokes scattering is weaker than Stokes scattering due to the population from the Boltzmann equation (131, 132).

On modern Raman spectrometers, a microscope may be integrated with the spectrometer. The microscope is used to observe the surface of the microscopic samples. **Figure 3.10** shows an arrangement for the coupling microscope with the Raman spectrometer. The laser is focussed through a pinhole and then collected as an expanded parallel beam. The radiation is arranged to hit a notch filter. The CCD detector monitories the light that passed into monochromator (131).

For Raman measurements, there is no special sample preparation, the nanoparticle is separated in the microscope slides and analysed under Renishaw in Via Raman spectrometer with a green Ar^+ laser (λ=514.5 nm) excitation source.

Raman spectroscopy is one of the powerful tools to investigate electrolyte materials. The Raman active mode for oxygen-cerium F_{2g} mode vibration is detected at 450–470 cm^{-1}. This F_{2g} band can be asymmetric and shift to the higher or lower frequencies with doping on the ceria system (81).

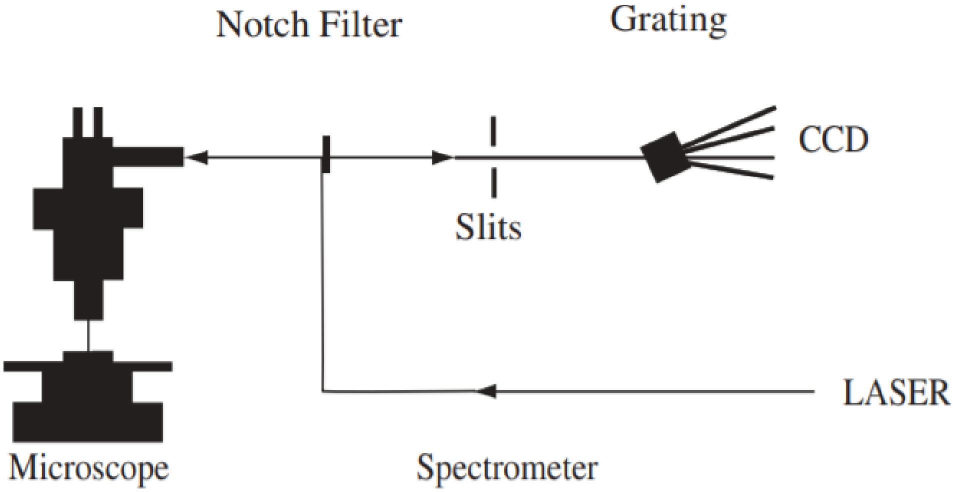

Figure 3.10. Diagram of Raman spectrometer and microscope, using a visible laser, notch filter, spectrometer and CCD detector (131).

3.8 AC-Impedance Spectroscopy

Impedance spectroscopy (IS) is a characterisation method used to investigate the electrical properties of materials and their interfaces with electronically conducting electrodes. This spectroscopy can be divided into two main categories: electrochemical IS (EIS), and another IS. Electrochemical IS (EIS) is an important tool for the study of fuel cells, batteries and corrosion, because this instrument involves measurements and analysis of materials which have mainly ionic conductivity. The remaining category of IS applies to dielectric materials, which involves dipolar rotation and material with dominant electronic conduction. Most impedance is designed as complex impedance or ac-impedance, which is an important tool for measuring ionic conductivity (134-137).

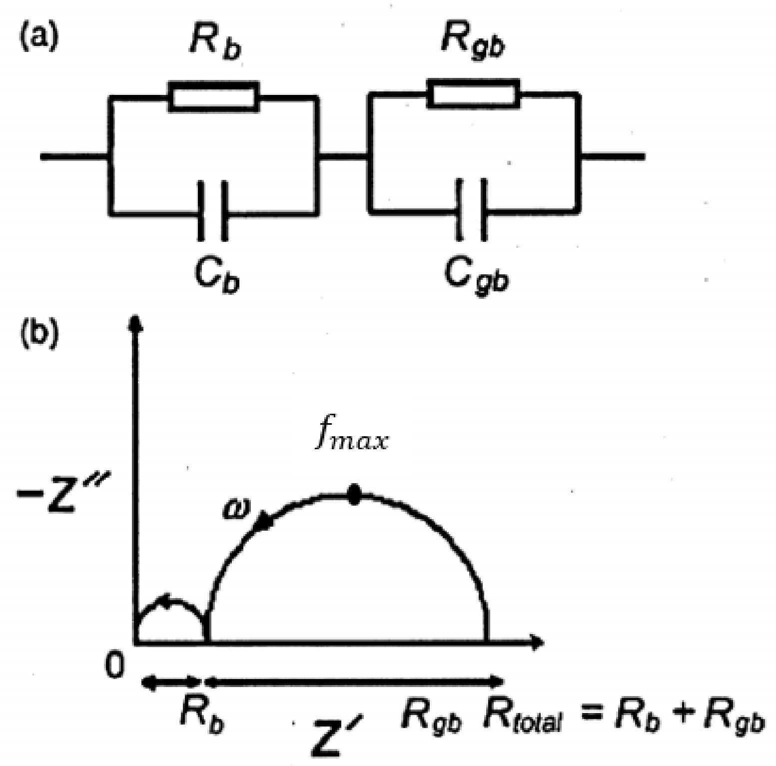

Figure 3.11. Simulated complex plane impedance plot response of a polycrystalline ceramic with corresponding equivalent circuit; a. RC circuit; b. impedance plane plot (3).

Impedance is a complex vector quantity, which representing complex plane (Z’ plotted against Z”) as a result of EIS investigation. **Figure 3.11** shows the simulated complex plane impedance plot of a polycrystalline ceramic, which represents the bulk and grain boundaries. The intercept of semicircles with abscissa (Z’) can be used to find the values of bulk (R_b), grain boundary (R_{gb}), and electrode resistances (R_e) from the sample. Resistance (R) and capacitance (C) are used to characterise the different areas of the test system (134-137).

The electrochemical impedance measurement system used to analyse AC properties of the electrochemical cell by measuring the current through the cell (134-137).

$$RC = \frac{1}{2\pi f_{max}}; R = \rho\,\frac{L}{A}\ ;\ \sigma = \frac{1}{\rho} \tag{3.7}$$

Where:

- R is resistance (Ω)
- C is capacitance (F)
- f_{max} is maximum frequency in one semi-circle (Hz)
- ρ is solution resistivity (Ωcm)
- L is thickness of the pellet (cm)
- A is the area of the pellet (cm^2)
- σ is conductivity (Siemens cm^{-1})

In addition, the activation energy (E_a) for ionic conduction can be obtained using Arrhenius equations:

$$\sigma_T = \sigma_0 \exp\left(-\frac{E_a}{RT}\right) \tag{3.8}$$

$$\ln\sigma_T = \ln\sigma_0 + \left(-\frac{E_a}{R}\right)\frac{1}{T} \tag{3.9}$$

where:

- σ_0 is pre-exponential conductivity
- E_a is activation energy (J mol^{-1})
- R is gas constant (8.314 J $mol^{-1}K^{-1}$)

Impedance spectroscopy was performed on the dense pellets using a Solartron SI 1260 FRA instrument. Ag-ink coated on each sides of the pellets and fired at 800°C for 1 h with heating and cooling rates of 5°C min^{-1}. The resulting pellets were mounted in a spring-loaded quartz rig and were placed in the stainless-steel horizontal inside the tube furnace (Lenton Tube Furnace, Lenton Thermal Designs Ltd, UK). The impedance measurements were carried out from 300 to 500°C with intervals of 50°C, during heating and cooling ramps. The type K thermocouple was used to monitor the actual temperature at the sample surface. The DC potential of 50 mV was applied, and the frequency was swept from 1.0 x 10^{-1} Hz to 1 x 10^{6} Hz. At each measurement temperature, the measurements are performed after 30 mins stabilisation time in order to obtain stable spectra. ZView and ZPlot software (Scribner Associates Inc., USA) were used to control the SI1260 instrument and, model and analyse the impedance data.

Chapter 4 Results and Discussions

In this chapter, the details of results and discussions are provided. The chapter is being divided into four sections; 4.1 optimisation of the process, 4.2 Synthesis of $Ce_{0.8}Dy_{0.2-x}Gd_xO_{1.9}$ nanoparticles, 4.3 Fabrication of $Ce_{0.8}Ho_{0.2-x}Gd_xO_{1.9}$ nanoparticles, and 4.4 Production of $Ce_{0.8}Er_{0.2-x}Gd_xO_{1.9}$ nanoparticles.

4.1 Optimisation of the process

The co-doped cerium gadolinium nanoparticles were synthesised by sodium alginate (SAL) methods (138 – 140). In this section, only four compositions (CGO, Dy10, Ho10, Er10) were made and tested for the optimisation. The optimisation of the process, including the synthesis and the densification, are discussed below.

4.1.1 Bead Method

The details of the process of preparation of metal ion exchanged beads is described earlier in Chapter 3. Thermal analysis of dried metal complex-ALG bead is conducted under the air flow rate of 50cc/min from ambient temperature until 700^{o}C with heating rate 10C/min without any holding time. **Figure 4.1** shows the thermal gravimetric analysis for Gd-doped and co-doped cerium-ALG beads, other compositions shown in **Figure A.1**. The black line indicates the percentages of samples weight (TGA), the red line indicates the first derivative of weight, and the blue line is the heat flow (DSC). The thermal analysis was done to determine the best possible calcination temperature from the decomposition processes.

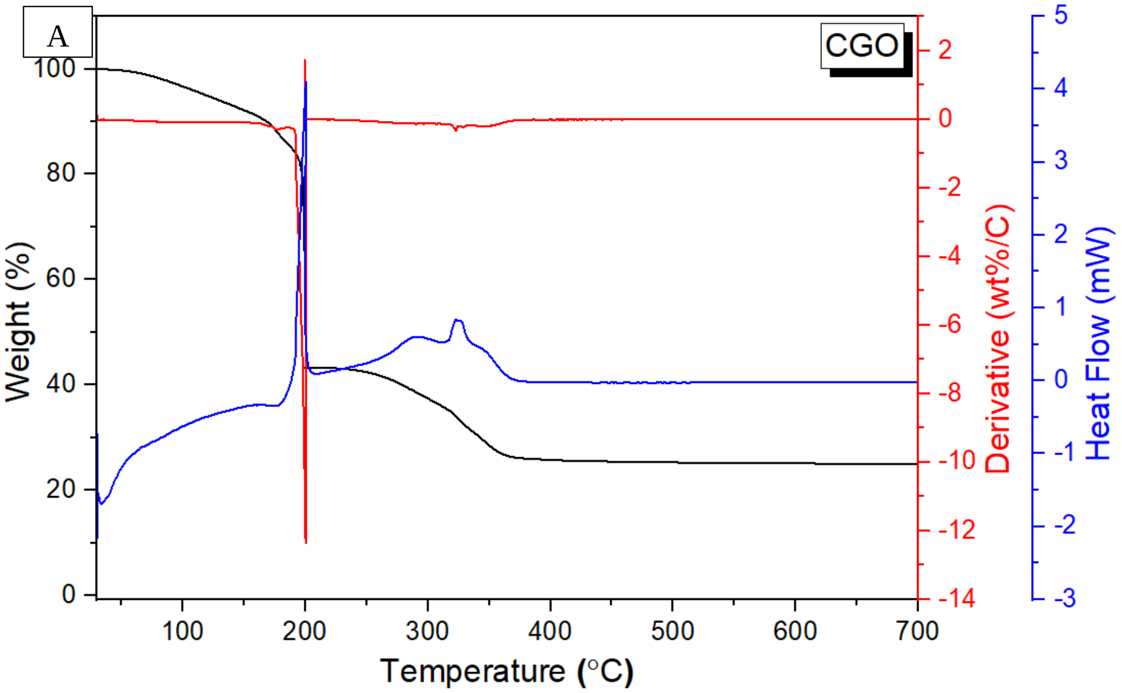
A
CGO
Weight (%)
0
20
40
60
80
100
Temperature (°C)
100
200
300
400
500
600
700
Derivative (wt%/C)
2
0
-2
-4
-6
-8
-10
-12
-14
Heat Flow (mW)
5
4
3
2
1
0
-1
-2
-3

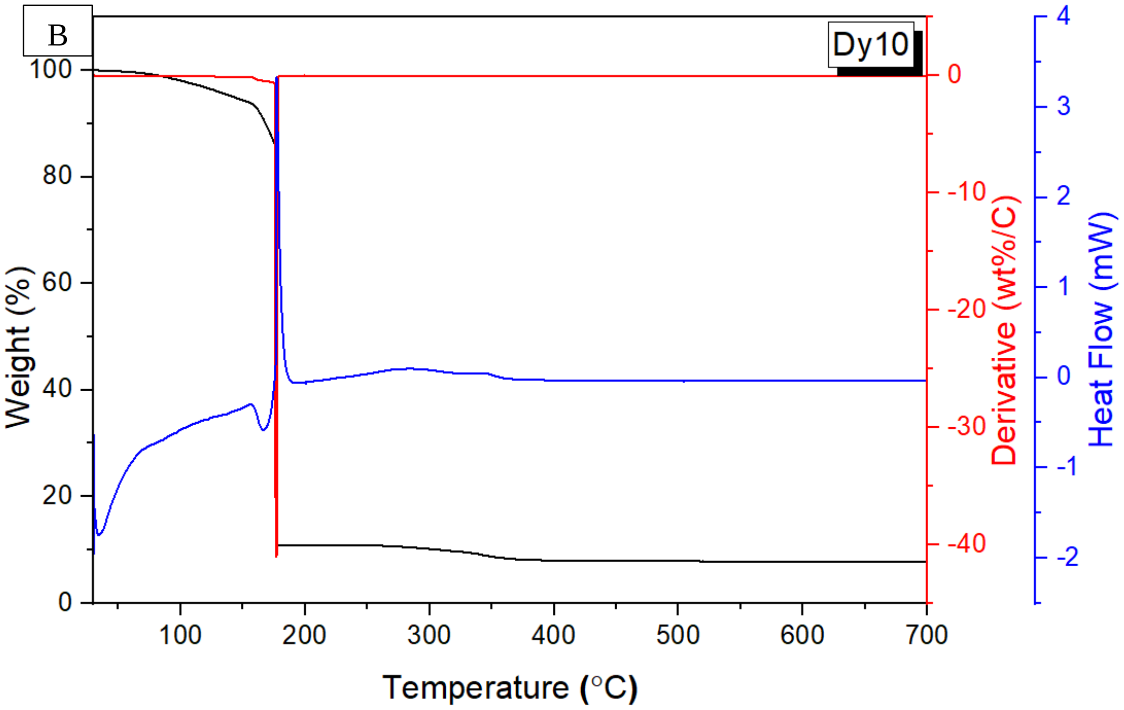
B
Dy10
Weight (%)
0
20
40
60
80
100
Temperature (°C)
100
200
300
400
500
600
700
Derivative (wt%/C)
0
-10
-20
-30
-40
Heat Flow (mW)
4
3
2
1
0
-1
-2

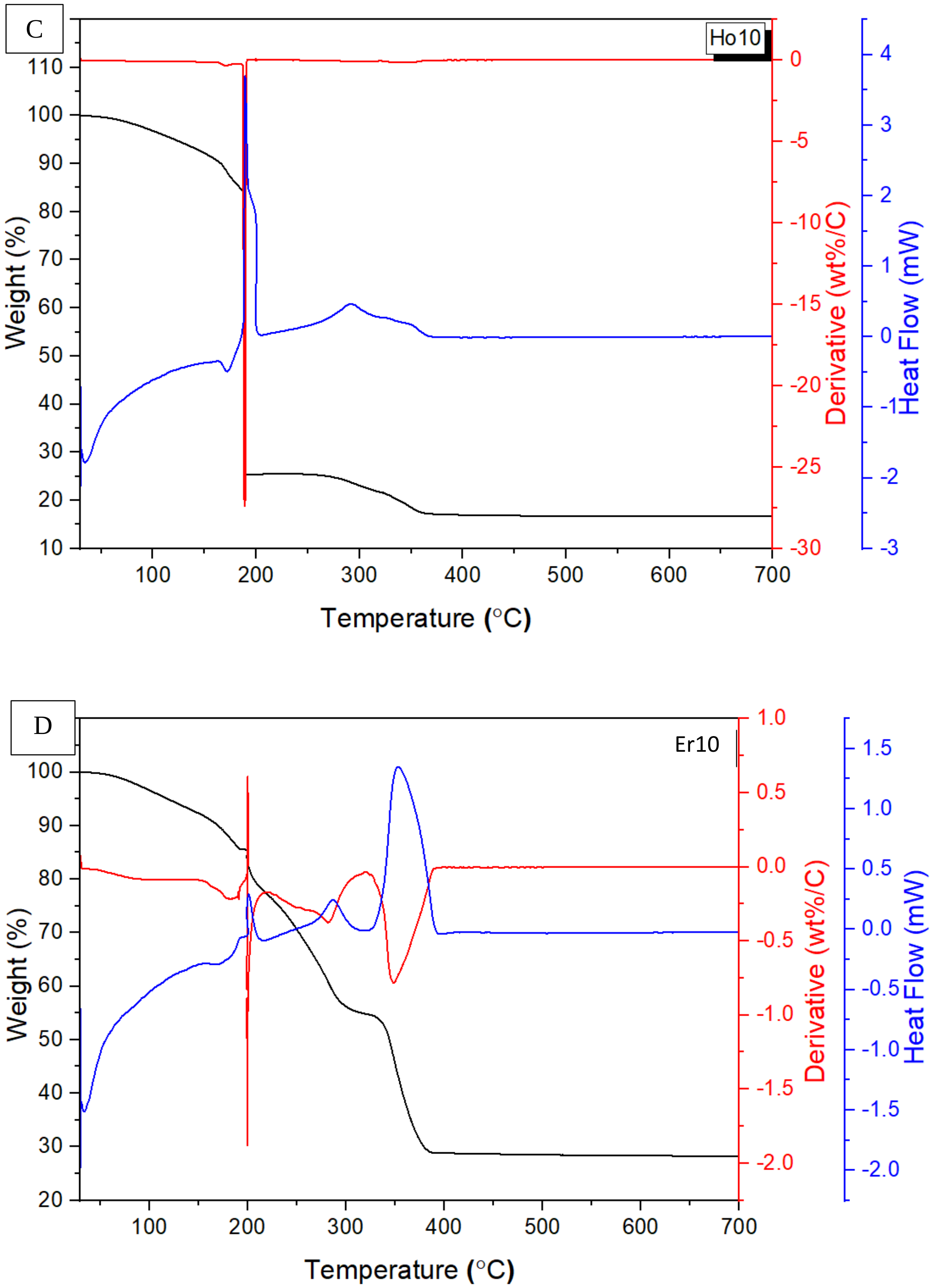

Figure 4.1. TGA (weight), derivative (wt%/C), and DSC (heat flow) of CGO (A), Dy10 (B), Ho10 (C), Er10 (D) dried beads in controlled atmosphere of air.

In general, the decomposition process of doped and co-doped cerium alginate (M-ALG) dried bead occurs in the four stages. However, the temperature for every stage is different for individual compositions. This mechanism of decomposition of metal complex alginate is similar to that reported by Wang et al. (141).

1. At temperature between ambient and around 180°C, the first endothermic decomposition peak is observed. This endothermic process happens because the hydrate evaporate during the heat-treatment process. The weight loss for this process almost 12 – 13 % for every metal complex-ALG beads, shown in **Figure 4.2**. From high-temperature XRD data (**Figure 4.3)**, it shows that no XRD peaks were found at a temperature below 200°C, indicating that at this temperature, the fluorite structure did not form.
2. At higher temperature (180 – 250°C), the exothermic oxidative decomposition is observed. At temperature between 180 – 250°C, the weight loss drops the deepest, almost 44% from the previous stage for CGO (**Figure 4.2**); this is caused by cleavage of linking G–G, G–M, and M–M which is weaker linkages in the alginate polysaccharide molecule and causing substantial evolution of oxygen.
3. Further decomposition has occurred at a temperature of 250 - 320°C. The small exothermic peak was observed at temperature between 250 - 320°C due to the decomposition of oxides to more stable oxides and resulted in small weight loss in TGA profile. From HT-XRD, it shows that the XRD peak became narrower along with the increasing temperature.
4. Further increase at the temperature around 400°C completely oxidized the remaining β-D-mannuronic acid (M) and α-L-guluronic acid (G) leading to a small exothermic peak in the DSC profile for CGO, and Ho10 but the large exothermic peak for Er10. The significant exothermic decomposition in the second stage for co-doped dysprosium (Dy10) makes the final step combined with the third stage. While for co-doped erbium (Er10) small exothermic

decomposition in the second stage for remaining more M/G residue in the final stage.

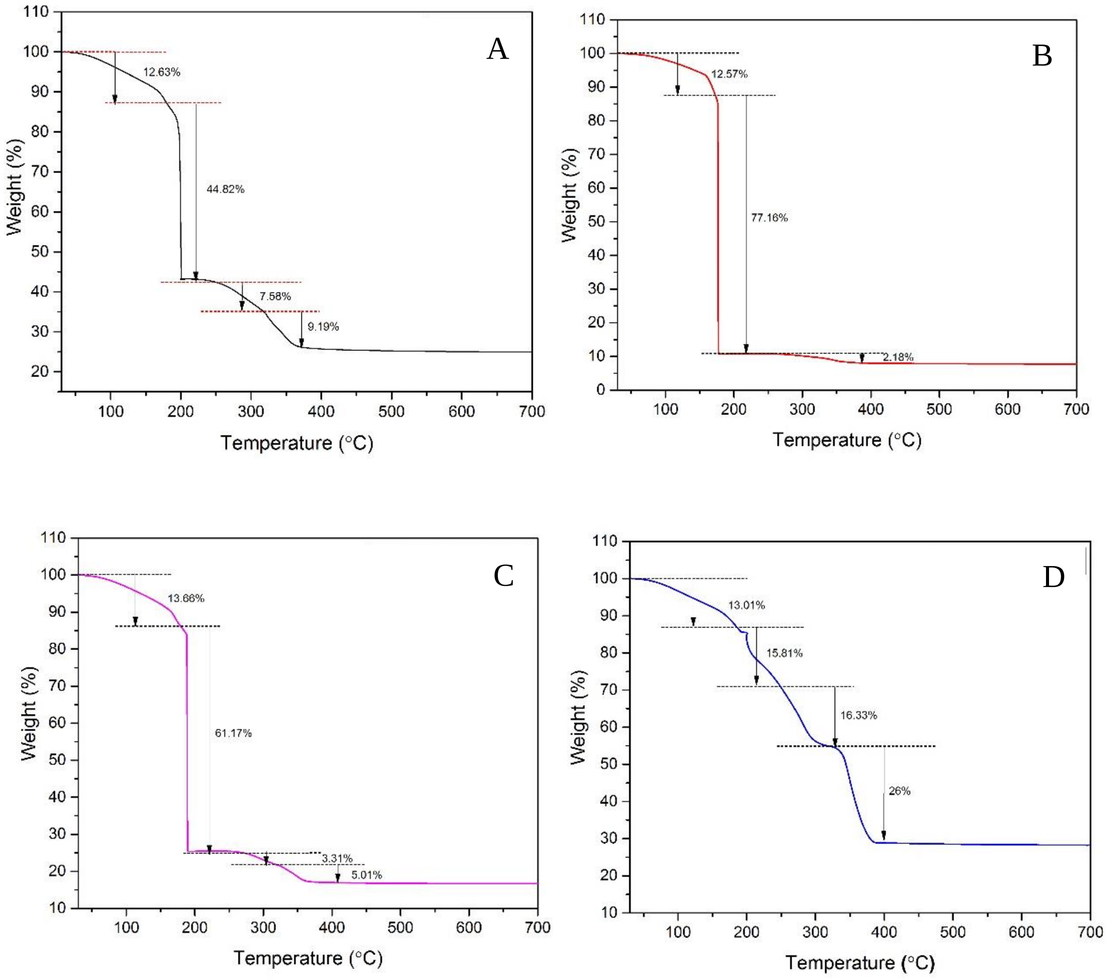

Figure 4.2. TGA analysis of CGO (A), Dy10 (B), Ho10 (C), Er10 (D) dried beads in controlled atmosphere of air.

High-temperature XRD (HT-XRD) is used to determine the phase transition from dried metal complex-ALG bead to nanoparticles. Dried bead was crushed using mortar and pestle to get the fine powder. The XRD patterns were recorded from 20-100° 2θ, in the temperature range $25 \leq T \leq 800$°C. The samples were heated in air using a heating rate of 5°C/min and held at each temperature for 30 min to record the diffraction data. **Figure 4.3** shows the HT-XRD of cerium gadolinium alginate dried bead at different temperature conditions. At temperature 200°C no peaks were detected from the XRD; however, at temperature 250°C, the clean fluorite structure starts to form. This is in good agreement with TGA curve; temperature 200°C is the inflection point when the process of the decomposition has not to finish while at temperature 250°C is the end of the decomposition process. The oxidation of complex metal in alginate structure forms a mixture of stable and metastable metal oxides phases.

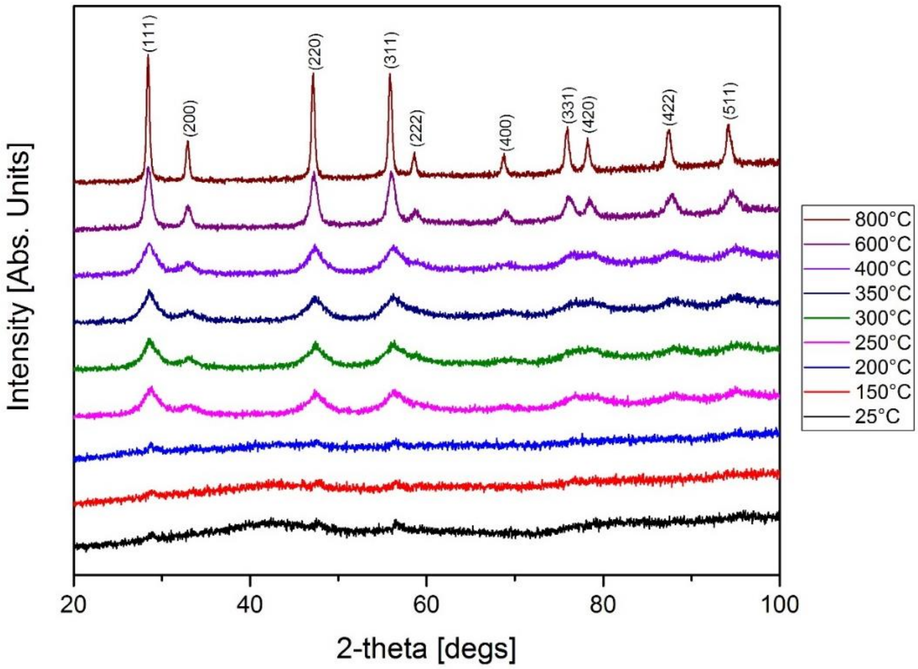

Figure 4.3. High-temperature XRD of CGO-ALG dried bead at different temperatures. The patterns are indexed as fluorite structure at the top of the peaks.

No further weight loss and decomposition found after temperature 400°C in TGA profiles. Hence, the calcination temperature was set as 500 and 700°C. XRD, SEM, and TEM analysis were used to determine the optimum calcination temperature.

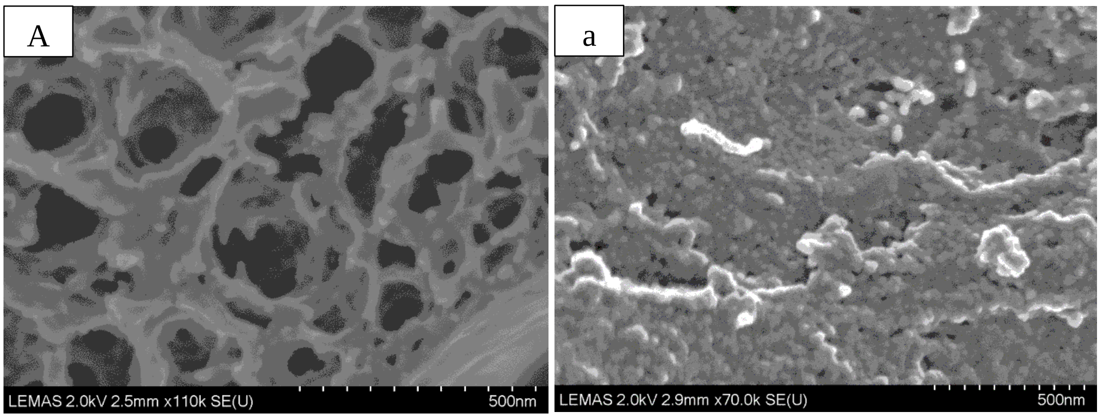

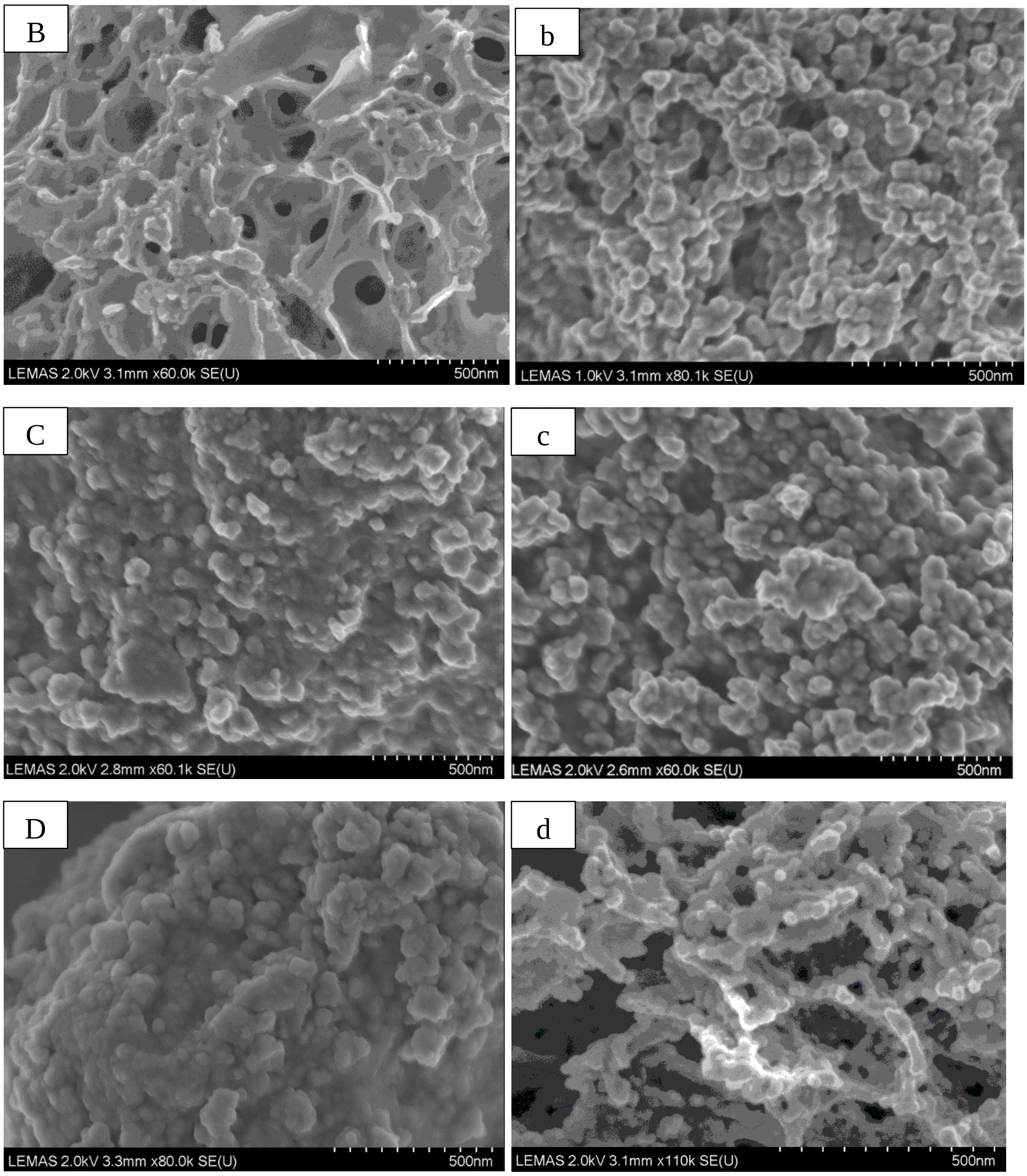

Figure 4.4. SEM images of nanoparticles at two different temperatures for 2 hrs: CGO nanoparticles at 500 (A) and 700°C (a); Dy10 nanoparticles at 500 (B) and 700°C (b); Ho10 nanoparticles at 500 (C) and 700°C (c); Er10 nanoparticles at 500 (D) and 700°C (d).

Scanning electron microscopy (SEM) is used to analyses the morphology of doped and co-doped cerium oxide after calcination processes at 500 and 700°C for 2 h, shown in **Figure 4.4**. The images show like egg-box model structure (**Figure 2.25**); this is caused during the ion-exchange process, which leads to the production of gel alginate (3, 109).

A

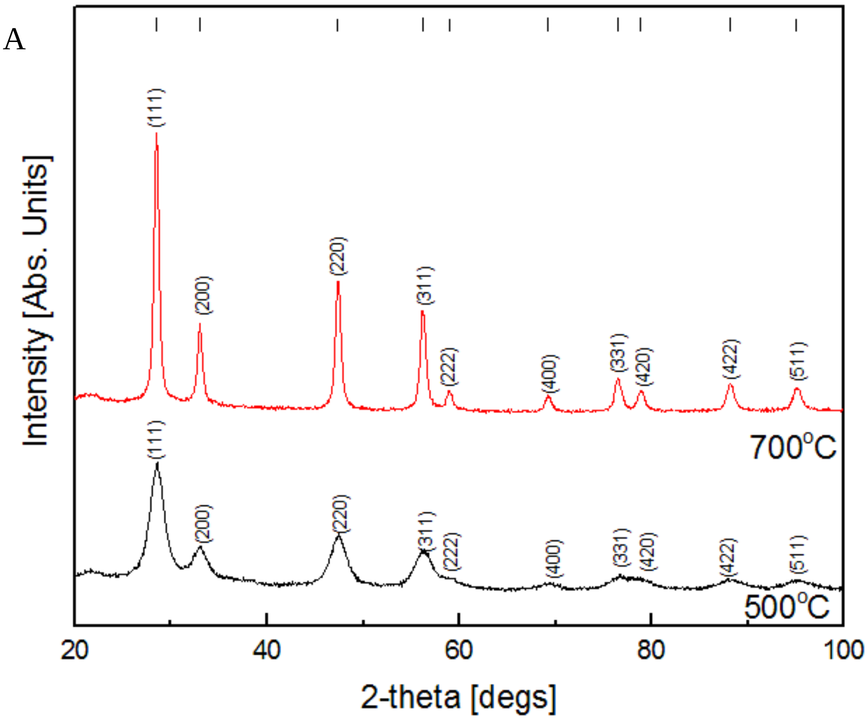
Intensity [Abs. Units]
2-theta [degs]
20
40
60
80
100
(111)
(200)
(220)
(311)
(222)
(400)
(331)
(420)
(422)
(511)
700°C
(111)
(200)
(220)
(311)
(222)
(400)
(331)
(420)
(422)
(511)
500°C

B

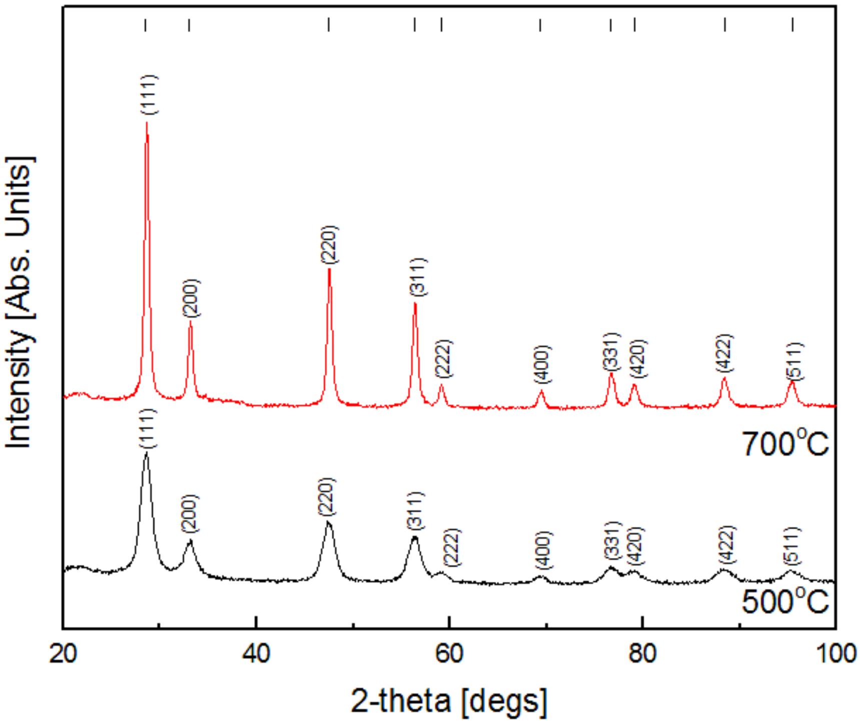
Intensity [Abs. Units]
2-theta [degs]
20
40
60
80
100
(111)
(200)
(220)
(311)
(222)
(400)
(331)
(420)
(422)
(511)
700°C
(111)
(200)
(220)
(311)
(222)
(400)
(331)
(420)
(422)
(511)
500°C

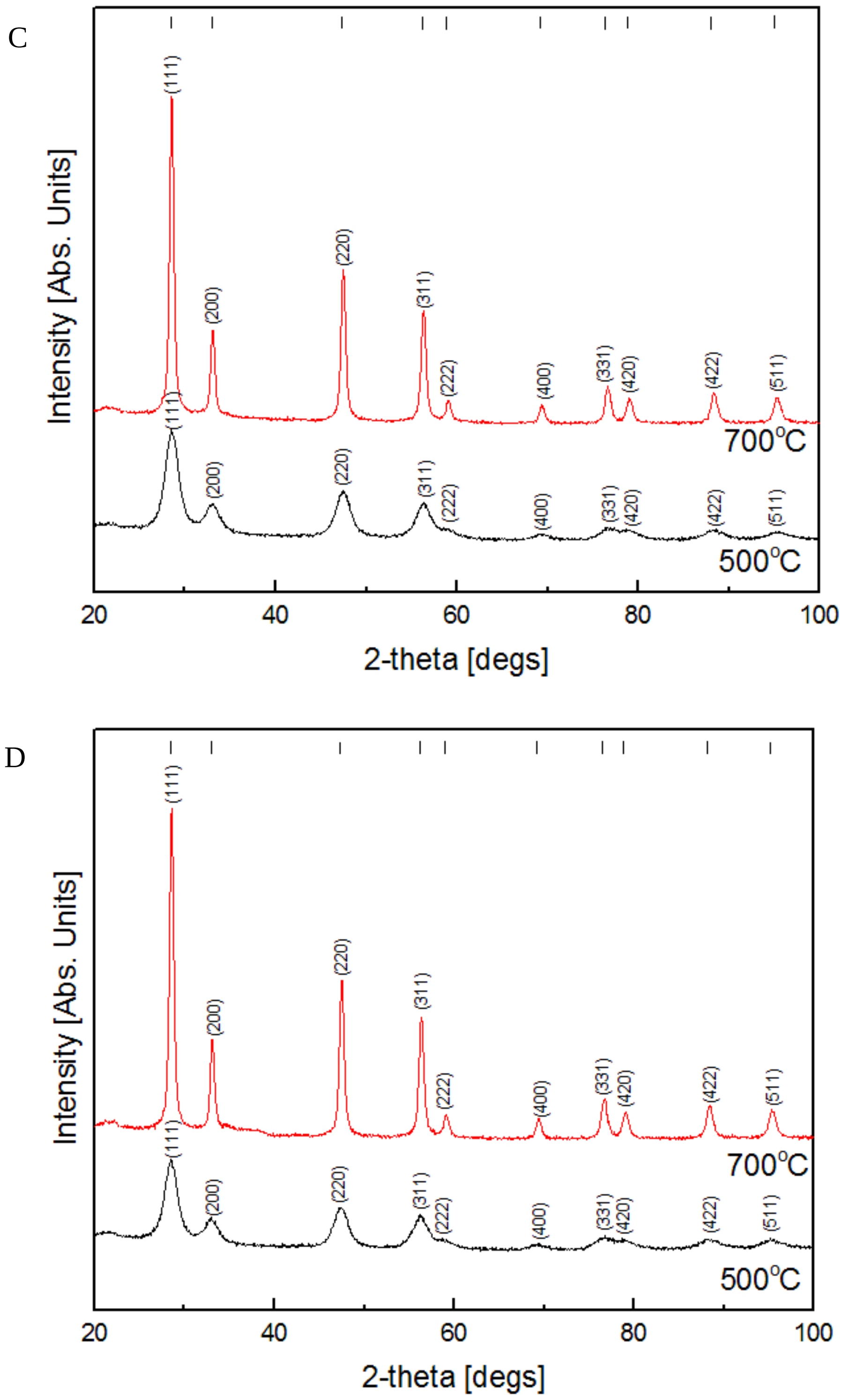

Figure 4.5. XRD patterns of (A) CGO; (B) Dy10; (C) Ho10; (D) Er10 at different calcination temperature synthesised using bead method. All the patterns are indexed as fluorite structure at the top of the peaks.

XRD peaks from CGO and doubly doped ceria (Dy10, Ho10, and Er10) at different temperatures are shown in **Figure 4.5**. Rietveld analysis was carried out using the program *GSAS*. The crystal structure features such as changes in lattice parameters, atomic occupancies, isotropic displacement parameters, scale and four polynomial background parameters in the shifted Chebyschev function were refined.

All peaks confirm the pure cubic fluorite crystal structure with $Fm\bar{3}m$ space group. There is no signature of any secondary phase or hybrid phase detected for all compositions. The partial substitution of Ce^{4+} with Gd^{3+} and Dy^{3+}, Ho^{3+}, or Er^{3+} forming a substitutional solid solution, and the position of atoms do not change. The difference between the ionic radii of Ce^{4+} in fluorite structure and $Gd^{3+}/Dy^{3+}/Ho^{3+}/Er^{3+}$ is less than 15% and therefore obeys Hume-Rothery laws (142) of substitutional solid solution. This result is similar to the analysis performed by Artini and co-workers (143), where it is stated that substitution of Gd^{3+} of less than x = 0.2 in $Ce_{1-x}M_xO_{1.9}$ adopts the fluorite structure (143, 144).

Refined structural parameter, agreement factors, crystallite size and theoretical density for gadolinium (CGO) and co-doped (Dy10, Ho10, and Er10) ceria nanoparticles calcined at 500 and 700°C for 2 h presented in **Table 4.1**. The lattice parameter of each composition was obtained by Rietveld refinement of XRD data using GSAS. Cerium gadolinium oxide has the highest lattice parameter compare with co-doped materials. This is because the ionic radius of gadolinium ions is the highest among others co-dopant elements (Dy^{3+}, Ho^{3+}, and Er^{3+}) (**Table 2.3**). It shows that doped cerium with smaller ionic radius leads the lattice contractions. The evidence of lattice contraction is the smaller inerplanar spacing (d value) and unit cell volume, shown in **Table 4.1** and **4.2**. Moreover, the smallest ionic radius has the smallest lattice parameter.

Table 4.1. Refined structural parameter, agreement factors, crystallite size and theoretical density for Gd-doped and co-doped ceria nanoparticles calcined at 500 and 700°C for 2 h.

	CGO		**Dy10**		**Ho10**		**Er10**	
	500°C	**700°C**	**500°C**	**700°C**	**500°C**	**700°C**	**500°C**	**700°C**
Rp	0.021	0.026	0.024	0.031	0.023	0.026	0.026	0.027
Rexp	0.0126	0.027	0.016	0.031	0.0129	0.029	0.015	0.031
χ^2	5.34	1.562	4.494	1.613	6.25	1.254	5.954	1.232
V (Å^3)	160.16 (2)	160.17 (7)	159.47 (2)	159.56 (1)	159.35 (2)	159.24 (1)	158.79 (2)	158.99 (1)
a (Å)	5.43061 (2)	5.43016 (5)	5.4228 (2)	5.42388 (11)	5.4215 (2)	5.42018 (8)	5.4151 (2)	5.41737 (9)
D_{XRD} (Å)	111.759	362.81	115.74	347.99	107.896	266.047	106.984	184.348
ρ_{Th} (g/cm^3)	7.214	7.216	7.267	7.263	7.283	7.288	7.318	7.309

The mean crystallite size presented in **Table 4.1** has been calculated using a modified Debye-Scherrerr equation from GSAS (equation 3.6). Broad peaks in XRD patterns calcined at 500°C indicates a very small crystallite size in the powder sample are typically in the nanometer range (~11 nm). While sharp peaks observed in the calcined samples at 700°C indicate that the crystallites are bigger than in the sample calcined at 500°C. This result is similar to a study that reported by Wang, et al (141) and Pezeshkpour, et al. (142, 143) the higher calcination temperature, bigger nanocrystals were produced.

The morphology particles and selected area electron diffraction (SAED) patterns, from four different compositions samples, are shown in **Figures 4.6 – 4.9**. The TEM images show a mixture of hexagonal and square shape morphologies depending on their orientation on the holey carbon-coated copper grid, confirming the cubic fluorite structure. The particles size of samples calcined at 500°C has a smaller size than calcined at 700°C.

This is a good agreement with the slightly higher values reported by the XRD Rietveld refinement procedure.

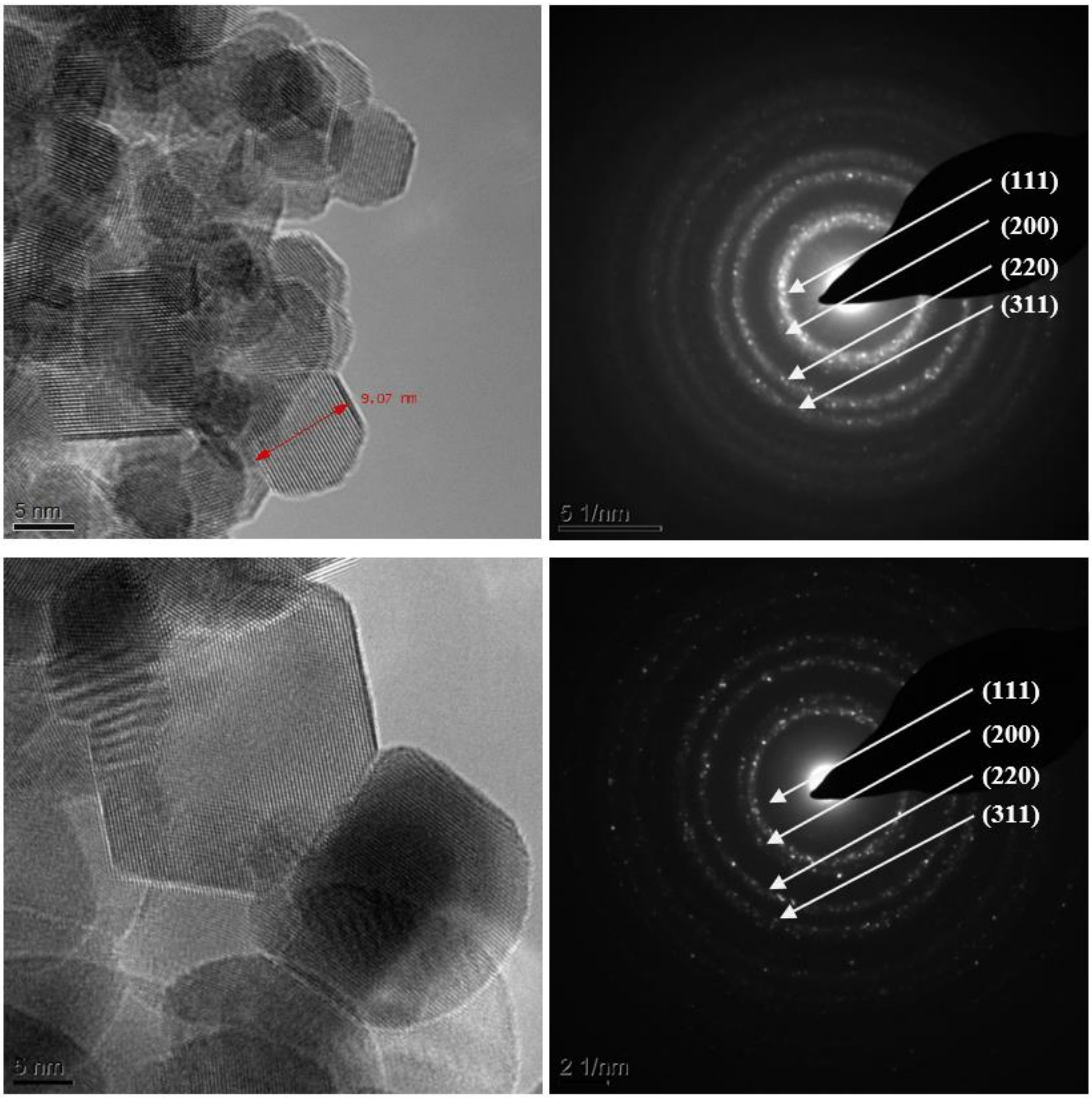

Figure 4.6. TEM images and SAED patterns of CGO samples calcined at 500 (above) and 700°C (down) for 2 h, respectively.

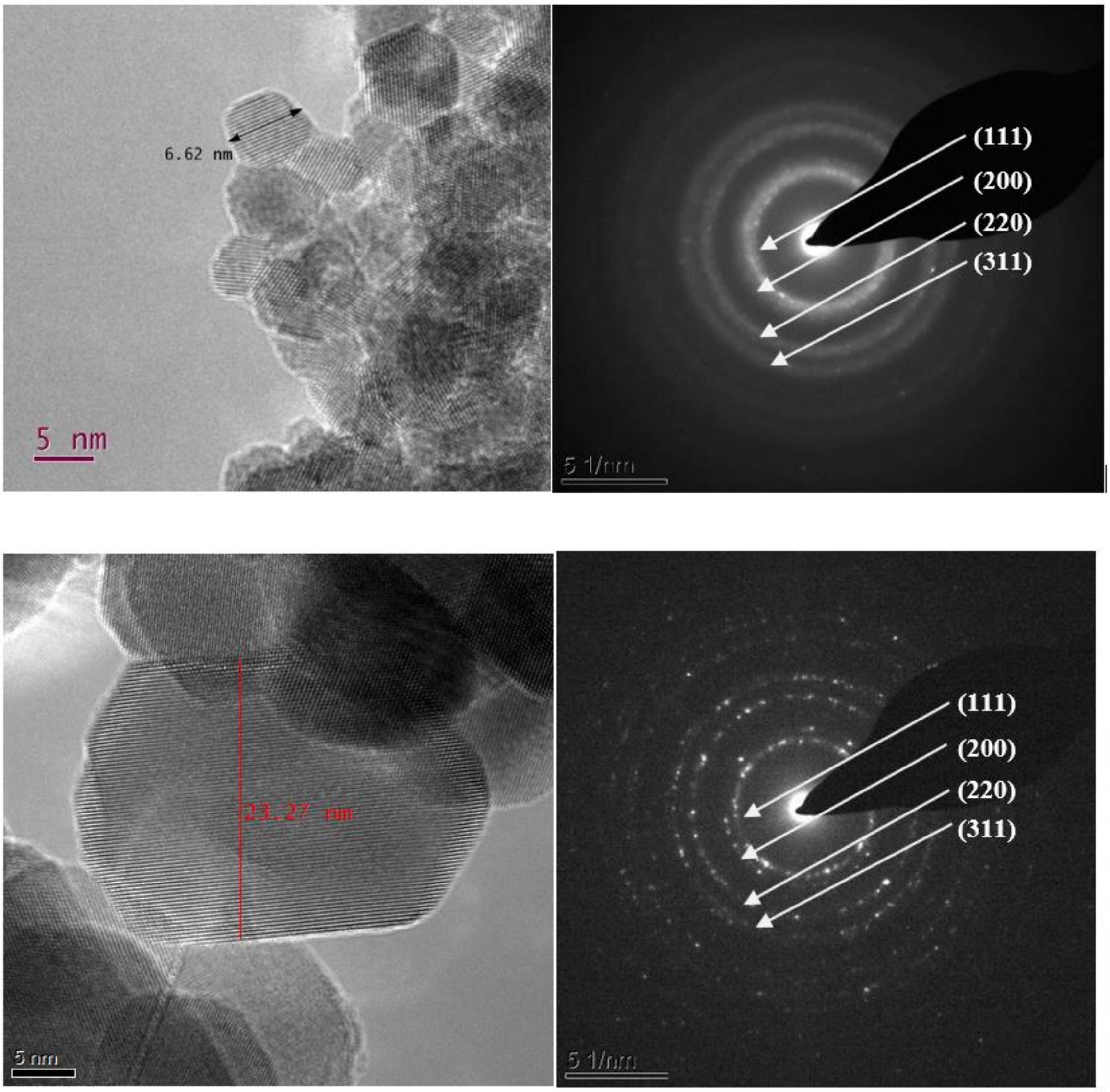

Figure 4.7. TEM images and SAED patterns of Dy10 samples calcined at 500 (above) and 700°C (down) for 2 h, respectively.

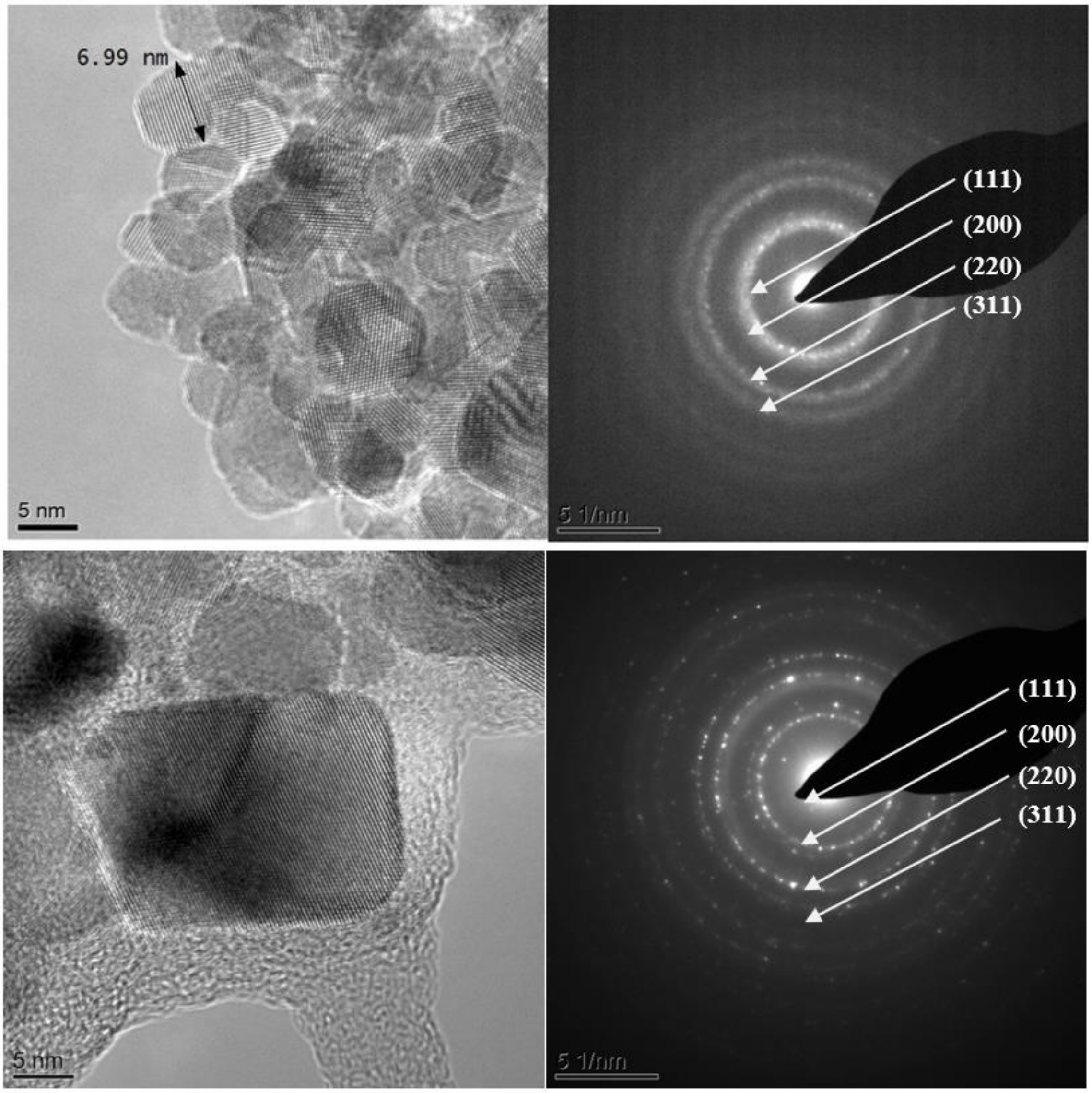

Figure 4.8. TEM images and SAED patterns of Ho10 sample calcined at 500 (above) and 700°C (down) for 2 h, respectively.

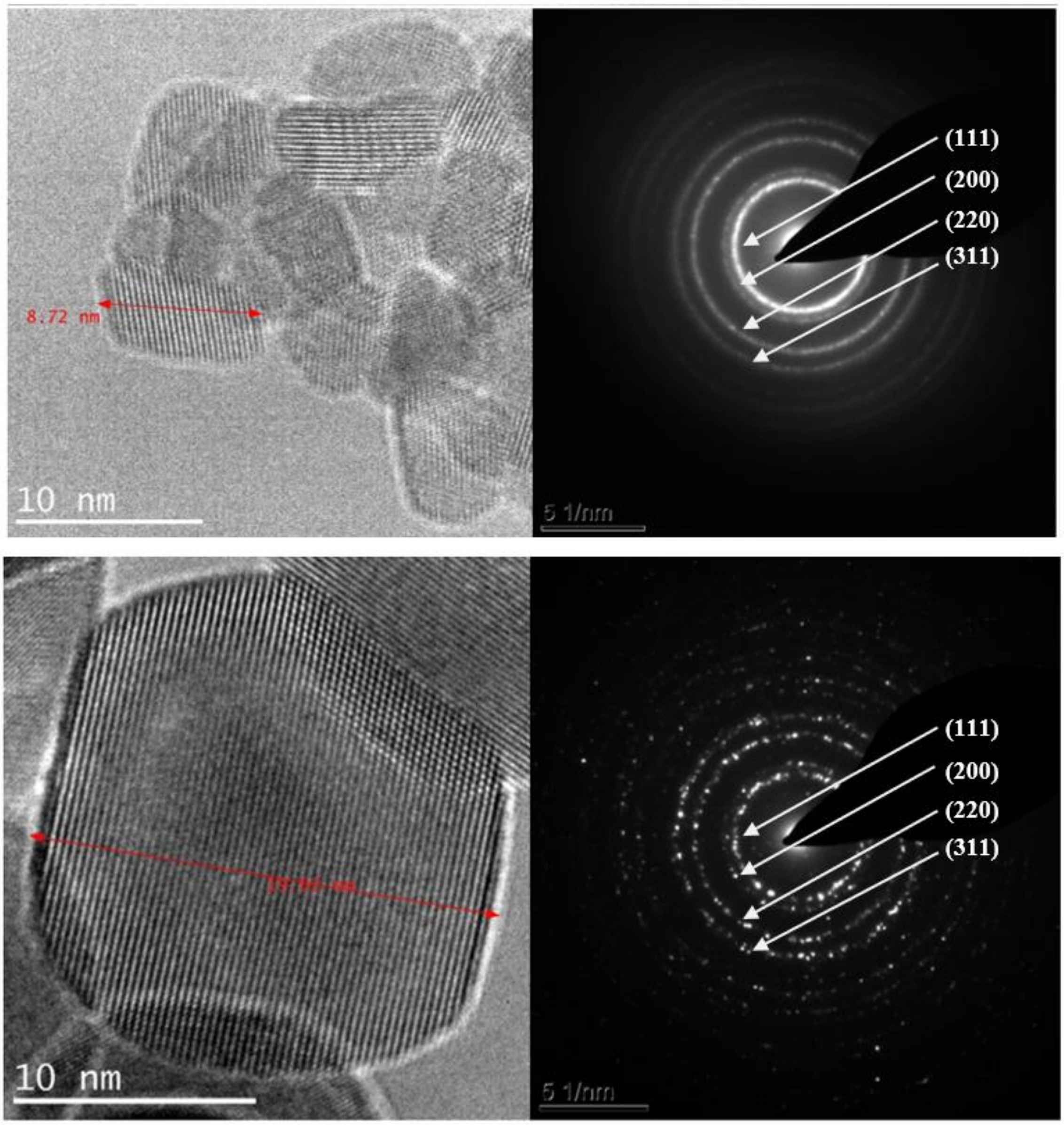

Figure 4.9. TEM images and SAED patterns of Er10 calcined at 500 (above) and 700°C (down) for 2 h, respectively.

In **Figures 4.6 – 4.9**, the SAED pattern shows crystalline structure and continuous rings without any additional secondary phases spots and rings detected. The first four rings of SAED patterns are assigned to (111), (200), (220) and (311) reflections of fluorite phase. The d-spacing from SAED was obtained by measuring the diameter of concentric rings. The measurement limited within 10% due to the height specimen sensitivity and magnetic hysterics of TEM lenses (147-149). **Table 4.2** shows the comparison of d-spacing from

SAED TEM and XRD. The d-spacing from XRD is obtained using equation 3.3. All the values are congruent with each other method.

Table 4.2. Comparison of d-spacing from TEM and XRD Rietveld refinement of doped and co-doped cerium nanoparticles from beads method

Samples name	h	k	l	XRD d/(Å)		TEM d/(Å)	
				500°C-2h	700°C-2h	500°C-2h	700°C-2h
CGO	1	1	1	3.120(5)	3.125(5)	3.145	3.135
	2	0	0	2.703(8)	2.707(3)	2.71	2.715
	2	2	0	1.913(6)	1.914(9)	1.938	1.918
	3	1	1	1.632(5)	1.633(3)	1.658	1.636
Dy10	1	1	1	3.119(9)	3.111(9)	3.195	3.015
	2	0	0	2.702(7)	2.696(9)	2.710	2.599
	2	2	0	1.912(2)	1.909(6)	1.918	1.862
	3	1	1	1.631(1)	1.629(3)	1.636	1.567
Ho10	1	1	1	3.116(5)	3.122(1)	3.117	3.065
	2	0	0	2.700(1)	2.704(1)	2.661	2.654
	2	2	0	1.910(8)	1.912(5)	1.871	1.895
	3	1	1	1.560(8)	1.631(2)	1.599	1.614
Er10	1	1	1	3.107(7)	3.119(6)	3.131	3.288
	2	0	0	2.693(1)	2.702(1)	2.717	2.942
	2	2	0	1.906(8)	1.911(3)	1.927	2.111
	3	1	1	1.626(9)	1.630(1)	1.643	1.792

The particle coarsening or well known as Ostwald ripening has happened because the elevated temperature may allow grain growth to occur in a stable structure. The diffusion of solute content will occur from smaller particles to larger particles. The large particles have the lower equilibrium solute content than a smaller particle hence transport from small particle to a larger particle will occur until small particle restore the solute to the equilibrium level so that the particle becomes smaller. The process will continue, resulting in the growth of the larger particle and disappearance of the small particles (107, 122, 150-152).

4.1.2 Granule Method

Thermal gravimetric analysis for CGO, Dy10, Ho10, and Er10-ALG granules are shown in **Figure 4.10**. The thermal analysis is conducted under air flow rate of 50cc/min from ambient temperature until 650°C with a heating rate 10C/min without any holding time. Similar to the thermal mechanism in bead method described in the earlier (section 4.1.1), the decomposition mechanism in the granule method found in the four stages. However, the large exothermic decomposition found in the fourth stage for all the composition not in the second stage, like in the bead route. This is probably because the linking G–G, G–M, and M–M in this method has stronger linkages than in the bead due to the large concentration of alginate present in the granules. Small exothermic decomposition found in the co-doped holmium around 500°C this is probably due to the oxidation decomposition from metastable to stable oxide and the residual M/G. The details mechanism of decomposition of metal complex alginate granules is discussed below:

1. The endothermic decomposition peak of hydrate evaporate during the heat-treatment process is observed at a temperature between room temperature and around 200°C. The weight loss for this around 12 – 15 % for every metal complex-ALG granule, shown in **Figure 4.11**.
2. The exothermic oxidative decomposition of linking G–G, G–M, and M–M has occurred at a temperature between 200 – 300°C. At this temperature, the most significant mass loss has occurred although the weight loss is not as profound as in the bead method. This oxidation process produces a mixture of phases of stable and metastable metal oxides.
3. The overlapping exothermic peak was observed at a temperature of 300 - 360°C. The metastable oxides phases transformed to more stable oxides in this stage.
4. The future exothermic peak from the remaining decomposition of β-D-mannuronic acid (M) and α-L-guluronic acid (G) is found in the temperature of

360 – 400°C. Different from bead method, the DSC curve show the highest heat flow at the final step.

A

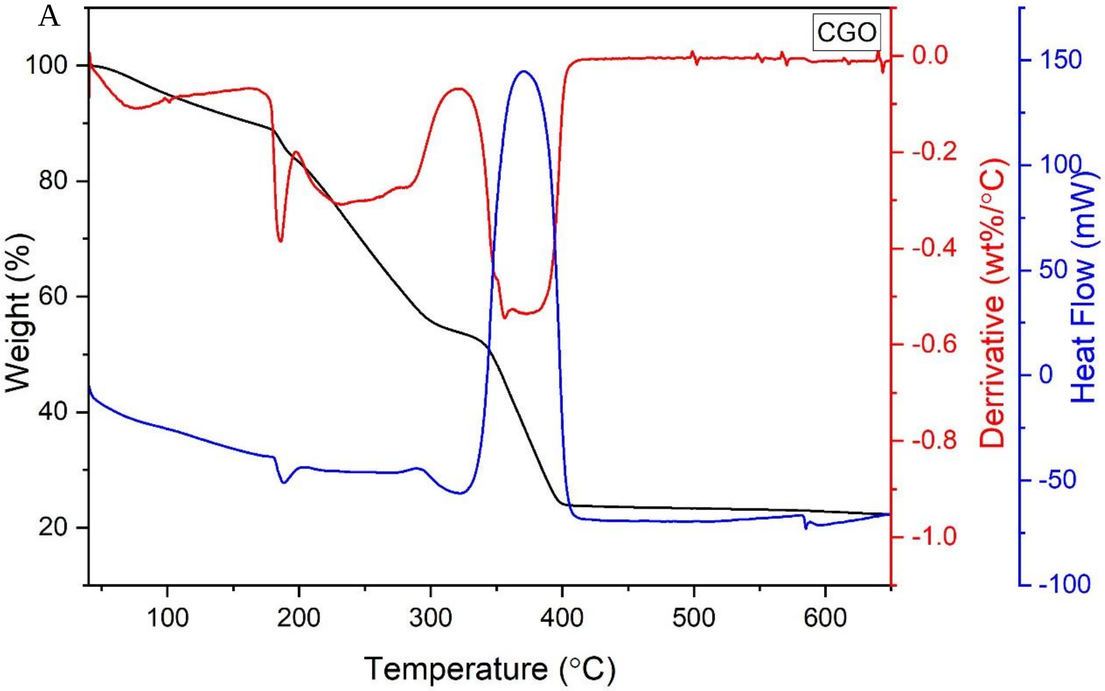

B

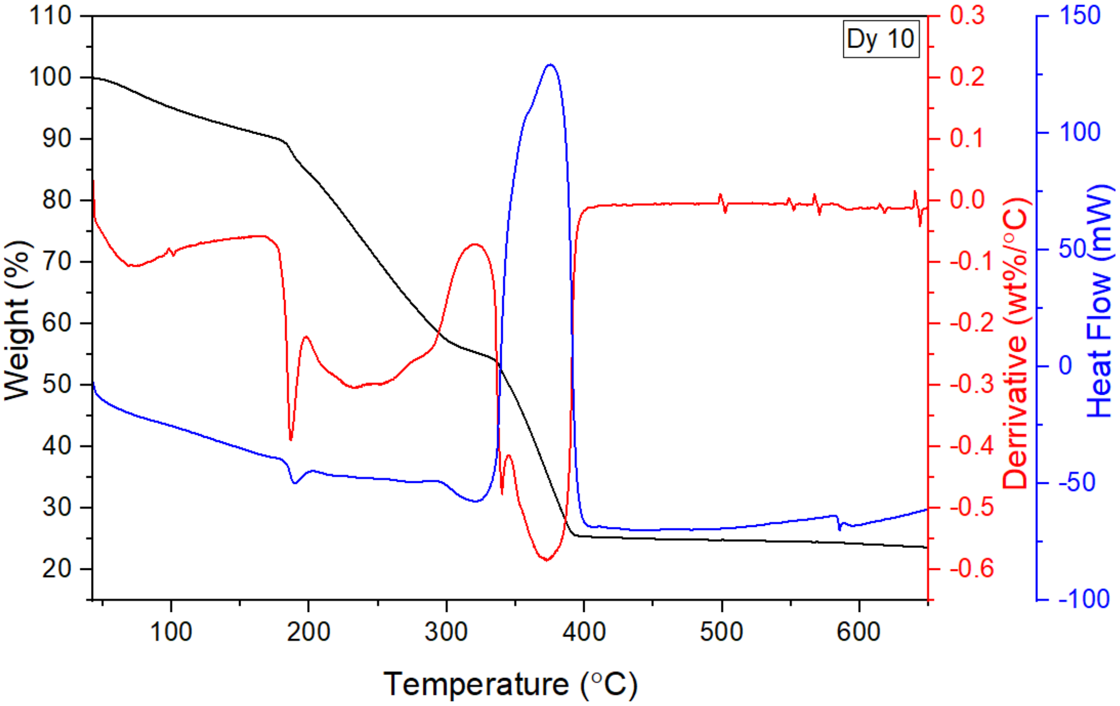

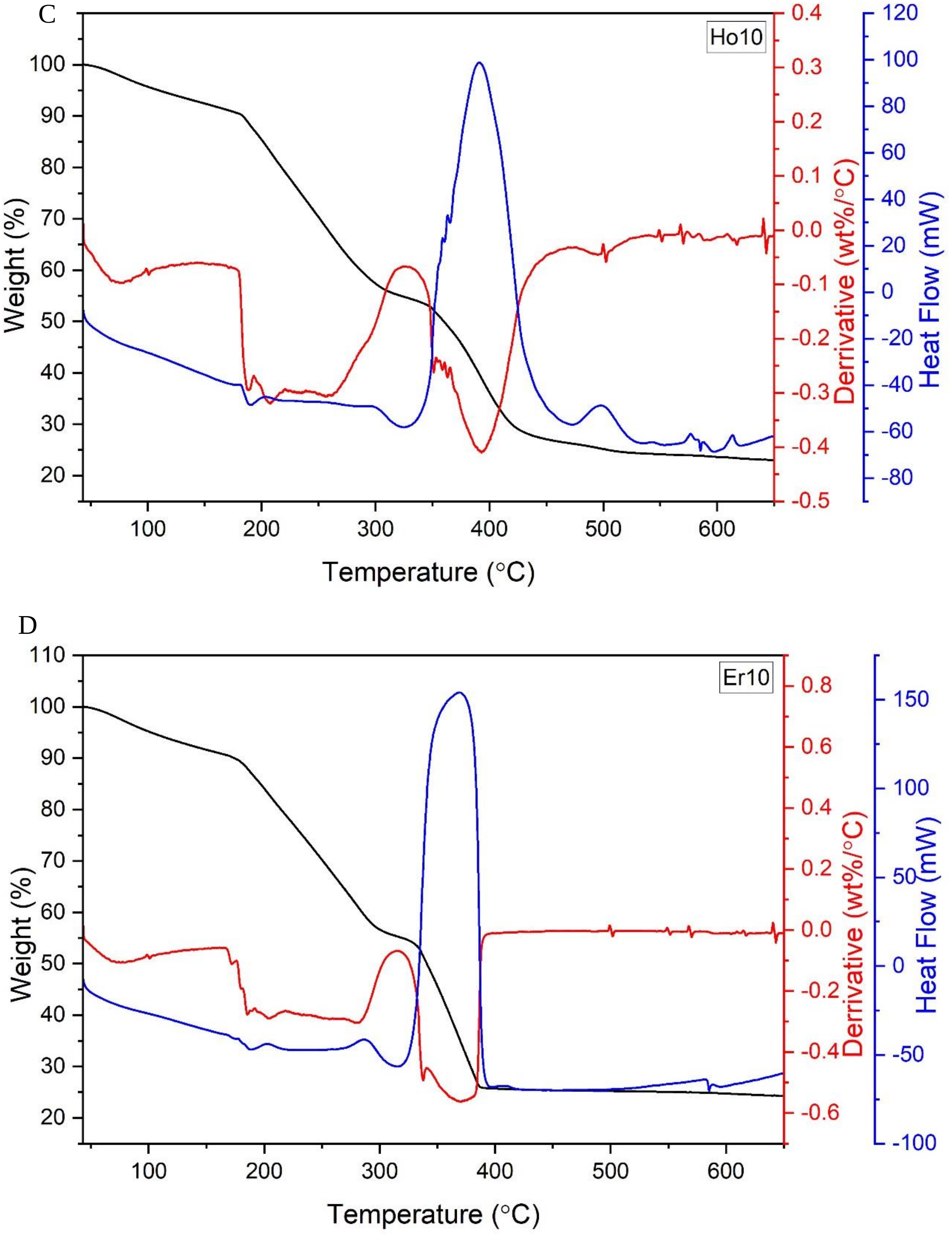

Figure 4.10. TGA (black line), derivative (red line), and DSC (blue line) of CGO (A), Dy10 (B), Ho10 (C), Er10 (D) dried granules in controlled atmosphere of air.

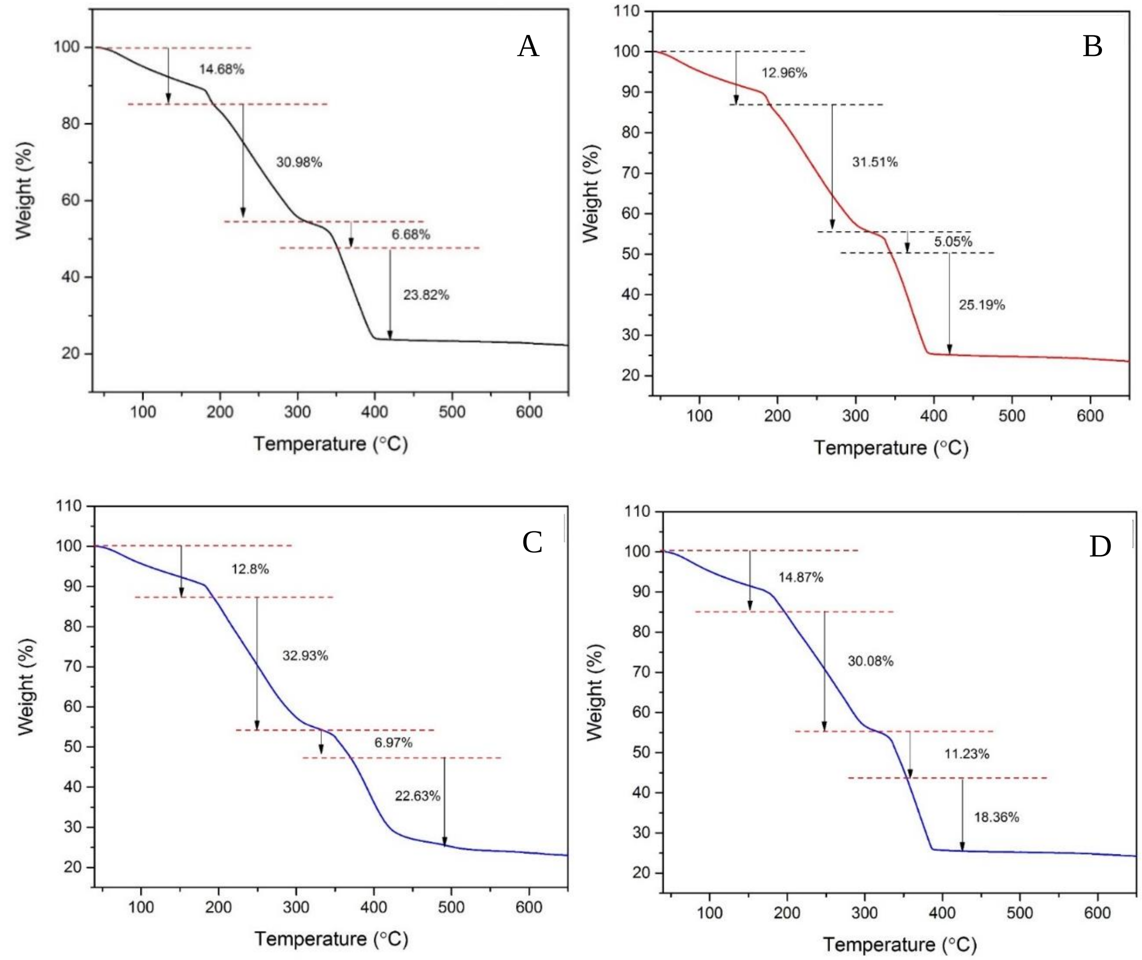

Figure 4.11. TGA analysis of CGO (A), Dy10 (B), Ho10 (C), Er10 (D) dried granules in controlled atmosphere of air

Figure 4.12 presents the XRD patterns of doped and co-doped cerium nanoparticles after calcination at two different temperatures with annealing time 2h. All compositions show pure cubic fluorite crystal structure with $Fm\overline{3}m$ space group. Similar with nanoparticle produced by bead method (section 4.1.1) there are no secondary phase detected for all compositions.

A

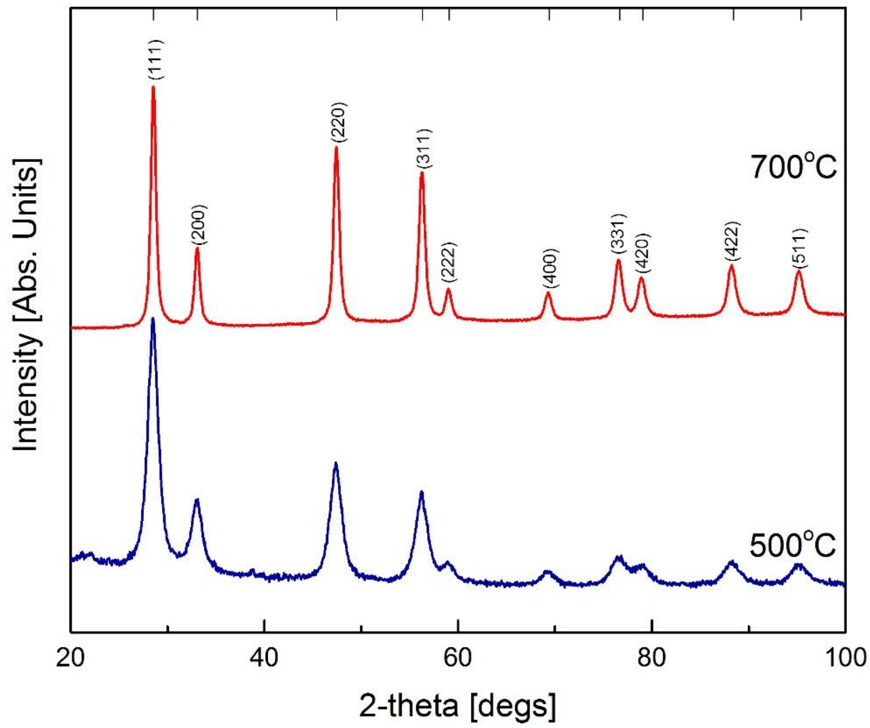
(111)
(200)
(220)
(311)
(222)
(400)
(331)
(420)
(422)
(511)
700°C
500°C
Intensity [Abs. Units]
20
40
60
80
100
2-theta [degs]

B

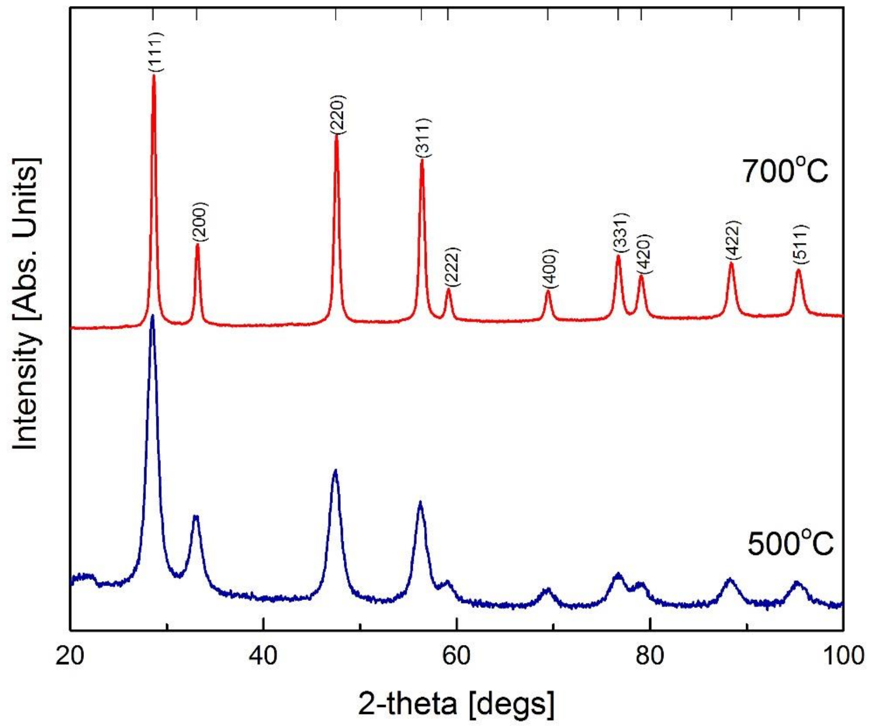
(111)
(200)
(220)
(311)
(222)
(400)
(331)
(420)
(422)
(511)
700°C
500°C
Intensity [Abs. Units]
20
40
60
80
100
2-theta [degs]

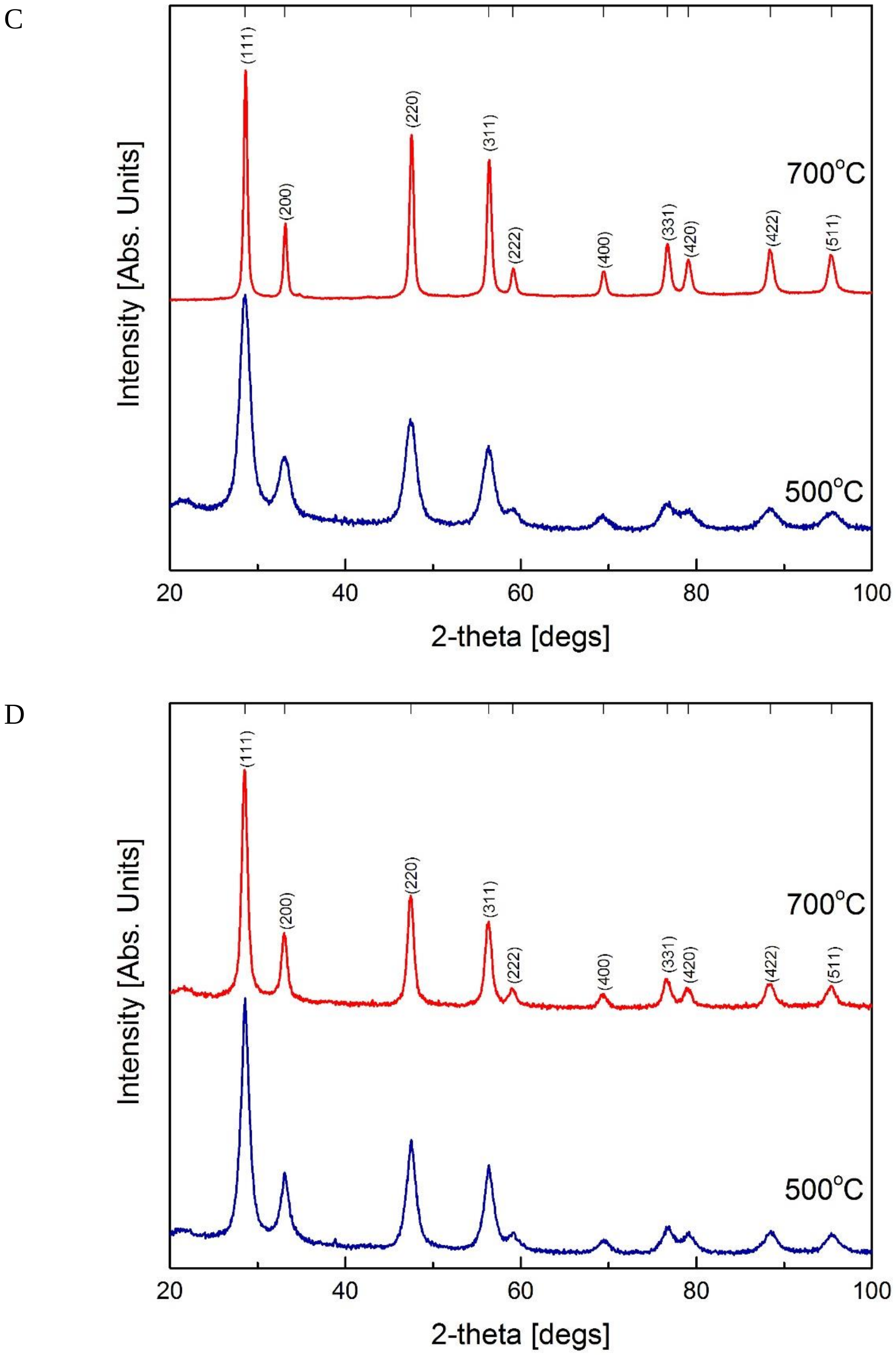

Figure 4.12. XRD patterns of CGO at the different temperature calcination (A); Dy10 nanoparticles (B); Ho10 nanoparticles (C); Er10 nanoparticles (D) synthesised using granules method.

Table 4.3 show the refined structural parameter, agreement factors, crystallite size and theoretical density for cerium gadolinium and co-doped (Dy10, Ho10, and Er10) nanoparticles calcined at 500 and 700°C for 2 h synthesised using granule method. The lattice parameter of each compositions shows same values with nanoparticles produced by the bead method. Lattice contraction is observed in smaller d-spacing (**Table 4.4**) and lower lattice parameter along with smaller ionic radii of co-dopants.

Table 4.3. Refined structural parameter, agreement factors, crystallite size and theoretical density for doped and co-doped cerium nanoparticles calcined at 500 and 700°C for 2 h synthesised using granule method

	CGO		**Dy10**		**Ho10**		**Er10**	
	500°C	**700°C**	**500°C**	**700°C**	**500°C**	**700°C**	**500°C**	**700°C**
Rp	0.026	0.011	0.025	0.014	0.026	0.013	0.028	0.015
Rexp	0.028	0.010	0.028	0.010	0.030	0.010	0.028	0.011
χ^2	1.346	2.592	1.232	4.928	1.210	3.764	1.538	4.928
V (Å^3)	160.10 (2)	160.14 (1)	159.25 (2)	159.32 (1)	159.30 (2)	159.35 (1)	158.82 (2)	158.84 (1)
a (Å)	5.4300 (3)	5.43037 (8)	5.4204 (2)	5.42114 (8)]	5.47209 (3)	5.42147 (7)	5.4154 (2)	5.41568 (16)
D_{XRD} (Å)	12.178	22.39	12.249	38.803	11.92	33.759	10.705	31.685
ρ_{Th} (g/cm^3)	7.217	7.215	7.277	7.274	7.285	7.283	7.317	7.316

Figures 4.13 – 4.16 shows the transmission electron microscopy (TEM) images and selected area electron diffraction (SAED) patterns of doped and co-doped cerium nanoparticles after calcination

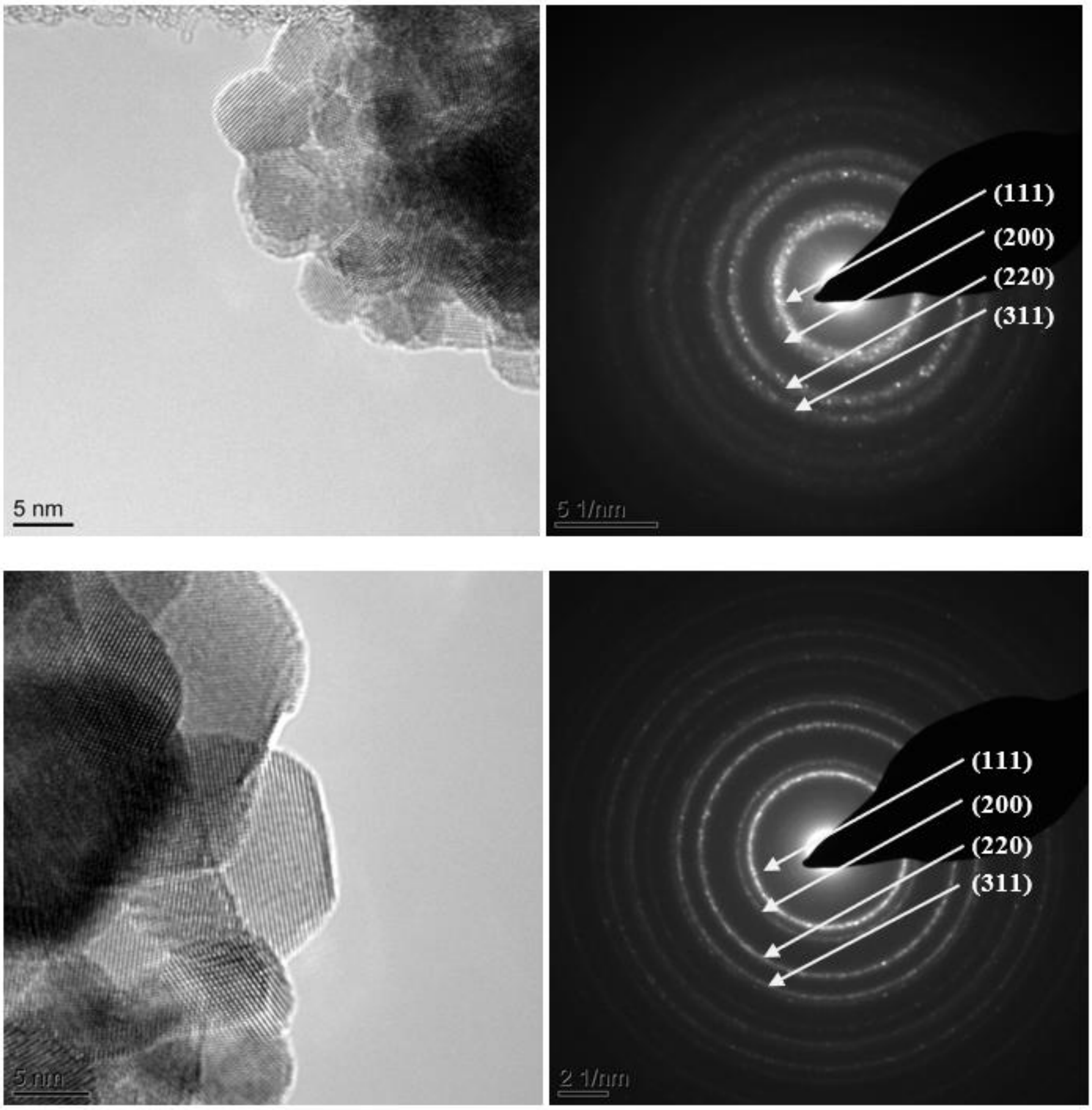

Figure 4.13. TEM and SAED images of CGO samples calcined at 500 (above) and 700°C (down) for 2 h, respectively.

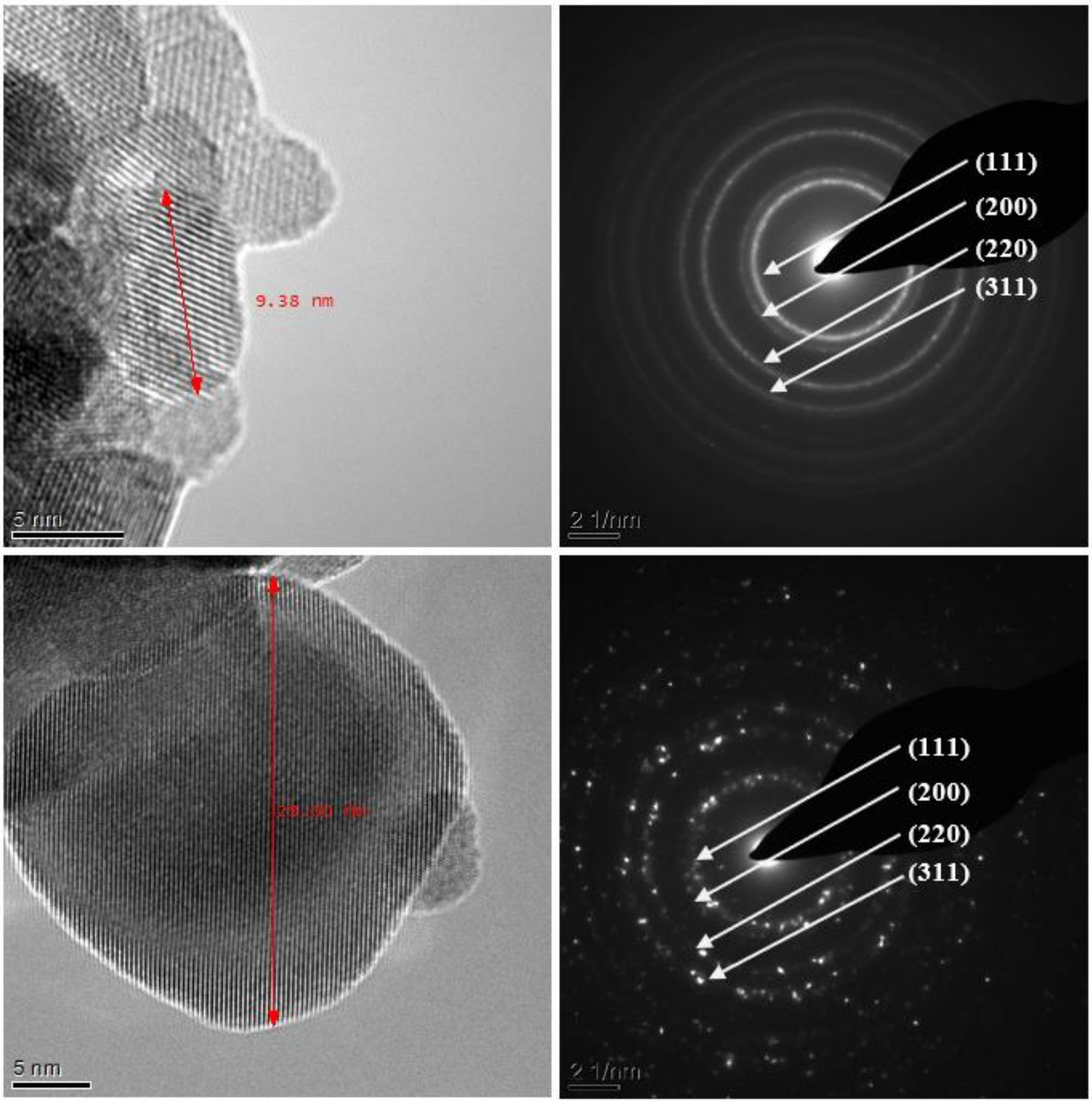

Figure 4.14. TEM and SAED images of Dy 10 samples calcined at 500 (above) and 700°C (down) for 2 h, respectively

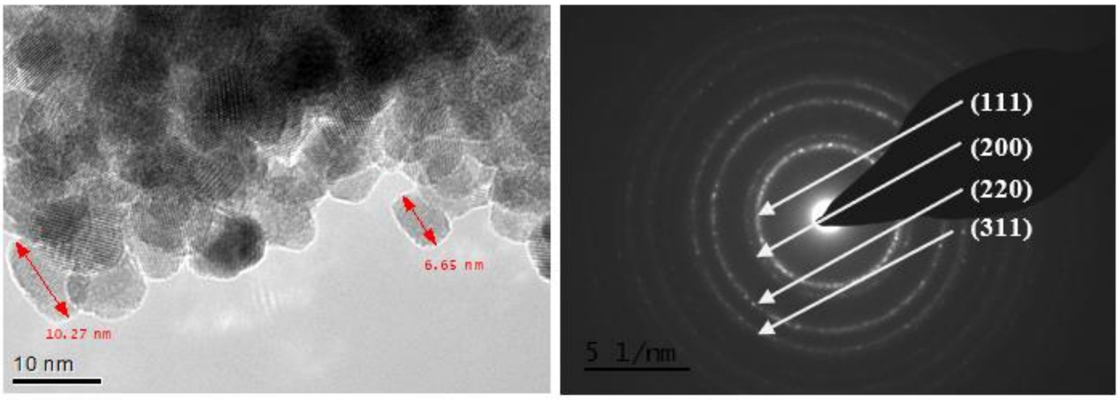

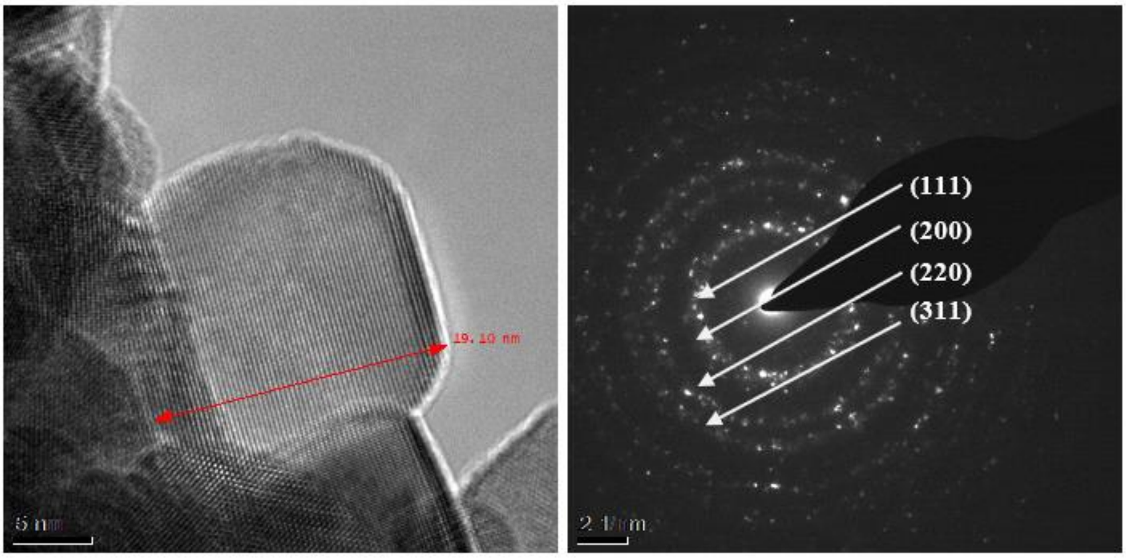

Figure 4.15. TEM and SAED images of Ho10 samples calcined at 500 (above) and 700°C (down) for 2 h, respectively

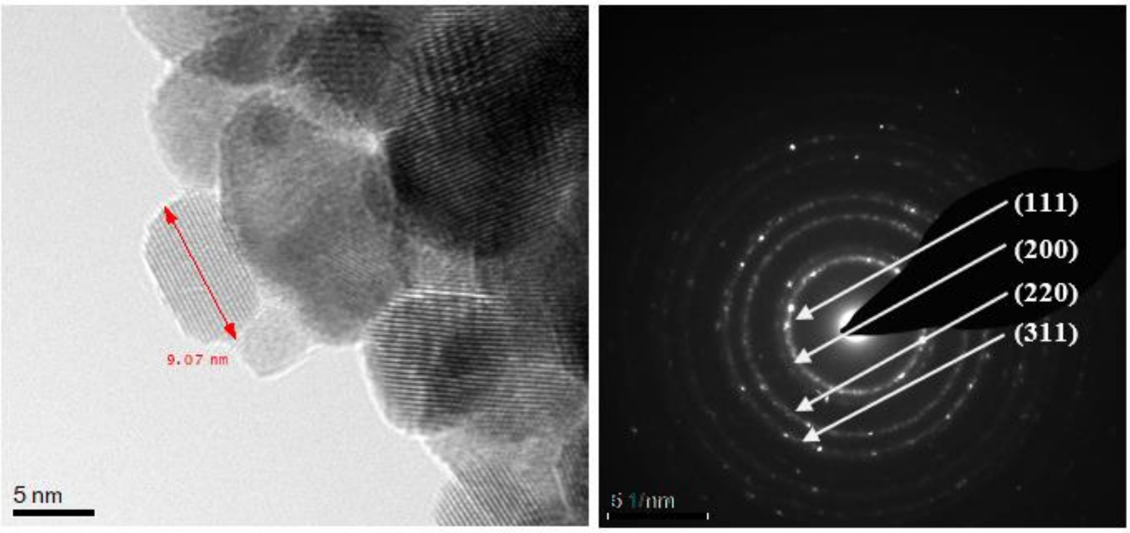

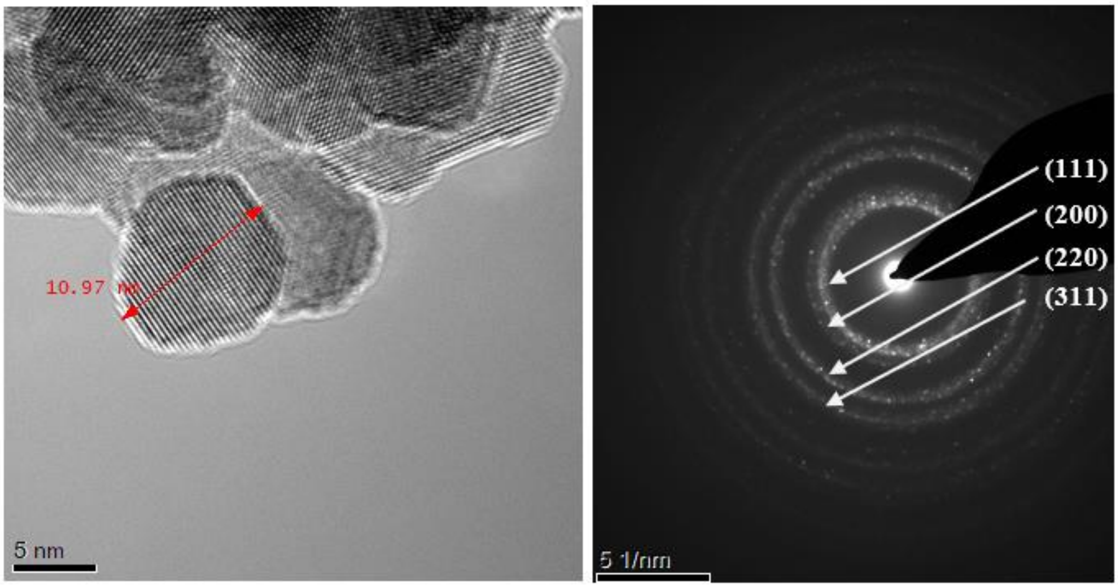

Figure 4.16. TEM and SAED images of Er10 samples calcined at 500 (above) and 700°C (down) for 2 h, respectively.

The calcination temperature affects the mean crystallite size. Higher temperature produces bigger crystallite size than lower calcination temperature. The calculated crystallite sizes by XRD are harmonious with the observed morphology of particles from TEM images. Broad peak in XRD patterns and continous ring patterns in SAED from powder calcinaed at 500°C are the manifestion of nanoparticles (~11-12nm). **Figures 4.13-4.16** show the TEM morphology of fluorite structure in hexagonal and square shape morphologies are detected.

Table 4.4. Comparison of d-spacing from TEM and XRD Rietveld refinement of doped and co-doped cerium nanoparticles from beads method

Samples name	h	k	l	XRD d/(Å)		TEM d/(Å)	
				500°C-2h	700°C-2h	500°C-2h	700°C-2h
CGO	1	1	1	3.126	3.122	3.122	3.136
	2	0	0	2.708	2.704	2.703	2.675
	2	2	0	1.916	1.914	1.857	1.862
	3	1	1	1.634	1.633	1.586	1.588
Dy10	1	1	1	3.128	3.113	3.136	3.289
	2	0	0	2.708	2.697	2.739	2.964
	2	2	0	1.915	1.909	1.932	1.951
	3	1	1	1.633	1.629	1.649	1.747
Ho10	1	1	1	3.122	3.113	3.079	3.462
	2	0	0	2.704	2.698	2.664	2.975
	2	2	0	1.912	1.909	1.893	2.162
	3	1	1	1.631	1.629	1.583	1.950
Er10	1	1	1	3.119	3.097	3.117	3.107
	2	0	0	2.702	2.685	2.71	2.619
	2	2	0	1.911	1.903	1.893	1.874
	3	1	1	1.629	1.624	1.601	1.523

The novel sol-gel sodium alginate has been successfully synthesising the nanoparticles of doped (CGO) and co-doped (Dy10, Ho10 and Er10) ceria-based electrolytes. The calcination temperature at 500°C for 2h showed the optimum temperature to obtain the particles size ~11nm for both methods. The granule method showed having higher heat flow in DSC curve than the bead method due to the larger concentration of alginate present. For the rest of compositions, the bead route was employing to synthesise the materials.

4.1.3 Sintering process

Figure 4.17 shows the relative density of doped and co-doped ceria pellets sintered from 1300 to 1500°C with annealing time 2h. The heating rate was maintained at 3°C/min during the process. The variation of sintering temperature used to ensure the maximum density of the compact ceramic is achieved. Clearly from the graph that the higher the sintering temperature, the denser the ceramics pellets can be produced.

Herring's scaling law proposes the effect of particle size on the sintering rate. The model predicts the periods of sintering time to get the same degree of sintering when the particle with similar shape, but different sizes are sintered under the same sintering mechanism and conditions. Moreover, for two kinds of powder with radii a_1 and a_2, where $a_2 = \lambda a_1$, the sintering time to get same densification level is proportional to $(\lambda)^3$ (153).

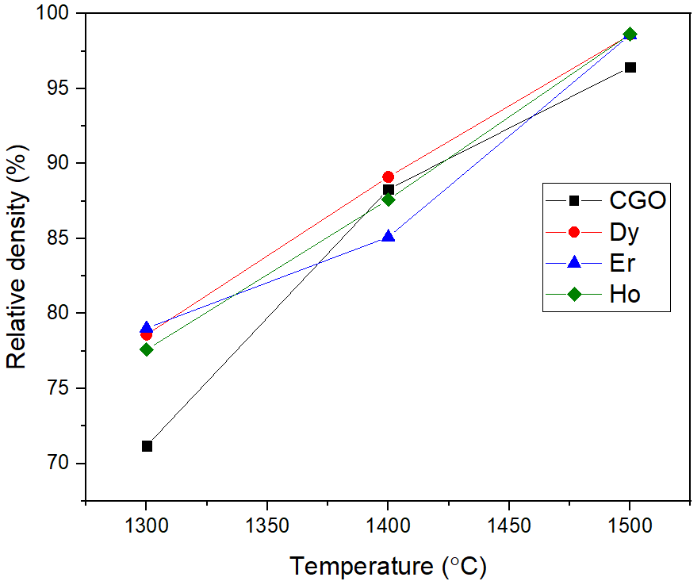

Figure 4.17. Densification curve of doped and co-doped cerium oxide ceramics after sintering in various temperatures.

The relative density result is in a good agreement with the SEM images of sintered pellets, shown in **Figure 4.18 – 4.20**. At sintering temperature 1300°C, the microstructure shows the first step of intermediate sintering stage when rapid inter-particle neck growth and intermediate equilibrium pore shape with continuous porosity growing. For higher temperature, at 1400°C, the porosity shrinking and became unstable and pinch off. The microstructure images show isolated and continuous pore, which are the evidence of the intermediate stage and constitutes the beginning of the final step. Pellet ceramics sintered at 1500°C show the microstructure in the final stage, **Figure 4.20**. The pores disappear or pinches off and become isolated at the grain corners.

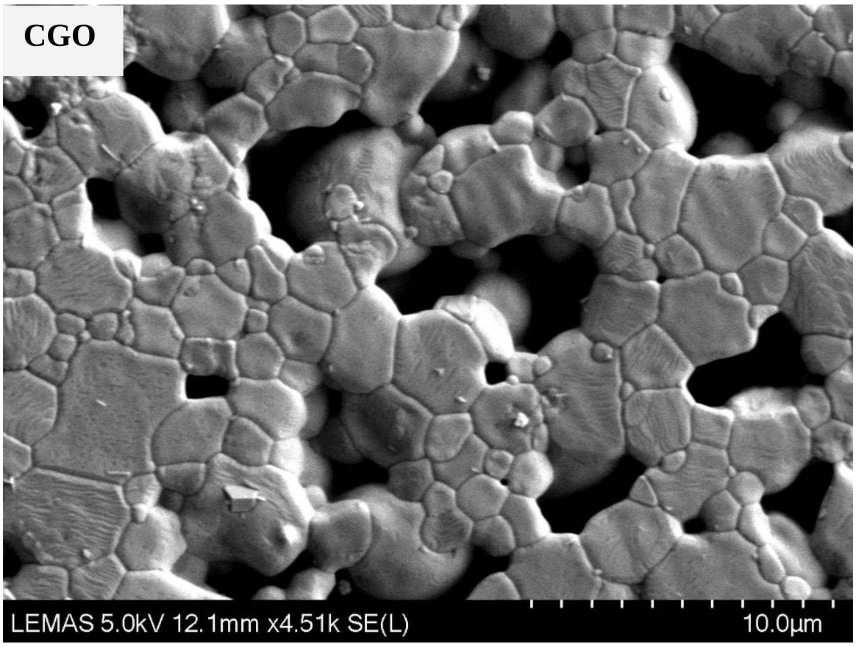

Figure 4.18. SEM micrographs of CGO ceramics sintered at 1300°C for 2 h

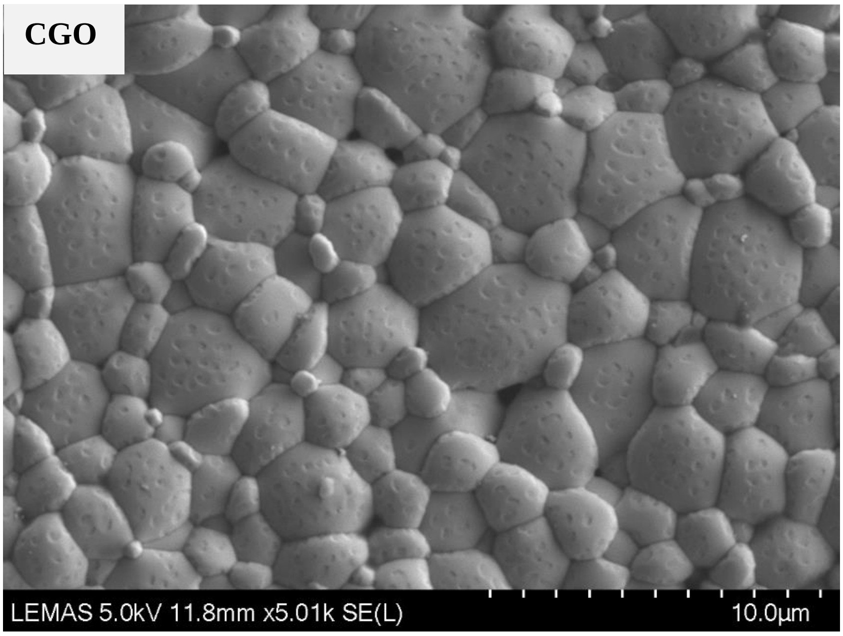

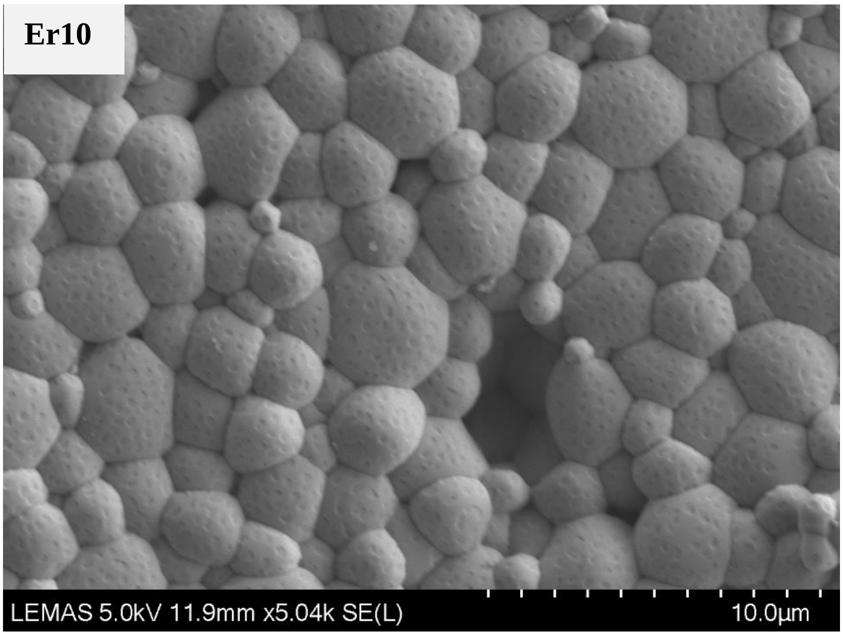

Figure 4.19. SEM micrographs of doped and co-doped cerium ceramics sintered at 1400°C for 2 h

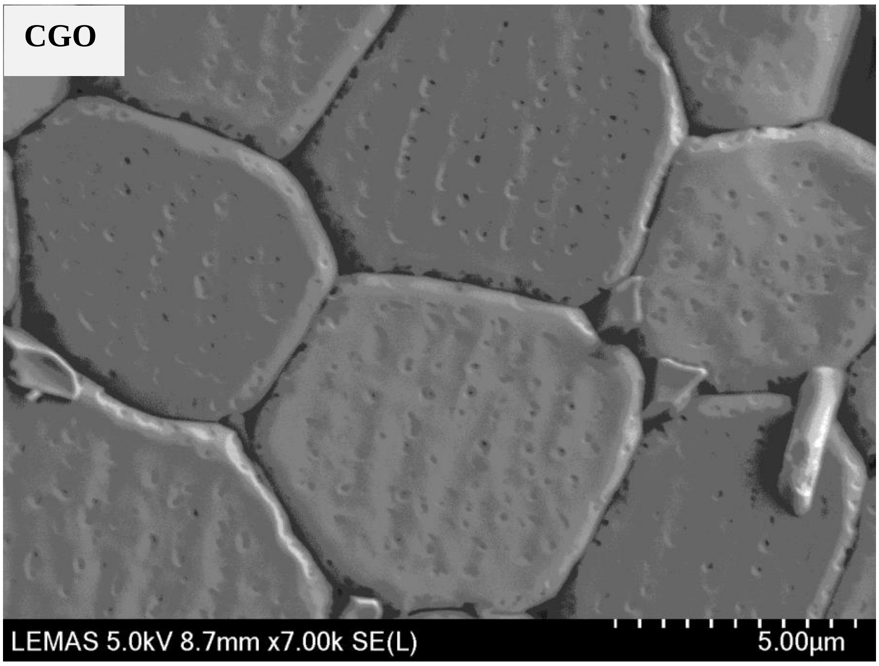

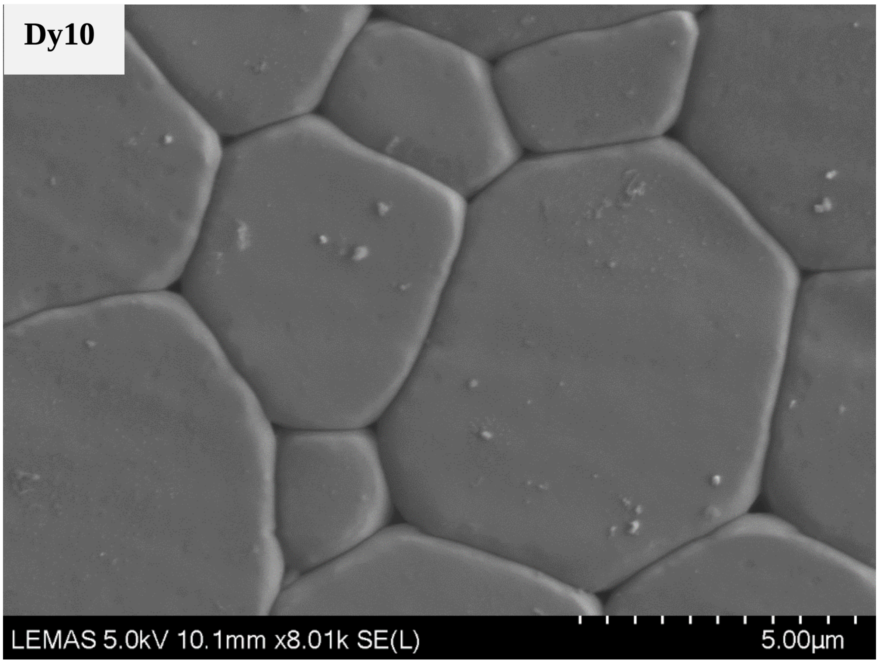
Dy10
LEMAS 5.0kV 10.1mm x8.01k SE(L)
5.00µm

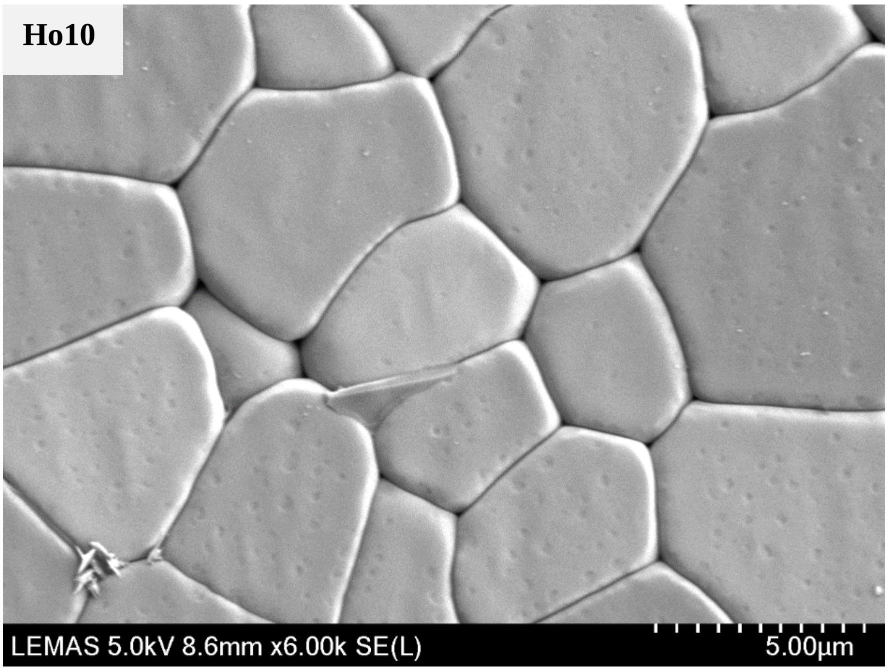
Ho10
LEMAS 5.0kV 8.6mm x6.00k SE(L)
5.00µm

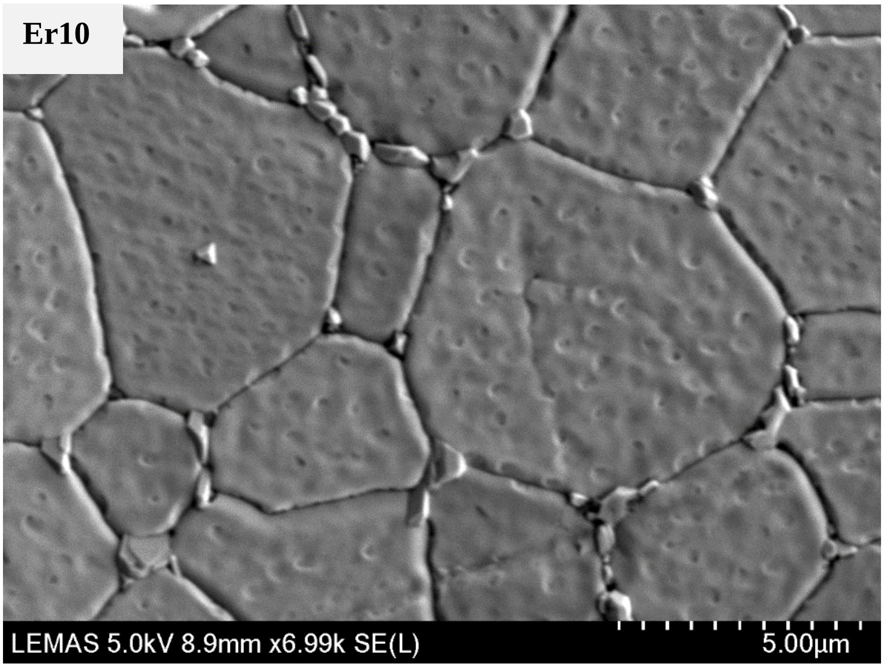

Figure 4.20. SEM micrographs of doped and co-doped of cerium ceramics sintered at 1500°C for 2 h.

4.2 Synthesis of $Ce_{0.8}Dy_xGd_{0.2-x}O_{1.9}$ ($0 \leq x \leq 0.2$) nanoparticle

4.2.1 Material characterisation

The $Ce_{0.8}Dy_xGd_{0.2-x}O_{1.9}$ ($0 \leq x \leq 0.2$) nanoparticles were analysed by X-ray diffraction (XRD) using a PANalytical X'Pert XRD. The morphology, size and chemical analysis of nanoparticles were examined under high resolution transmission electron microscopy (HRTEM) (FEI Tecnai TF20 operated at 200kV fitted with a Gatan Orius CCD camera and Oxford instruments 80 mm^2)

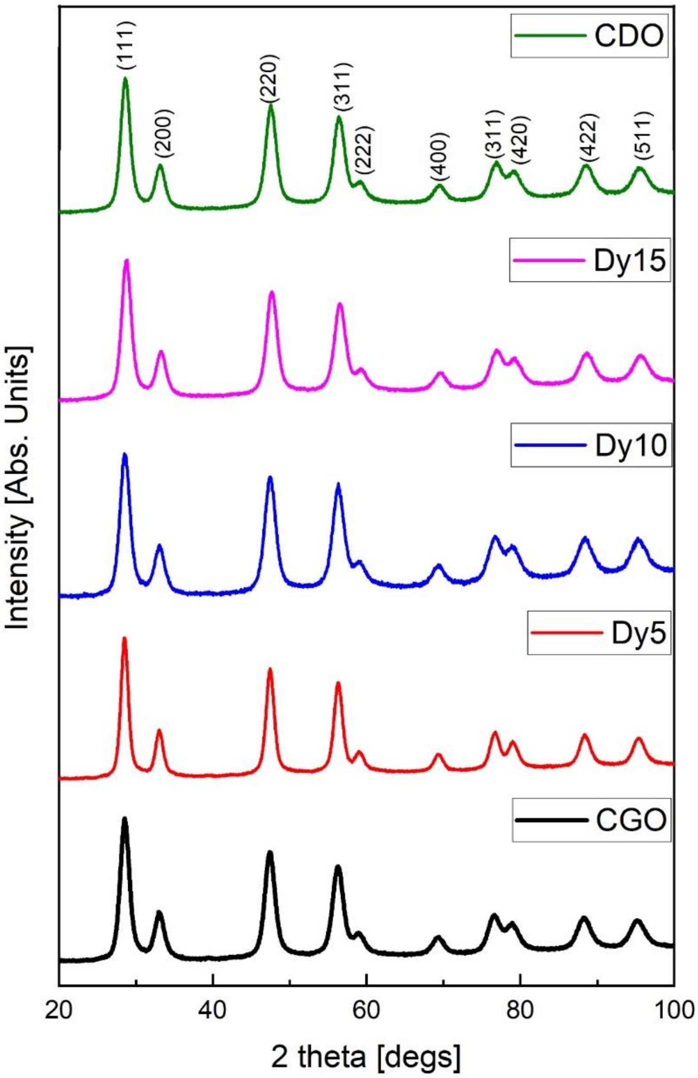

Figure 4.21. XRD patterns for nanoparticles of $Ce_{0.8}Dy_xGd_{0.2-x}O_{1.9}$ ($0 \leq x \leq 0.2$) calcinated at 500°C for 2h.

XRD patterns of $Ce_{0.8}Dy_xGd_{0.2-x}O_{1.9}$ ($0 \leq x \leq 0.2$) nanoparticles calcined at 500°C for 2h are shown in **Figure 4.21**. All peaks confirm the single fluorite phase without any secondary phase detected. The partial substitution of Ce^{4+} with Dy^{3+} and Gd^{3+} in ceria matrix formed a complete solid solution in the composition range of $0 \leq x \leq 0.2$. Broad peaks in XRD pattern indicate a small crystallite size in the powder sample typically in the nanometer range. This nano range was also observed in the continuous SAED ring pattern (**Figure 4.22**). The nanosize of particles is confirmed with crystallite size calculation (**Table 4.5**) and TEM images (**Figure 4.22**), even though the calculated crystallite size from XRD (11 – 15 nm) is bigger than the observed TEM images (~10nm).

Table 4.5. Refined structural parameter, agreement factors, crystallite size and theoretical density for $Ce_{0.8}Dy_{0.2-x}Gd_xO_{1.9}$ nanoparticles calcined at 500°C for 2 h.

	CGO	**Dy5**	**Dy10**	**Dy15**	**CDO**
Rp	0.021	0.025	0.024	0.024	0.023
Rexp	0.0126	0.014	0.016	0.014	0.014
χ^2	5.34	5.954	4.494	5.617	5.523
V (Å^3)	160.16 (2)	159.73 (1)	159.47 (2)	159.05 (2)	159.05 (2)
a (Å)	5.43061 (2)	5.42580 (14)	5.4228 (2)	5.41811 (18)	5.4150 (2)
D_{XRD} (Å)	111.759	150.643	115.740	123.984	120.269
ρ_{Th} (g/cm^3)	7.214	7.244	7.267	7.297	7.321

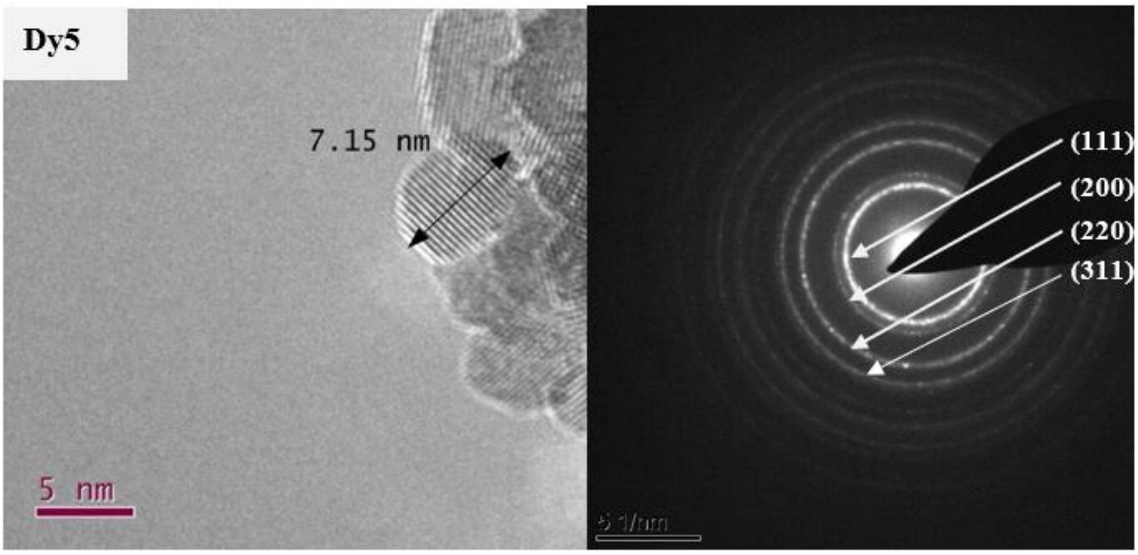
Dy5
7.15 nm
5 nm
(111)
(200)
(220)
(311)
5 1/nm

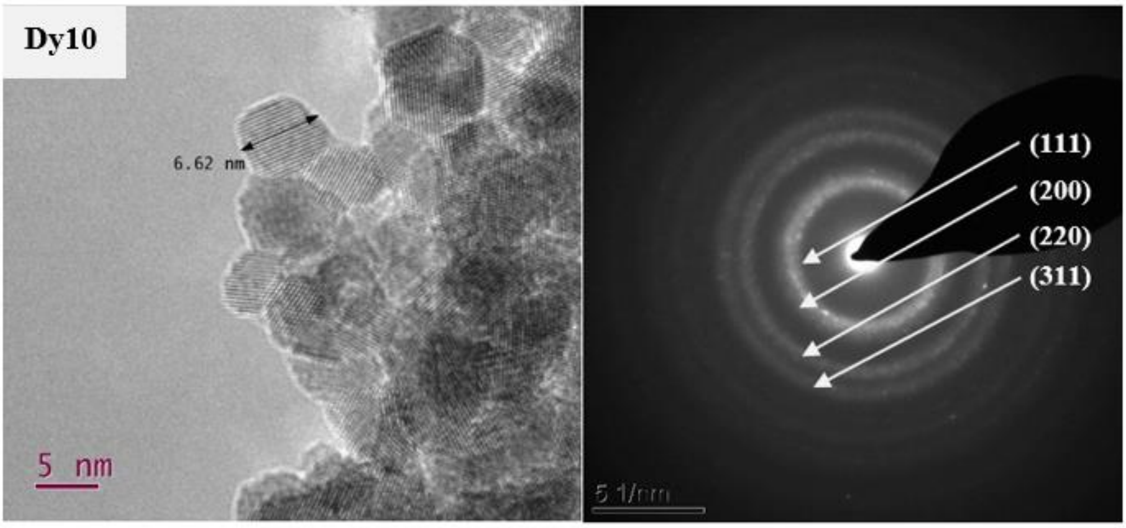
Dy10
6.62 nm
5 nm
(111)
(200)
(220)
(311)
5 1/nm

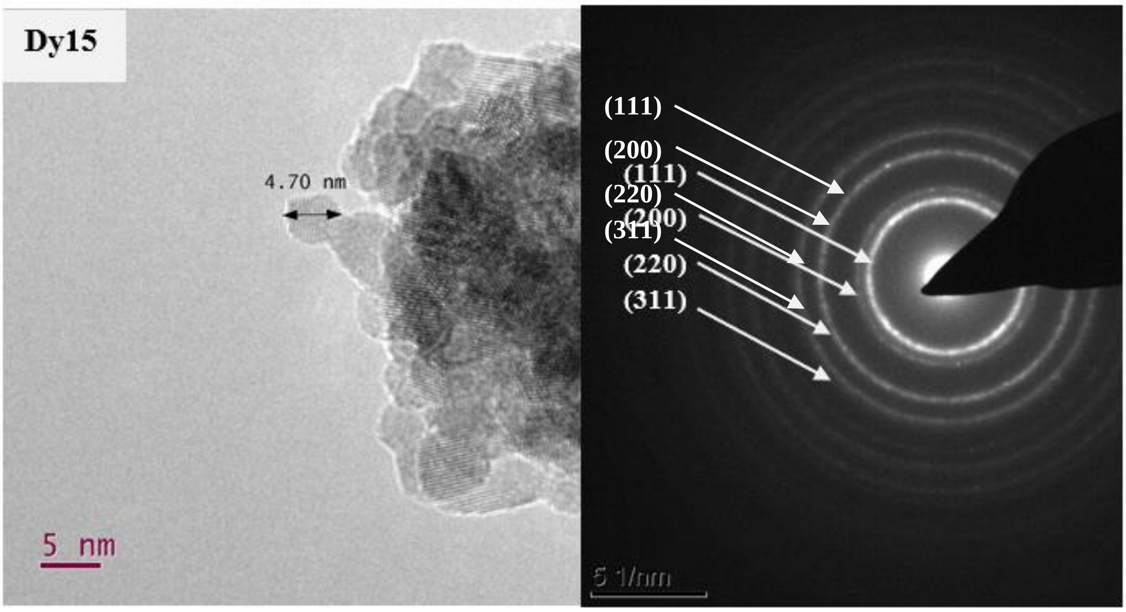
Dy15
4.70 nm
5 nm
(111)
(200)
(220)
(311)
(111)
(200)
(220)
(311)
5 1/nm

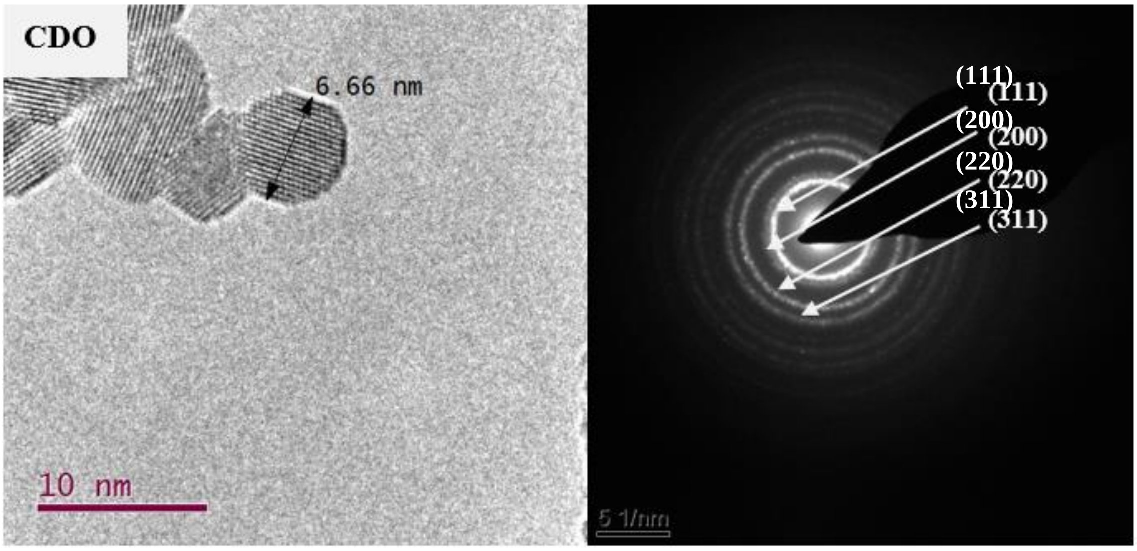

Figure 4.22. TEM and SAED images of of $Ce_{0.8}Dy_xGd_{0.2-x}O_{1.9}$ ($0 \leq x \leq 0.2$) nanoparticles calcined at 500°C for 2 h, respectively

The morphology particles show fluorite structure forming in a mixture of hexagonal and square shape depending on their orientation on the TEM grid. The lattice parameter decreased with an increasing Dy content is shown in **Figure 4.23**. The linear trend indicates that the materials obey Vegard's Law (154).

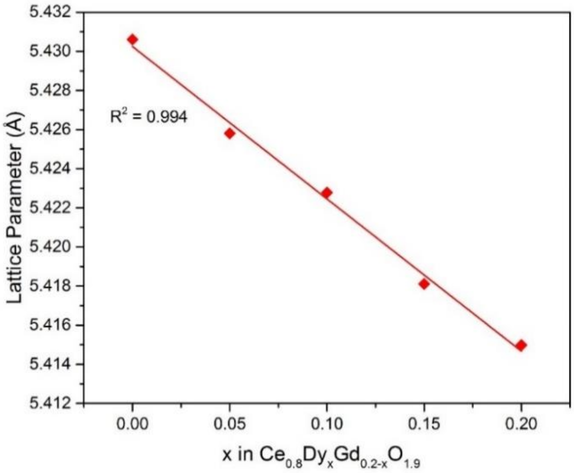

Figure 4.23. Dependence of lattice parameter on the composition of $Ce_{0.8}Dy_xGd_{0.2-x}O_{1.9}$ ($0 \leqslant x \leqslant 0.2$).

A lattice contraction trend was observed for partial doping and full replacement of Gd^{3+} by smaller sized Dy^{3+} ions into the ceria matrix. The interplanar spacing (*d* value) shifted into smaller value and changed the peak to a higher diffraction angle. The peak shift to higher diffraction angle from (111) peak is shown in **Figure 4.24**. Moreover, **Table 4.6** also shows the evidence of lattice contraction in *d*-spacing from XRD and TEM. This contraction occurred because Dy^{3+} ions (CN 6 = 0.912 Å) substituted Gd^{3+} (CN 6 = 0.938Å) ions that have higher ionic radius (63).

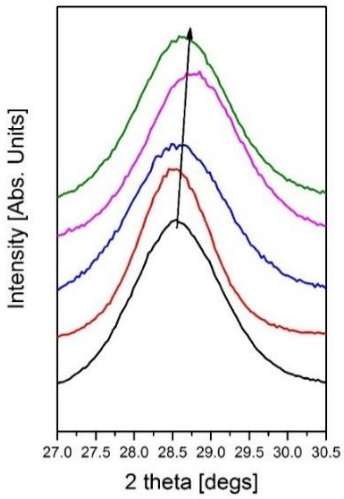

Figure 4.24. XRD patterns at (111) peak: Black: CGO, red: Dy5, blue: Dy10, pink: Dy15, and green: CDO.

Table 4.6. Comparison of d-spacing from XRD Rietveld refinement and SAED TEM ring patterns of $Ce_{0.8}Dy_xGd_{0.2-x}O_{1.9}$ nanoparticles.

h	k	l	XRD d/(Å)				TEM d/(Å)			
			Dy5	Dy10	Dy15	CDO	Dy5	Dy10	Dy15	CDO
1	1	1	3.125	3.119	3.099	3.114	3.127	3.195	3.042	3.037
2	0	0	2.703	2.703	2.687	2.698	2.710	2.710	2.626	2.619
2	2	0	1.913	1.912	1.904	1.909	1.918	1.918	1.852	1.834
3	1	1	1.632	1.631	1.625	1.628	1.636	1.636	1.585	1.568

TEM-EDS was used to analyse the elements present in the calcined nanoparticles. **Figure 4.25** shows a typical TEM-EDS spectrum from calcined Dy5. It is clearly seen from the spectrum that carbon and copper elements from TEM grids are detected. The weight percentages from EDS analysis were used to calculate the mole fractions of the elements (**Table 4.7**). The calculated mole fractions of Ce, Dy, and Gd in the entire series of samples prepared in this study are in excellent agreement with their respective nominal mole fractions.

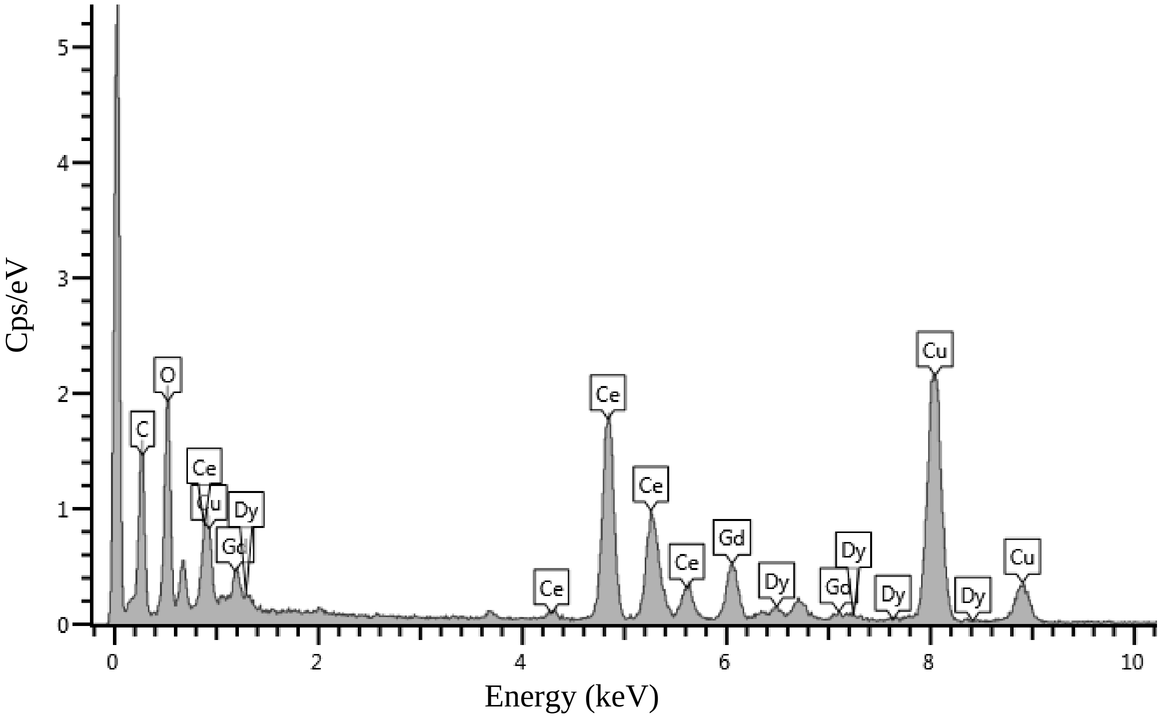

Figure 4.25. TEM – EDS spectrum illustrates the composition of Dy5 nanoparticles after calcination at 500°C for 2h.

Table 4.7. Weight precentages and calcutaed mole fractions obtained from TEM – EDS analysis of $Ce_{0.8}Dy_xGd_{0.2-x}O_{1.9}$ ($0 \leqslant x \leqslant 0.2$) nanoparticles.

Samples	Elements	Wt (%)	Mole	Mole %	Nominal
Dy5	Ce	42.02	0.299	0.798	80
	Dy	2.64	0.017	0.447	5
	Gd	9.6	0.059	0.157	15
Dy10	Ce	53.09	0.379	0.809	80
	Dy	7.39	0.045	0.097	10
	Gd	6.91	0.044	0.093	10
Dy15	Ce	48.2	0.344	0.806	80
	Dy	9.68	0.062	0.144	15
	Gd	3.45	0.021	0.049	5
CDO	Ce	47.88	0.341	0.817	80
	Dy	12.41	0.076	0.183	20

Raman measurements were also carried out to investigate the structural arrangement of $Ce_{0.8}Dy_xGd_{0.2-x}O_{1.9}$ ($0 \leq x \leq 0.2$) nanoparticles using a Renishaw in Via Raman spectrometer with a green Ar^+ laser (λ=514.5 nm) excitation source. **Figure 4.26** shows the Raman spectra of $Ce_{0.8}Dy_xGd_{0.2-x}O_{1.9}$ ($0 \leqslant x \leqslant 0.2$) compounds. The peak at 463cm^{-1} is F_{2g} mode which corresponds to anionic-cationic stretching Raman band of ceria (155 – 158), whereas peak positions at 558 cm^{-1} and 611 cm^{-1} are associated with D1 and D2 bands. The D1 band represents the oxygen vacancies associated with defect complexes, while D2 band associates with the formation of defect species with O_h symmetry. The ratio between I_{D1}/I_{D2} presents the relative concentration of the two types of defect complexes (156). **Table 4.8** shows the ratio for $Ce_{0.8}Dy_xGd_{0.2-x}O_{1.9}$ ($0 \leq x \leq 0.2$) nanoparticles. It shows that partially substitution with Dy, not significantly changes the ratio.

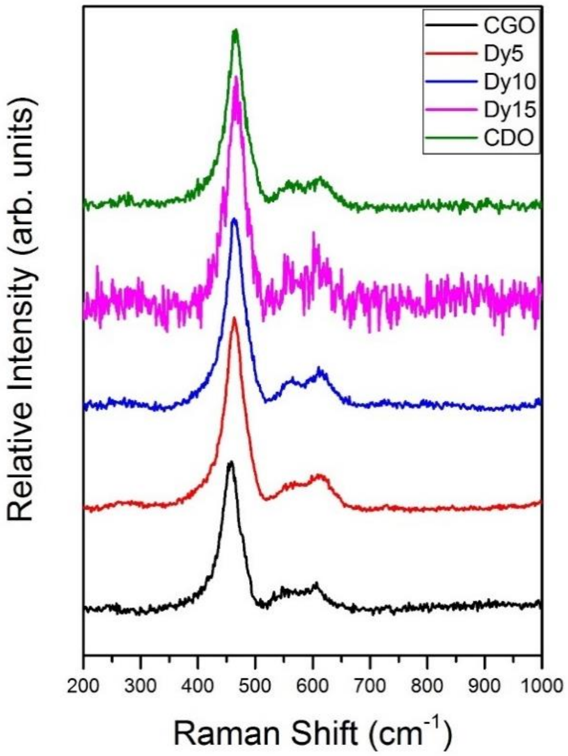

Figure 4.26. Raman spectra of $Ce_{0.8}Dy_xGd_{0.2-x}O_{1.9}$ ($0 \leq x \leq 0.2$) nanoparticles after calcination at 500°C for 2h.

Table 4.8. Ratio I_{D1}/I_{D2} from Raman peaks of $Ce_{0.8}Dy_xGd_{0.2-x}O_{1.9}$ ($0 \leq x \leq 0.2$)

Sample code	I_{D1}/I_{D2}
CGO	0.71
Dy5	0.75
Dy10	0.77
Dy15	0.79
CDO	0.79

The F_{2g} band of $Ce_{0.8}Dy_xGd_{0.2-x}O_{1.9}$ ($0 \leqslant x \leqslant 0.2$) compounds is shown in **Figure 4.27**. Fitting was done by OriginPro using a Lorentzian function for all peaks. The peak shifted to higher frequencies along and became asymmetric with the increasing dysprosium ions.

Partial doping and full replacement of Gd^{3+} by smaller sized Dy^{3+} in ceria matrix decreased the M-O bond length and shifted the vibrational frequency to higher energies.

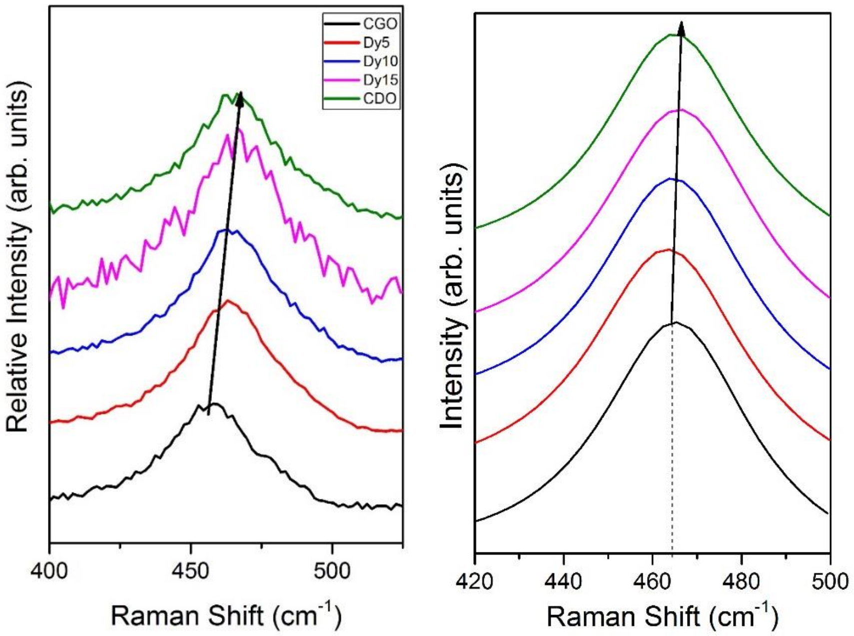

Figure 4.27. (a) F_{2g} band at 463 cm^{-1} of $Ce_{0.8}Dy_xGd_{0.2-x}O_{1.9}$ ($0 \leqslant x \leqslant 0.2$); (b) fitted F_{2g} band at 463 cm^{-1}

4.2.2 High temperatures X-ray diffraction (HT-XRD) studies

A study of co-doped Cerium Oxide is useful for understanding the effect of co-doping Gd^{3+} and Dy^{3+} on the cation sublattice, and the crystallographic features especially around the operating temperatures of IT-SOFC. The nanoparticles were analysed by X-ray diffraction (XRD) using a PANalytical X'Pert XRD diffractometer equipped with an Anton Paar HTK heating attachment. The XRD patterns were recorded in the 2θ 20-100° over the temperature range between room temperature and $300 \leq T \leq 700$°C in 50°C intervals. The samples were heated in air using a heating rate of 5°C/min and held at each temperature for 30 min to record the diffraction data.

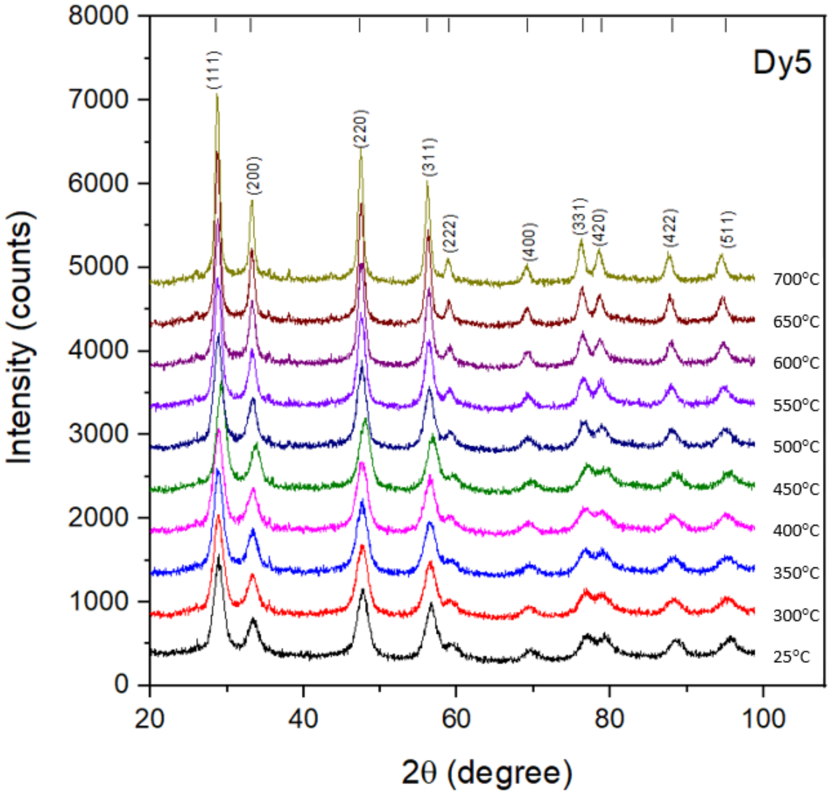
Dy5
Intensity (counts)
2θ (degree)
(111)
(200)
(220)
(311)
(222)
(400)
(331)
(420)
(422)
(511)
700°C
650°C
600°C
550°C
500°C
450°C
400°C
350°C
300°C
25°C
0
1000
2000
3000
4000
5000
6000
7000
8000
20
40
60
80
100

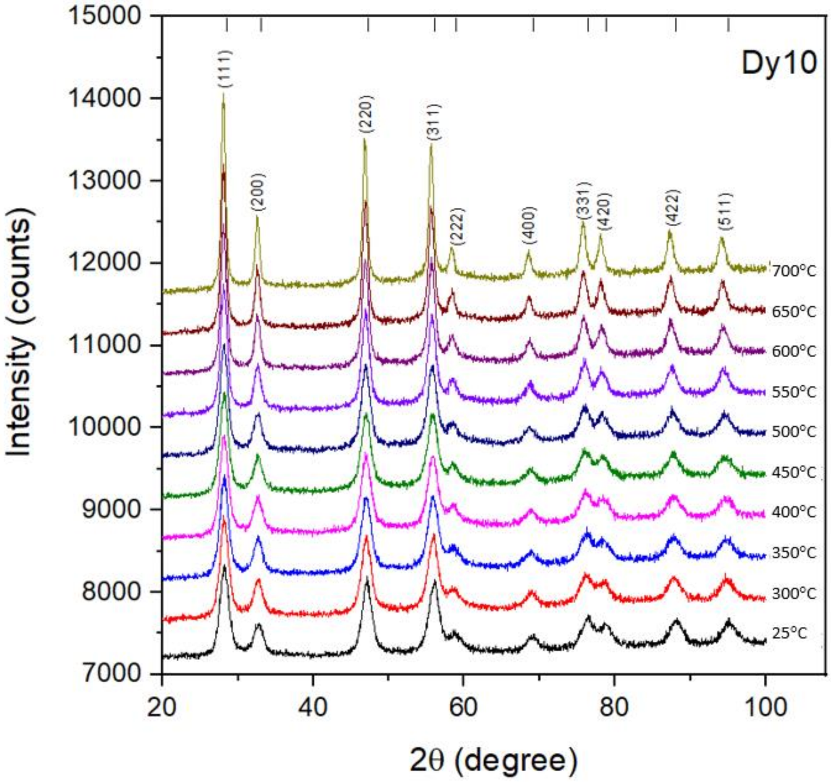
Dy10
Intensity (counts)
2θ (degree)
(111)
(200)
(220)
(311)
(222)
(400)
(331)
(420)
(422)
(511)
700°C
650°C
600°C
550°C
500°C
450°C
400°C
350°C
300°C
25°C
7000
8000
9000
10000
11000
12000
13000
14000
15000
20
40
60
80
100

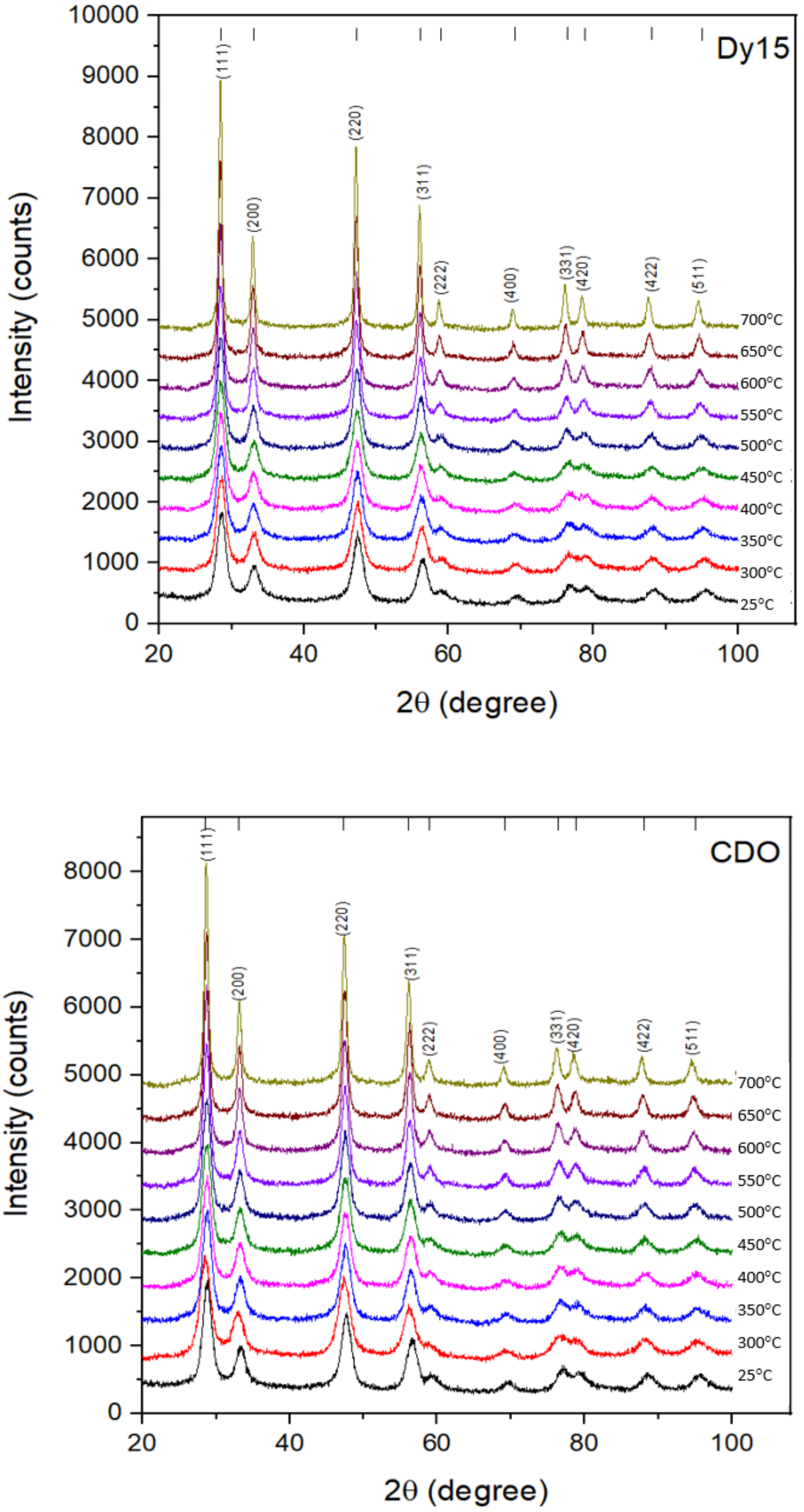

Figure 4.28. High-Temperature XRD of $Ce_{0.8}Dy_xGd_{0.2-x}O_{1.9}$ ($0.05 \leq x \leq 0.2$) from room temperature to 700°C.

The crystal structure at IT-SOFCs operating temperature shows a stable pure fluorite phase with space group $Fm\bar{3}m$; no secondary or hybrid phase was found in the entire composition and temperature ranges (**Figure 4.28**). At higher temperatures, the thermal energy results in unit cell expansion as expected for stable oxide materials. Moreover, increasing operating temperature shifts the peak to lower angles along with an increase in d-spacing according to Braggs law (159). The quadratic polynomial trend used to fit the lattice parameter with dependence on temperature (**Figure 4.29**). The lattice parameter expanded with increasing temperature at each composition.

$$\text{Dy5} : \alpha_T = 5.41884 + 9.044 \text{ x } 10^{-6} \text{ T} + 4.774 \text{ x } 10^{-8} \text{ T}^2 \tag{4.1}$$

$$\text{Dy10} : \alpha_T = 5.41596 + 4.944 \text{ x } 10^{-6} \text{ T} + 4.931 \text{ x } 10^{-8} \text{ T}^2 \tag{4.2}$$

$$\text{Dy15} : \alpha_T = 5.4148 - 1.745 \text{ x } 10^{-6} \text{ T} + 5.396 \text{ x } 10^{-8} \text{ T}^2 \tag{4.3}$$

$$\text{CDO} : \alpha_T = 5.41204 - 4.059 \text{ x } 10^{-6} \text{ T} + 5.762 \text{ x } 10^{-8} \text{ T}^2 \tag{4.4}$$

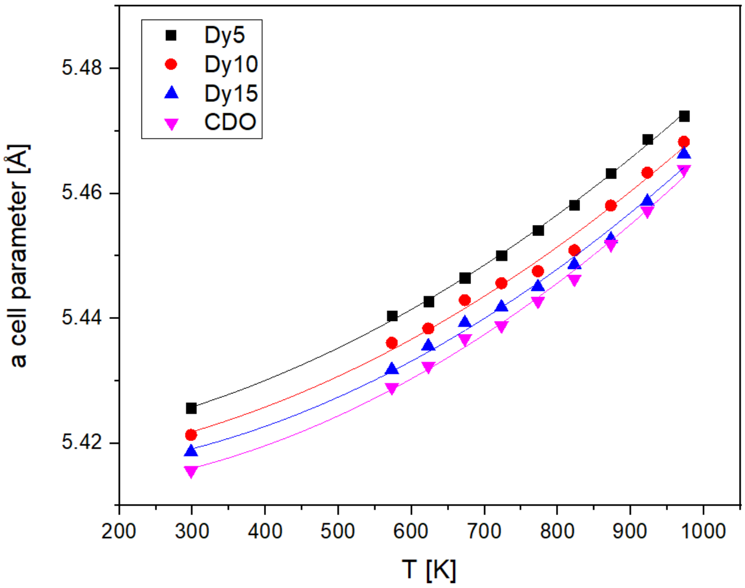

Figure 4.29. Lattice parameter of $Ce_{0.8}Dy_xGd_{0.2-x}O_{1.9}$ ($0.05 \leq x \leq 0.2$) as a function of temperature.

The lattice thermal expansion (%LTE) was studied using data in the 2θ range of 20-100° over a temperature range of 573 K $\leqslant$ T $\leqslant$ 973 K. The maximum change of lattice parameter as a function of temperature can be calculated using percentage lattice thermal expansion (% LTE):

$$\%LTE = 100\,\frac{(\alpha_T - \alpha_{298K})}{\alpha_{298K}} \tag{4.5}$$

where α_{298K} is the value of the cell parameter at room temperature and α_T is the value of the cell parameter at a selected temperature in Å (143). In **Figure 4.30**, % LTE, calculated using the lattice parameters obtained from the refinements, is shown. The calculated % LTE was fitted as a function of temperature using a quadratic polynomial regression analysis.

$$\text{Dy5} : \%\ LTE = 0.02302 - 2.205 \times 10^{-4}\ T + 1.126 \times 10^{-6}\ T^2 \tag{4.6}$$

$$\text{Dy10} : \%\ LTE = 0.4816 - 0.0014\ T + 1.8703 \times 10^{-6}\ T^2 \tag{4.7}$$

$$\text{Dy15} : \%\ LTE = 0.45523 - 0.0014\ T + 1.866 \times 10^{-6}\ T^2 \tag{4.8}$$

$$\text{CDO} : \%\ LTE = 0.3297 - 0.0011\ T + 1.719 \times 10^{-6}\ T^2 \tag{4.9}$$

-

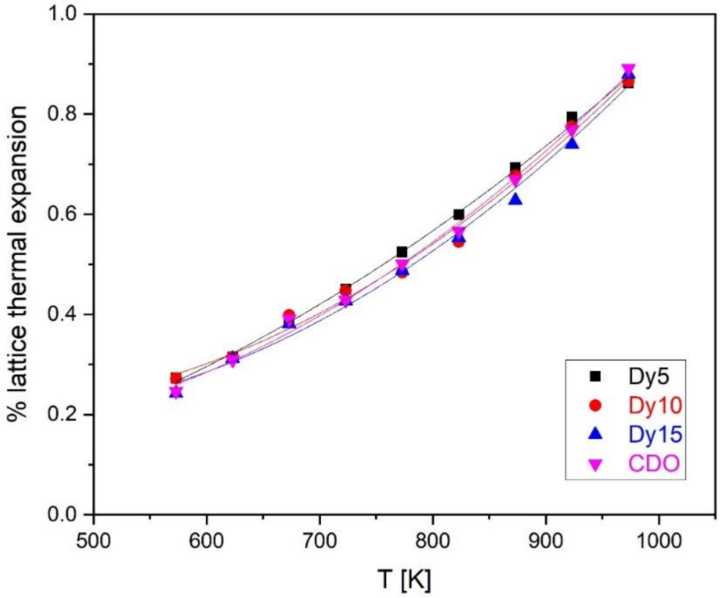

Figure 4.30. Percentage of lattice thermal expansion of $Ce_{0.8}Dy_xGd_{0.2-x}O_{1.9}$ ($0.05 \leqslant x \leqslant 0.2$) as a function of temperature.

The coefficient of thermal expansion (CTE) of $Ce_{0.8}Dy_xGd_{0.2-x}O_{1.9}$ ($0.05 \leqslant x \leqslant 0.2$) is calculated at the highest temperature (973 K) using equation (5.10)

$$CTE\ [K^{-1}] = \frac{1}{\alpha_{298K}}\ x\ \frac{(\alpha_T - \alpha_{298K})}{T-298} \qquad (5.10)$$

Chavan and Tyagi (160) observed thermal expansion in $Ce_{0.5}RE_{0.5}O_{1.75}$ (RE is trivalent rare earth ion) system. It was found that the coefficient of thermal expansion (CTE) from the partial substitution of Ce by trivalent ions in the CeO_2 matrix was less than pure CeO_2. This reduction takes place when a structural distortion occurs due to the introduction of oxygen vacancies (defects) in relation to a room temperature value (143, 161). CTE of electrolyte materials is an important property in IT-SOFCs because the matched CTE can avoid microcrack formation between anode and electrolyte or between cathode and electrolyte at the operating temperature.

Table 4.9 exhibits the calculated CTE of $Ce_{0.8}Dy_{0.2-x}Gd_xO_{1.9}$ samples between RT – 700°C. Increasing Dy content in partially and fully substituted CGO leads to an increase in CTE and a decrease in the unit cell parameter. The results are in good agreement with previous studies (161 – 165). CTE of 13.204 x 10^{-6} K^{-1} for CDO is very similar to the 13.20 x 10^{-6} K^{-1} obtained by Madhusadan et al. (81) using dilatometer.

Table 4.9. CTE of cerium dysprosium gadolinium oxide ($Ce_{0.8}Dy_xGd_{0.2-x}O_{1.9}$)

Sample code	**CET (10^{-6} K^{-1}) RT–973K**
CGO (166)	12.21
Dy5	12.774
Dy10	12.823
Dy15	13.027
CDO	13.204

4.2.3 Density and micrographs analysis

The density of pellets was measured using a standard density bottle method (**ρ**) based on the Archimedes principle while the theoretical density (**ρ_{Th}**) was determined from lattice volume. The relative density was calculated by the ratio of the density of pellets and the theoretical density (**Figure 4.31**). The high relative density of sintered ceramics agrees with the fully dense structure of SEM micrographs (**Figure 4.32**). Furthermore, the microstructure grains observed, which are in interlocked equiaxed and hexagonal shape without any open pore, are evidence that sintering already achieved final stage. In general, co-doping with Dy ions increases densification due to the decrease in average cation size, which enhances the cation diffusion rate and improves the sintering ability of samples (22). Similar phenomenon was reported by Khakpour and co-workers who found that co-doping could improve the densification because of the decrease in atomic migration to grain boundaries (167).

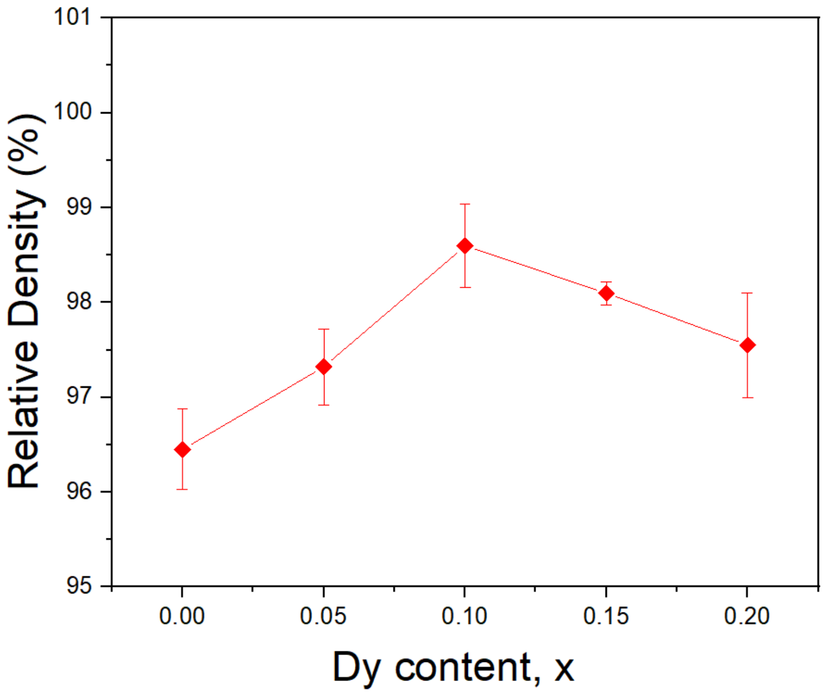

Figure 4.31. Densification curve of $Ce_{0.8}Dy_xGd_{0.2-x}O_{1.9}$ ($0 \leq x \leq 0.2$) ceramics sintered at 1500°C for 2h.

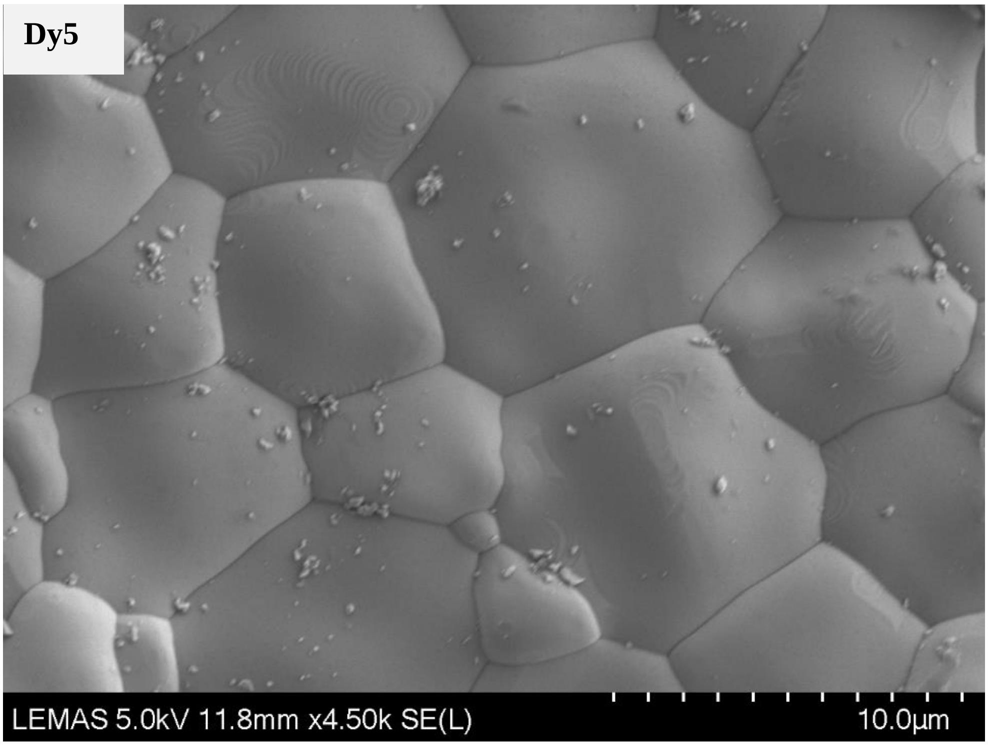
Dy5
LEMAS 5.0kV 11.8mm x4.50k SE(L)
10.0μm

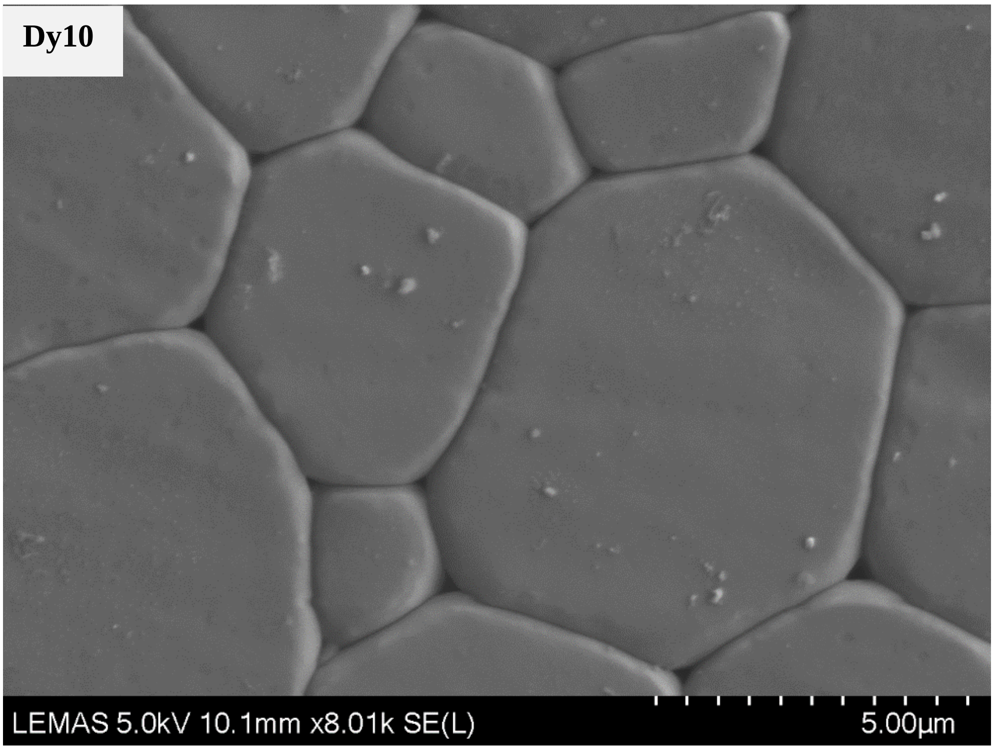
Dy10
LEMAS 5.0kV 10.1mm x8.01k SE(L)
5.00μm

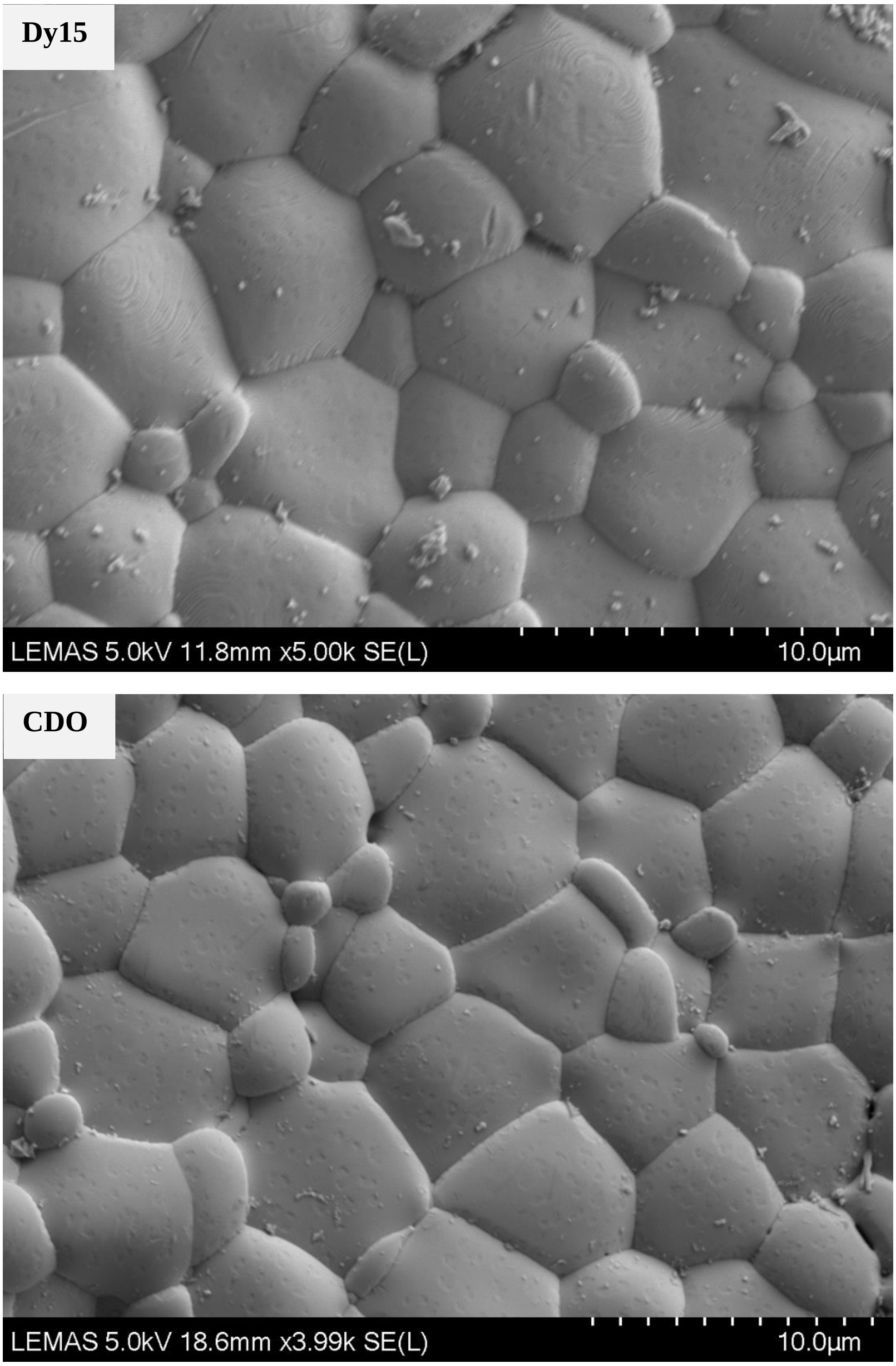

Figure 4.32. SEM micrographs of $Ce_{0.8}Dy_xGd_{0.2-x}O_{1.9}$ ($0 \leq x \leq 0.2$) ceramics sintered at 1500°C for 2 h.

The elemental mapping from Dy5 dense pellet consisting of oxygen (O), ceria (Ce), dysprosium (Dy) and gadolinium (Gd) is presented in **Figure 4.33**. The complete solid solution formation from EDS mapping observed a homogeneous chemical distribution across the microstructure. **Table 4.10** shows the overall weight percentages from EDS analysis and the mole fractions of elements in $Ce_{0.8}Dy_xGd_{0.2-x}O_{1.9}$ sintered ceramics. Calculated mole fractions show an excellent agreement with suggested nominal mole fractions. The SEM-EDS report also gives similar result with the TEM-EDS analysis from the nanoparticles.

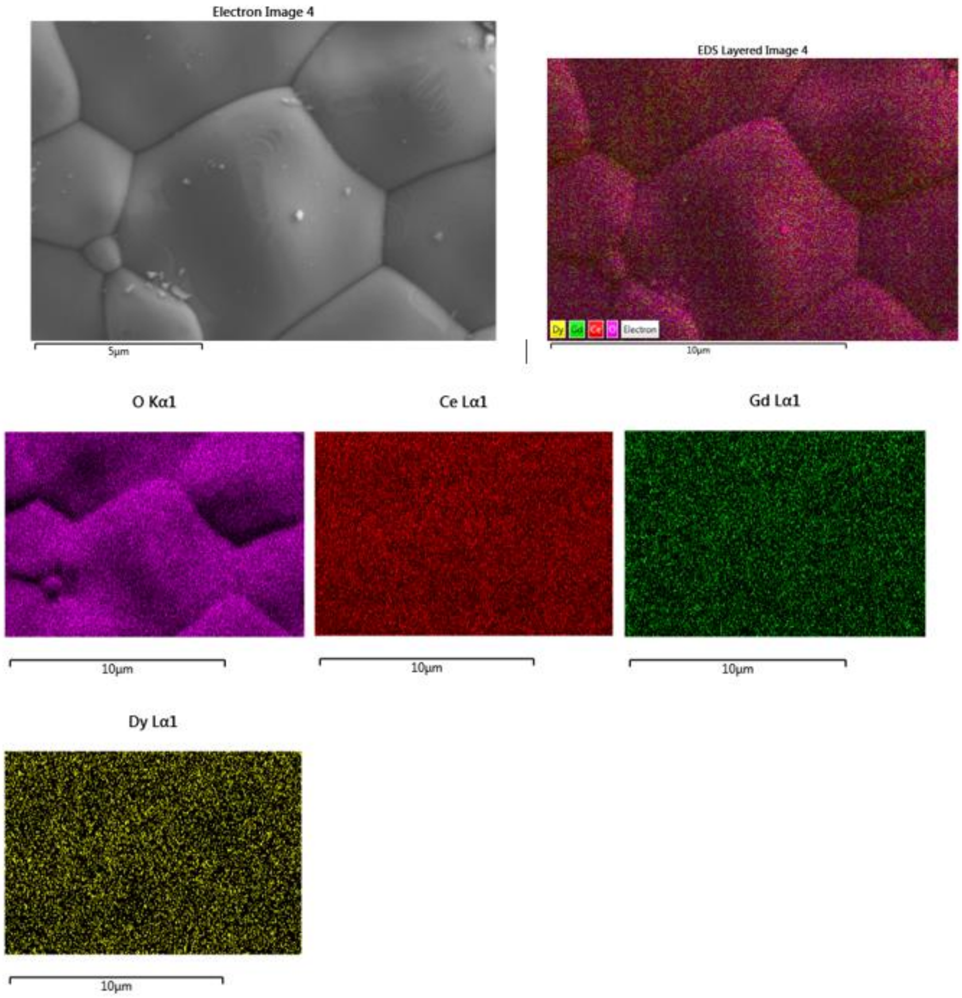

Figure 4.33. SEM image of the microstructure and a layered elemental map followed by the EDS elemental map of Dy5 sintered pellet consisting of cerium in red, oxygen in purple, gadolinium in green and dysprosium in yellow colour.

Table 4.10. Weight precentages and calcuated mole fractions obtained from SEM-EDS analysis of $Ce_{0.8}Dy_xGd_{0.2-x}O_{1.9}$ ($0 \leq x \leq 0.2$) sintered pellets

Composition	Element	Weight % from EDS	Atomic weight	Mole	Mole %	Nominal
CGO	Ce	59.6	140.116	0.425	0.802	0.80
	Gd	16.5	157.2	0.105	0.198	0.20
	Total mole of Ce + Gd			0.530		
	O	12.4	15.99	1.119		
Dy5	Ce	63.16	140.116	0.451	0.798	0.80
	Dy	2.77	162.5	0.017	0.046	0.05
	Gd	12.11	157.2	0.077	0.156	0.15
	Total mole of Ce + Dy + Gd			0.545	1	
	O	21.96	15.99	1.373		
Dy10	Ce	64.49	140.116	0.460	0.802	0.80
	Dy	7.04	162.5	0.043	0.107	0.10
	Gd	9.14	157.2	0.058	0.091	0.10
	Total mole of Ce + Dy + Gd			0.561	1	
	O	19.33	15.99	1.209		
Dy15	Ce	36.14	140.116	0.258	0.797	0.80
	Dy	8.23	162.5	0.051	0.156	0.15
	Gd	2.35	157.2	0.015	0.046	0.05
	Total mole of Ce + Dy + Gd			0.278	1	
	O	21.96	15.99	1.213		
CDO	Ce	63.3	140.116	0.452	0.802	0.80
	Dy	18.4	162.5	0.111	0.198	0.20
	Total mole of Ce + Dy			0.563	1	
	O	6.3	15.99	0.394		

4.2.4 Electrical conductivity investigation

Dense sintered pellets of each composition were coated on both flat polished surfaces with conductive silver ink and fired at 800°C to obtain a strongly adherent conductive coating for impedance measurements. The alternating current (ac) conductivity measurements of $Ce_{0.8}Dy_xGd_{0.2-x}O_{1.9}$ ($0 \leq x \leq 0.2$) dense pellets were performed by the frequency response analyser (SI-1260, Solartron Analytical Instruments, Farnborough, UK) in the temperature range 300-500°C in both heating and cooling cycles. During the measurements, the induced electric field was earthed by housing the sample rig inside a

Faraday cage. Complex impedance plots of dense pellets $Ce_{0.8}Dy_xGd_{0.2-x}O_{1.9}$ ($0 \leq x \leq 0.2$) ceramic measured at 300 and 500°C are shown in **Figure 4.34 - 4.35**, respectively.

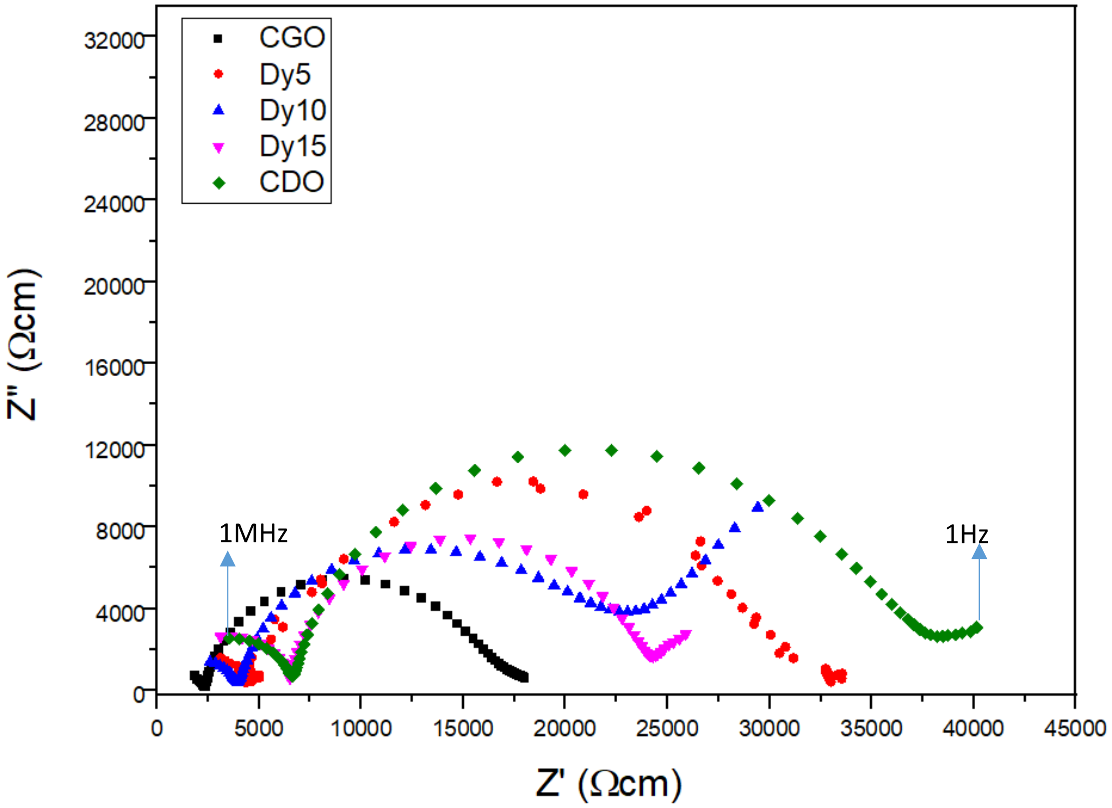

Figure 4.34. The complex plane impedance plots of dense $Ce_{0.8}Dy_xGd_{0.2-x}O_{1.9}$ ($0 \leq x \leq 0.2$) ceramic measured at 300°C in air.

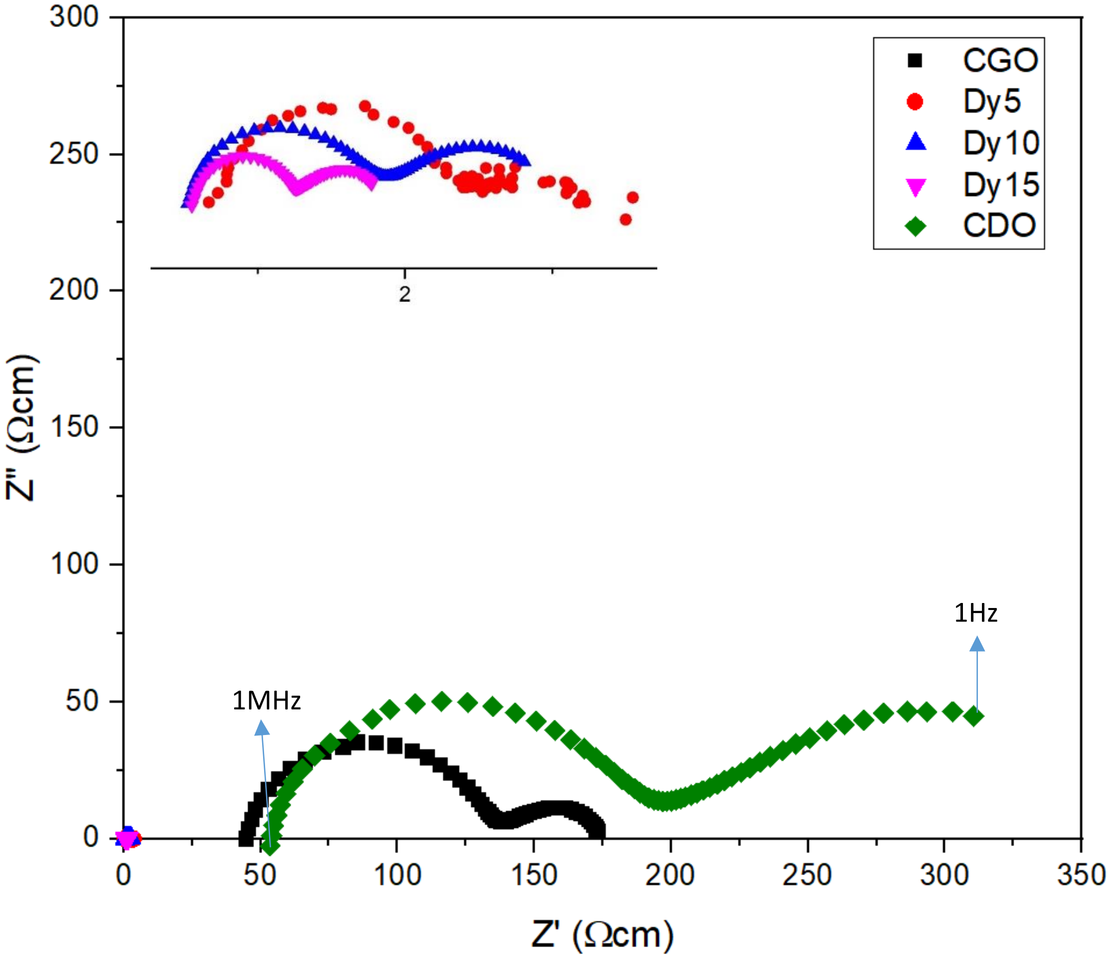

Figure 4.35. The complex plane impedance plots of dense $Ce_{0.8}Dy_xGd_{0.2-x}O_{1.9}$ ($0 \leq x \leq 0.2$) ceramic measured at 500 °C in air. The inset plot is the low range of Z' (Ωcm).

AC impedance spectroscopy was used to determine the grain, grain boundary, and total conductivities of sintered pellets. **Figures 4.34** and **4.35** show the impedance plot of $Ce_{0.8}Dy_xGd_{0.2-x}O_{1.9}$ ($0 \leqslant x \leqslant 0.2$) at 300 and 500°C. The impedance data of $Ce_{0.8}Dy_xGd_{0.2-x}O_{1.9}$ solid-solution systems for $0 \leqslant x \leqslant 0.2$ was fitted using ZView Software aided by the selected equivalent circuit to represent the observed frequency response, a combination of resistor (R) and constant phase elements (CPE). In order to account for possible compositional and microstructural variations, CPE was used for fitting impedance data instead of regular capacitor (81). At low temperature (300°C), a semicircle at high-frequency is associated with grain interior (bulk; R1//CPE1), the intermediate is related to inter-grain area (grain boundary; R2//CPE2), and the low-frequency region is assigned to electrode impedance (W) at the interface (15, 168, 169). At low frequencies, the impedance is dominated by mass transport. The straight line with a slope of 45° is the notice of Warburg impedance appears. However, at intermediate and high temperatures, the bulk arch was obscured because of the limit of ac signal frequency (16, 170). Thus, bulk conductivity was obtained from the first intercept on the real axis (Z' axis) (R1), whereas grain boundary conductivity was obtained from the first arc (R2//CPE2) and the second arc (R3//CPE3) was associated with electrode. **Figure 4.36**. illustrates the Nyquist plots and fitting of Dy10 along with the equivalent circuit model used for fitting of the impedance data.

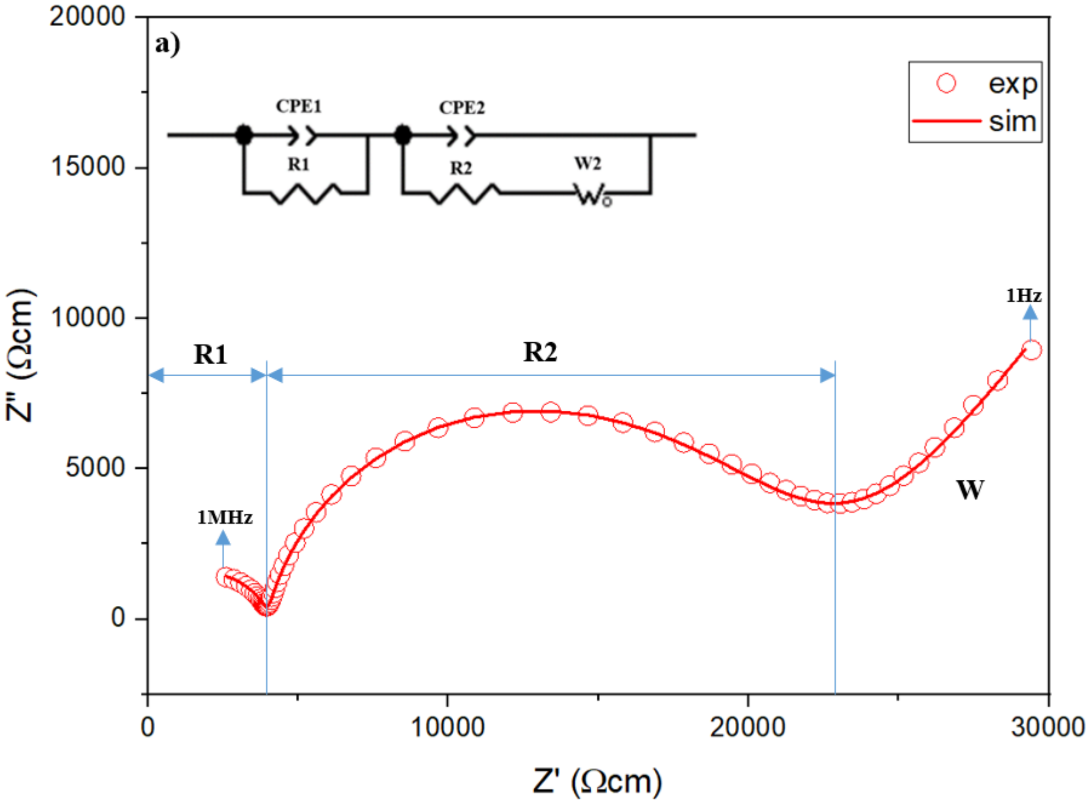

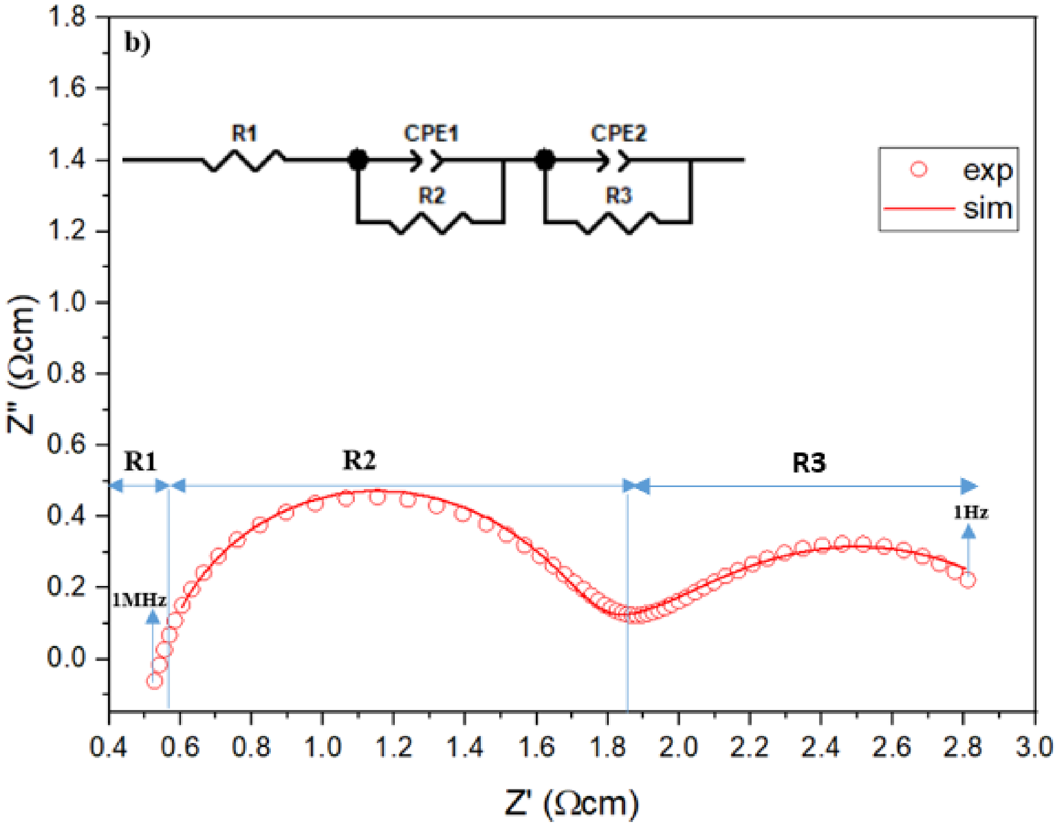

Figure 4.36. Nyquist plots and fitting of Dy10 dense pellet at: (a) 300°C and (b) 500°C. Inserted image is equivalent circuit model used for fitting of the impedance data.

The Arrhenius plots (equation 3.9) of grain, grain boundary and total conductivities of $Ce_{0.8}Dy_xGd_{0.2-x}O_{1.9}$ ($0 \leqslant x \leqslant 0.2$) ceramics in the temperature range of 300°C to 500°C are shown in **Figure 4.37**. The results show that bulk conductivity is higher than grain boundary conductivity of the entire series. At temperature between 300°C and 350°C, total conductivity was highest for CGO and was lowest for CDO. However, at 400°C and 500°C, total conductivity was highest for Dy10. In the case of grain boundary conductivity between 300°C and 350°C, CGO was the highest and for temperature above 400°C Dy15 was the highest. It is seen from the Arrhenius plots that the conductivity curves of doubly doped ceria system exhibit an abnormal increase at a temperature around 400°C, while the singly doped ceria system shows no such discontinuity. Recent studies by Shirbhate and co-workers (17, 171) also found a small change slope break in the conductivity curve for aliovalent dopant pair at temperature between 450 and 500°C, which is associated with intrinsic oxygen vacancies dissociation. However, in this research the abnormal increase is pleasantly surprising and further investigations are in progress to elucidate the appropriate conduction mechanism. We believe that one possible contributing factor for the observed phenomenon is the application of novel alginate process for the synthesis of nanoparticle compositions, since the phenomena did not show in the study reported by Khakpour and co-workers on Gd^{3+} and Dy^{3+} co-doping ceria-based solid electrolytes using solid-state method (167).

Ionic conductivity depends on several factors such as type and concentration of dopant, ionic radius, synthesis method and sintering temperature (172 – 174). The creation of oxygen vacancies in terms of Kröger–Vink notation for co-doping of dysprosium and gadolinium is:

$$Dy_2O_3 + CeO_2 \rightarrow 2Dy_{Ce}^{'} + 3O_o^x + V_o^{''} \qquad (4.11)$$

$$Gd_2O_3 + CeO_2 \rightarrow 2Gd_{Ce}^{'} + 3O_o^x + V_o^{''} \qquad (4.12)$$

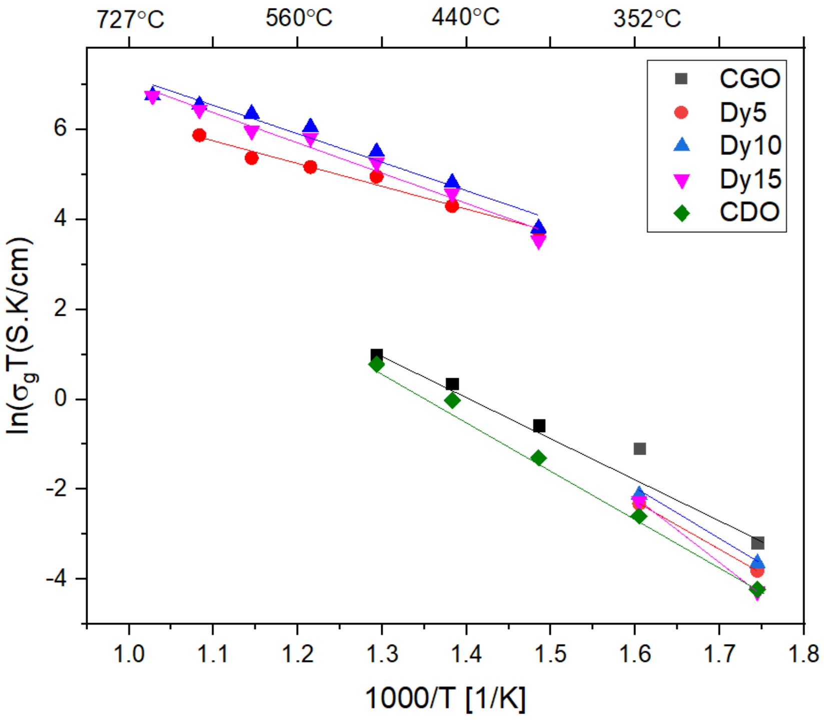

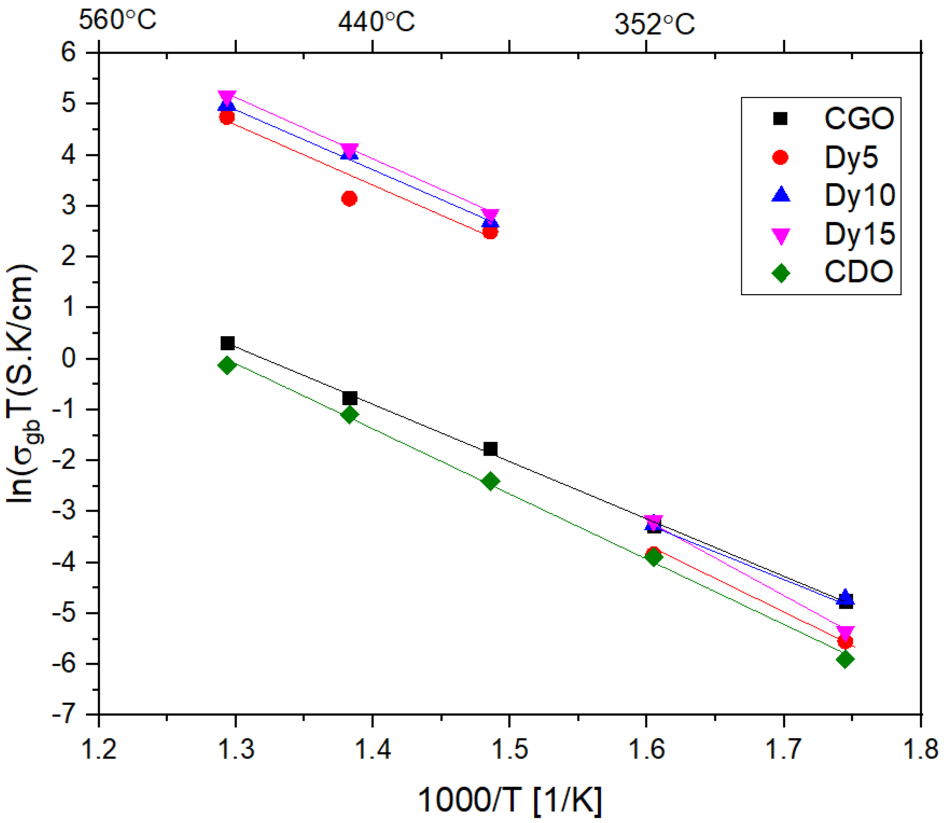

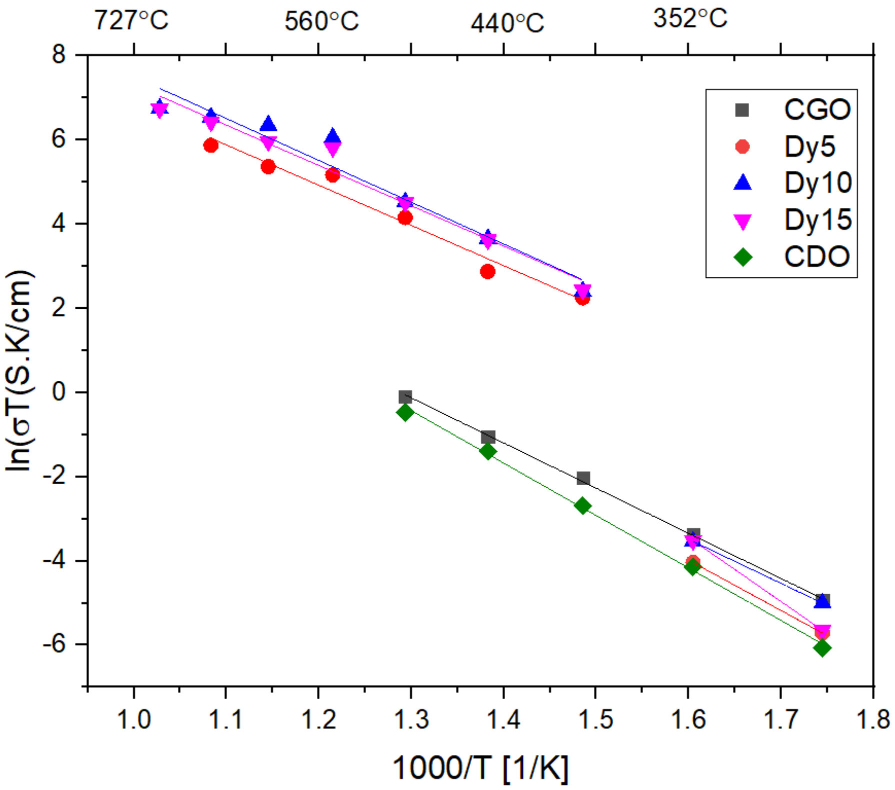

Figure 4.37. The Arrhenius plots of bulk, grain boundary and total conductivities for $Ce_{0.8}Dy_xGd_{0.2-x}O_{1.9}$ ($0 \leqslant x \leqslant 0.2$).

Table 4.11 presents the conductivities measured at 500°C and activation energies for bulk and grain boundary of $Ce_{0.8}Dy_xGd_{0.2-x}O_{1.9}$ ($0 \leqslant x \leqslant 0.2$) ceramic electrolytes. It is observed that the doubly doped material can enhance ionic conductivity nearly 100 times higher than the singly doped from 0.00351 S cm^{-1} for CGO to 0.3169 S cm^{-1} for Dy10 at the same temperature. Similar improvement was also reported by Shirbhate et al. (171) in doped ceria. The ionic conductivity of doubly doped $Ce_{0.85}Sm_{0.075}Ca_{0.15}O_{1.9}$ (1.47x 10^{-1} S cm^{-1}) was found to be more than 100 times higher than the singly doped $Ce_{0.85}Sm_{0.15}O_{1.9}$ (8.73 x 10^{-4} S cm^{-1}) at 600°C.

The ionic conductivity of CGO (3.5 × 10^{-3} Scm^{-1} at 500°C) obtained in this research is slightly lower than the one obtained by Steele (5.3 × 10^{-3} Scm^{-1} at 500°C) (4). However, the value at 400°C (8.35 × 10^{-4} Scm^{-1}) is higher than the previous work for the same composition synthesised via SAL process (7.24 × 10^{-4} Scm^{-1} at 422°C) by Wang et al. (106). This enhanced conductivity is achieved potentially due to the higher level of densification of samples in this study compared with the previous work, according to Perez-Coll, et al. (105). The improvement in conductivity was also detected on CDO, where total conductivity of 3.4 × 10^{-4} Scm^{-1} at 400°C in this study is higher than the 1.5 × 10^{-4} Scm^{-1} and 6 × 10^{-5} Scm^{-1} observed by Khakpour and co-workers (167) for CDO at the same temperature using conventional and two-step sintering.

Table 4.11. Bulk (GI), grain boundary (GB) and total conductivities measured at 500°C, with activation energies for bulk and grain boundary of $Ce_{0.8}Dy_xGd_{0.2-x}O_{1.9}$ ($0 \leqslant x \leqslant 0.2$) ceramic electrolytes.

Electrolytes	**σ_{GI} (S cm^{-1})**	**σ_{GB} (S cm^{-1})**	**σ_{Total} (S cm^{-1})**	**Ea_{ionic} (eV)**	**Ea_{GB} (eV)**
CGO	0.00351	0.0018	0.0012	0.878	0.993
Dy5	0.1821	0.1497	0.0822	0.932	1.05
Dy10	0.3169	0.1538	0.1190	0.964	1.066
Dy15	0.2482	0.2253	0.1181	1.244	1.338
CDO	0.00281	0.0012	0.00081	0.971	1.164

At high temperature, the Arrhenius plots start to bend due to the different bulk conduction mechanism which is associated with dissociation of defect complexes (typically higher than 400°C) (4, 102 – 104, 175). Zhang and co-workers (49) proposed a critical temperature to explain this phenomenon. The critical temperature model demonstrated that the oxygen vacancies combine with the dopant cations to form larger complex defects below Tc, while above Tc, the association of defects decreases and therefore the oxygen vacancies appear to be mobile without any interaction with the dopant cations (49). For CeO_2–Gd_2O_3 system, the Tc is observed at temperature range 200 to 550°C.

The total activation energy in the doped ceria system is the sum of the enthalpy change (ΔH_m) of oxygen ions migration and the association enthalpy (ΔH_a) of oxygen vacancies with the defect clusters (dimer or trimer type) (17, 49).

$$E_a = \Delta H_m + \Delta H_a \tag{4.13}$$

At low temperatures, below Tc, the gradient of the activation energy curve is proportional to the sum of the enthalpy of migration and enthalpy of association. In contrast, at a higher temperature, above Tc, the defect clusters are insignificant, and the slope is proportional to migration enthalpy of the oxygen ions only, ΔH_m. The migration enthalpy is independent of temperature and dopants concentrations (58, 176). Thus, by obtaining gradient below and above the critical temperature, values for migration enthalpy and association enthalpy can be calculated. For singly doped the critical temperature is assumed at around 410°C, while for co-doped materials Tc is assumed before the conductivity break in the Arrhenius plots (49).

In general, the activation energy for grain boundary is higher than the activation energy for bulk and total conductivity. The activation energy of 0.95 and 0.97 eV for conventional sintering and two-step sintering CGO obtained by Khakpour et al. (167) is comparable with this present study of 0.97 eV. However, it is higher than reported by Dikmen (0.83 eV) or Zhang et.al. (0.881 eV) for the same composition (177, 178). Acharya (179) obtained the energy activation for dysprosium-doped ceria between 0.86 – 1.05 eV. This is comparable to the value of 1.1 eV for CDO in this study.

In this present study, the partial substitution of dysprosium in CGO leads to an increase in the activation energy. Winck et al. (180) also reported that double doping can increase the activation energy due to the mobility reduction of ionic vacancies. The activation energy of 0.984 eV for $Ce_{0.8}Sm_{0.2}$ was increased to 1.143 eV for $Ce_{0.8}Sm_{0.1}Gd_{0.1}$.

The association enthalpy for co-doped materials has been found to be greater than that for singly doped CeO_2, **Figure 4.38**. At low temperature, below the Tc, the defect clusters such as dimer ($V_O^{\cdot\cdot} - M_{Ce}^{\prime}$) and trimer ($M_{Ce}^{\prime} - V_O^{\cdot\cdot} - M_{Ce}^{\prime}$) are commonly formed, where M is Ce^{3+}, Gd^{3+} or Dy^{3+}. The formation of defect clusters causes the oxygen vacancies to be trapped, blocked, and immobilised (17). Therefore, we believe that the conductivity decreases at low temperature for doubly doped ceria system probably due to the presence of deep traps of oxygen vacancies, resulting in the higher activation energy that is required to move oxide anions in the lattice compared with the singly doped. The highest ionic conductivity was observed on CGO below Tc and on Dy10 above Tc. Thus, Dy10 has the most optimum composition among ceria electrolytes at intermediate temperature.

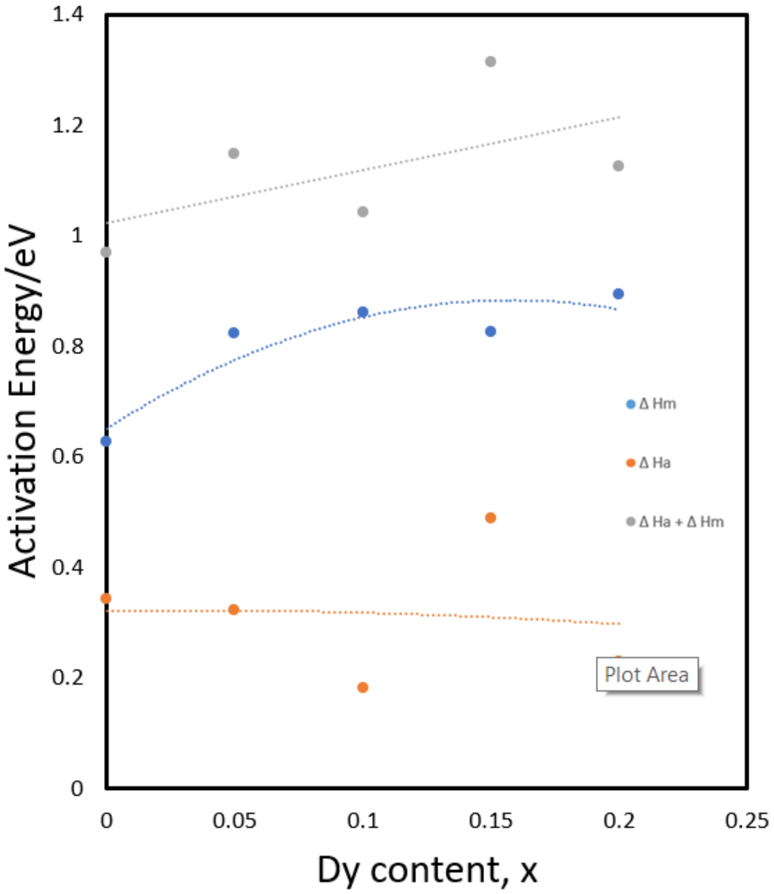

Figure 4.38. Activation energy for total conductivity, below Tc ($\Delta H_m + \Delta H_a$), above Tc (ΔH_m), and ΔH_a of $Ce_{0.8}Dy_xGd_{0.2-x}O_{1.9}$ ($0 \leqslant x \leqslant 0.2$) ceramic electrolytes.

4.3 Fabrication of $Ce_{0.8}Ho_xGd_{0.2-x}O_{1.9}$ ($0 \leq x \leq 0.2$) nanoparticle

4.3.1 Powder characterisation

The XRD patterns of $Ce_{0.8}Ho_xGd_{0.2-x}O_{1.9}$ ($0 \leq x \leq 0.2$) nanoparticles after calcination are shown in **Figure 4.39**. All peaks confirm the pure cubic fluorite crystal structure with $Fm\bar{3}m$ space group. There is no signature of any secondary phase or hybrid phase detected for all compositions. The partial substitution of Ce^{4+} with Ho^{3+} and Gd^{3+} in CeO_2 formed a complete solid solution in the composition range of $0 \leqslant x \leqslant 0.2$.

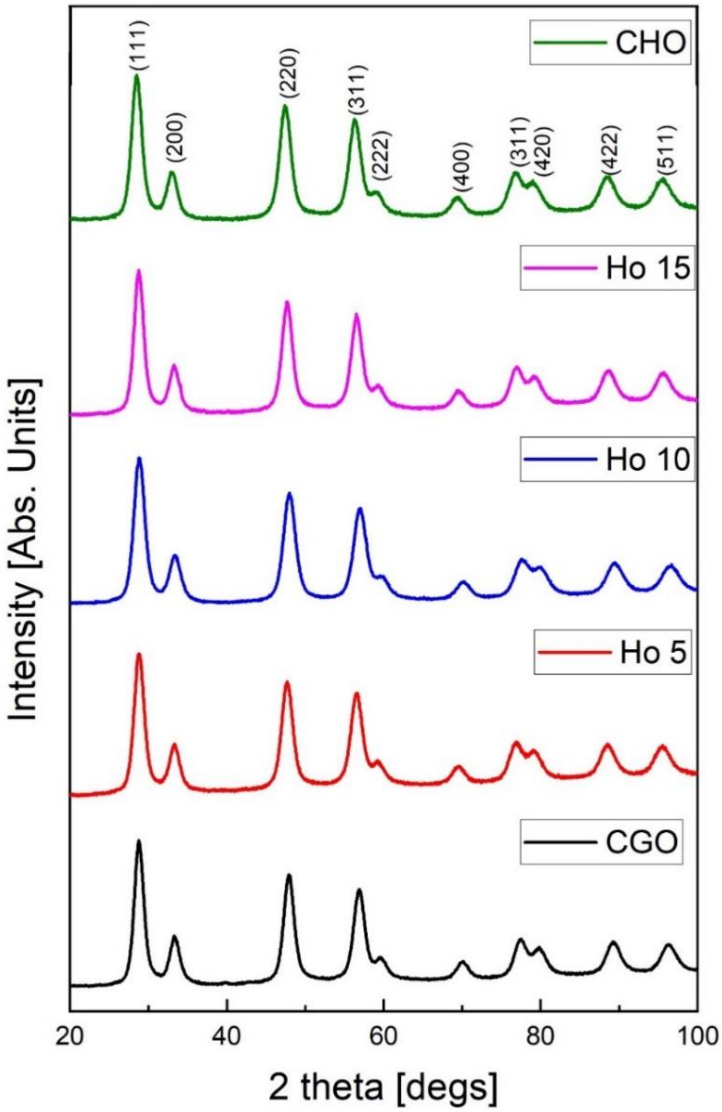

Figure 4.39. XRD patterns of $Ce_{0.8}Ho_xGd_{0.2-x}O_{1.9}$ ($0 \leq x \leq 0.2$) nanoparticles calcinated at 500°C for 2h

The refined structural parameter, agreement factors, crystallite size and theoretical density for entire series detailed in **Table 4.12**. It is clearly seen that this method produces nanoparticles (~10 nm).

Table 4.12. Refined structural parameter, agreement factors, crystallite size and theoretical density for $Ce_{0.8}Ho_xGd_{0.2-x}O_{1.9}$ nanoparticles calcined at 500°C for 2 h

	CGO	**Ho5**	**Ho10**	**Ho15**	**CHO**
Rp	0.021	0.031	0.023	0.025	0.025
Rexp	0.0126	0.0181	0.0129	0.025	0.025
χ^2	5.34	5.11	6.25	5.24	3.25
V (Å^3)	160.16 (2)	159.88 (1)	159.35 (2)	159.12 (9)	158.57 (8)
a (Å)	5.43061 (2)	5.42794 (9)	5.4215 (2)	5.419	5.413
D_{XRD} (Å)	111.759	107.896	107.896	115.268	108.186
ρ_{Th} (g/cm^3)	7.214	7.242	7.283	7.309	7.350

The lattice parameter of each composition was obtained by Rietveld refinement of XRD data using GSAS. The decreasing lattice parameter with an increasing x, from 5.428 Å (CGO) to 5.414 Å (CHO), shows a linear dependence (**Figure 4.40**). This indicates that these materials obey the Vegard's Law (154).

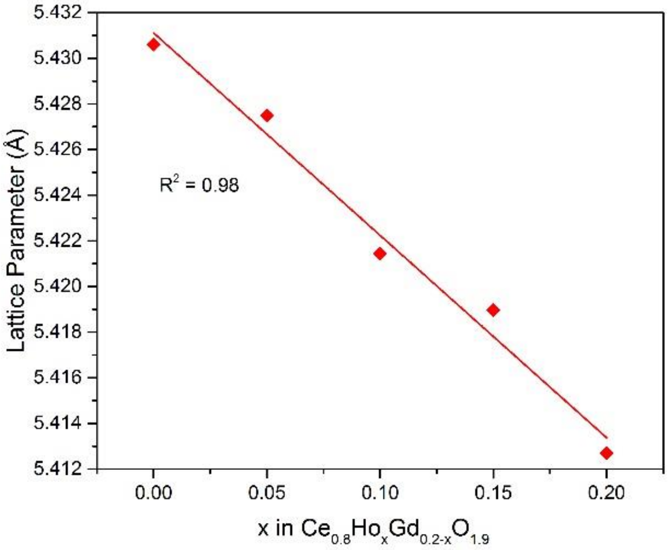

Figure 4.40. Dependence of lattice parameter on the composition of $Ce_{0.8}Ho_xGd_{0.2-x}O_{1.9}$

The magnified view of the strongest intensity (111) peak from all $Ce_{0.8}Ho_xGd_{0.2-x}O_{1.9}$ compositions shown in **Figure 4.41** indicates that with increasing Ho content, the peak shifts to the higher diffraction angle or smaller interplanar spacing (*d* value). The shift in direction of 2-theta is due to smaller ionic radius of Ho^{3+} (CN 6 = 0.901 Å) compared with Gd^{3+} (CN 6 = 0.938Å) (63). This is an evidence of lattice contraction.

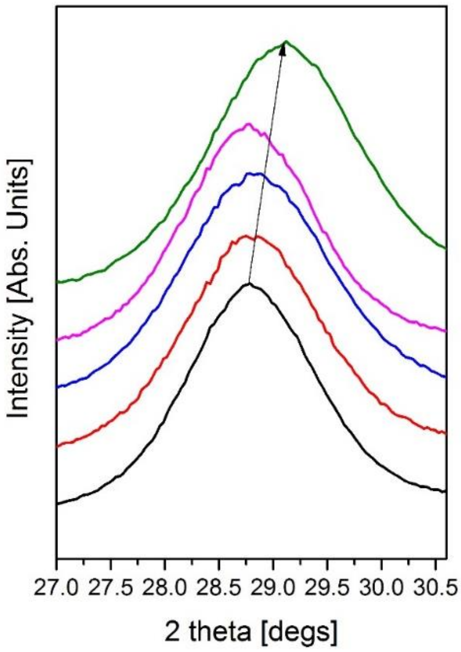

Figure 4.41. XRD patterns at (111) peak. Black: CGO, red: Ho5, blue: Ho10, pink: Ho15, and green: CHO.

The lattice contraction is also proven by the decreasing trend in interplanar spacing from XRD and TEM shown in **Table 4.13**. Although the d spacings of Ho5 from XRD are slightly lower than TEM results, in general both instruments give similar d values.

Table 4.13. Comparison of d-spacing from XRD Rietveld refinement and SAED TEM ring patterns of $Ce_{0.8}Ho_xGd_{0.2-x}O_{1.9}$ nanoparticles.

h	k	l	XRD d/(Å)				TEM d/(Å)			
			Ho5	Ho10	Ho15	CHO	Ho5	Ho10	Ho15	CHO
1	1	1	3.103	3.117	3.098	3.064	3.156	3.117	3.097	3.079
2	0	0	2.690	2.700	2.686	2.665	2.747	2.661	2.629	2.758
2	2	0	1.907	1.911	1.904	1.884	1.927	1.871	1.824	1.861
3	1	1	1.628	1.561	1.625	1.606	1.635	1.599	1.563	1.580

The morphology particles and selected area electron diffraction (SAED) patterns from five different samples are shown in **Figure 4.8** and **4.42**. The images, which show a mixture of hexagonal and square shape morphologies depending on their orientation on the holey carbon-coated copper grid, confirm the fluorite structure. The particle size from TEM, which is less than 10 nm, is in a good agreement with the slightly higher values ranging from 10 to12 nm reported by the XRD Rietveld refinement procedure. SAED patterns are also in agreement with XRD results in which the particle dimension is in nanometer range and in the fluorite structure.

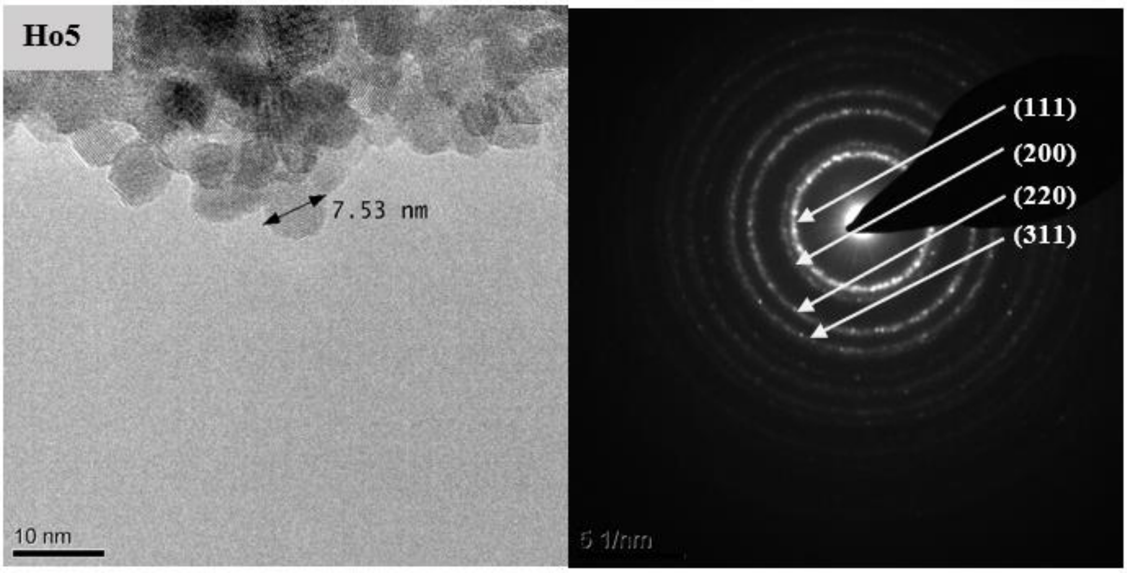

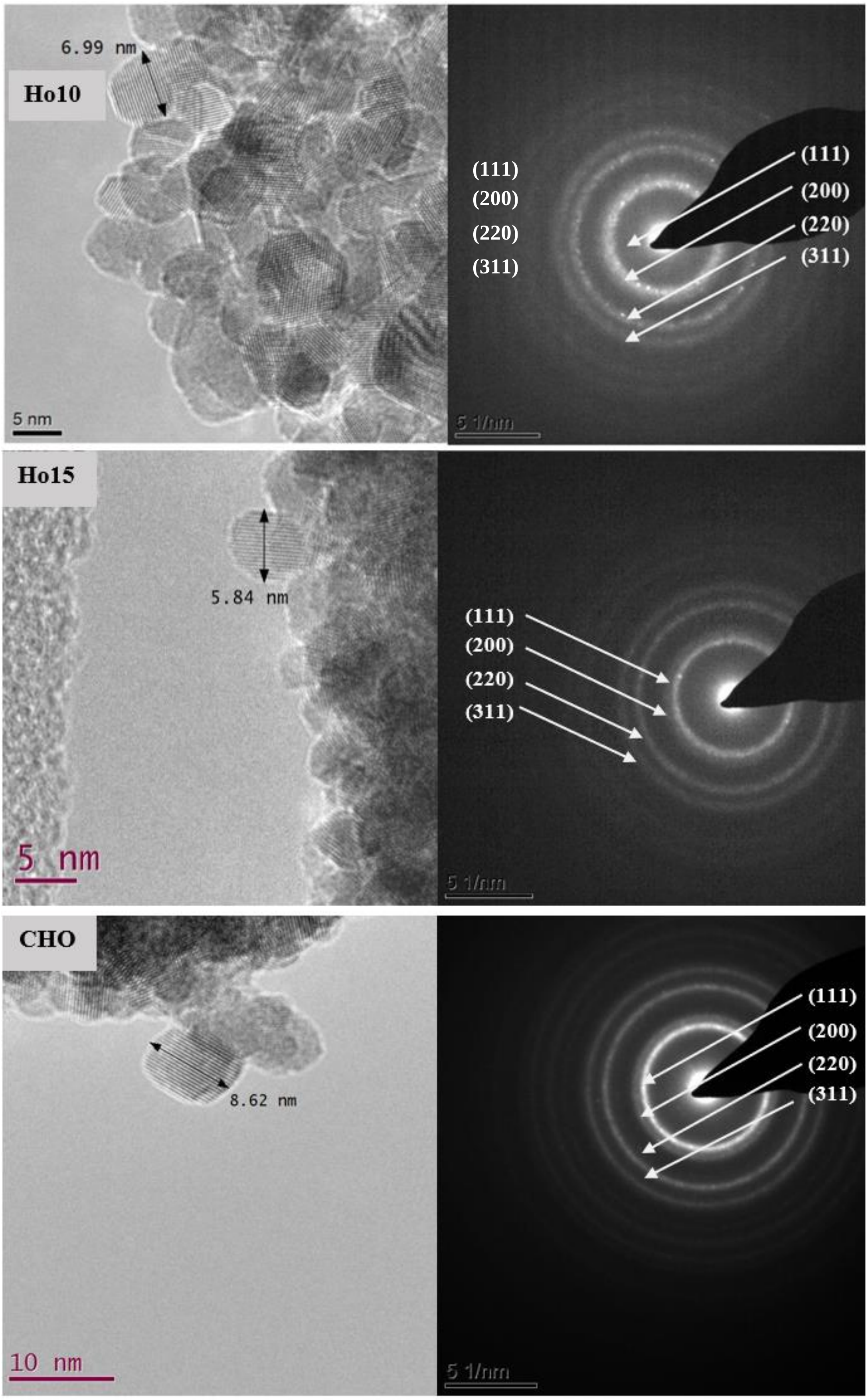

Figure 4.42. TEM and SAED images of $Ce_{0.8}Ho_xGd_{0.2-x}O_{1.9}$ ($0 \leq x \leq 0.2$) nanoparticles calcined at 500°C for 2 h, respectively

The spectrum of TEM-EDS for Ho5 is shown in **Figure 4.43**. The holey carbon-coated copper grid was excluded from EDS spectra. Consequently, the spectra of samples shown in **Table 4.14** show a good agreement between the calculated chemical analysis from TEM-EDS and the nominal mole fraction.

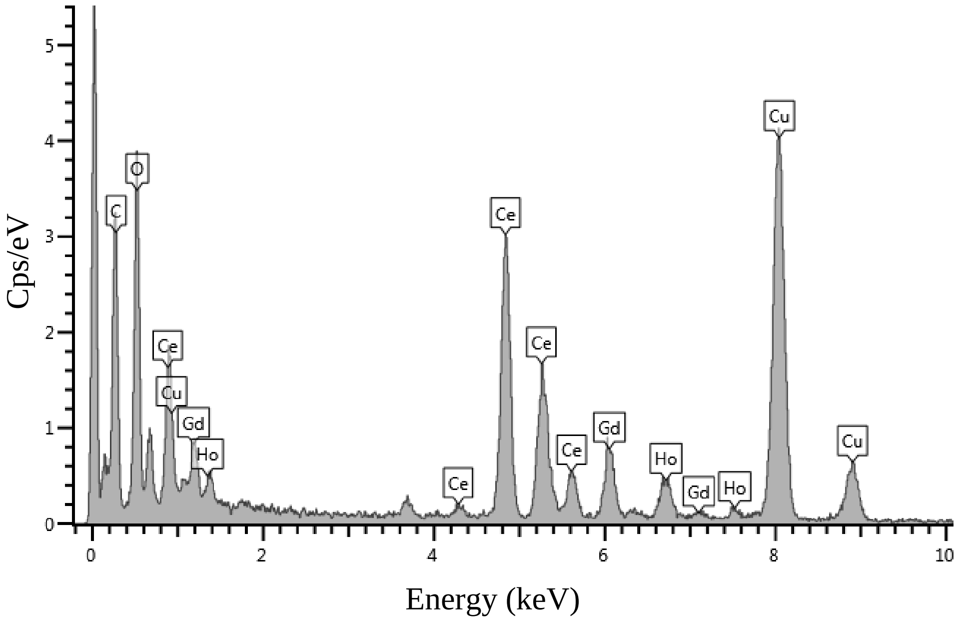

Figure 4.43. TEM–EDS spectrum illustrates the composition of Ho5 nanoparticles after calcination at 500°C for 2h.

Table 4.14. TEM-EDS analysis of cerium holmium gadolinium oxide samples

Samples	Elements	Wt (%)	Mole	Mole %	Nominal
Ho5	Ce	39.49	0.2818	0.809	80
	Ho	2.73	0.0166	0.047	5
	Gd	8.09	0.0498	0.149	15
Ho10	Ce	74.76	0.5336	0.773	80
	Ho	14.13	0.0857	0.124	10
	Gd	11.11	0.0707	0.103	10
Ho15	Ce	43.07	0.3074	0.796	80
	Ho	9.73	0.0195	0.153	15
	Gd	3.17	0.0589	0.051	5
CHO	Ce	42.28	0.3018	0.812	80
	Ho	11.36	0.0699	0.188	20

Raman spectra of $Ce_{0.8}Ho_xGd_{0.2-x}O_{1.9}$ ($0 \leqslant x \leqslant 0.2$) compounds which are illustrated in **Figure 4.44**, confirms the formation of a fluorite structure. The Raman active mode at $465 cm^{-1}$ is corresponding to oxygen-cerium F_{2g} mode vibration for cubic fluorite $Fm\bar{3}m$ crystal structure (155 – 158).

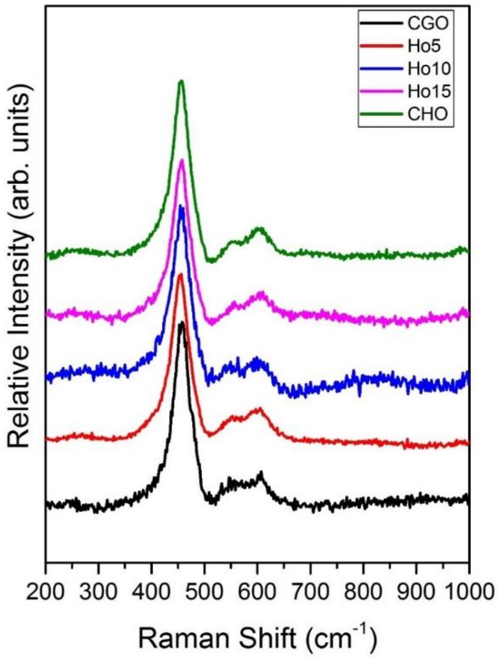

Figure 4.44. Raman spectra of $Ce_{0.8}Ho_xGd_{0.2-x}O_{1.9}$ ($0 \leq x \leq 0.2$) nanoparticles after calcination at 500°C for 2h.

In **Figure 4.45**, the F_{2g} band became asymmetric and shifted to the higher frequencies along with the doubly and singly doping of Gd^{3+} by Ho^{3}. Partial and full doping of Gd^{3+} by smaller sized Ho^{3+} ions in ceria-based electrolytes decrease the M-O bond length and shift the vibrational frequency to the higher energies. Compared to co-doped dysprosium (Section 4.2), the F_{2g} in co-doped holmium shifted to the higher energy due to the smaller ionic radius of Ho^{3+}. The spectra shifted to the higher frequency due to smaller radius dopant of doped Ho (467 cm^{-1}) and Dy (464 cm^{-1}) was also reported by Pikalova et al (181).

Similar to co-doped dysprosium (Section 4.2), the D bands were also detected in the compositions. The peak positions at 558 cm^{-1} and 615 cm^{-1} correspond to the disorder band (D band) that is useful for investigating the defect association in ceramic materials. The D_2 band (615 cm^{-1}) corresponds to the formation of defect species with O_h symmetry that consists of the dopant cation in 8-fold coordination of oxygen ion (155). Furthermore, the D_1 band (558 cm^{-1}) represents the oxygen vacancy associated with defect complexes (155, 156). The Raman ratio between I_{D1}/I_{D2} is shown in **Table 4.15**. The Ho10 composition has the highest value of I_{D1}/I_{D2} ratio among the compounds implying that this compound has highest concentration of oxygen vacancies associated defects in comparation with 8-fold coordination of oxygen ion.

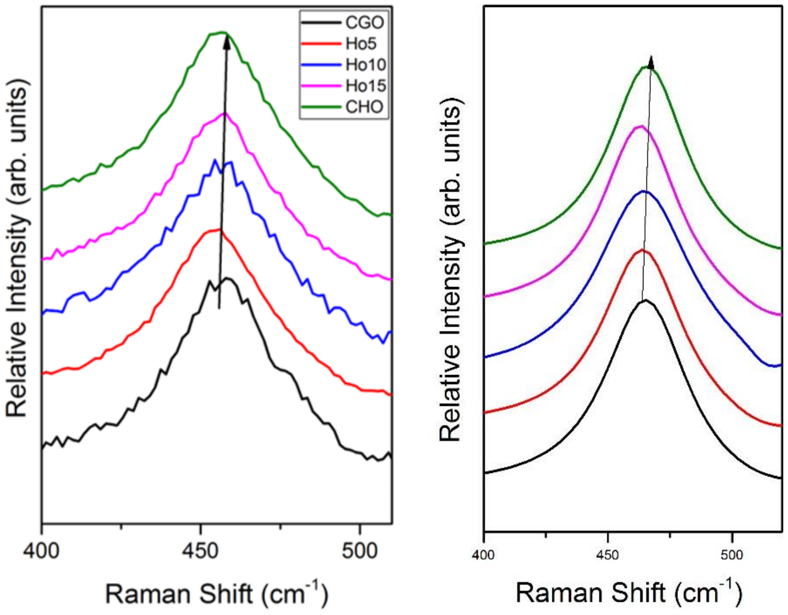

Figure 4.45.(a) Magnified view of F_{2g} band at 465cm^{-1}; (b) Fitted of F_{2g} band at 465cm^{-1}

Table 4.15. Ratio I_{D1}/I_{D2} from Raman peaks of $Ce_{0.8}Ho_xGd_{0.2-x}O_{1.9}$ ($0 \leq x \leq 0.2$)

Sample code	I_{D1}/I_{D2}
CGO	0.71
Ho5	0.58
Ho10	1.20
Ho15	0.43
CHO	0.69

4.3.2 Stability at high temperature studies

The high-temperature XRD of $Ce_{0.8}Ho_xGd_{0.2-x}O_{1.9}$ ($0.05 \leq x \leq 0.2$) samples at temperatures operation of IT-SOFC are shown in **Figure 4.46**. The structure from room temperature to 700°C shows a stable fluoritic structure; there was no second phase or hybrid phase detected in the operating temperature range of IT-SOFC. The co-doped Gd^{3+} and Ho^{3+} ions substituting for Ce^{4+} in the fluoritic structure of CeO_2 form a substitutional solid solution, and as a consequence the position of atoms do not change.

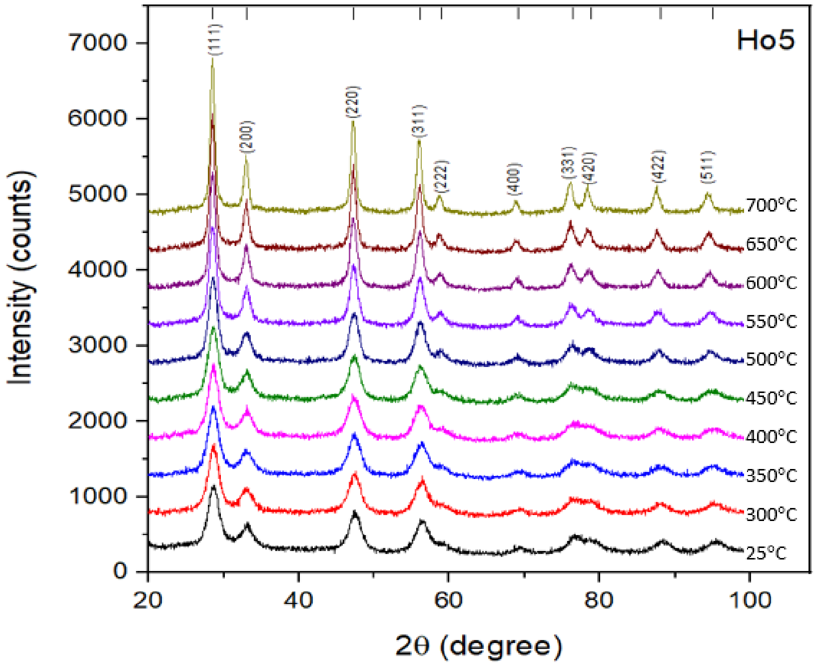

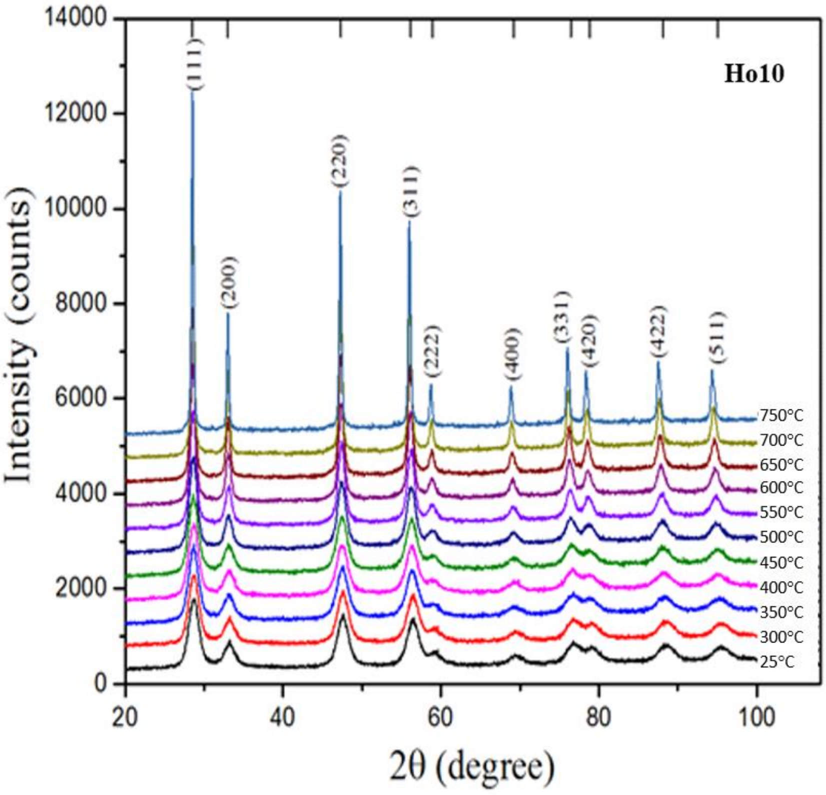
Ho10
Intensity (counts)
2θ (degree)
0
2000
4000
6000
8000
10000
12000
14000
20
40
60
80
100
(111)
(200)
(220)
(311)
(222)
(400)
(331)
(420)
(422)
(511)
750°C
700°C
650°C
600°C
550°C
500°C
450°C
400°C
350°C
300°C
25°C

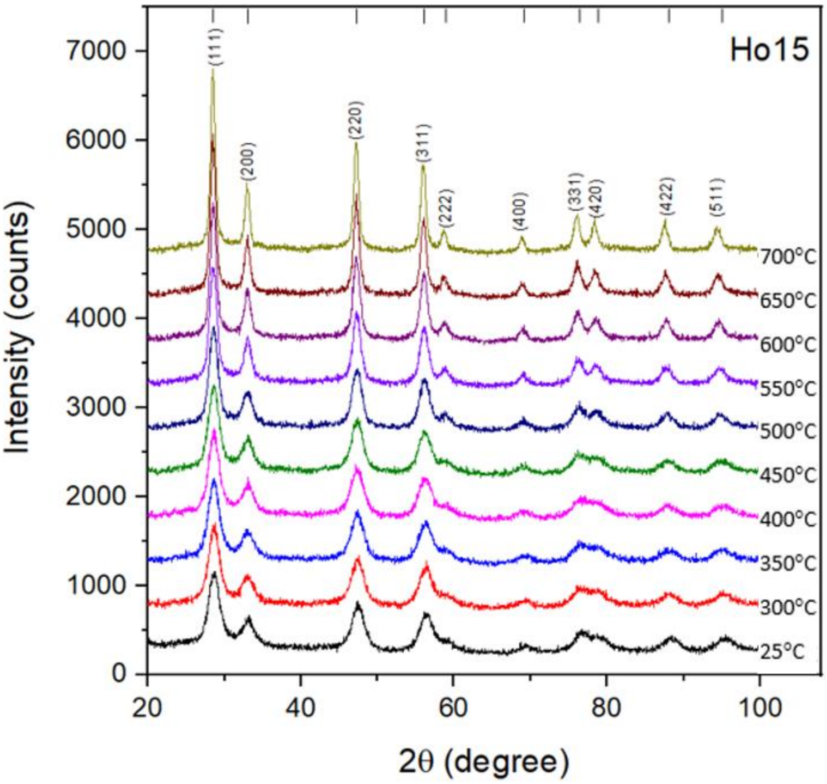
Ho15
Intensity (counts)
2θ (degree)
0
1000
2000
3000
4000
5000
6000
7000
20
40
60
80
100
(111)
(200)
(220)
(311)
(222)
(400)
(331)
(420)
(422)
(511)
700°C
650°C
600°C
550°C
500°C
450°C
400°C
350°C
300°C
25°C

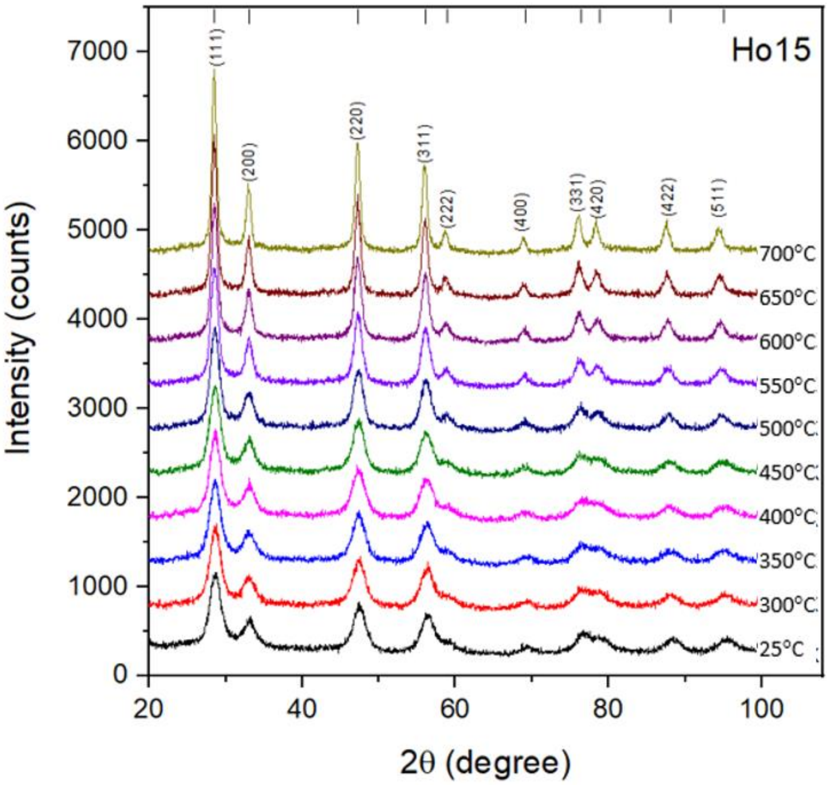

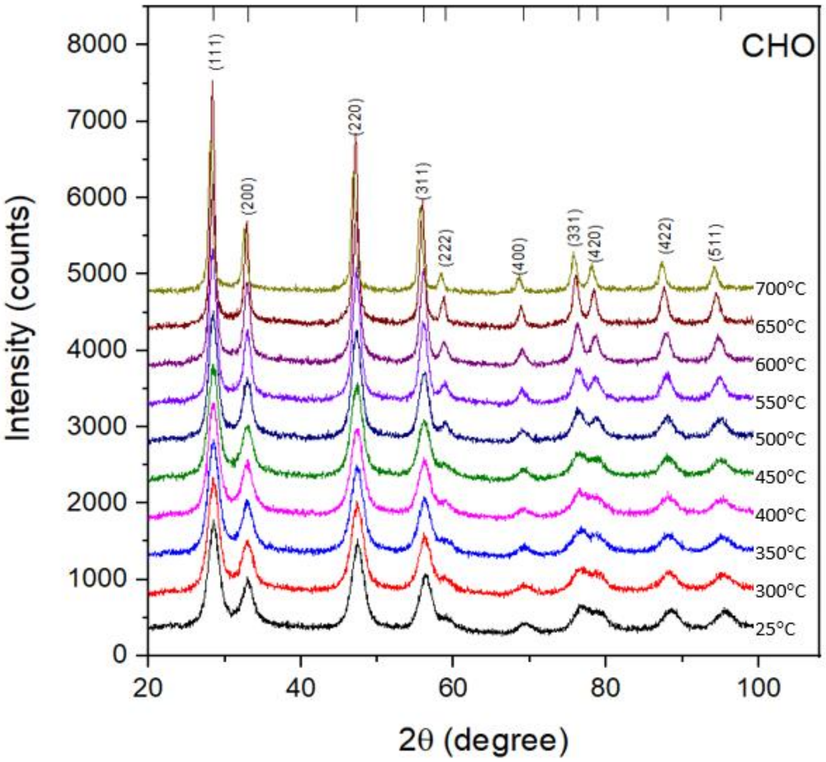

Figure 4.46. High-Temperature XRD of $Ce_{0.8}Ho_xGd_{0.2-x}O_{1.9}$ ($0.05 \leq x \leq 0.2$) samples from room temperature until 700°C.

Similar to previous materials, the temperature dependence of lattice parameter shows a polynomial trend, as exhibited in **Figure 4.47**. The trend in lattice parameter shows an increase with increasing temperatures, which can be modelled by the quadratic polynomial function represented by equation (4.14 – 4.17).

Ho5 : $\alpha_T = 5.4255 - 1.421 \times 10^{-5}\ T + 6.208 \times 10^{-8}\ T^2$ (4.14)

Ho10 : $\alpha_T = 5.41596 + 4.944 \times 10^{-6}\ T + 4.931 \times 10^{-8}\ T^2$ (4.15)

Ho15 : $\alpha_T = 5.4131 + 2.9166 \times 10^{-6}\ T + 5.153 \times 10^{-8}\ T^2$ (4.16)

CHO : $\alpha_T = 5.405 + 6.5845 \times 10^{-6}\ T + 4.7122 \times 10^{-8}\ T^2$ (4.17)

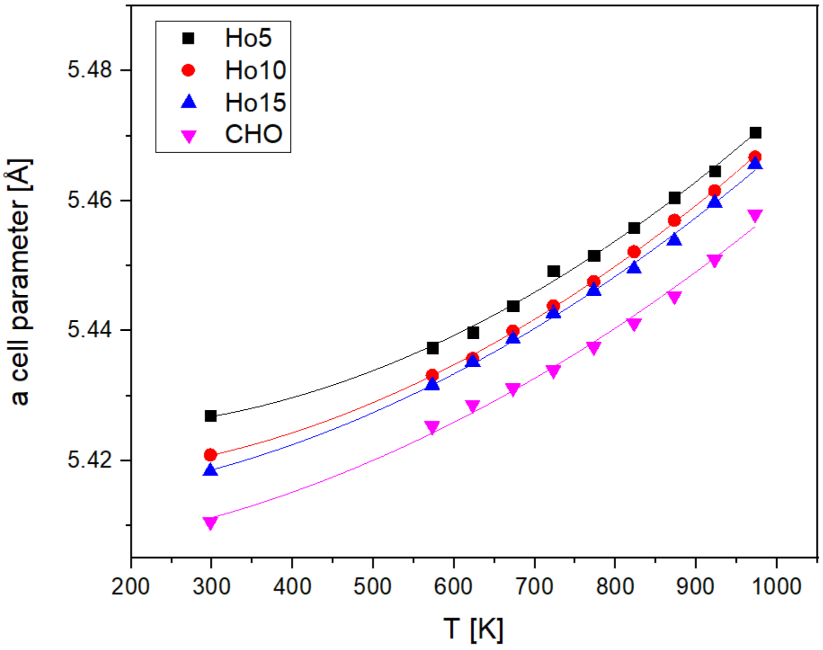

Figure 4.47. Lattice parameter of $Ce_{0.8}Ho_xGd_{0.2-x}O_{1.9}$ ($0.05 \leq x \leq 0.2$) as a function of temperature.

The calculated % LTE (**Figure 4.48**) was fitted as a function of temperature using a quadratic polynomial regression analysis as follows:

Ho5 : $\% \text{LTE} = -0.24208 + 2.991 \times 10^{-4}\ T + 7.878 \times 10^{-7}\ T^2$ (4.18)

Ho10 : $\% \text{LTE} = 0.4816 - 0.0014\ T + 1.8703 \times 10^{-6}\ T^2$ (4.19)

Ho15 : $\% \text{LTE} = 0.07953 - 4.083 \times 10^{-4}\ T + 1.244 \times 10^{-6}\ T^2$ (4.20)

CHO : $\% \text{LTE} = 0.5734 - 0.00164\ T + 1.9904 \times 10^{-6}\ T^2$ (4.21)

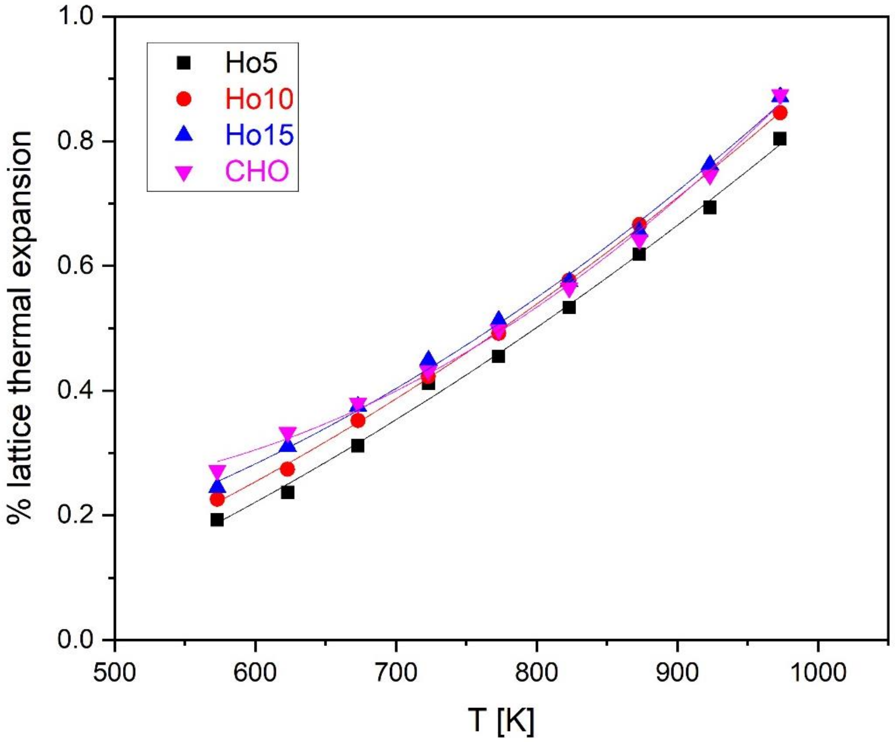

Figure 4.48. Percentage of lattice thermal expansion of $Ce_{0.8}Ho_xGd_{0.2-x}O_{1.9}$ ($0.05 \leqslant x \leqslant 0.2$) as a function of temperature.

The CTE of $Ce_{0.8}Ho_xGd_{0.2-x}O_{1.9}$ ($0.05 \leqslant x \leqslant 0.2$) samples can be calculated using equation 5.10, as reported in **Table 4.16**. The thermal expansion coefficient analysed in this study from room temperature until 700°C increases with increasing holmium ion content. The CTE in CGO obtained by Mogensen et al. (166) is higher than Ho5 in this study, since the CGO analysis was done at an elevated temperature (1000°C). Higher temperature observation can give a higher CTE value, as Kumar et al. reported that the CTE of CGO is 12.21 x 10^{-6} C^{-1} at RT-800°C and 12.69 x 10^{-6} C^{-1} at RT-1000°C. Similar to co-doped dysprosium, the increase in CTE with increased Ho^{3+} is caused by the decreasing lattice parameter (161 – 165). However, the singly doped holmium with ceria has a lower thermal expansion coefficient than the dysprosium doped ceria because the melting point of holmium is higher than that of DyO_2 (182).

Table 4.16. CTE of cerium holmium gadolinium oxide ($Ce_{0.8}Ho_xGd_{0.2-x}O_{1.9}$)

Sample code	**CET (10^{-6} K^{-1}) RT–973K**
CGO (166)	12.21
Ho5	11.908
Ho10	12.898
Ho15	12.908
CHO	12.959

4.3.3 Scanning Electron Microscopy (SEM) and density analysis

Figure 4.49 exhibits the densification curve of $Ce_{0.8}Ho_xGd_{0.2-x}O_{1.9}$ ($0 \leq x \leq 0.2$) pellets. All the micrographs of $Ce_{0.8}Ho_xGd_{0.2-x}O_{1.9}$ sintered ceramics show fully dense structures (**Figure 4.50**), which agree with the high relative density of all ceramics typically greater than 96.4%. In general, the relative density appears to be increasing with the increasing co-dopant concentration up to x=0.1 and then decreases for x=0.15 – 0.2. The decreasing average cation size increases the cation diffusion rate and hence contributes towards improving the degree of sinterability of the samples. Similar to our study, Coles-Aldridge et al. (15) observed that the increasing average cation size can decrease the crystallite size and cation diffusion rate. In low concentration, the substitution of holmium ion acts as the sintering aid to improve densification rate. Therefore, an optimum density is achieved at holmium content between 5 – 10 %mol.

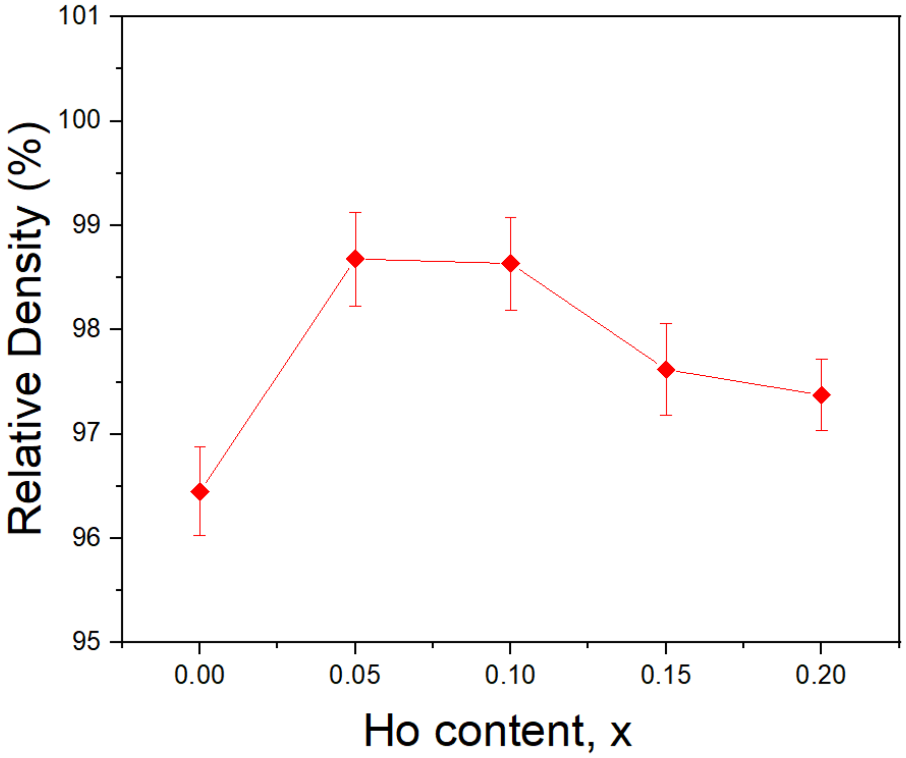

Figure 4.49. Densification curve of $Ce_{0.8}Ho_xGd_{0.2-x}O_{1.9}$ ($0 \leq x \leq 0.2$) ceramics sintered at 1500°C for 2h.

The microstructure consisting of nonporous, equiaxed and hexagonal shaped interlocked grains was observed in all compositions. Co-doped Ho10 shows uniform grain growth with uniform grain size. A small grain growth was noticed in the doped (CGO and CHO) samples and comparatively more observed in co-doped materials (Ho5 and Ho15), potentially due to a reduced mass transport across the grain boundary in co-doped samples (182). Moreover, the inhomogeneous grain growth in the materials can be induced by the solute drag (183 – 185).

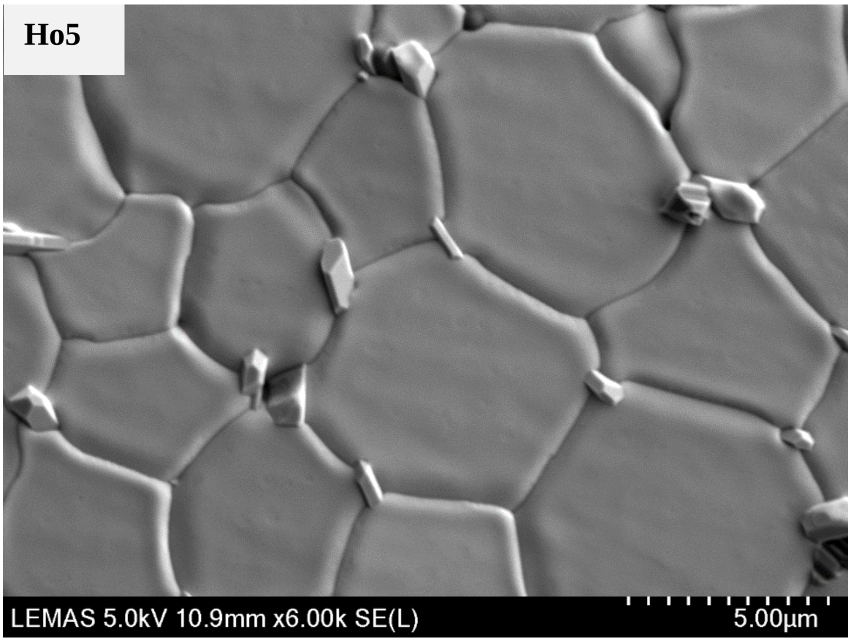
Ho5
LEMAS 5.0kV 10.9mm x6.00k SE(L)
5.00µm

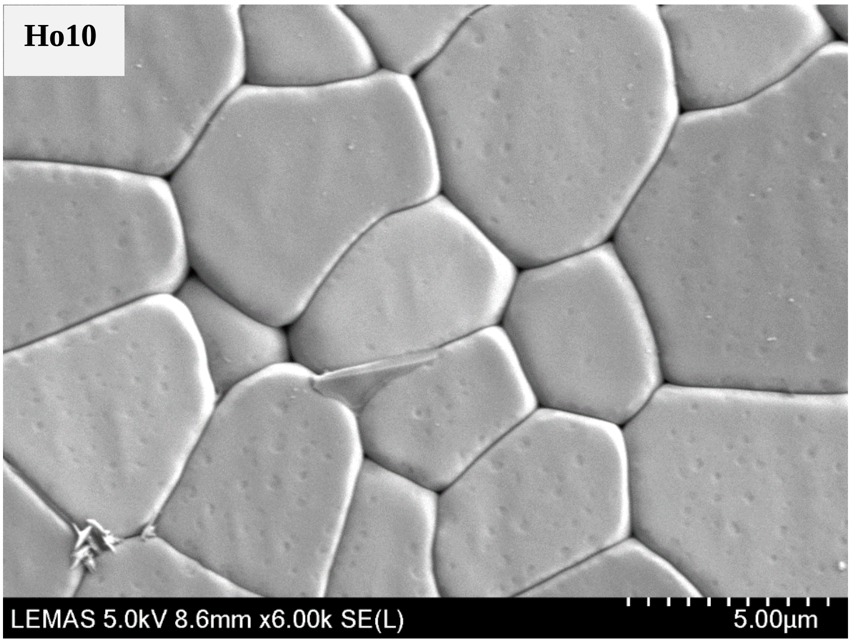
Ho10
LEMAS 5.0kV 8.6mm x6.00k SE(L)
5.00µm

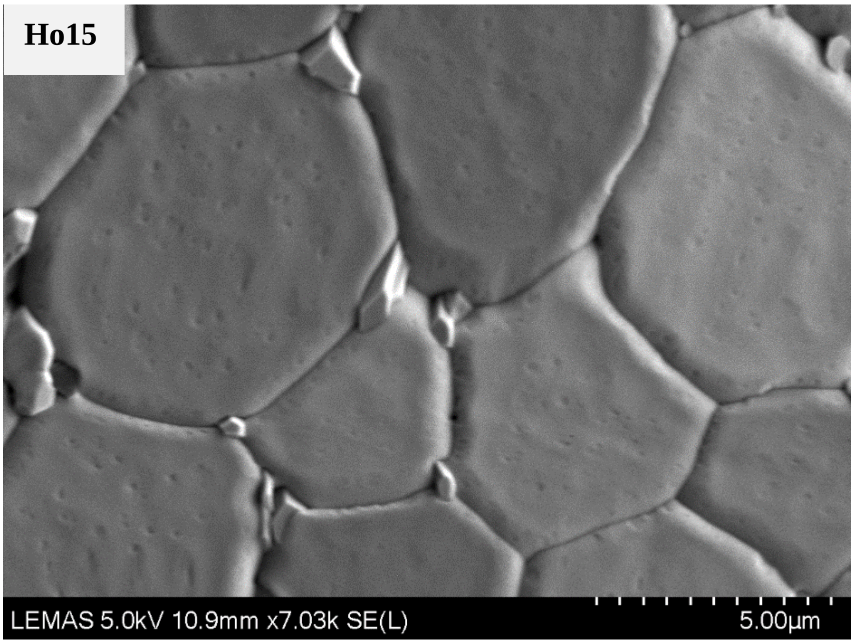

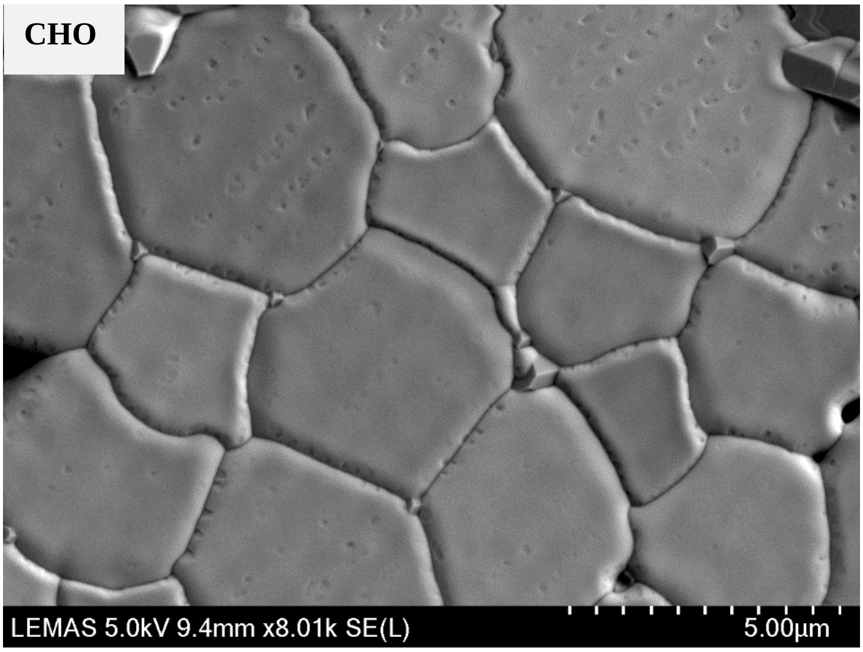

Figure 4.50. SEM micrographs of $Ce_{0.8}Ho_xGd_{0.2-x}O_{1.9}$ ($0.05 \leq x \leq 0.2$) ceramics sintered at 1500°C for 2 h.

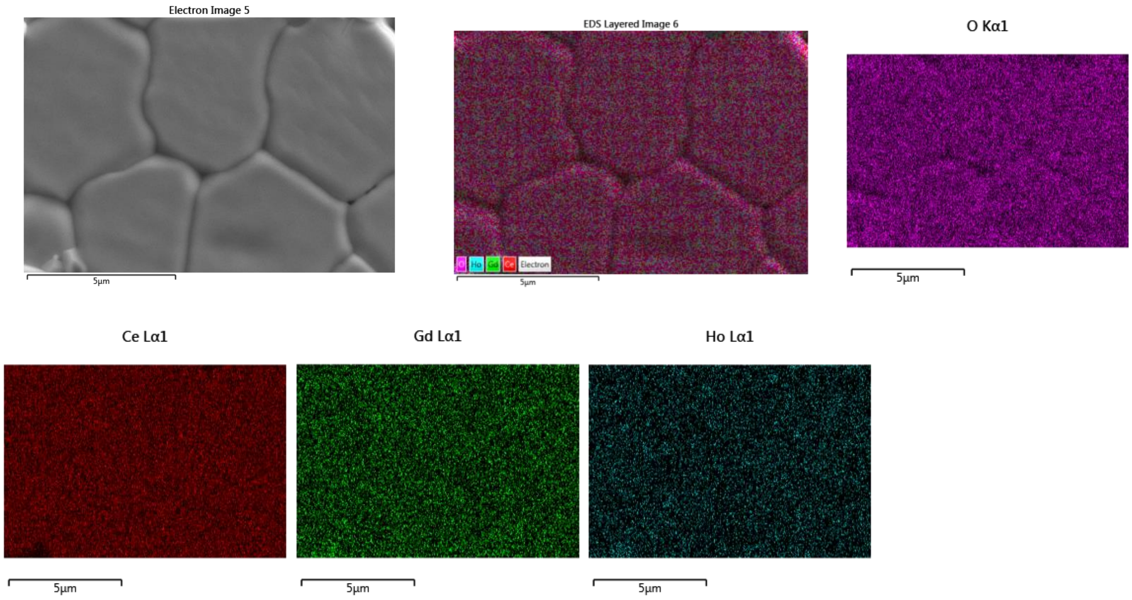

Figure 4.51. SEM image of the microstructure and a layered elemental map followed by the EDS elemental map of Ho5 sintered pellet consisting of oxygen in purple, cerium in red, gadolinium in green and holmium in blue colour.

The energy-dispersive spectrum (EDS) spectroscopy was used to map various elements present in the sintered multielement pellets. **Figure 4.51** shows results of a typical EDS elemental mapping of oxygen (O), ceria (Ce), gadolinium (Gd), and holmium (Ho) from a Ho5 dense pellet. The elements are clearly distinctive and homogeneously distributed within the grain across the entire microstructure, suggesting a complete solid solution formation. EDS elements analysis of $Ce_{0.8}Ho_xGd_{0.2-x}O_{1.9}$ sintered ceramics are shown in **Table 4.17**. The weight percentages from EDS analysis were used to calculate the mole fraction of each element (91). The calculated mole fractions of Ce, Ho, and Gd in the entire series of samples prepared in this study are in excellent agreement with their respective nominal mole fraction. This suggests the efficacy of the process used in synthesising nanoparticles of this complex solid solution series.

Table 4.17. Weight precentages and calcutaed mole fractions obtained from EDS analysis of $Ce_{0.8}Ho_xGd_{0.2-x}O_{1.9}$ ($0 \leqslant x \leqslant 0.2$) sintered pellets

Composition	**Element**	**Weight % from EDS**	**Atomic weight**	**Mole**	**Mole %**	**Nominal**
CGO	Ce	59.6	140.116	0.425	0.802	0.80
	Gd	16.5	157.2	0.105	0.198	0.20
	Total mole of Ce + Gd			0.530		
	O	12.4	15.99	1.119		
Ho5	Ce	63.16	140.116	0.451	0.798	0.80
	Ho	2.77	164.9303	0.017	0.046	0.05
	Gd	12.11	157.2	0.077	0.156	0.15
	Total mole of Ce + Ho + Gd			0.545	1	
	O	21.96	15.99	1.373		
Ho10	Ce	64.49	140.116	0.460	0.819	0.80
	Ho	7.04	164.9303	0.043	0.082	0.10
	Gd	9.14	157.2	0.058	0.099	0.10
	Total mole of Ce + Ho + Gd			0.561	1	
	O	19.33	15.99	1.209		
Ho15	Ce	31.4	140.116	0.448	0.804	0.80
	Ho	6.5	164.9303	0.079	0.141	0.15
	Gd	2.4	157.2	0.031	0.055	0.05
	Total mole of Ce + Ho + Gd			0.278	1	
	O	19.4	15.99	1.213		
CHO	Ce	63.3	140.116	0.452	0.802	0.80
	Ho	18.4	164.9303	0.111	0.198	0.20
	Total mole of Ce + Ho			0.563	1	
	O	6.3	15.99	0.394		

4.3.4 Electrical properties analysis

The measured impedance spectra for $Ce_{0.8}Ho_xGd_{0.2-x}O_{1.9}$ ($0 \le x \le 0.2$) dense pellets measured at two different temperatures are shown in **Figure 4.52 - 4.53**, respectively.

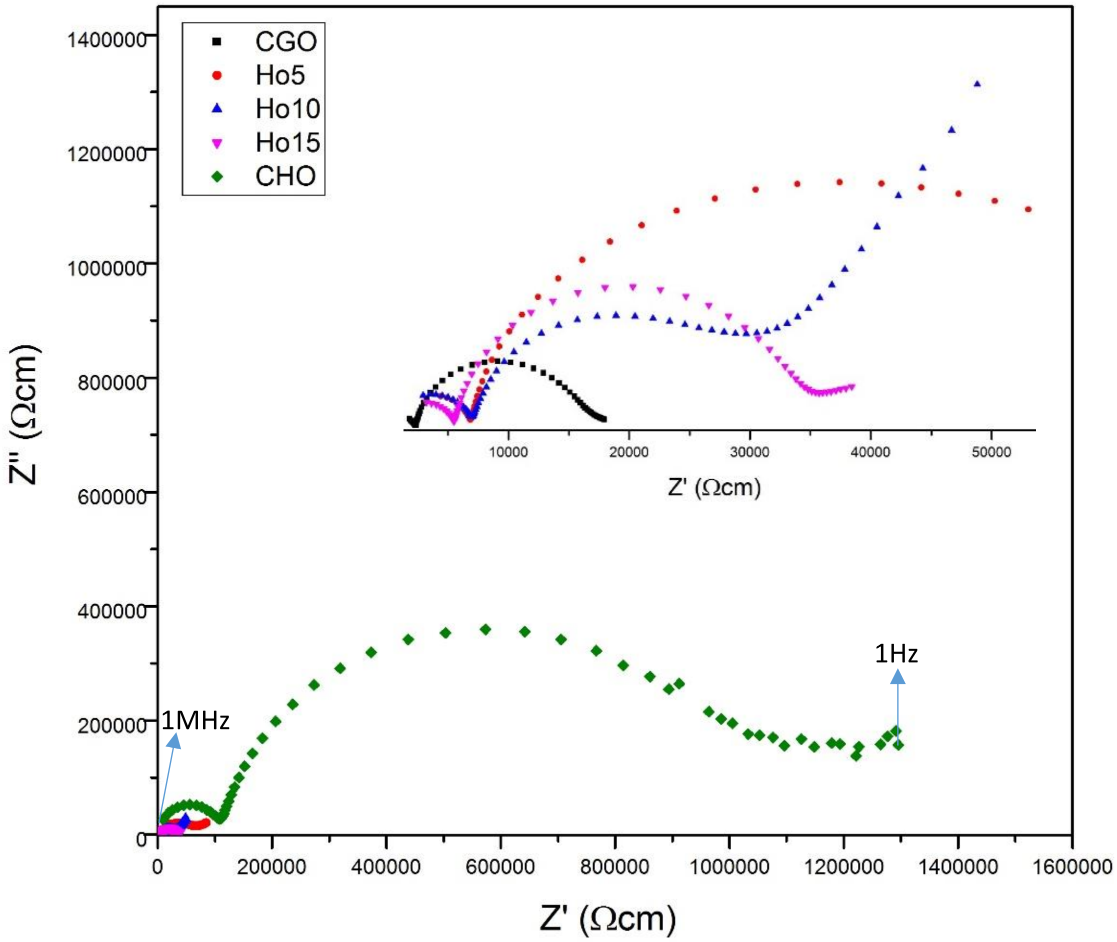

Figure 4.52. The complex plane impedance plots of dense $Ce_{0.8}Ho_xGd_{0.2-x}O_{1.9}$ ($0 \le x \le 0.2$) ceramic measured at 300 °C in air. The inset plot is the low range of Z’ (Ωcm).

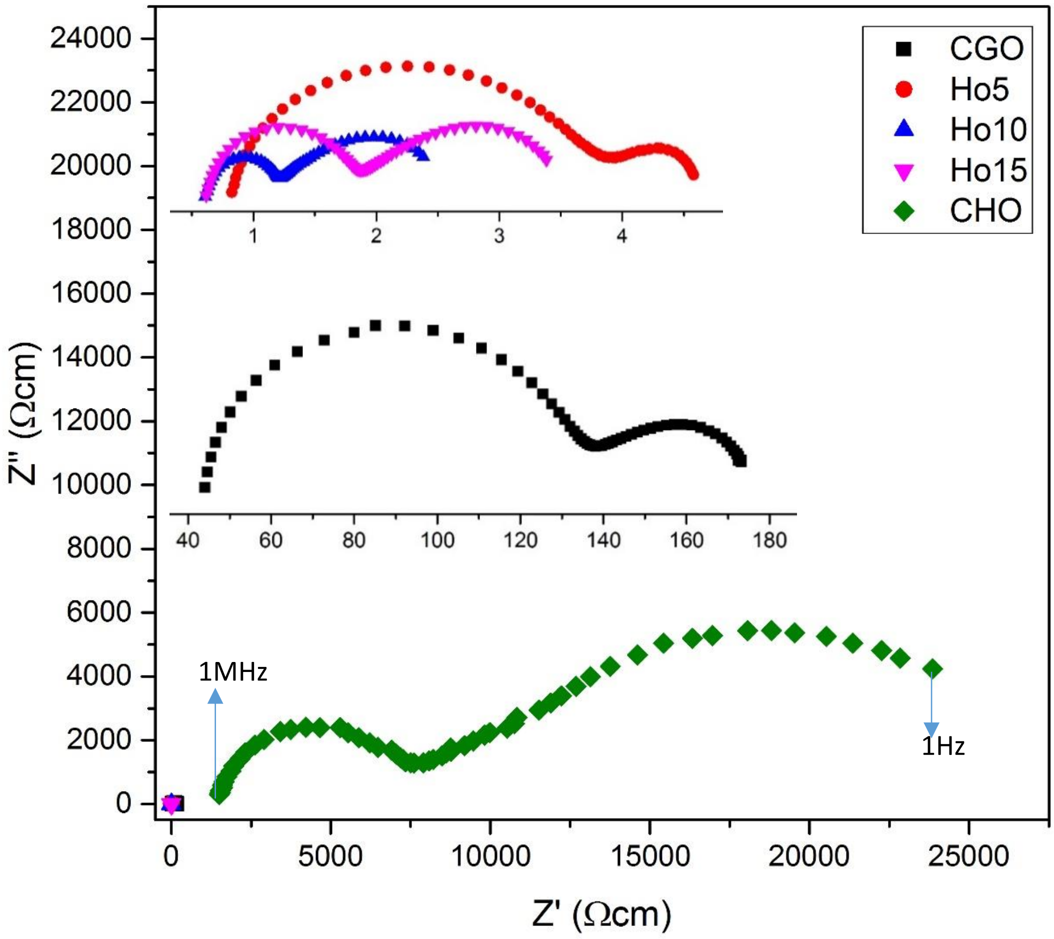

Figure 4.53. The complex plane impedance plots of dense $Ce_{0.8}Ho_xGd_{0.2-x}O_{1.9}$ ($0 \le x \le 0.2$) ceramic measured at 500°C in air. The inset plot is the low range of Z' (Ωcm).

The impedance spectra of $Ce_{0.8}Ho_xGd_{0.2-x}O_{1.9}$ ($0 \leqslant x \leqslant 0.2$) at 300 and 500°C are shown in **Figures 4.52** and **4.53**, respectively. At 300°C two arcs were observed from the spectra for all compositions. Moreover, **Figure 4.54 (a)** shows the fitting of Nyquist plots and an equivalent circuit model for Ho10. The first arc was assigned to grain-interior (R1//CPE1), and the second arc was associated with grain-boundary (R2//CPE2), while the linear straight line is assigned to electrode impedance (W). At 500°C (**Figure 4.54(b)**), the first arc was related to grain-boundary (R2//CPE2) and the second semicircle was associated with an electrode (R3//CPE3). The bulk conductivity was calculated from the intercept on Z' axis (R1), because the semicircle was shifted to a higher frequency above the operating frequency spectrometer (16, 170). Total conductivity was calculated from the sum of bulk and grain boundary conductivity.

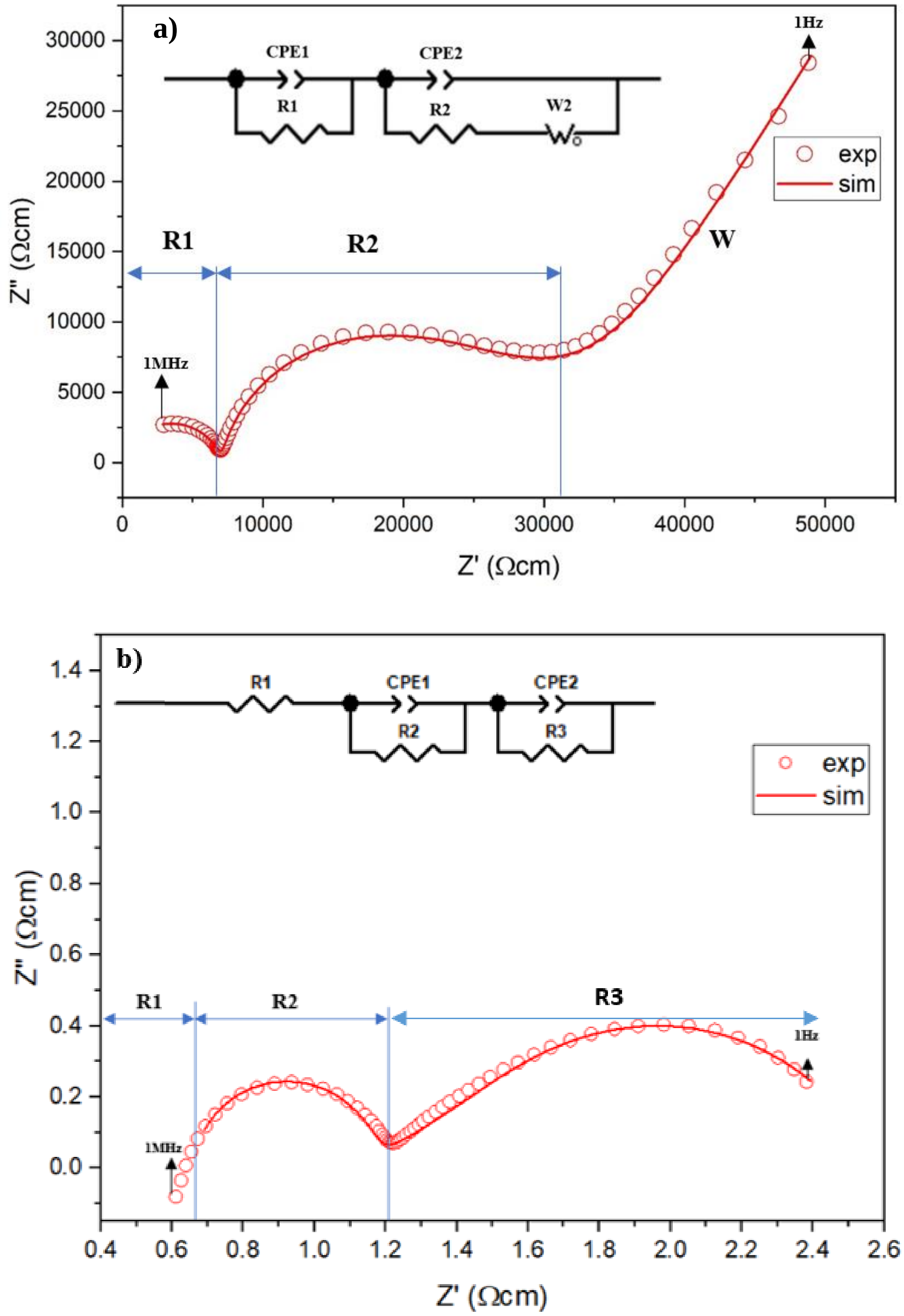

Figure 4.54. Nyquist plots and fitting for Ho10 dense pellet at a) 300°C and b) 500°C. Inserted image is equivalent circuit model used for fitting of the impedance data.

Figure 4.55 displays the Arrhenius plots of bulk, grain boundary and total conductivities for $Ce_{0.8}Ho_xGd_{0.2-x}O_{1.9}$ ($0 \leqslant x \leqslant 0.2$) ceramics at the temperature range between 300 and 500°C. It is seen from the Arrhenius plots, especially for the co-doped materials, that after a critical temperature (Tc) of approximately 420°C the conductivity exhibits an anomalous increase. Similar to co-doped with dysprosium (Section 4.2.4), the unusual increase in the conductivities was also detected in the co-doped holmium; however, the jumping temperature for these materials is slightly higher than the co-doped dysprosium. This is probably due to the smaller ionic radius of Ho^{3+} ion (CN 6 = 0.901 Å) compared to Dy^{3+} ion (CN 6 = 0.912 Å). The increase in critical temperature was reported by Zhang et al. (49), who observed that doped ceria with Y^{3+} (CN 6 = 0.9 Å) has higher critical temperature than Gd^{3+} ion (CN 6 = 0.938 Å) due to the higher association enthalpy.

At temperature between 300°C and 400°C, the total conductivity was highest for CGO and was lowest for CHO. However, between 400°C and 500°C the total conductivity was highest for Ho15. On the other hand, grain boundary conductivity for Ho10 was observed as the highest among other samples. The enhancement of grain boundary conductivity for Ho10 is due to the uniform and smaller grain size compared to other materials (50, 186).

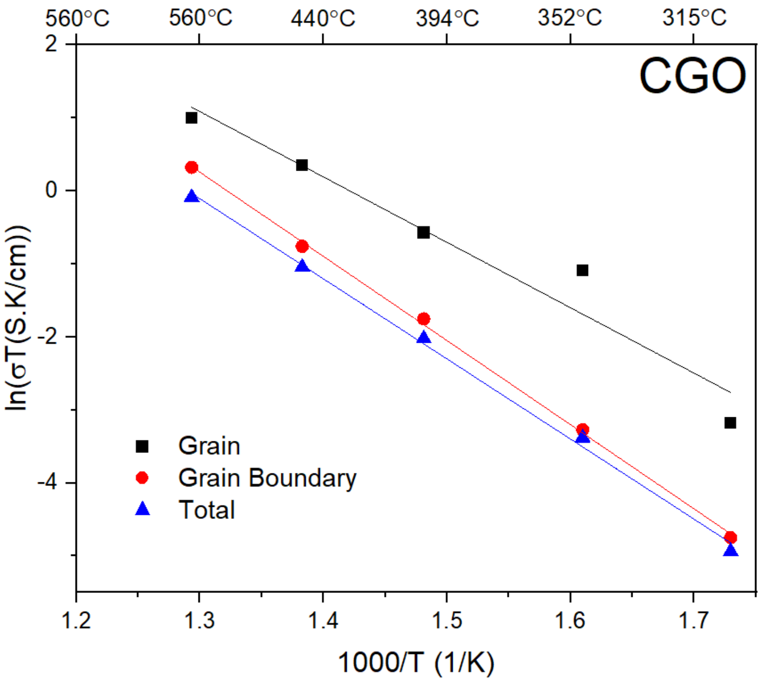
CGO
560°C
560°C
440°C
394°C
352°C
315°C
2
0
-2
-4
ln(σT(S.K/cm))
1.2
1.3
1.4
1.5
1.6
1.7
1000/T (1/K)
Grain
Grain Boundary
Total

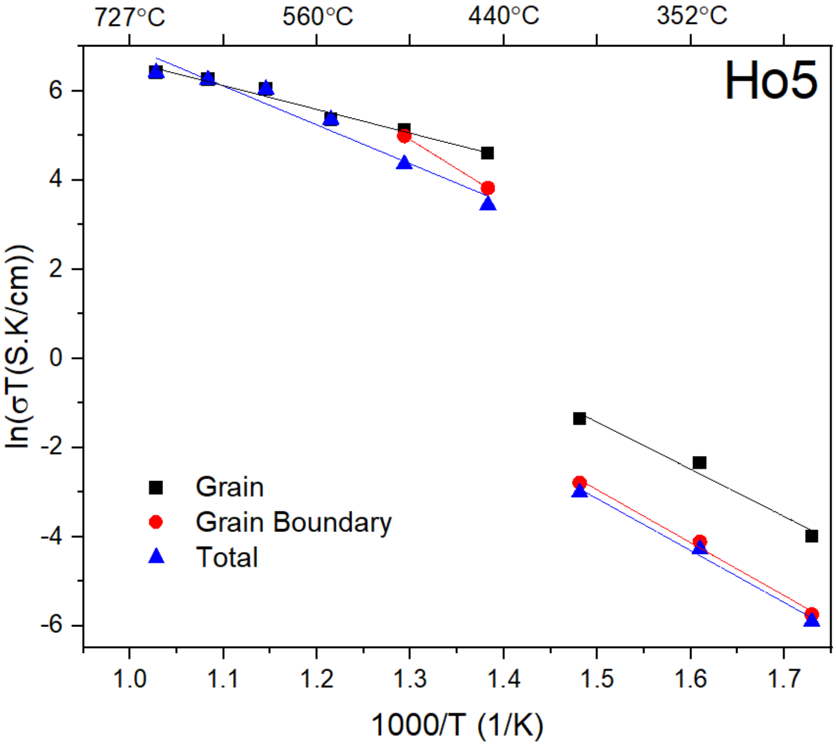
Ho5
727°C
560°C
440°C
352°C
6
4
2
0
-2
-4
-6
ln(σT(S.K/cm))
1.0
1.1
1.2
1.3
1.4
1.5
1.6
1.7
1000/T (1/K)
Grain
Grain Boundary
Total

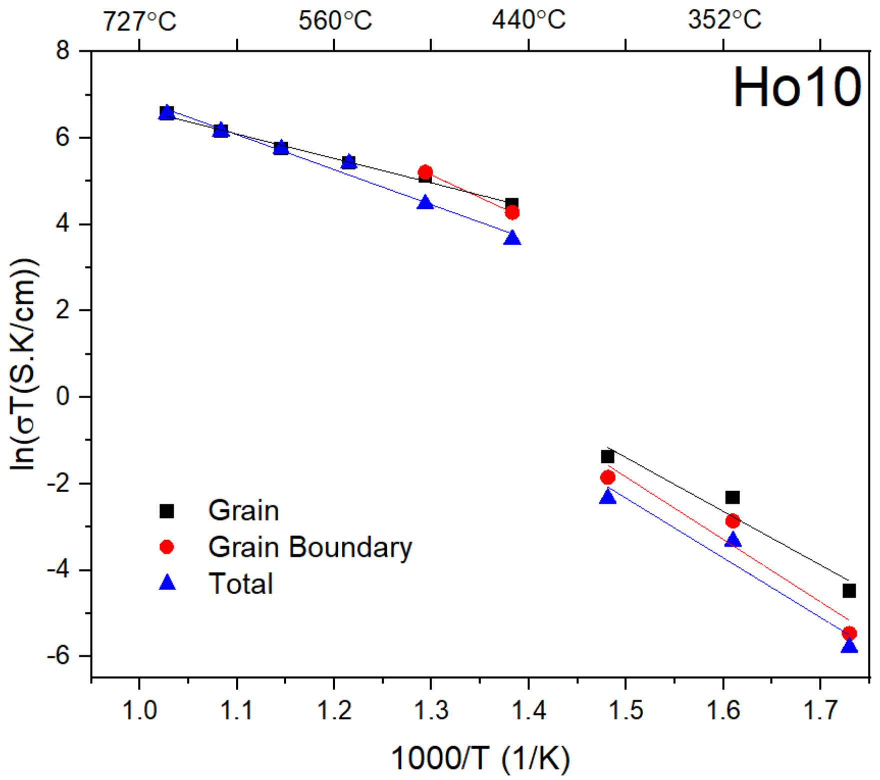
Ho10
727°C
560°C
440°C
352°C
8
6
4
2
0
-2
-4
-6
ln(σT(S.K/cm))
1.0
1.1
1.2
1.3
1.4
1.5
1.6
1.7
1000/T (1/K)
Grain
Grain Boundary
Total

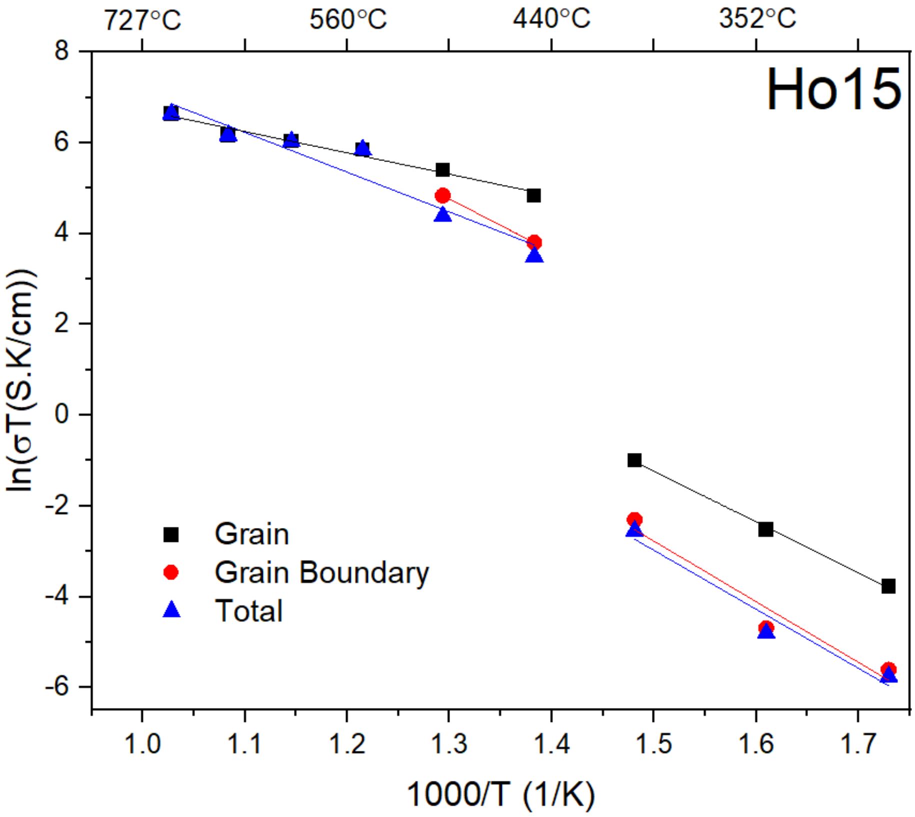
Ho15
727°C
560°C
440°C
352°C
8
6
4
2
0
-2
-4
-6
ln(σT(S.K/cm))
1.0
1.1
1.2
1.3
1.4
1.5
1.6
1.7
1000/T (1/K)
Grain
Grain Boundary
Total

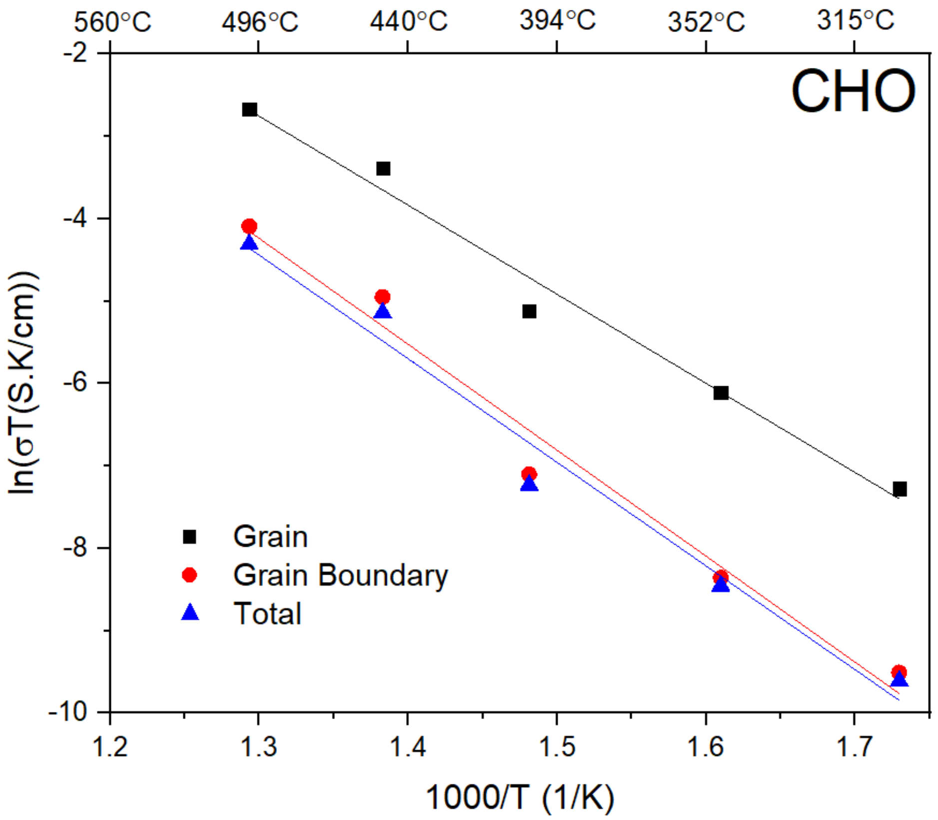

Figure 4.55. The Arrhenius plots for $Ce_{0.8}Ho_xGd_{0.2-x}O_{1.9}$ $(0 \leqslant x \leqslant 0.2)$ ceramics.

Table 4.18 presents conductivity measured at 500°C and activation energies for bulk and grain boundary for $Ce_{0.8}Ho_xGd_{0.2-x}O_{1.9}$ $(0 \leqslant x \leqslant 0.2)$ ceramic electrolytes. It is seen that co-doping materials can significantly enhance conductivity of materials, especially after critical temperature. The total conductivities at 500°C were 0.0012 S cm^{-1} for CGO and improved to 0.1497 S cm^{-1} for Ho10. This is comparable to results by Shirbhate et al. (171), who found the improvement of total conductivity at 600°C from 4.29 x 10^{-4} S cm^{-1} for $Ce_{0.85}Sm_{0.15}O_{1.9}$ to 4.56 x 10^{-2} S cm^{-1} for $Ce_{0.85}Sm_{0.075}Ca_{0.15}O_{1.9}$. In the present study, the creation of oxygen vacancies in terms of Kröger–Vink notation for co-doping of holmium and gadolinium is:

$$Ho_2O_3 + CeO_2 \rightarrow 2Ho_{Ce}^{'} + 3O_o^x + V_o^{''} \tag{4.22}$$

$$Gd_2O_3 + CeO_2 \rightarrow 2Gd_{Ce}^{'} + 3O_o^x + V_o^{''} \tag{4.23}$$

The total conductivity of 3.16 x 10^{-5} S cm^{-1} at 500°C for CHO prepared by citrate auto ignition method was observed by Baral and Sankaranarayanan (187). This is slightly higher than 2.02 x 10^{-5} S cm^{-1} for the same composition and temperature obtained in this present study. However, the activation energy of 0.825 eV in the present study is lower than 1.26 eV reported by Baral and Sankaranarayanan (187, 188). Ou and co-workers (64, 189) found a kink in the Arhenius plot for both 20 and 15mol% holmium doped ceria due to the inhomogeneity inside the grains, whereas in the present study single slope was observed and it followed the Arrhenius behaviour.

Table 4.18. Bulk (GI), grain boundary (GB) and total conductivities measured at 500°C, with activation energies for bulk and grain boundary for $Ce_{0.8}Ho_xGd_{0.2-x}O_{1.9}$ ($0 \leqslant x \leqslant 0.2$) ceramic electrolytes.

Electrolytes	**σ_{GI} (S cm^{-1})**	**σ_{GB} (S cm^{-1})**	**σ_{Total} (S cm^{-1})**	**Ea_{ionic} (eV)**	**Ea_{GB} (eV)**
CGO	0.00351	0.0018	0.0012	0.878	0.993
Ho5	0.2155	0.1894	0.1008	0.932	1.05
Ho10	0.2871	0.3127	0.1497	0.964	1.066
Ho15	0.2859	0.1632	0.1039	1.244	1.338
CHO	9.9 x 10^{-5}	2.5 x 10^{-5}	2.02 x 10^{-5}	0.971	1.164

The values of bulk, grain boundary and total activation energy measured in this study are close to 1 eV which agree with the typical of oxygen ion conductors (190, 191). The increasing Ho^{3+} ion content in CGO leads to an increase in the activation energy. This phenomenon was also reported by Winck and co-workers (180).

The association enthalpy for co-doped materials in **Figure 4.56** has been found to be greater than that for the single doped ceria. Below the critical temperature, oxygen vacancies are easy to be trapped, blocked and immobilised due to the formation of dimer ($V_O^{\cdot\cdot} - M_{Ce}^{'}$) and trimer ($M_{Ce}^{'} - V_O^{\cdot\cdot} - M_{Ce}^{'}$) (17). Above the critical temperature, co-doped materials have higher ionic conductivities and lower migration enthalpies than CGO and CHO. In these temperature regimes, all the oxygen vacancies are mobile without any interaction with dopant cations.

The highest conductivity is achieved by double doped samples containing 10 mol% Ho and 10 mol% Gd. This makes this composition an optimum ceria electrolyte for intermediate temperature. The high conductivity is achieved by the combination of the synergetic effect of the highest oxygen vacancies concentration generated by doping ceria with both cations and the increased oxygen ion mobility due to the increased ionic radius of the dopant cation.

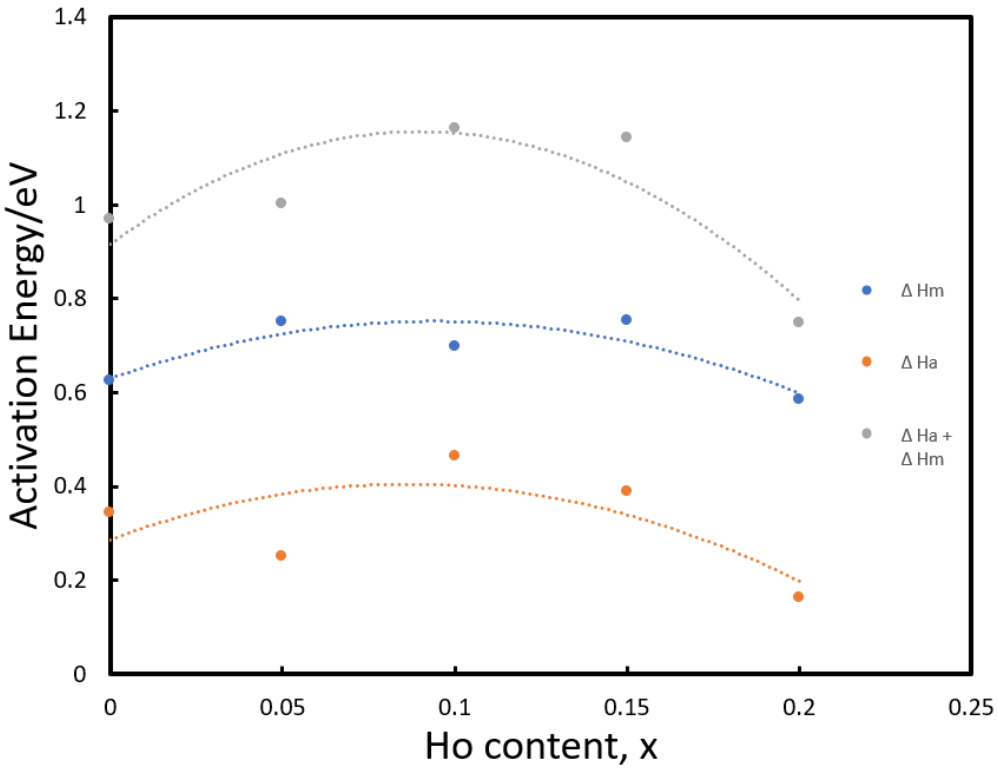

Figure 4.56. Activation energy for total conductivity, below Tc ($\Delta H_m + \Delta H_a$), above Tc (ΔH_m), and ΔH_a of $Ce_{0.8}Ho_xGd_{0.2-x}O_{1.9}$ ($0 \leq x \leq 0.2$) ceramic electrolytes.

4.4 Production of $Ce_{0.8}Er_xGd_{0.2-x}O_{1.9}$ ($0 \leq x \leq 0.2$) nanoparticle

4.4.1 Characterisation of nanoparticles

Figure 4.57 exhibits the XRD patterns of $Ce_{0.8}Er_xGd_{0.2-x}O_{1.9}$ ($0 \leq x \leq 0.2$) nanoparticles calcined at 500° for 2h. All peaks confirm the pure cubic fluorite crystal structure with $Fm\overline{3}m$ space group. There is no signature of any secondary phase or hybrid phase detected in all compositions. The partial substitution of Er^{3+} and Gd^{3+} in CeO_2 matrix formed a complete solid solution in the composition range of $0 \leq x \leq 0.2$.

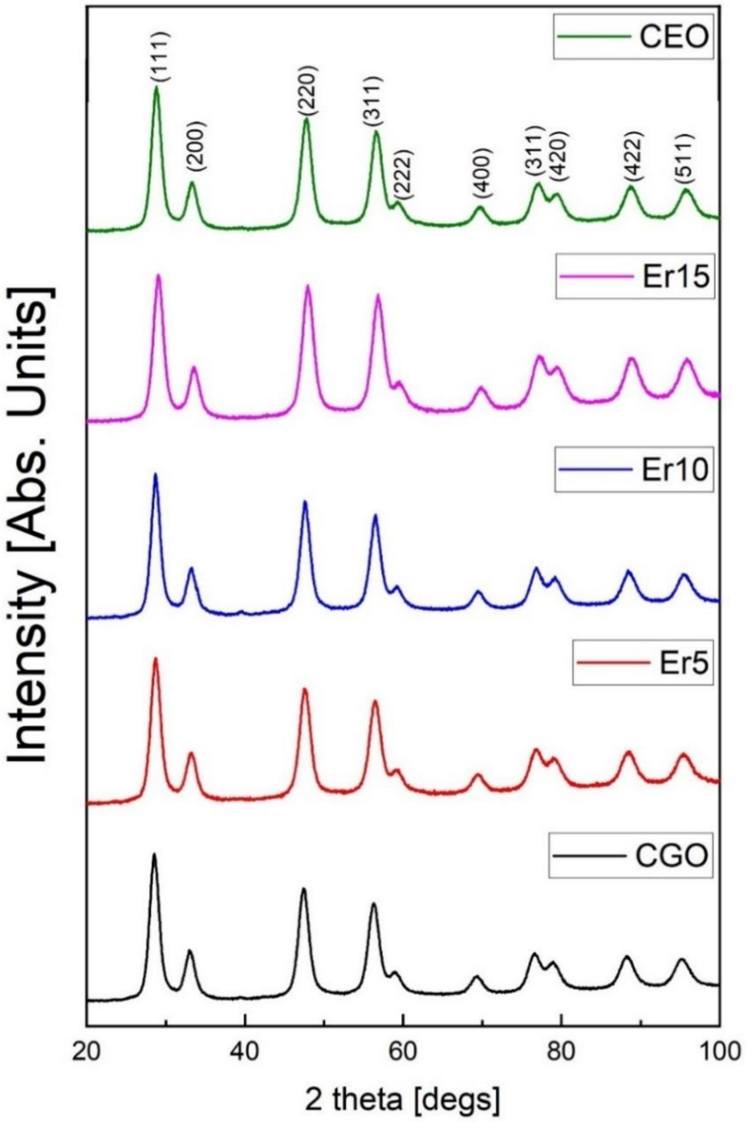

Figure 4.57. XRD patterns for nanoparticles of $Ce_{0.8}Er_xGd_{0.2-x}O_{1.9}$ ($0 \leq x \leq 0.2$) calcined at 500°C for 2h.

Similar to two previous materials (Section 4.2.1 and 4.3.1), board peaks in XRD patterns were also detected in these entire compositions as an indication of the nano range. This nano range was also confirmed by the estimated crystallite size from XRD (**Table 4.19**) and TEM images (**Figure 4.58**). The difference between D_{XRD} and D_{TEM} values is because of the assumption in XRD calculation, including strain and instrumental broadening effects. Particle morphology shows a mixture of hexagonal and square shape as evidence of typical fluorite structure.

Table 4.19. Refined structural parameter, agreement factors, crystallite size and theoretical density for $Ce_{0.8}Er_xGd_{0.2-x}O_{1.9}$ $(0 \leq x \leq 0.2)$ nanoparticles calcined at 500°C for 2 h.

	CGO	**Ho5**	**Ho10**	**Ho15**	**CHO**
Rp	0.021	0.025	0.026	0.029	0.025
Rexp	0.0126	0.015	0.015	0.015	0.014
χ^2	5.34	5.198	5.954	6.812	5.570
V (Å^3)	160.16 (2)	159.34 (2)	158.79 (2)	158.20 (2)	157.82 (2)
a (Å)	5.43061 (2)	5.4213 (2)	5.4151 (2)	5.4084 (3)	5.4041 (19)
D_{XRD} (Å)	111.759	115.6185	106.984	84.4942	89.8704
ρ_{Th} (g/cm^3)	7.214	7.272	7.318	7.366	7.405

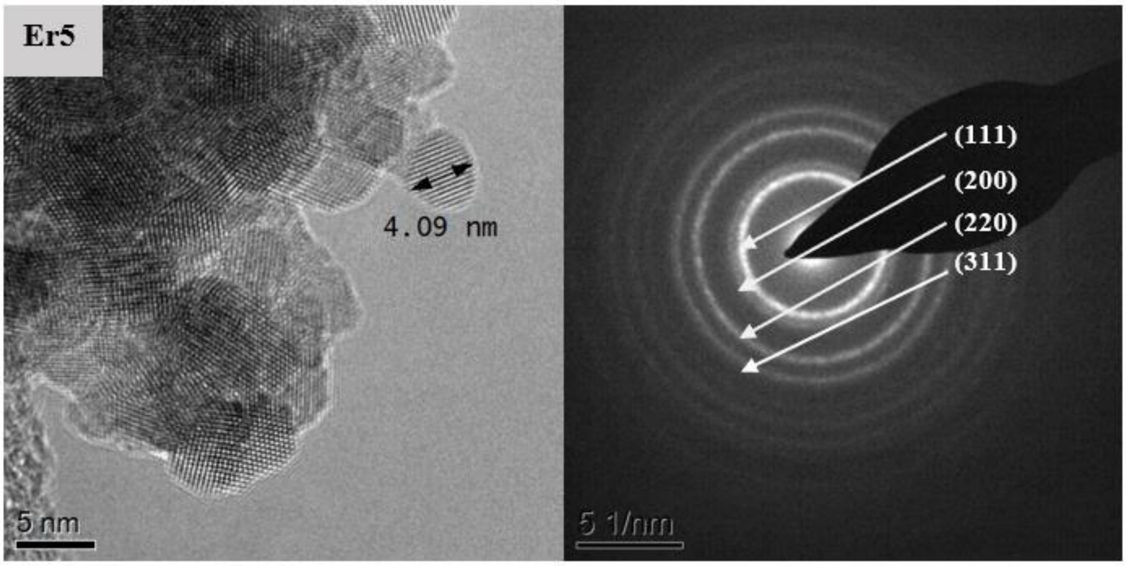

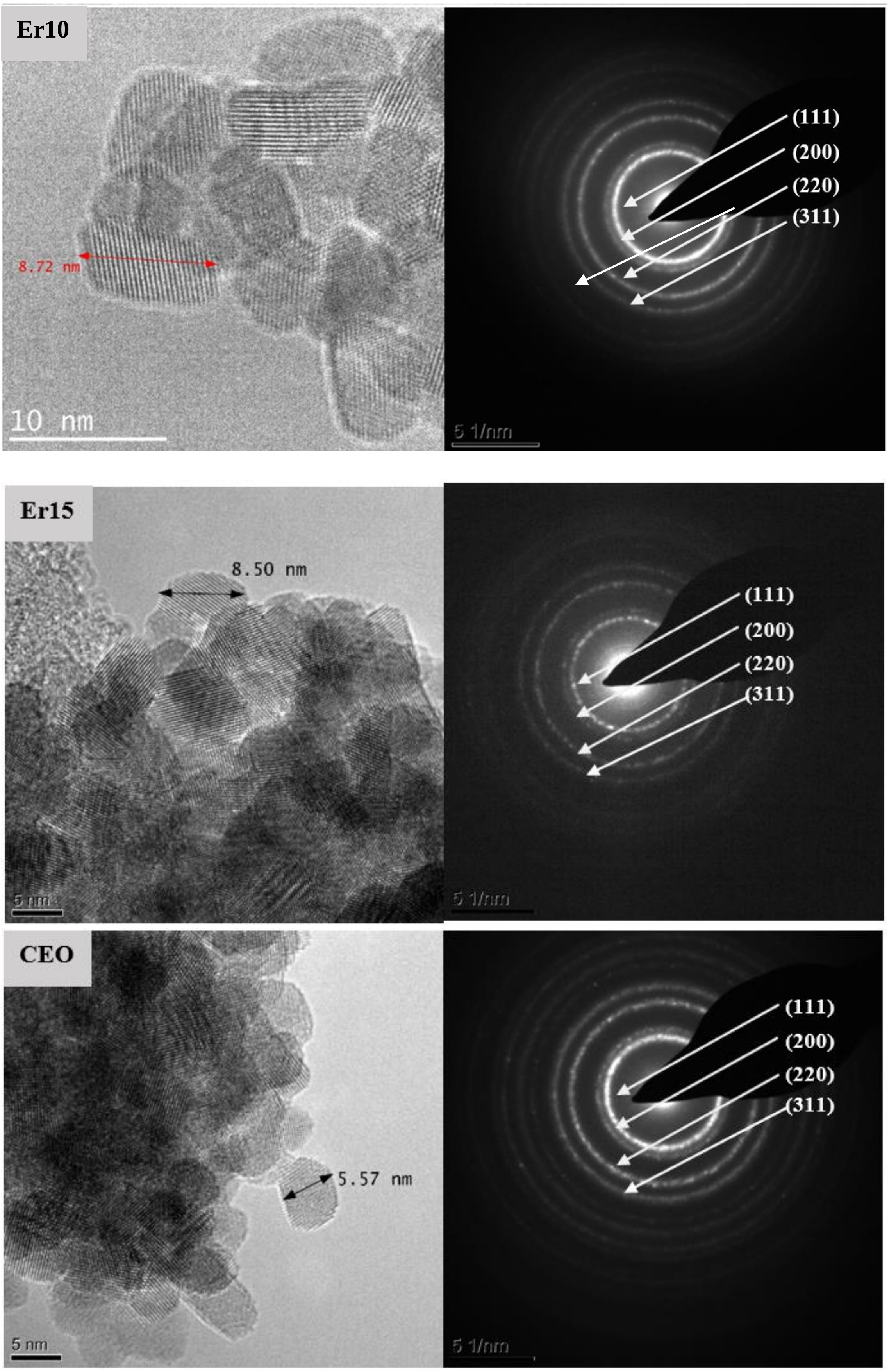

Figure 4.58. TEM and SAED images of of $Ce_{0.8}Er_xGd_{0.2-x}O_{1.9}$ ($0 \leq x \leq 0.2$) nanoparticles calcined at 500°C for 2 h, respectively.

Figure 4.59 illustrates that the lattice parameter (determined by Rietveld refinement) decreased from 5.43 Å (CGO) to 5.404 Å (CEO). The lattice parameter of 5.404 Å for CEO is very similar to the 5.4021 Å obtained by Stojmenović and co-workers (192) for CEO synthesised using self-propagating reaction. The lattice parameter showed linear dependence against the erbium content, which adhered to Vegard's Law (154). This is because the ionic radius of Er^{3+} (CN 6 = 0.89 Å) is smaller than the ionic radius of Gd^{3+} (CN 6 = 0.938Å) (63). Thus, it was expected that the lattice undergoes minimal contraction with the partial and full replacement of erbium ions (180). Another evidence of lattice contraction is the right shift from (111) peaks to higher diffraction angle (**Figure 4.60**) and smaller interplanar spacing (**Table 4.20**).

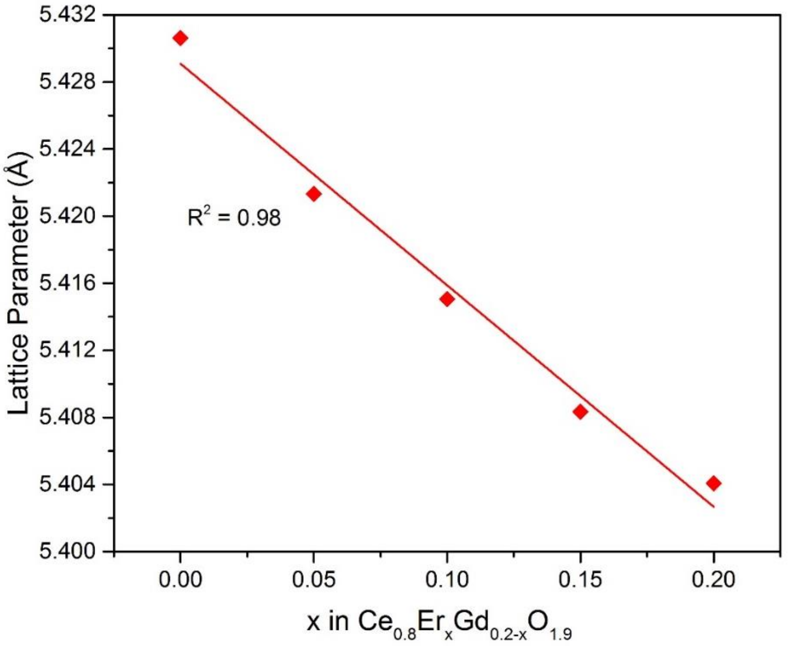

Figure 4.59. Dependence of lattice parameter on the composition of $Ce_{0.8}Er_xGd_{0.2-x}O_{1.9}$ ($0 \leqslant x \leqslant 0.2$).

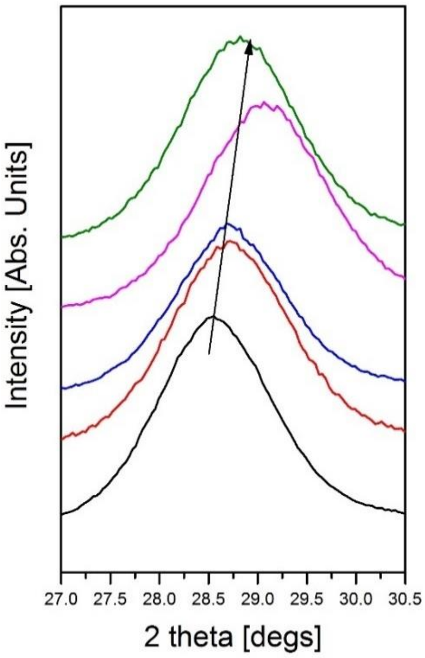

Figure 4.60. XRD patterns at (111) peak: Black: CGO, red: Er5, blue: Er10, pink: Er15, and green: CEO.

Selected area electron diffraction (SAED) patterns with bright circular spots corresponding to (111), (200), (220) and (311) planes confirm the crystalline planes of fluorite structure (**Figure 4.58**). No other rings patterns were corresponding to secondary or hybrid phase, which indicated that the materials formed a complete solid solution. **Table 4.20** summarises the comparable values of d spacing obtained from XRD and SAED ring pattern. The interplanar spacing shows a decreasing trend with increasing erbium ions content related to the decreased cation size.

Table 4.20. Comparison of d-spacing from XRD Rietveld refinement and SAED TEM ring patterns of $Ce_{0.8}Er_xGd_{0.2-x}O_{1.9}$ ($0 \leqslant x \leqslant 0.2$) nanoparticles.

h	k	l	XRD d/(Å)				TEM d/(Å)			
			Er5	Er10	Er15	CEO	Er5	Er10	Er15	CEO
1	1	1	3.104	3.104	3.075	3.095	3.011	3.131	3.029	2.998
2	0	0	2.689	2.695	2.669	2.689	2.664	2.717	2.629	2.675
2	2	0	1.909	1.908	1.894	1.884	1.871	1.927	1.824	1.844
3	1	1	1.629	1.628	1.618	1.624	1.571	1.643	1.563	1.561

The EDS spectrum of Er15 from TEM is shown in **Figure 4.61**. Like two previous co-doped materials (Section 4.2.1 and 4.3.1), carbon and cooper elements from TEM grids were identified in EDS spectrum. Excellent comparable values of mole fraction and nominal mole fraction are reported in **Table 4.21**.

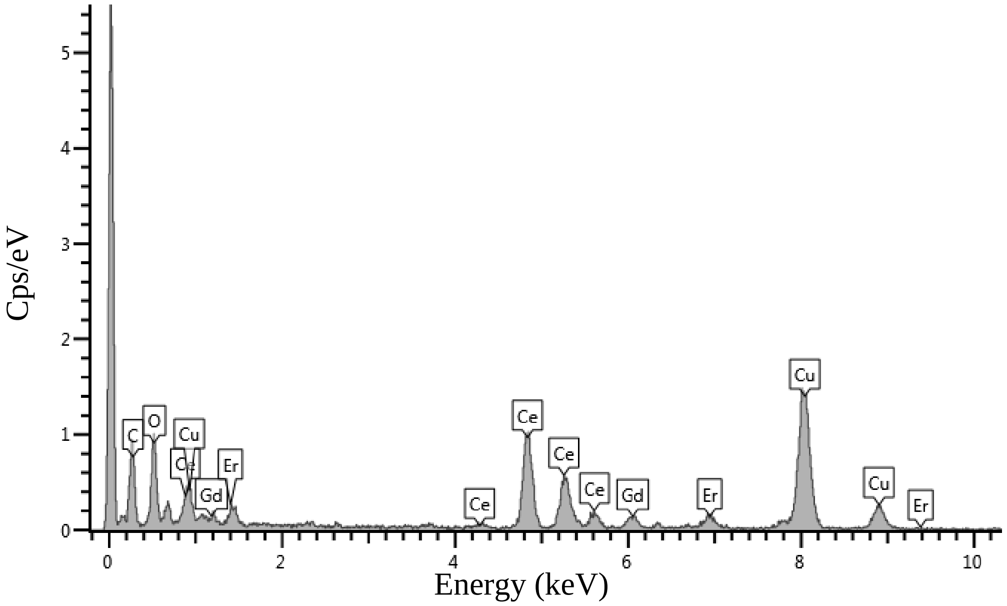

Figure 4.61. TEM–EDS spectrum illustrates the composition of Er15 nanoparticles.

Table 4.21. Weight precentages and calcutaed mole fractions obtained from TEM – EDS analysis of $Ce_{0.8}Er_xGd_{0.2-x}O_{1.9}$ $(0 \leqslant x \leqslant 0.2)$ nanoparticles.

Samples	Elements	Wt (%)	Mole	Mole %	Nominal
Er5	Ce	24.62	0.1757	0.806	80
	Er	1.57	0.0095	0.044	5
	Gd	5.16	0.0328	0.151	15
Er10	Ce	21.31	0.1521	0.822	80
	Er	2.15	0.0130	0.071	10
	Gd	3.12	0.0198	0.107	10
Er15	Ce	40.6	0.2897	0.803	80
	Er	8.73	0.0522	0.145	15
	Gd	3.07	0.0189	0.052	5
CEO	Ce	50.24	0.3586	0.801	80
	Er	14.96	0.0894	0.199	20

The Raman spectrum of $Ce_{0.8}Er_xGd_{0.2-x}O_{1.9}$ ($0 \leqslant x \leqslant 0.2$) (**Figure 4.62**) exhibits a sharp band of ceria at 465 cm^{-1} (193), which can be ascribed to the Ce-O Raman-active vibrational band (F_{2g}) of the fluorite-type structure. This Raman shift is similar to findings by Schmitt et al. (194) for $Ce_{0.8}Er_{0.2}O_{1.9}$ prepared by solid-state synthesis. The partial substitution with erbium makes the frequencies shifted to the higher energies because the ionic radii or erbium is smaller. Weak broad peaks at ~558 cm^{-1} and ~611 cm^{-1} were observed in the spectrum results. The first peak can be attributed to oxygen vacancies due to the interaction between the oxygen vacancy and the six next-nearest-neighbouring O atoms (195). Furthermore, the spectrum at ~611 cm^{-1} is attributed to defect spaces with Oh symmetry forming ReO_8- type complex and not containing oxygen vacancies (196).

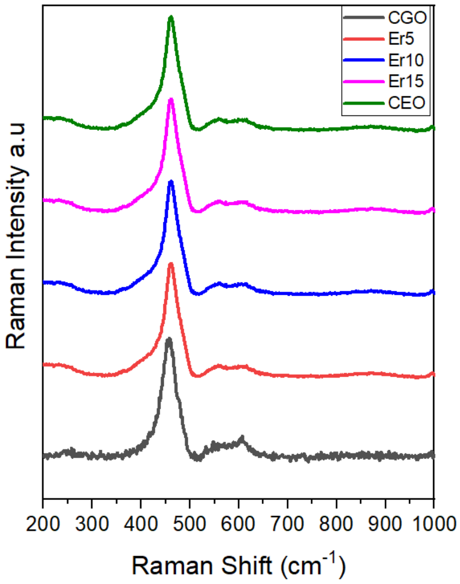

Figure 4.62. Raman spectra of $Ce_{0.8}Er_xGd_{0.2-x}O_{1.9}$ ($0 \leq x \leq 0.2$) nanoparticles after calcination at 500°C for 2h.

4.4.2 Analysis of coefficient thermal expansion (CTE)

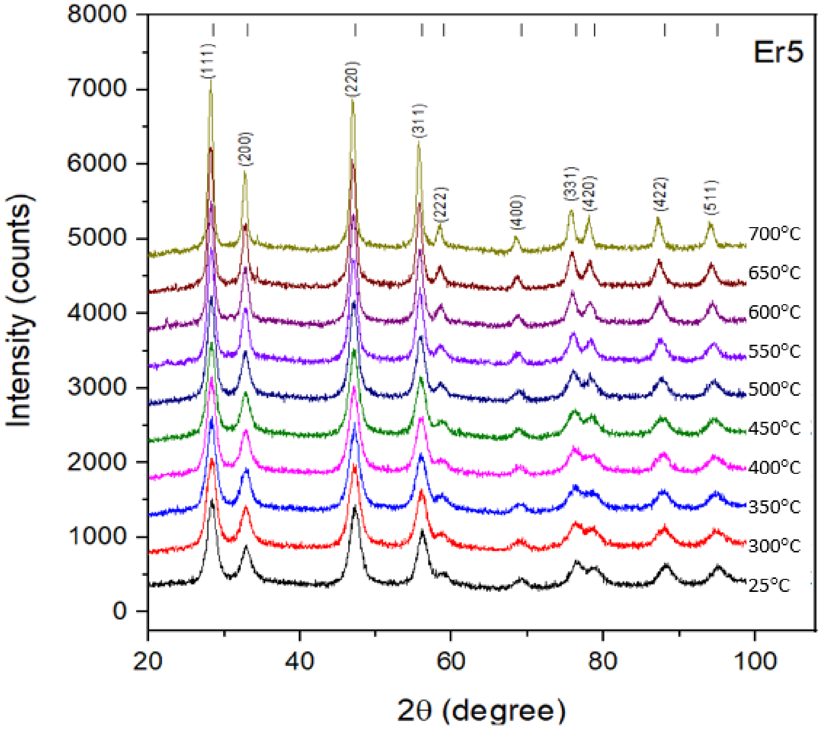

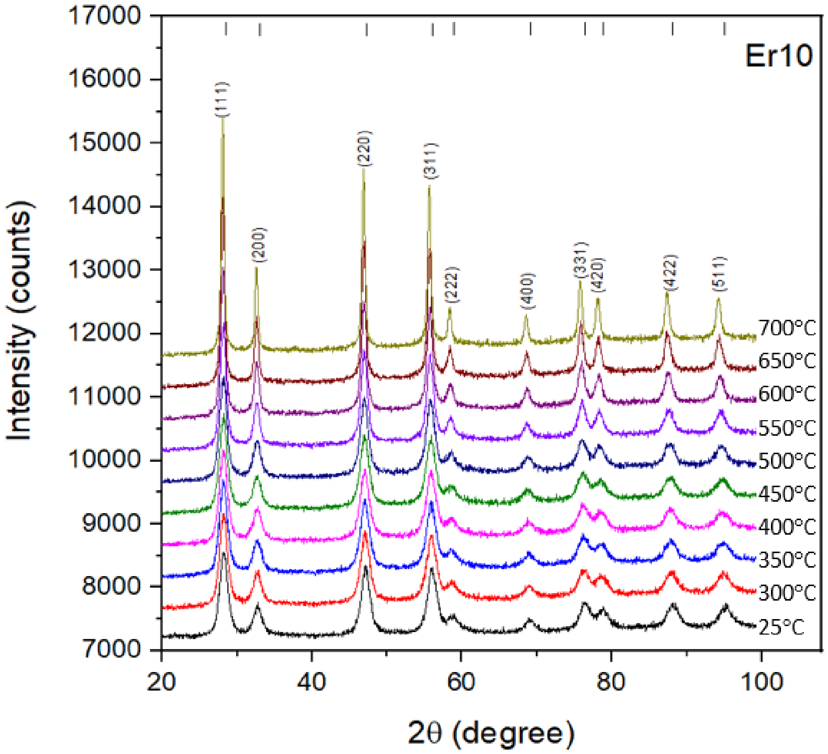

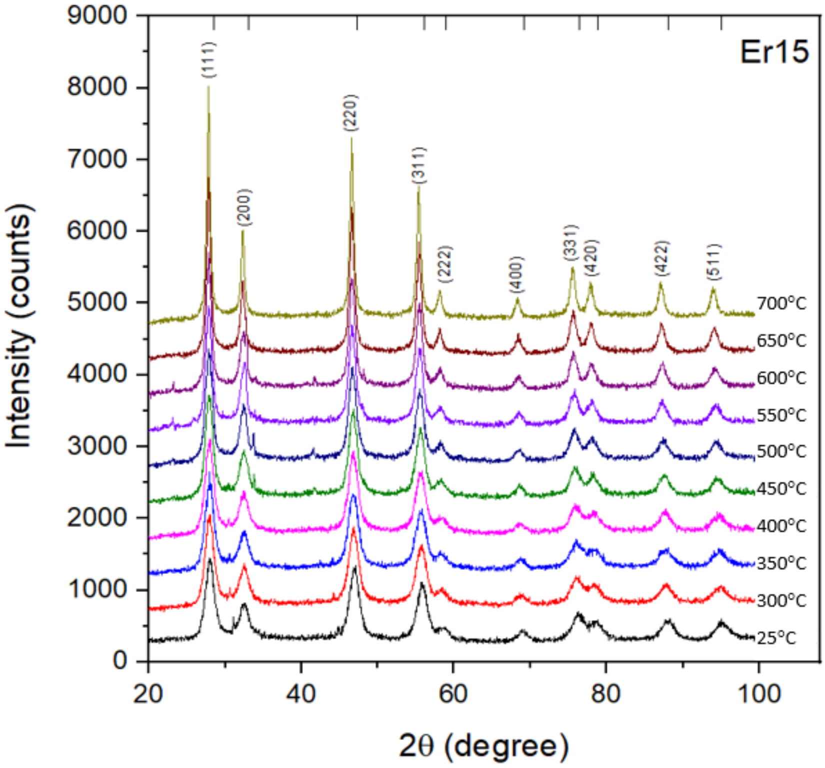

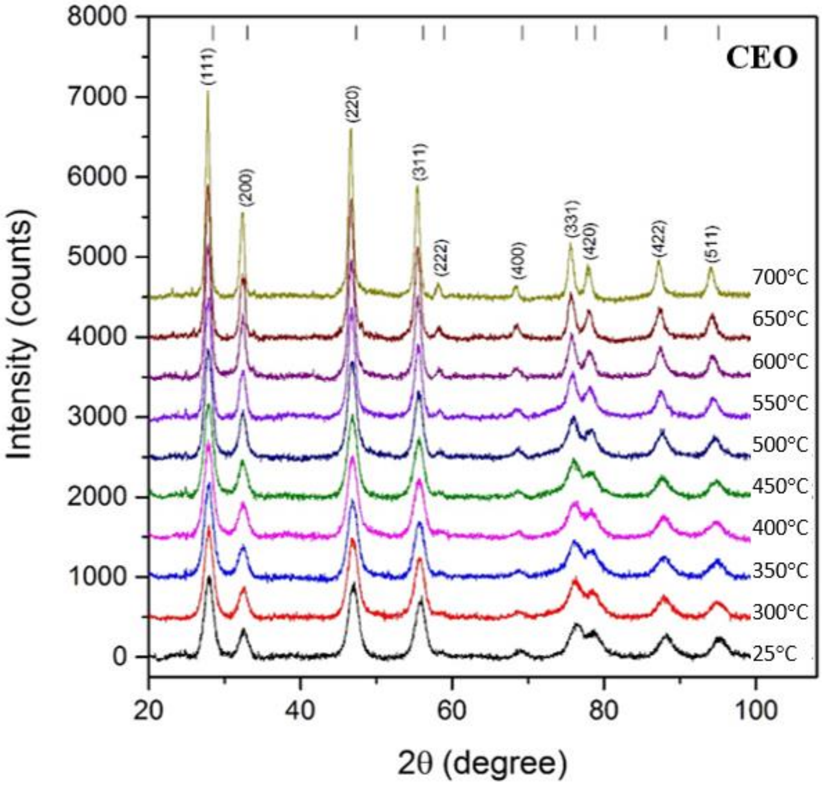

Figure 4.63. High-Temperature XRD of $Ce_{0.8}Er_{x}Gd_{0.2-x}O_{1.9}$ ($0.05 \leq x \leq 0.2$) samples from room temperature to 700°C.

Figure 4.63 displays high-temperature XRD patterns of $Ce_{0.8}Er_xGd_{0.2-x}O_{1.9}$ ($0.05 \leqslant x \leqslant 0.2$) samples from room temperature until 700°C in stable fluorite structure. No hybrid or second phase was detected at the temperature range, indicating a cation substitution (Er^{3+} and Gd^{3+}) in the ceria matrix-forming solid solution. The equations 4.24 – 4.27 show a quadratic polynomial model of lattice parameter for $Ce_{0.8}Er_xGd_{0.2-x}O_{1.9}$ ($0.05 \leqslant x \leqslant 0.2$) samples (**Figure 4.64**).

Er5 : $\alpha_T = 5.4061 + 4.213 \times 10^{-5}\ T + 1.812 \times 10^{-8}\ T^2$ (4.24)

Er10 : $\alpha_T = 5.408 - 1.493 \times 10^{-6}\ T + 5.058 \times 10^{-8}\ T^2$ (4.25)

Er15 : $\alpha_T = 5.393 + 3.262 \times 10^{-5}\ T + 3.001 \times 10^{-8}\ T^2$ (4.26)

CEO : $\alpha_T = 5.387 + 3.219 \times 10^{-5}\ T + 3.117 \times 10^{-8}\ T^2$ (4.27)

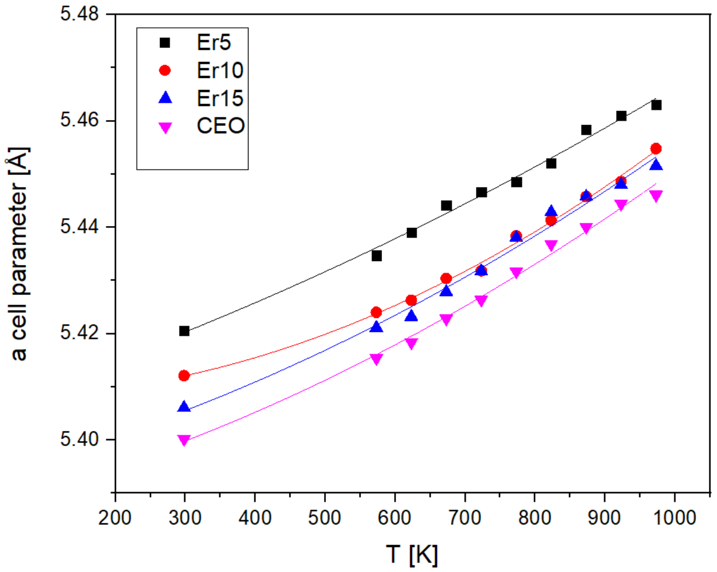

Figure 4.64. Lattice parameter of $Ce_{0.8}Er_xGd_{0.2-x}O_{1.9}$ ($0.05 \leqslant x \leqslant 0.2$) as a function of temperature.

The calculated % LTE was fitted as a function of temperature using a quadratic polynomial (**Figure 4.65**) regression analysis as follows:

Er5 : % LTE = $-0.622 + 1.7 \times 10^{-3}\ T - 2.529 \times 10^{-7}\ T^2$ (4.28)

Er10 : % LTE = $-0.106 + 5.323 \times 10^{-5}\ T + 8.832 \times 10^{-7}\ T^2$ (4.29)

Er15 : $\% \text{ LTE} = -0.993 + 0.00256\, T - 6.886 \times 10^{-7}\, T^2$ (5.30)

CEO : $\% \text{ LTE} = -0.833 + 0.00215\, T - 4.079 \times 10^{-7}\, T^2$ (5.31)

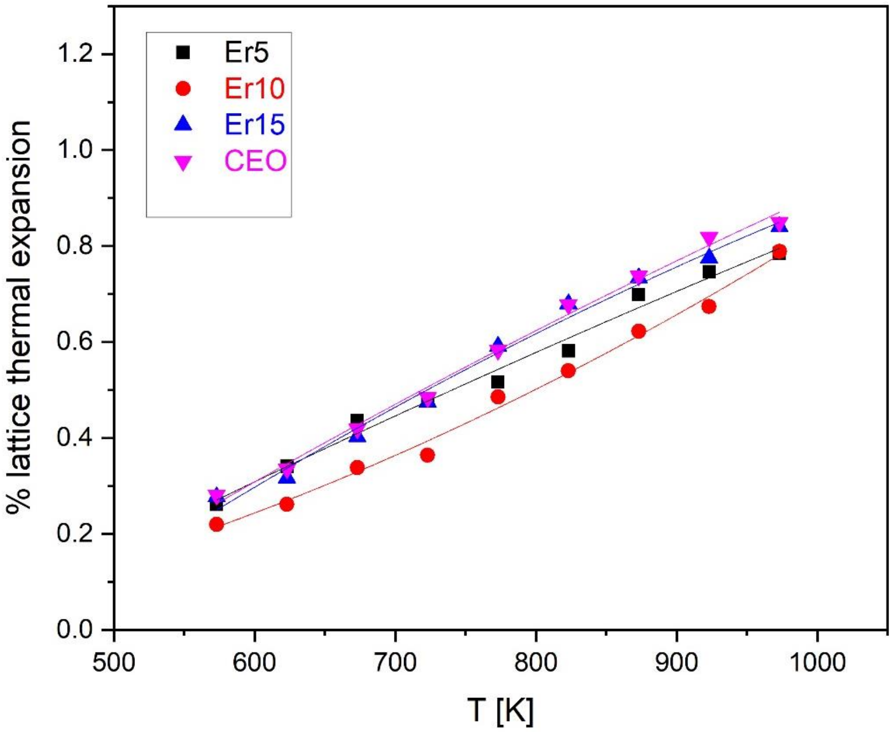

Figure 4.65. Percentage of lattice thermal expansion of $Ce_{0.8}Er_xGd_{0.2-x}O_{1.9}$ ($0.05 \leqslant x \leqslant 0.2$) as a function of temperature.

Table 4.22 summarises the CTE values of $Ce_{0.8}Er_xGd_{0.2-x}O_{1.9}$ ($0.05 \leqslant x \leqslant 0.2$) system. Compared to previous systems, singly doped erbium ions in the ceria-based electrolytes gave lower CTE due to Er_2O_3 having higher a melting point than Dy_2O_3 and Ho_2O_3. A similar trend was reported by Mandal and co-workers who observed that CTE for CHO (RT-1273K 11.33 x 10^{-6} K^{-1}) was higher than CEO (RT-1273K 10.96 x 10^{-6} K^{-1}) (197). However, partial substitution of erbium ions with the gadolinium in ceria matrix showed an increasing trend because of decreasing lattice parameter (161 – 165). The Er5 and Er10 showed lower CTE than CGO due to different temperature observation of CGO from literature.

Table 4.22. CTE of cerium erbium gadolinium oxide ($Ce_{0.8}Er_xGd_{0.2-x}O_{1.9}$)

Sample code	**CTE (10^{-6} K^{-1}) RT–973K**
CGO (166)	12.21
Er5	11.628
Er10	11.689
Er15	12.459
CEO	12.579

4.4.3 Microstructure and density analysis

The densification curve and SEM images of $Ce_{0.8}Er_xGd_{0.2-x}O_{1.9}$ ($0 \leq x \leq 0.2$) ceramics are shown in **Figure 4.66 and 4.67**. The typical EDS elemental mapping of oxygen(O), cerium (Ce), gadolinium (Gd), and erbium (Er) from Er15 dense pellet is shown in **Figure 4.68**. In **Figure 4.66**, relative density of dense pellets is plotted against erbium concentration. The doubly doped ceria-based electrolytes enhanced the density in the ceramic system until the optimum density was achieved at 10% mol doped of Er and Gd. A further increase in erbium dopant concentration leads to a decrease in the ceramic density.

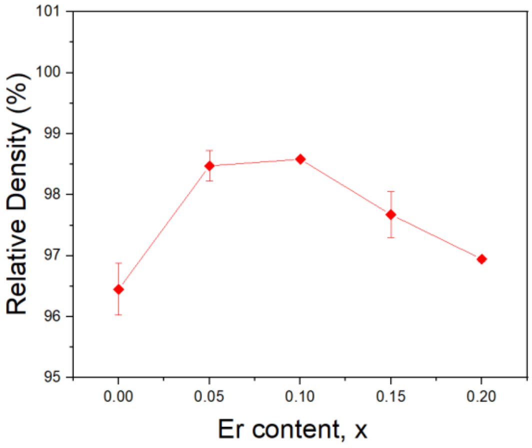

Figure 4.66. Densification curve of $Ce_{0.8}Er_xGd_{0.2-x}O_{1.9}$ ($0 \leq x \leq 0.2$) ceramics sintered at 1500°C.

The SEM microstructure images in **Figure 4.67** show excellent agreement with the relative density curve. Furthermore, no open pore or crack was detected in the microstructural images of $Ce_{0.8}Er_xGd_{0.2-x}O_{1.9}$ ($0 \leqslant x \leqslant 0.2$). The small grains fraction around large grains observed at Er5 and Er10 ceramics indicated that grain growth had occurred through Ostwald ripening mechanism (192).

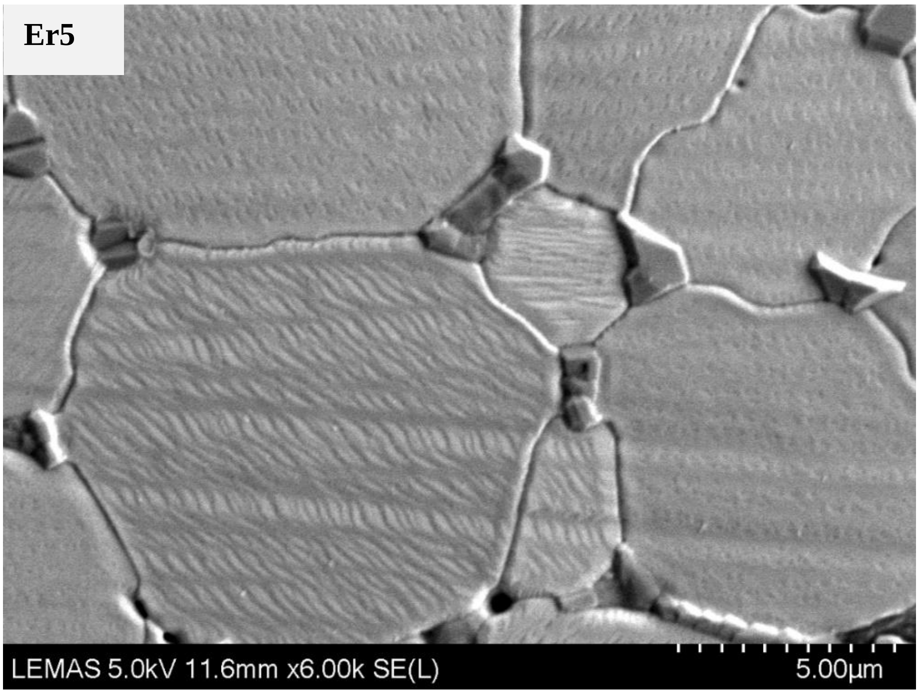

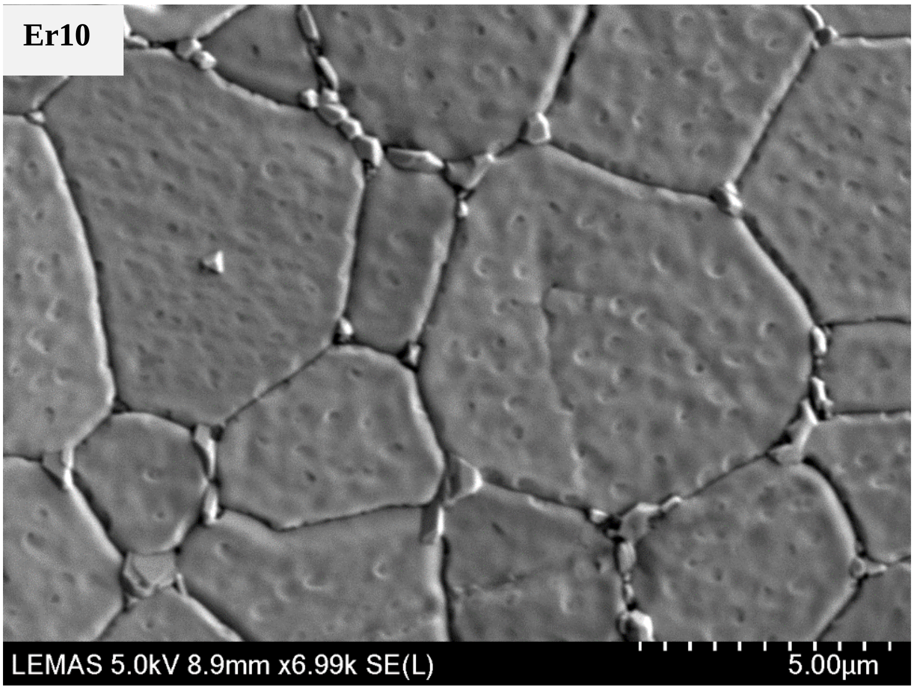

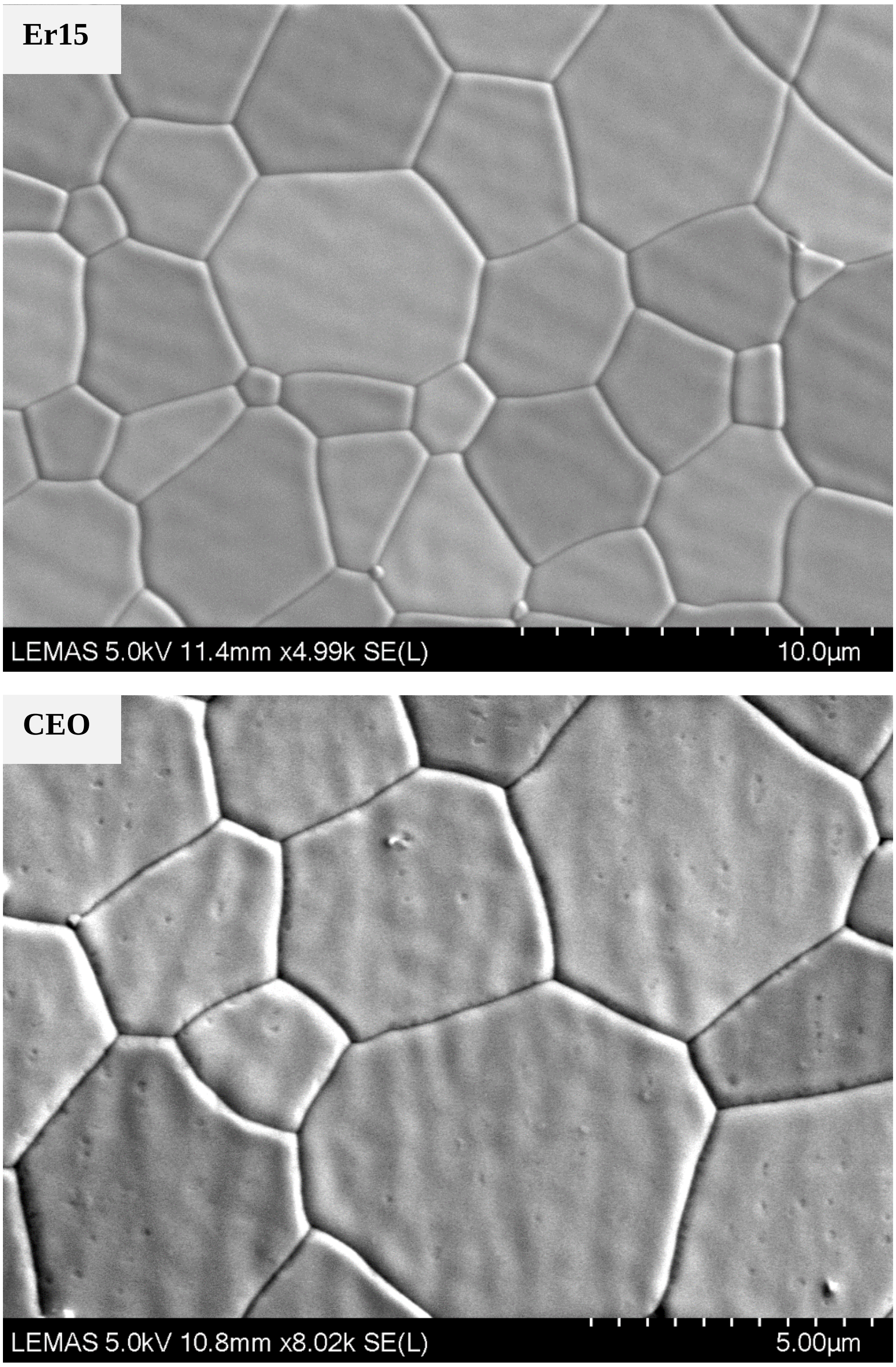

Figure 4.67. SEM micrographs of $Ce_{0.8}Er_xGd_{0.2-x}O_{1.9}$ ($0.05 \leq x \leq 0.2$) ceramics sintered at 1500°C for 2 h.

Figure 4.68 presents the elemental mapping analysis of Er15 sintered pellet. The homogeneous distribution of cerium, erbium, gadolinium and oxygen were observed across the microstructure grains which formed a solid solution series. **Table 4.23**

summarises the comparison of mole fraction and nominal mole fraction of $Ce_{0.8}Er_xGd_{0.2-x}O_{1.9}$ ($0.05 \leqslant x \leqslant 0.2$) system, which are in harmony with the TEM-EDS results.

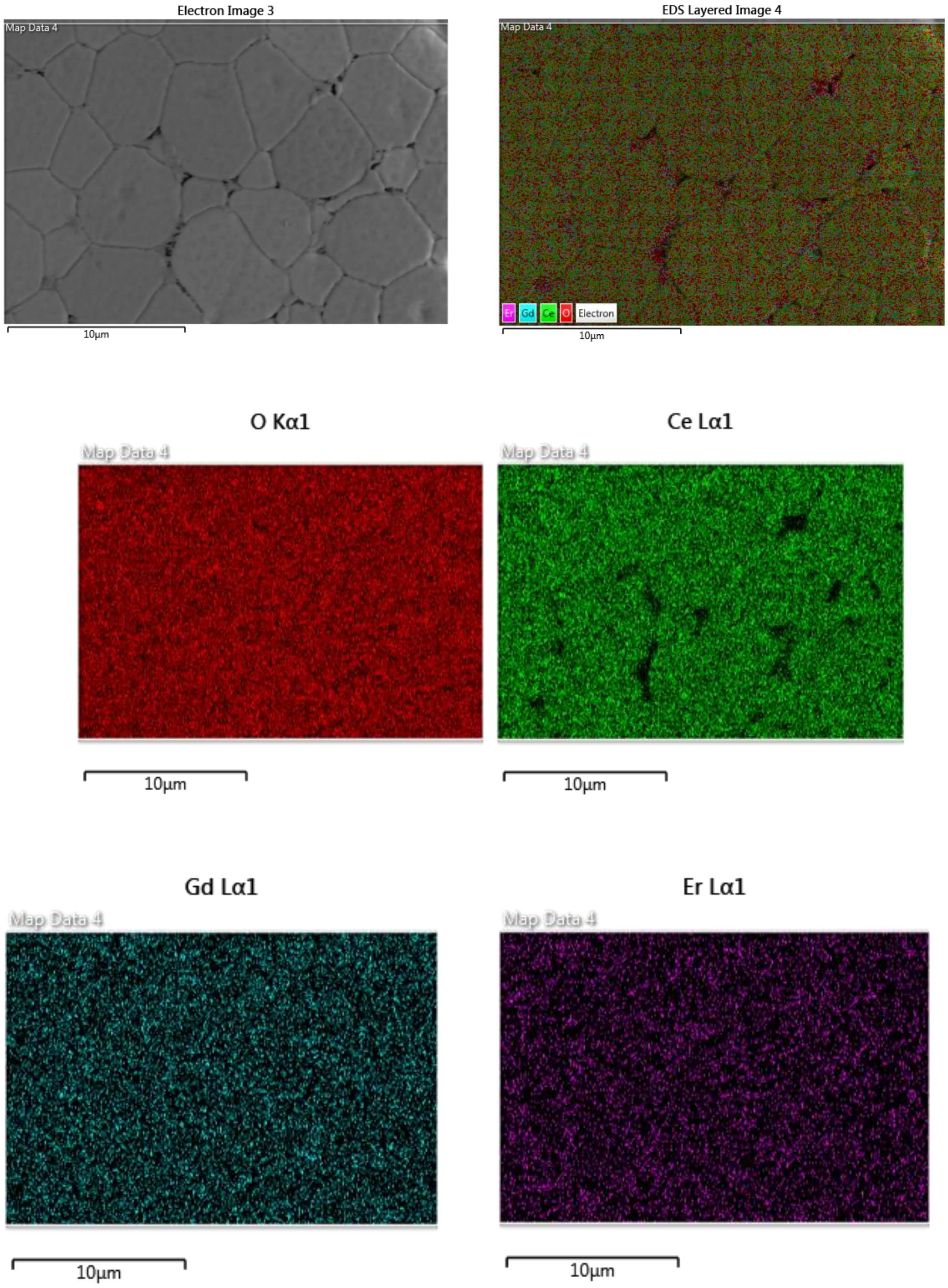

Figure 4.68. SEM image of the microstructure and a layered elemental map followed by the EDS elemental map of Er15 sintered pellet consisting of oxygen in red, cerium in green, gadolinium in blue and holmium in purple colour.

Table 4.23. Weight precentages and calcutaed mole fractions obtained from EDS analysis of $Ce_{0.8}Er_xGd_{0.2-x}O_{1.9}$ ($0.05 \leqslant x \leqslant 0.2$) sintered pellets

Composition	**Element**	**Weight % from EDS**	**Atomic weight**	**Mole**	**Mole %**	**Nominal**
CGO	Ce	59.6	140.116	0.425	0.802	0.80
	Gd	16.5	157.2	0.105	0.198	0.20
	Total mole of Ce + Gd			0.530		
	O	12.4	15.99	1.119		
Er5	Ce	63.16	140.116	0.451	0.798	0.80
	Er	2.77	164.9303	0.017	0.046	0.05
	Gd	12.11	157.2	0.077	0.156	0.15
	Total mole of Ce + Er + Gd			0.545	1	
	O	21.96	15.99	1.373		
Er10	Ce	64.49	140.116	0.460	0.819	0.80
	Er	7.04	164.9303	0.043	0.082	0.10
	Gd	9.14	157.2	0.058	0.099	0.10
	Total mole of Ce + Er + Gd			0.561	1	
	O	19.33	15.99	1.209		
Er15	Ce	31.4	140.116	0.448	0.804	0.80
	Er	6.5	164.9303	0.079	0.141	0.15
	Gd	2.4	157.2	0.031	0.055	0.05
	Total mole of Ce + Er + Gd			0.278	1	
	O	19.4	15.99	1.213		
CEO	Ce	63.3	140.116	0.452	0.802	0.80
	Er	18.4	164.9303	0.111	0.198	0.20
	Total mole of Ce + Er			0.563	1	
	O	6.3	15.99	0.394		

4.4.4 Conductivity analysis

The measured impedance spectra for $Ce_{0.8}Er_xGd_{0.2-x}O_{1.9}$ ($0 \leq x \leq 0.2$) dense pellets prepared at 300 and 500°C are shown in **Figure 4.69 - 4.70**, respectively.

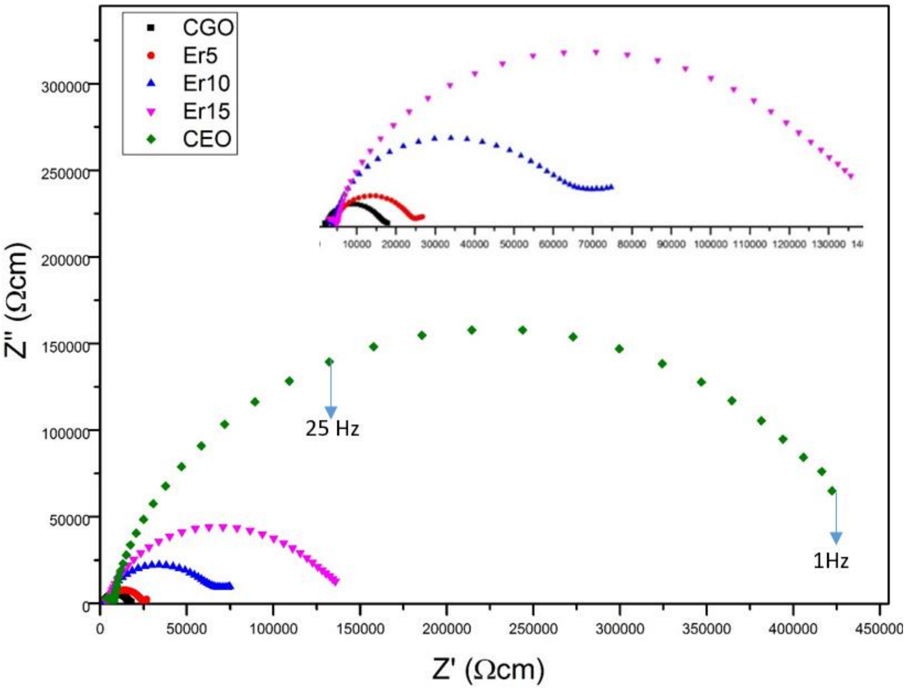

Figure 4.69. The complex plane impedance plots of dense $Ce_{0.8}Er_xGd_{0.2-x}O_{1.9}$ ($0 \leq x \leq 0.2$) ceramic measured at 300°C in air. The inset plot is the low range of Z’ (Ωcm).

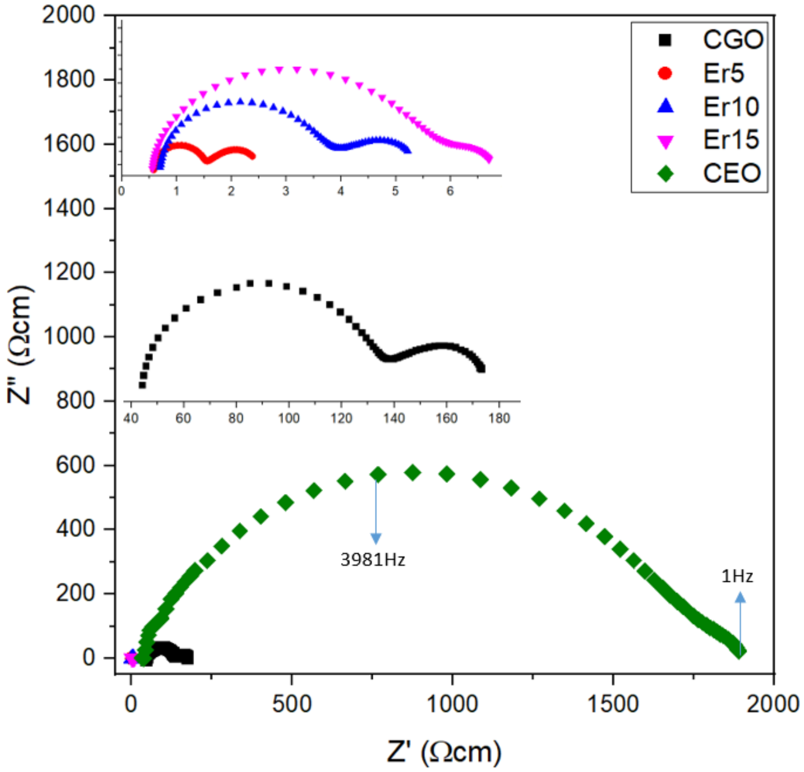

Figure 4.70. The complex plane impedance plots of dense $Ce_{0.8}Er_xGd_{0.2-x}O_{1.9}$ ($0 \leq x \leq 0.2$) ceramic measured at 500°C in air. The inset plot is the low range of Z’ (Ωcm).

At 300°C, two arcs were observed from the spectra for all compositions with fitting for Er10 shown in **Figure 4.71 (a)**. Small arc at high frequency was associated with grain interior (R1//CPE1), bigger semicircle was assigned to grain-boundary (R2//CPE2) and small electrode impedance (W). At 500°C (**Figure 4.71 (b)**), the intercept on Z’ axis (R1) was used to calculate the grain interior. At the same time, the first arc was related to grain-boundary (R2//CPE2) and the second semicircle was associated with an electrode (R3//CPE3).

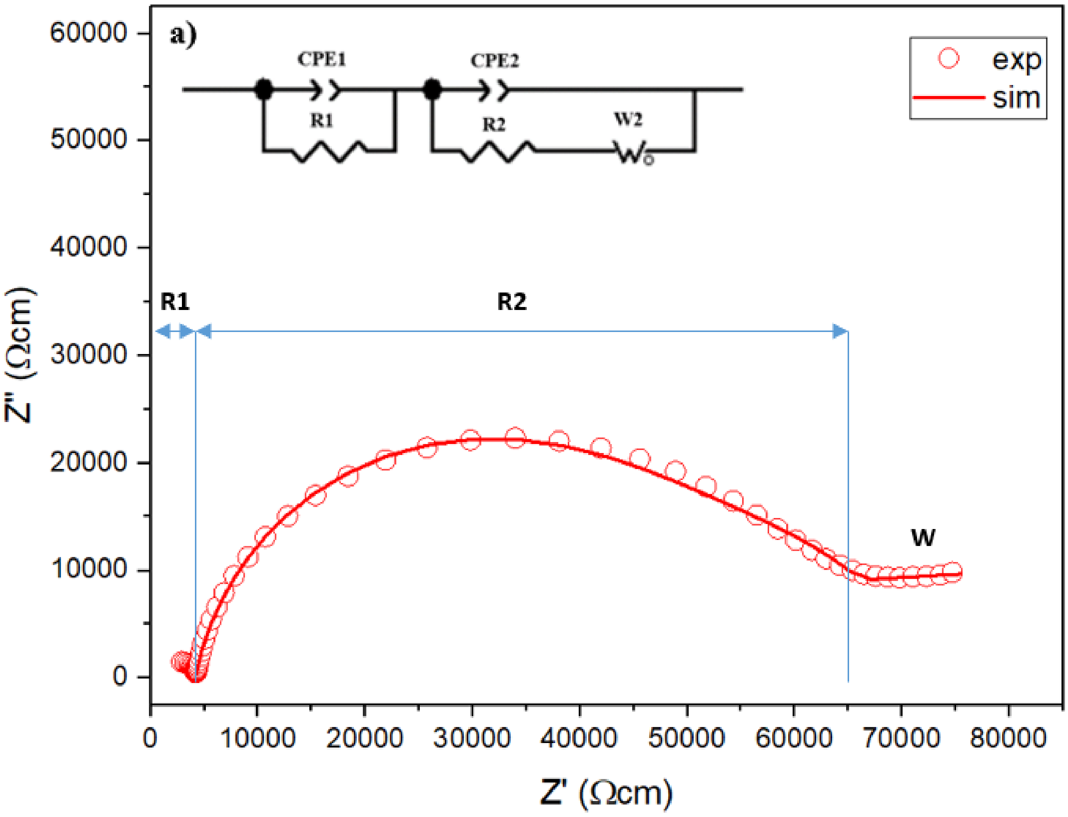

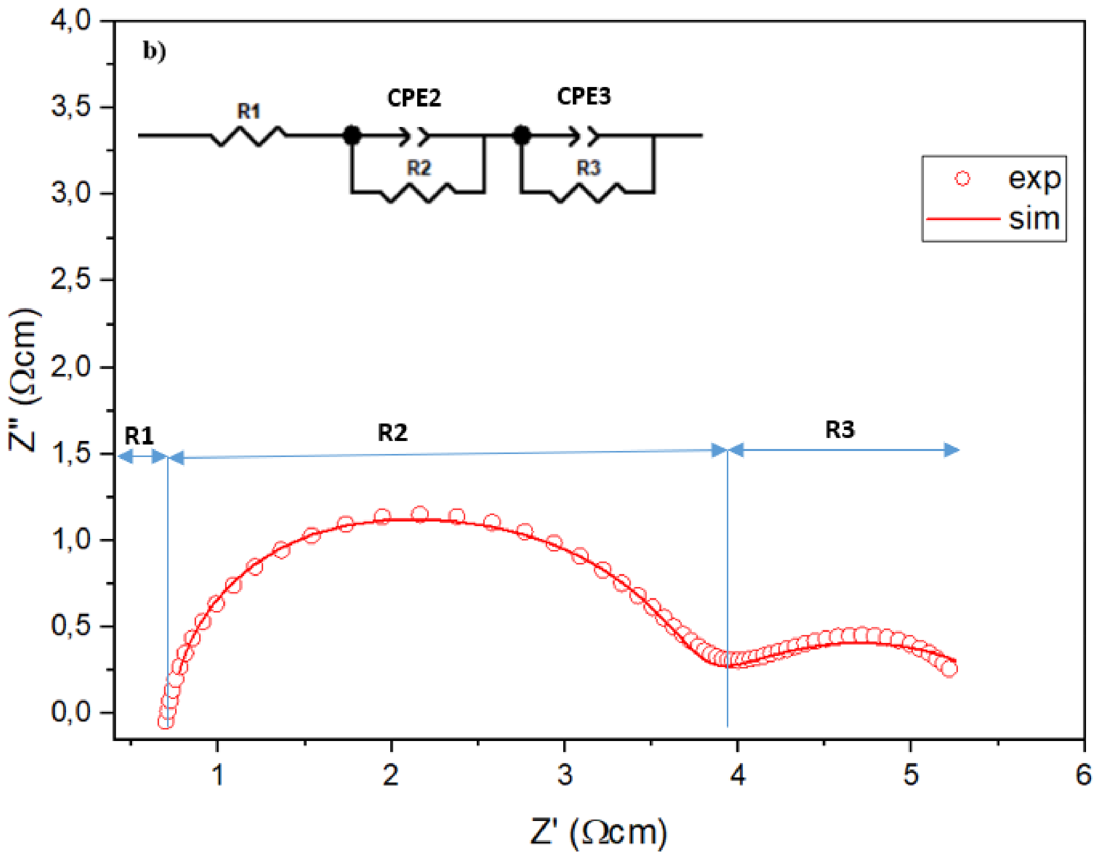

Figure 4.71. Nyquist plots and fitting for Er10 dense pellet at a) 300°C and b) 500°C. Inserted image is equivalent circuit model used for fitting of the impedance data.

The Arrhenius plots of bulk, grain boundary and total conductivities for $Ce_{0.8}Er_xGd_{0.2-x}O_{1.9}$ ($0 \leqslant x \leqslant 0.2$) ceramics in the temperature range of 300°C and 500°C are shown in **Figure 4.72**. Similar to previous co-doping materials, the clear slope break with an unusual increase in the conductivities were observed on the co-doped erbium with CGO. However, the critical temperature between different concentration in co-doped erbium is not the same. The critical temperature was observed at 420°C for Er5, whereas it was 470°C for Er10 and Er15. The increase in the critical temperature is depending on the dopant content. A similar phenomenon was reported by Zhang and co-workers (49), who found that the critical temperature was increased from 380°C to 440°C on Gd-doped system with dopant content from x = 0.05 to x = 0.25.

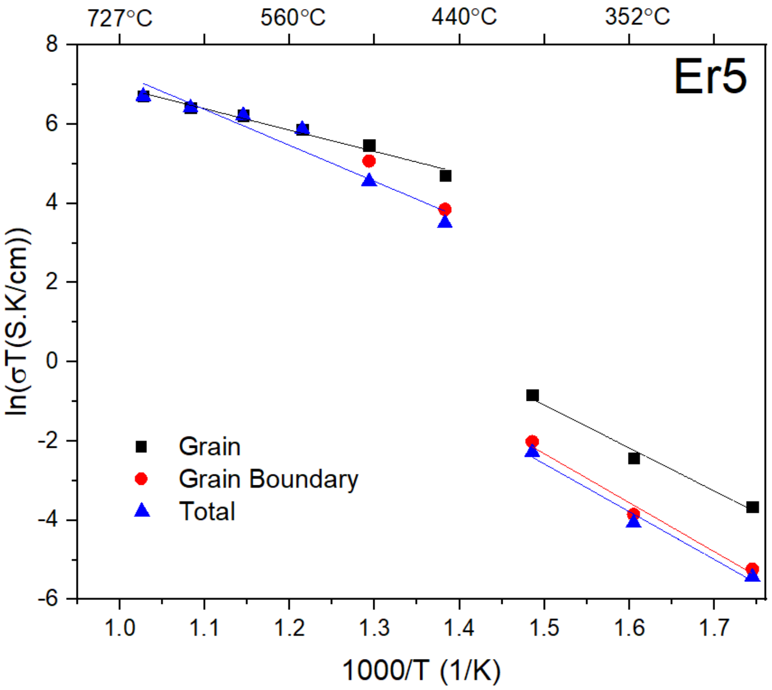
727°C
560°C
440°C
352°C
Er5
8
6
4
2
0
-2
-4
-6
ln(σT(S.K/cm))
1.0
1.1
1.2
1.3
1.4
1.5
1.6
1.7
1000/T (1/K)
Grain
Grain Boundary
Total

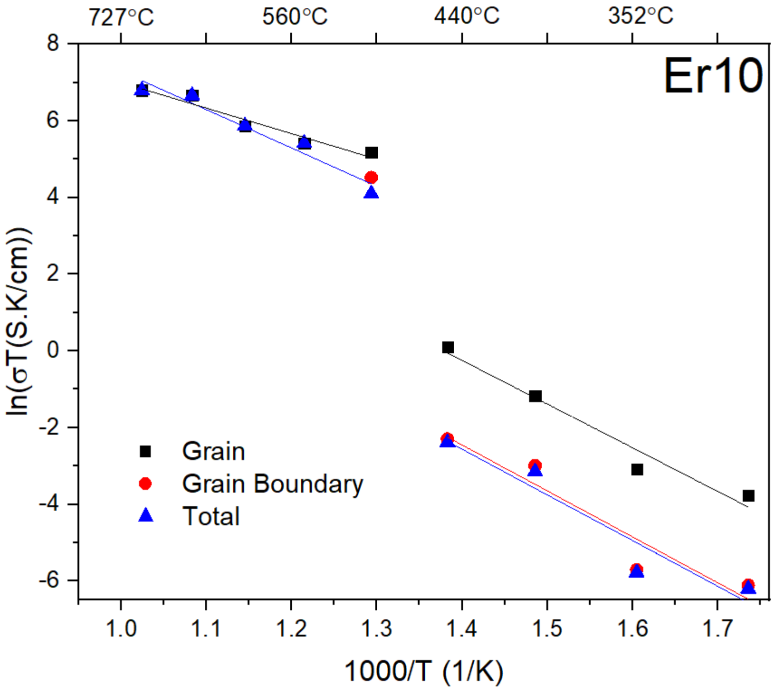
727°C
560°C
440°C
352°C
Er10
8
6
4
2
0
-2
-4
-6
ln(σT(S.K/cm))
1.0
1.1
1.2
1.3
1.4
1.5
1.6
1.7
1000/T (1/K)
Grain
Grain Boundary
Total

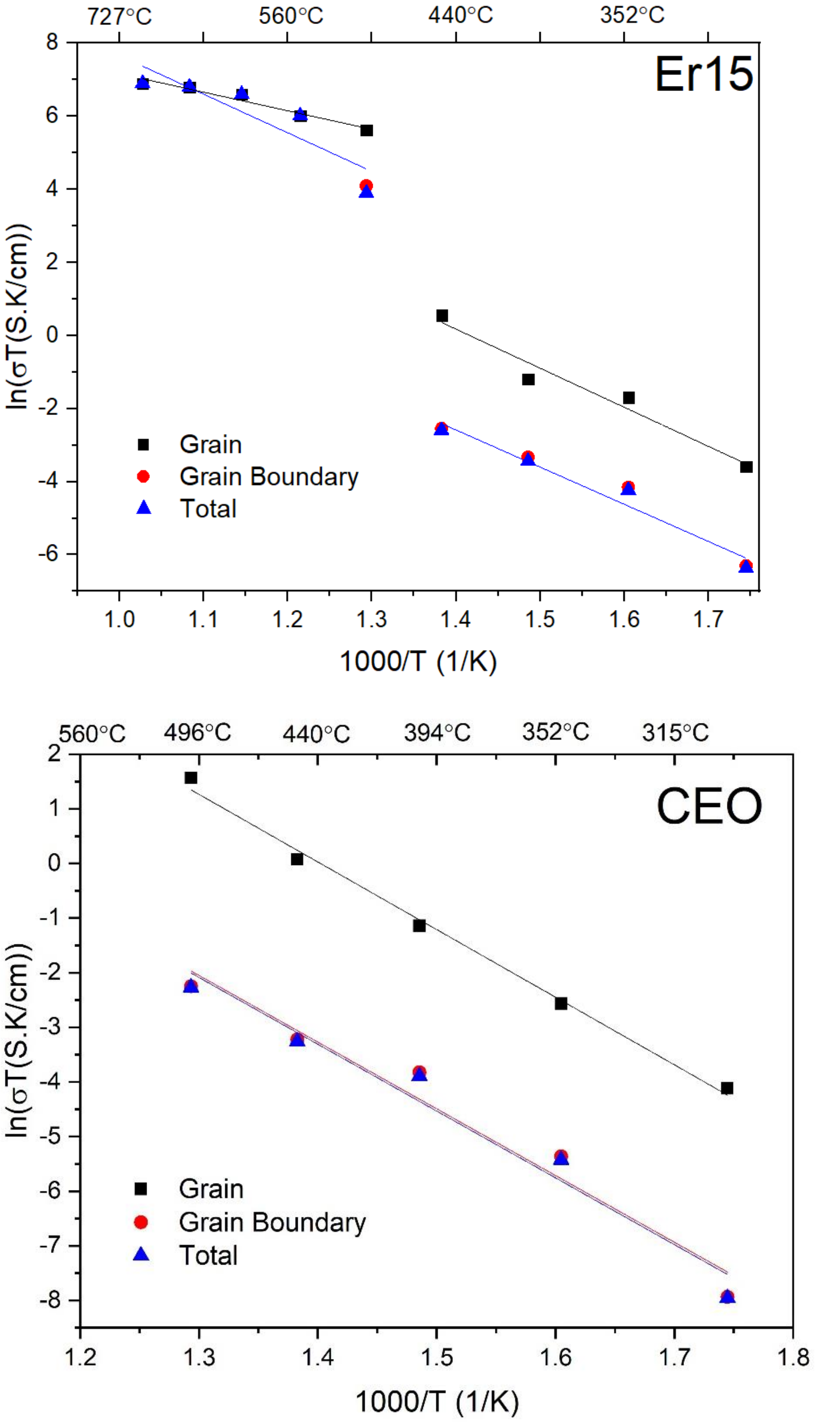

Figure 4.72. The Arrhenius plots of $Ce_{0.8}Er_xGd_{0.2-x}O_{1.9}$ ceramics for ($0.05 \leqslant x \leqslant 0.2$).

At low temperatures (300 – 400°C), CGO was observed as the most conductive material with the highest total and ionic conductivities. However, as the temperature increases, the co-doped materials have the highest total conductivity. **Table 4.24** shows the comparison between the conductivities and activation energy of $Ce_{0.8}Er_xGd_{0.2-x}O_{1.9}$ ($0 \leqslant x \leqslant 0.2$) at

500°C. The creation of oxygen vacancies in terms of Kröger–Vink notation for co-doping erbium gadolinium is:

$$Er_2O_3 + CeO_2 \rightarrow 2Er_{Ce}^{\prime} + 3O_O^x + V_O^{''} \qquad (4.32)$$

$$Gd_2O_3 + CeO_2 \rightarrow 2Gd_{Ce}^{\prime} + 3O_O^x + V_O^{''} \qquad (4.33)$$

Bulk conductivity was highest for Er15 at 500°C and lowest for CGO. However, the total conductivity at similar temperature was highest for Er5 due to the high grain boundary conductivity and was the lowest for CEO because of the lowest grain boundary conductivity. Improving the grain boundary can lead to enhanced total conductivities.

In this study, the enhancement of conductivity by co-doping was especially observed after the critical temperature. Torun and co-workers (172) also reported the improvement of conductivity using doubly doped ceria electrolytes. The total conductivity was increased from 7.37 x 10^{-3} S cm^{-1} for $Ce_{0.83}Er_{0.17}O_2$ at 1123K to 1.15 x 10^{-2} S cm^{-1} for $Ce_{0.8}Er_{0.1}Gd0_{.1}O_2$ at the same temperature. However, the improvement was not as much as in the present study since the total conductivity of 0.078 S cm^{-1} for Er10 at 500°C is much higher than 1.3 x 10^{-4} S cm^{-1} for CEO at the same temperature. The different value of total conductivity for Er10 may be linked to the synthesis method (15).

The ionic conductivity of 1.78 x 10^{-3} S cm^{-1} at 500°C for CEO synthesised by Stojmenović and co-workers (192) with self-propagating reaction is lower than the 6.2 x 10^{-3} S cm^{-1} at the same temperature obtained from this study. However, the total activation energy of 1.36 eV for CEO in this present study is much higher than 1.07 eV observed by Pikalova et al. (181) or 1.15 eV reported by Kuharuangrong (198). This value is comparable to the total activation energy of 1.36 eV for pure CeO_2 (181).

Table 4.24. Bulk (GI), grain boundary (GB) and total conductivities measured at 500°C, with activation energies for bulk and grain boundary of $Ce_{0.8}Er_xGd_{0.2-x}O_{1.9}$ ($0 \leqslant x \leqslant 0.2$) ceramic electrolytes.

Electrolytes	**σ_{GI} (S cm^{-1})**	**σ_{GB} (S cm^{-1})**	**σ_{Total} (S cm^{-1})**	**Ea_{ionic} (eV)**	**Ea_{GB} (eV)**
CGO	0.00351	0.0018	0.0012	0.878	0.993
Er5	0.3063	0.2063	0.1233	0.935	1.065
Er10	0.2278	0.1187	0.078	0.988	1.015
Er15	0.3573	0.0776	0.0637	0.921	0.876
CEO	0.0062	0.0002	0.00013	0.987	1.374

Figure 4.73 shows the total activation energy, migration enthalpy (ΔH_m) and association enthalpy (ΔH_a) of $Ce_{0.8}Er_xGd_{0.2-x}O_{1.9}$ ($0 \leq x \leq 0.2$) ceramic electrolytes. The activation energy for CEO is the highest among the entire systems, and this is linked to the lowest total conductivity due to the lowest value of association enthalpy (49). In contrast, Er15 was observed to have the lowest activation energy among the ceramic electrolytes, which represented a lower energy to activate the conduction process (180).

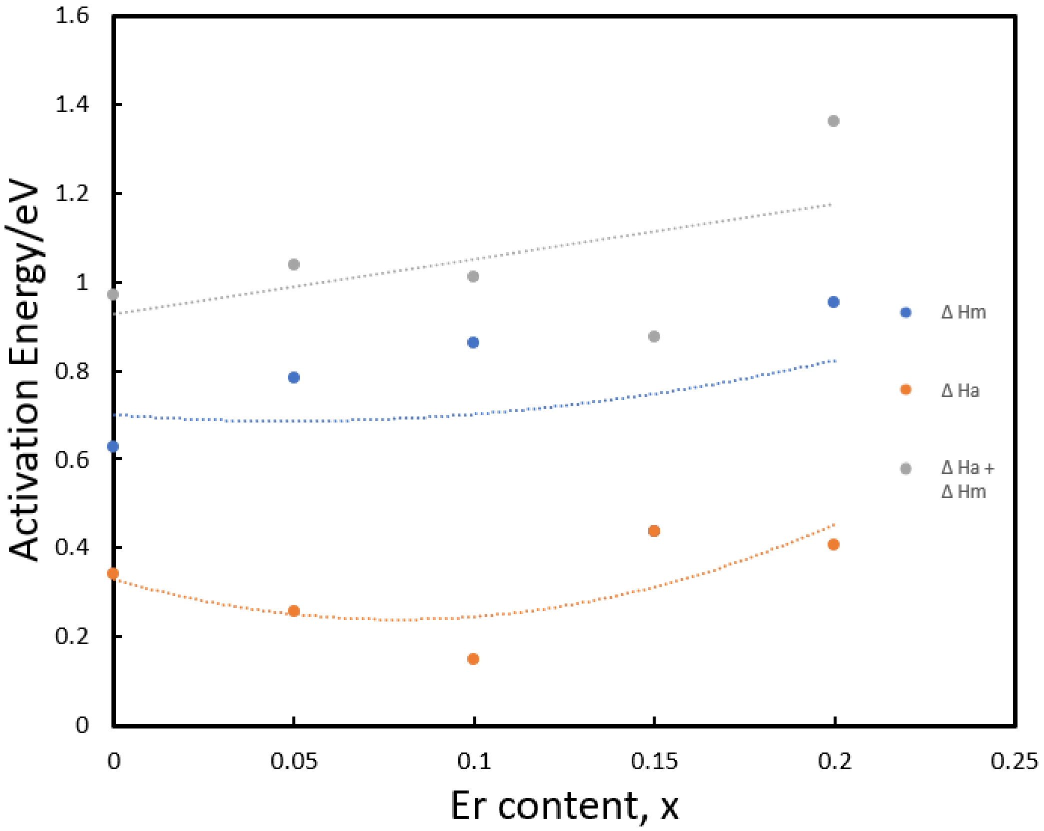

Figure 4.73. Activation energy for total conductivity, below Tc ($\Delta H_m + \Delta H_a$), above Tc (ΔH_m), and ΔH_a of $Ce_{0.8}Er_xGd_{0.2-x}O_{1.9}$ ($0 \leq x \leq 0.2$) ceramic electrolytes.

Chapter 5 Conclusion

The main achievements of this study are: (a) producing nanoparticles using low-temperature processing. An optimum route of facile, low temperature and environmentally friendly sodium alginate (SAL) has been developed to provide a single crystal with high purity of nanoparticles. (b) developing electrolyte materials with appropriate thermal expansion coefficient. CTE of electrolyte materials is an essential property in IT-SOFCs because the matched CTE can avoid microcrack formation between anode and electrolyte or between cathode and electrolyte at the operating temperature. (c) developing material which has higher ionic conductivity as an option for promising IT-SOFCs electrolytes. Co-doped materials showed to have high ionic conductivities above the critical temperature. These values are higher than the ionic conductivity of cerium gadolinium as the most commonly used as the electrolyte in IT-SOFCs.

Firstly, the development of the optimum process to produce nanoparticles is reported in this research. Doped (CGO) and co-doped (Dy10, Ho10, and Er10) ceria-based electrolyte nanoparticles have been successfully obtained using bead and granule methods. TGA/DSC results were used to decide the suitable calcination temperature. High-temperature XRD was used to investigate the phase transformation and it showed an excellent agreement with the decomposition cure obtained from TGA curve. The calcination temperatures were used as an essential factor to get the final crystallite size. Scherrer's equation from XRD was used to calculate the crystallite size. It was found that the nanoparticles calcined at 500°C for 2h had a crystallite size around 10 nm, based on calculation and TEM observations. However, at elevated temperature (700°C for 2h), the calculated and observed crystallite size increased twice bigger than that of samples calcined at 500°C. The higher the calcination temperature, the bigger nanoparticles would be produced. The optimum sintering route was also reported in this study. Sintering at 1500°C for 2h showed fully dense ceramics with higher relative density obtained.

The co-doped cerium rear-earth oxide solid solution series $Ce_{0.8}RE_xGd_{0.2-x}O_{1.9}$ (RE = Dy, Ho, and Er; $0 \leqslant x \leqslant 0.2$) have been successfully synthesised using sodium alginate (SAL) method. Rietveld refinement of the XRD data showed a single-phase fluorite structure in the entire solid solution series. The nanoparticles had lattice parameters from 5.4306 to 5.4041 Å and were high in purity. Structural characterisation confirmed that lattice parameters in the co-doped ceria system depended on the ionic radius and adhered to Vegard's Law. The crystallite size calculated from XRD were in good agreement with those observed from TEM (~10nm). The interplanar spacing values calculated by Rietveld refinement and SAED were comparable. Raman spectroscopy also confirmed the fluorite structure for the entire series and observed the defect structure in the nanoparticles.

Based on thermal expansion coefficient calculation, it was found that $Ce_{0.8}Dy_xGd_{0.2-x}O_{1.9}$ and $Ce_{0.8}Ho_xGd_{0.2-x}O_{1.9}$ solid solution series respectively showed 4.2% and 3.2% maximum difference in CTE compared to CGO. In contrast, $Ce_{0.8}Er_xGd_{0.2-x}O_{1.9}$ series showed similar CTE values with CGO. This indicates that the co-doped materials do not change CTE significantly and thus are appropriate to be an option for next IT-SOFCs electrolytes. A decrease in CTE values with lattice parameter and melting point was also observed.

Co-doping has helped improve the relative density which was confirmed with the microstructure analysis by SEM. The microstructure consisting of nonporous, equiaxed and hexagonal shaped interlocked grains was observed in all compositions. The element mapping from EDS showed that each element was distinguishable and homogeneously distributed within the grain across the entire microstructure, suggesting a complete solid solution formation. EDS analysis of powder and sintered pellets are in an excellent agreement with their respective nominal mole fractions.

AC impedance spectroscopy was used to determine the grain, grain boundary, electrode and total conductivities of sintered pellets. Bulk conductivity was much higher than the grain boundary conductivity for all samples. Co-doped materials led to an anomalous increase in the ionic conductivity above the critical temperature. Ionic conductivity observed almost 100 times higher than the singly doped at 500°C from 0.00351 S cm^{-1} for CGO to 0.3169 S cm^{-1}, 0.2871 S cm^{-1}, 0.3573 S cm^{-1} for Dy10, Ho10 and Er15, respectively. The increase in the critical temperature of solid solution series is dependent on the ionic radius and dopant content of co-dopant materials. Critical temperature (Tc) was observed at ~370°C and ~420°C respectively for $Ce_{0.8}Dy_xGd_{0.2-x}O_{1.9}$ and $Ce_{0.8}Ho_xGd_{0.2-x}O_{1.9}$ solid solution series. However, for $Ce_{0.8}Er_xGd_{0.2-x}O_{1.9}$ system, Tc depends on the dopant concentration. Tc of Er5 was observed at ~420°C, while increasing dopant concentration leads to an increase in Tc.

Finally, this project has fulfilled its aim and objectives. The sodium alginate method successfully produced the homogeneous nanoparticles with highly pure single fluorite structure. Furthermore, the significant enhancement of ionic conductivity in co-doped materials was observed. Thus, these materials can be used as promising IT-SOFCs electrolytes.

Chapter 6 Future Work

The present study has investigated the effect of calcination temperature, and co-doped materials on the ceria-based crystal structure using SAL bead and granule methods. In addition, the high-temperature stability, sintering ability, microstructure and electrical properties of ceria-based solid electrolytes with different compositions have been studied in this study. However, the break in the slope for co-doped material after critical temperature remains unclear. Further investigation needs to be conducted to tackle these problems. Different kinds of characterisation techniques such as X-ray photoelectron spectroscopy (XPS), X-ray Absorption Near Edge Structure (XANES) and Extended X-ray Absorption Fine Structure (EXAFS) can be used to monitor the local structure surrounding cations and anions in co-doped ceria during clustering and declustering. In contrast, high-temperature Raman can be used to detect oxygen vacancies dissociations at operating temperatures. Further work is also needed to investigate co-doping materials with higher ionic radius than the gadolinium ions (CN 6 = 0.938Å), e.g. samarium ions (CN 6 = 0.958Å), in order to see the effect on the ionic conductivity prepared by sodium alginate method.

Interactions of dopants, co-dopants and vacancies with the migrating oxygen vacancies result in a migration barrier. The effect of this on the oxygen ionic conductivity needs to be understood.

Even though the ceramic materials sintered at 1500°C for 2h had a high relative density, two-steps sintering method can be an option to further study the improvement of total conductivity due to its ability to produce small grain materials.

Since co-dopants materials showed an excellent ionic conductivity as promising IT-SOFC electrolytes, a further fabrication method and a qualitative analysis of the economic prospect need to be investigated. However, selecting suitable cathode/anode material with appropriate thermal expansion coefficient to avoid thermal shock resistance between electrolyte and electrode should be determined in advance.

Reference

1. Veldhuis, S.A., *A Wet-Chemical Approach to Perovskite and Fluorite-Type Nanoceramics*, Ph.D. thesis, University of Twente, 2015.
2. Karageorgakis, N.I., *Nanocrystalline Ceramic Thin Films for micro Solid Oxide Fuel Cells Prepared by Flame Spray Deposition*. Ph.D. thesis, ETH ZURICH, 2010.
3. Wang, Z., *Novel Sol-gel Synthesis and Characterization of Oxide Nanopowders for Solid Oxide Fuel Cells*, Ph.D. thesis, University of Leeds, 2012.
4. Steele, B.C.H., Appraisal of $Ce_{1-y}GdyO_{2-y/2}$ electrolytes for IT-SOFC operation at 500°C. *Solid State Ionics*, 2000. **129**(1–4): p. 95-110.
5. Shobit, O., Wachsman, E.D., Nino, J.C., Higher conductivity Sm^{3+} and Nd^{3+} co-doped ceria-based electrolyte materials. *Solid state Ionics*, 2008. 178: p. 1890 - 1897.
6. Kim, Y., Jeon, M.K. & Im, W. Crystal Structural Study of Ho-doped Ceria Using X-ray Powder Diffraction Data. *J Electroceram.* 2013, **31,** 254–259.
7. Wang, K., Kale, G.M. and Ghadiri, M. Synthesis and characterization of $Ce_xGd_{1-x}O_{2-\delta}$ nanopowders employing an alginate mediated ion-exchange process. *Chemical Engineering Journal*, 2012. **198–199**, p. 149–153.
8. Hui, S., Roller, J., Yick, Zhang, X., Decès-Petit, C., Xie, Y., Maric, R., Ghosh, D. A brief review of the ionic conductivity enhancement for selected oxide electrolytes. *Journal of Power Sources*, 2007. **172**(2): p. 493-502.
9. Kilner, J.A. and Burriel, M. Materials for Intermediate-Temperature Solid-Oxide Fuel Cells, *Annual Review of Materials Research*, 2014. **44**, p. 365-393.
10. Kim, D.-J. Lattice parameters, ionic conductivities, and solubility limits in fluorite-structure MO2 oxide [M = Hf^{4+}, Zr^{4+}, Ce^{4+}, Th^{4+}, U^{4+}] solid solutions. *J. Am. Ceram. Soc*. 1989. **72**, 1415–21.

11. Dikmen, S. Effect of co-doping with Sm^{3+}, Bi^{3+}, La^{3+}, and Nd^{3+} on the electrochemical properties of hydrothermally prepared gadolinium-doped ceria ceramics. *J. Alloys Compd*. 2010. **491**, 106–12.
12. Sun, Q. Fu, Z. Yang, Z. Effects of rare-earth doping on the ionic conduction of CeO_2 in solid oxide fuel cells. *Ceram. Int.,* 2018. **44**, 3707-3711.
13. Preethi, S., Abhiroop, M., Babu, K. S. Low temperature densification by lithium co-doping and its effect on ionic conductivity of samarium doped ceria electrolyte. *Ceram. Int.* 2019, **45**, 5819-5828.
14. Arabaci, A. Effect of Er, Gd, and Nd co-dopants on the properties of Sm-doped ceria electrolyte for IT-SOFC. *Metall. Mater. Trans.* 2017, **48A**, pp 2282-2288.
15. Coles-Aldridge, A. V., and Baker, R. T. Ionic conductivity in multiply substituted ceria-based electrolytes, *Solid State Ion.* 2018, **316**, 9-19.
16. Gupta, M., Shirbhate, S., Ojha, P., Acharya, S. Processing and conductivity behavior of La, Sm, Fe singly and doubly doped ceria: As electrolytes for IT-SOFCs. *Solid State Ion.* 2018, **320**, 199-209.
17. Shirbhate, S., Nayyar, R.N., Ojha, P.K., Yadav, A.K., Acharya, S. Exploration of Atomic Scale Changes during Oxygen Vacancy Dissociation Mechanism in Nanostructure Co-Doped Ceria: As Electrolytes for IT-SOFC. *J. Electrochem.* 2019, **166** (8), F544-F554.
18. Judkins, R.R. and Fulkerson, W. The Dilemma of Fossil Fuel Use and Global Climate Change, *Energy & Fuels*, 1993, **7**, 14-22.
19. Ehteshami, S.M.M., Chan, S.H. The role of hydrogen and fuel cells to store renewable energy in the future energy network–potentials and challenges, *Energy Policy*, 2014, **73**, 103–109.

20. Fu, Y., Theoretical and Experimental Study of Solid Oxide Fuel Cell (SOFC) using Impedance Spectra, in Department of Chemical Engineering. Ph.D. thesis, Massachusetts Institute of Technology, 2014.

21. Mahato, N., Banerjee, A., Gupta, A., Omar, S. Balani, K. Progress in material selection for solid oxide fuel cell technology: A review. *Progress in Materials Science*, 2015. **72**, p. 141-337.

22. Park, K., and Hwang, H.K. Electrical conductivity of $Ce_{0.8}Gd_{0.2-x}Dy_xO_{2-1}$ ($0 \leq x \leq 0.2$) co-doped with Gd^{3+} and Dy^{3+} for intermediate-temperature solid oxide fuel cells. *Journal of Power Sources*, 2011. **196**, p. 4996–4999.

23. Steele, B.C.H., and Heinzel, A. Materials for fuel-cell technologies. *Nature,* 2001. **414,** 345–352.

24. Ma, Y., *Ceria-based Nanocomposite Electrolyte for Low-Temperature Solid Oxide Fuel cells*, Ph.D. thesis, Royal Institute of Technology, 2009.

25. Fabbri, E., Pergolesi, D., and Traversa, E. Materials challenges toward proton-conducting oxide fuel cells: a critical review. *Chemical Society Reviews*, 2010. **39** (11): p. 4355-4369.

26. Singhal, S.C., K. Kendall, K. High Temperature Solid Oxide Fuel Cells. Fundamentals, design and applications. Elsevier, Oxford, 2003.

27. Brandon, N.P., Skinner, S. and Steele, B.C.H. Recent advances in materials for fuel cells. *Annual Review of Materials Research*, 2003. **33**: p. 183-213.

28. Vohs, J.M. and Gorte, R.J. High-Performance SOFC Cathodes Prepared by Infiltration. *Advanced Materials,* 2009. **21**(9): p. 943-956.

29. Gauckler, L.J., et al., Solid Oxide Fuel Cells: Systems and Materials. *CHIMIA International Journal for Chemistry,* 2004. **58**(12): p. 837-850.

30. Tao, S. and Irvine, J.T.S. Discovery and characterization of novel oxide anodes for solid oxide fuel cells. *The Chemical Record*, 2004. **4**(2): p. 83-95.

31. Jiang, S.P. and Chan, S.H. A review of anode materials development in solid oxide fuel cells. *Journal of Materials Science*, 2004. **39**(14): p. 4405-4439.

32. Spacil HS. 1970. Electrical device including nickel-containing stabilized zirconia electrode. US Patent No. 3,503,809

33. Inaba, H. and Tagawa, H. Ceria-based solid electrolytes, *Solid State Ionics*, 1996. **83**. 1- 16.

34. Etsell, T.H. and Flengas, S.N. The electrical properties of solid oxide electrolytes, *Chemical Reviews*, 1970, **70,** 339

35. Omar, S., Wachsman, E.D., Nino, J.C. A co-doping approach towards enhanced ionic conductivity in fluorite-based electrolytes, *Solid State Ionics*, 2006, **177**, 3199-3203.

36. Malavasi, L., Fisher, C.A.J., Islam, M.S. Oxide-ion and proton conducting electrolyte materials for clean energy applications: structural and mechanistic features, *Chem. Soc. Rev.* 2010. **39**. 4370-4387.

37. Goodenough, J. B. Oxide-ion electrolytes, *Annu. Rev. Mater. Res*., 2003, **33**, 91

38. Omar, S., Wachsman, E.D., Nino, J.C. Crystal Structure–Ionic Conductivity Relationships in Doped Ceria Systems, *J. Am. Ceram. Soc.*, 2009. **92** [11] 2674–2681.

39. Aguadero, A., Fawcett, L., Taub, S., Woolley, R., Wu, K.-T., Xu, N., Kilner, J., and Skinner, S. Materials development for intermediate-temperature solid oxide electrochemical devices, *J. Mater. Sci.*, 2012, **47**, 3925 —3948.

40. Li, Z-P., Mori, T., Zou, J., Drennan, J., Defects clustering and ordering in di- and trivalently doped ceria, *Materials Research Bulletin*, 2013. **48**. 807–812.

41. Sammes, N.M., Tompsett G.A., Nafe H., Aldinger F., Bismuth based oxide electrolytes— structure and ionic conductivity, *J Eur Ceram Soc*, 1999. **19**:1801.

42. Zhen, A., Kale, G.M., He, W., Liu, J. Microwave Plasma Sintered Nanocrystalline Bi_2O_3−HfO_2−Y_2O_3 Composite Solid Electrolyte, Chem. Mater. 2007, 19, 2, 203-210.
43. Verkerk, M.J., Keizer, K., Burggraaf, A.J., High oxygen ion conduction in of the Bi_2O_3-Er_2O_3 system, *J Appl Electrochem*, 1980. **10**:81.
44. Jaiswal, N., Tanwar, K., Suman, R., Kumar, D., Upadhyay, S., Parkash, Om., A brief review on ceria based solid electrolytes for solid oxide fuel cells, *Journal of Alloys and Compounds*, 2019, **781**. 984-1005
45. Basu, S., Sujatha, D., Maiti, H. S. Synthesis and Properties of Nanocrystalline Ceria Powders. *J. Mater. Res.* 2004, *19*, 3162−3171
46. Lucid, A.K., Keating, P.R.L., Allen, J.P., Watson, G.W. Structure and Reducibility of CeO_2 Doped with Trivalent Cations, *J. Phys. Chem. C*. 2016, **120**, 23430−23440.
47. Kilner, J.A., Brook, R.J. A study of oxygen ion conductivity in doped nonstoichiometric oxides, *Solid State Ionics*. 1982. **6**. 237-252.
48. Yahiro, H., Eguchi, K., Arai, H. Electrical properties and microstructure in the system ceria-alkaline earth oxide, *J. Mater. Sci.* 1988. **23**. 1036-1041.
49. Zhang, T., Ma, J., Kong, L., Chan, S., and Kilner, J. Aging behavior and ionic conductivity of ceria-based ceramics: a comparative study, *Solid State Ionics*, 2004, **170**, 209 —217
50. Sánchez-Bautista, C., Dos santos Garcia, A.J., Peña-Martínez, J., and Canales-Vázquez, J. The grain boundary effect on dysprosium doped ceria, *Solid State Ionics*, 2010, **181** , 1665 —1673
51. Tianshu, Z., Hing, P., Huang, H., and Kilner, J. Ionic conductivity in the CeO_2–Gd_2O_3 system ($0.05 \leq Gd/Ce \leq 0.4$) prepared by oxalate coprecipitation, *Solid State Ionics*, 2002, **148** , 567 —573

52. Fuentes, R.O. and Baker, R.T. Structural, morphological and electrical properties of $Gd_{0.1}Ce_{0.9}O_{1.95}$ prepared by a citrate complexation method, *J. Power Sources*, 2009, **186**, 268 —277

53. Huang, K., Feng, M. and Goodenough, J.B. Synthesis and Electrical Properties of Dense $Ce_{0.9}Gd_{0.1}O_{1.95}$ Ceramics, *J. Am. Ceram. Soc.*, 1998, **81**, 357 —362

54. Reddy, K.R. and Karan, K. Sinterability, Mechanical, Microstructural, and Electrical Properties of Gadolinium-Doped Ceria Electrolyte for Low-Temperature Solid Oxide Fuel Cells. *J. Electroceram.*, 2005, **15**, 45 —56

55. Cioatera, N., Pârvulescu, V., Rolle, A., and Vannier, R.N. Effect of strontium addition on europium-doped ceria properties. *Solid State Ionics*, 2009, **180** , 681 —687

56. Li, L.P., Lin, X. M., Li, G.S., and Inomata, H. Solid solubility and transport properties of $Ce_{1-x}Nd_xO_{2-\delta}$ nanocrystalline solid solutions by a sol-gel route, *J. Mater. Res.*, 2001, **16** , 3207

57. Aneflous, L., Musso, J.A., Villain, S., Gavarri, J.-R., and Benyaich, H. Effects of temperature and Nd composition on non-linear transport properties in substituted $Ce_{1-x}Nd_xO_{2-\delta}$ cerium dioxides, *J. Solid State Chem.*, 2004, **177**, 856 —865

58. Stephens, I., and Kilner, J. Ionic conductivity of $Ce_{1-x}Nd_xO_{2-x/2}$, *Solid State Ionics*, 2006, **177**, 669 —676

59. Zhu, J. X., Zhou, D. F., Guo, S. R., Ye, J. F., Hao, X. F., Cao, X.Q., and Meng, J. Grain boundary conductivity of high purity neodymium-doped ceria nanosystem with and without the doping of molybdenum oxide, *J. Power Sources*, 2007, **174**, 114 —123

60. Pérez-Coll, D., Marrero-López, D., Núñez, P., Piñol, S., and Frade, J. R. Oxygen-ion conductivity and defect interactions in yttria-doped ceria *Electrochim. Acta*, 2006, **51**, 6463 —6469

61. Koettgen, J., Grieshammer, S., Hein, P., Grope, B.O.H., Nakayama, M., Martin, M. Understanding the ionic conductivity maximum in doped ceria: trapping and blocking *Phys. Chem. Chem. Phys.*, 2018, **20**, 14291-14321.

62. Kilner, J.A. Fast anion transport in solids. *Solid State Ionics*, 1983. **8**(3): p. 201-207.

63. Shannon, R.D. and C.T. Prewitt, Effective ionic radii in oxides and fluorides. *Acta Crystallographica Section B*, 1969. **25**(5): p. 925-946.

64. Ou, D.R., Mori, T., Ye, F., Zou, J., Auchterlonie, G., & Drennan, J. Microstructural Inhomogeneity in Holmium-Doped Ceria and Its Influence on the Ionic Conduction *J. Electrochem. Soc.* 2007. **154**, B616-B622.

65. Artini, C., Pani, M., Lausi, A., Masini, R., & Costa, G.A. High Temperature Structural Study of Gd-Doped Ceria by Synchrotron X-ray Diffraction (673 K ≤ T ≤ 1073 K). *Inorg. Chem.* 2014. **53**, 10140-10149.

66. Chavan, S.V., Tyagi, A.K. Phase relations and lattice thermal expansion studies in the $Ce_{0.50}RE_{0.50}O_{1.75}$ (RE = rare-earths) (2005). *Mater. Sci. Eng.* A. **404**, 57−63.

67. Zhang, T., Ma, J., Kong, L., Chan, S., Hing, P., and Kilner, J. Effect of transition metal oxides on densification and electrical properties of Si-containing $Ce_{0.8}Gd_{0.2}O_{2-\delta}$ ceramics, *Solid State Ionics*, 2004, **168**, 187 —195.

68. Taub, S., Williams, R.E.A., Wang, X., McComb, D.W., Kilner, J., Atkinson, A. The effects of transition metal oxide doping on the sintering of cerium gadolinium oxide, Acta Materialia. 2014. **81**.128–140129

69. B. Rambabu, S. Ghosh, H. Jena, Novel wet-chemical synthesis and characterization of nanocrystalline CeO_2 and $Ce_{0.8}Gd_{0.2}O_{1.9}$ as solid electrolyte for intermediate temperature solid oxide fuel cell (IT-SOFC) applications, *J Mater Sci*. 2006. **41**:7530–7536.

70. Nakayama M., and Martin, M. First-principles study on defect chemistry and migration of oxide ions in ceria doped with rare-earth cations. *Phys. Chem. Chem. Phys.*, 2009. **11**, 3241.

71. Li, Z-P., Mori, T., Zou, J., and Drennan, J. Optimization of ionic conductivity in solid electrolytes through dopant-dependent defect cluster analysis, *Phys. Chem. Chem. Phys*., 2012, **14**, 8369–8375

72. Omar, S. Doped ceria for Solid Oxide Fuel Cells, Cerium oxide applications and attributes, Intech Open: Sher Bahadar Khan and Kalsoom Akhtar, 2019. https://doi.org/10.5772/intechopen.79170

73. Minervini, L., Zacate, M.O., Grimes, R.W. Defect cluster formation in M_2O_3-doped CeO_2, *Solid State Ionics*. 1999. **116**. 339–349.

74. Ohashi, T., Yamazaki, S., Tokunaga, T., Arita, Y., Matsui, T., Harami, T., Kobayashi, K. EXAFS study of $Ce_{1-x}Gd_xO_{2-x/2}$. *Solid State Ionics*. 1998. **113-115**. 559-564.

75. Nakayama, M., Ohshima, H., Nogamia, M., and Martin, M. A concerted migration mechanism of mixed oxide ion and electron conduction in reduced ceria studied by first-principles density functional theory, *Phys. Chem. Chem. Phys.*, 2012, **14**, 6079–6084.

76. Herle, J.V., Seneviratne, D., McEvoy, A.J. Lanthanide co-doping of solid electrolytes: AC conductivity behavior, *J. Eur. Ceram. Soc.* 1999. **19.** 837-841.

77. Andersson, D.A., et al., Optimization of ionic conductivity in doped ceria. *Proceedings of the National Academy of Sciences of the United States of America*, 2006. **103**(10): p. 3518-3521.

78. Mori, T., Drennan, J., Lee, J.H., Li, J.G., Ikegami, T. Oxide ionic conductivity and microstructures of Sm-or La-doped CeO_2-based systems, *Solid State Ionics*, 2002. **154**. 461-466.

79. Yamamura, H., Katoh, E., Ichikawa, M., Kakinuma, K., Mori, T., Haneda, H. Multiple doping effect on the electrical conductivity in the $(Ce_{1-x-y}La_xM_y)O_{2-\delta}$ (M = Ca, Sr) system, *Electrochem. Commun*. 2000. **68**. 455-459.

80. Venkataramana, K., Madhuri, C., Madhusudan, Ch., Reddy, Y.S., Bhikshamaiah, G., Reddy, C.V. Investigation on La^{3+} and Dy^{3+} co-doped ceria ceramics with an optimized average atomic number of dopants for electrolytes in IT-SOFCs. *Ceramics International*, 2018, **44**, 6300-6310.

81. Madhusudan, Ch., Venkataramana, K., Madhuri, C., Reddy, C.V. Structural, electrical and thermal studies on microwave sintered Dy and Pr co-doped ceria ceramics as electrolytes for intermediate temperature solid oxide fuel cells, *Journal of Materials Science: Materials in Electronics*. 2018. **29**:17067–17077.

82. Altaf, F., Batool, R., Gill, R., Abbas, G., Raza, R., Khan, M. A., Rehman, Z-ur., Ahmad, M.A. Synthesis and characterization of co-doped ceria-based electrolyte material for low temperature solid oxide fuel cell, *Ceramics International*. 2019. **45**. 10330–10333.

83. Santos, T. H., Grilo, J.P.F., Loureiro, F.J.A., Fagg, D.P., Fonseca, F.C., Macedo, D.A. Structure, densification and electrical properties of Gd^{3+} and Cu^{2+} codoped ceria solid electrolytes for SOFC applications: Effects of Gd_2O_3 content, *Ceramics International*. 2018. **44**. 2745–2751

84. Tanwar, K., Jaiswal, N., Kumar, D., Parkash, O. Synthesis & characterization of Dy and Ca Co-doped ceria based solid electrolytes for IT-SOFCs, *Journal of Alloys and Compounds*. 2016. **684.** 683-690.

85. Preethi, S., Suresh Babu, K. Divalent cations modified grain boundary scavenging in samarium doped ceria electrolyte for solid oxide fuel cells, *Journal of Alloys and Compounds*. 2019. **792**. 1068-1078

86. Kumar, S.A., Kuppusami, P., Amirthapandian, S., Fu, Y-P. Effect of Sm co-doping on structural, mechanical and electrical properties of Gd doped ceria solid electrolytes for intermediate temperature solid oxide fuel cells, *International Journal of Hydrogen Energy*, 2019 (In Press, Corrected Proof).

87. Accardo, G., Kim, G.S., Ham, H.C., Yoon, S.P. Optimized lithium-doped ceramic electrolytes and their use in fabrication of an electrolyte-supported solid oxide fuel cell, *Int J Hydrogen Energy*, 2019. **44**, pp. 12138-12150

88. Accardo, G., Frattini, D., Ham, H.C., Yoon, S.P. Direct addition of lithium and cobalt precursors to $Ce_{0.8}Gd_{0.2}O_{1.95}$ electrolytes to improve microstructural and electrochemical properties in IT-SOFC at lower sintering temperature, *Ceram Int*, 2019. **45**, pp. 9348-9358

89. Arabacı, A. Synthesis and characterization of Pr/Gd co-doped ceria by using the citric acid–nitrate combustion method, *Solid State Ion*, 2018. **326**, pp. 69-76

90. Spiridigliozzi, L., Dell'Agli, G., Accardo, G., Yoon, S., Frattini, D. Electro-morphological, structural, thermal and ionic conduction properties of Gd/Pr co-doped ceria electrolytes exhibiting mixed Pr^{3+}/Pr^{4+} cations, *Ceram Int*, 2019. **45**, pp. 4570-4580.

91. Anwar, M., SA, M.A., Baharuddin, N.A., Raduwan, N.F., Muchtar, A., Somalu, M.R. Structural, optical and electrical properties of $Ce_{0.8}Sm_{0.2-x}Er_xO_{2-\delta}$ (x= 0–0.2) Co-doped ceria electrolytes, *Ceram Int*, 2018. **44**, pp. 13639-13648

92. Bowman, W.J., Zhu, J., Sharma, R., Crozier, P.A., Electrical conductivity and grain boundary composition of Gd-doped and Gd/Pr co-doped ceria. *Solid State Ionics*, 2015. **272:** p. 9-17.

93. Dikmen, S., Hasan, A., Dikmen, E., Şahin, O. Hydrothermal preparation and electrochemical properties of Gd^{3+} and Bi^{3+}, Sm^{3+}, La^{3+}, and Nd^{3+} codoped ceria-

based electrolytes for intermediate temperature-solid oxide fuel cell. *Journal of Power Sources*, 2010. **195**(9): p. 2488-2495.

94. Li, B., Liu, Y., Wei, X., Pan, W. Electrical properties of ceria Co-doped with Sm^{3+} and Nd^{3+}. *Journal of Power Sources*, 2010. **195**(4): p. 969-976.

95. Jaiswal, N., Kumar, D., Upadhyay, S., Parkash, O. High electrical conductivity of nanocomposites based on $Ce_{0.82}Sm_{0.16}Sr_{0.02}O_{1.90}$ and $(Li/Na)_2$ CO_3 for low temperature solid oxide fuel cells. *Ceramics International*, 2016. **42**(7): p. 9004-9010.

96. Li, B., Wei, X., and Pan, W. Improved electrical conductivity of $Ce_{0.9}Gd_{0.1}O_{1.95}$ and $Ce_{0.9}Sm_{0.1}O_{1.95}$ by co-doping. *International Journal of Hydrogen Energy*, 2010. **35**(7): p. 3018-3022.

97. Kobi, S., Jaiswal, N., Kumar, D., Parkash, O. Ionic conductivity of Nd^{3+} and Y^{3+} co-doped ceria solid electrolytes for intermediate temperature solid oxide fuel cells. *Journal of Alloys and Compounds*, 2016. **658**: p. 513-519.

98. Ma, L., Zhao, K., Kim. B-K., Li, Q., Huang, J. Synthesis and characterizations of $Ce_{0.85}(Sm_xNd_{1-x})_{0.15}O_{2-\delta}$ ceramics. *Journal of Alloys and Compounds*, 2014. **601**: p. 260-266.

99. Hardian, A., Choi, G.M., Suendo, V., Ismunandar Structure and Ionic Conductivity of Codoped Ceria for IT-SOFC Electrolytes. *Journal of The Australian Ceramic Society*, 2014. **50**(2): p. 99-109

100. Dudek, M., Some Structural Aspects of Ionic Conductivity in Co-Doped Ceria-Based Electrolytes, *Archives of Metallurgy and Materials*. 2013. **58**. p. 1355.

101. Kilner, J.A. Fast oxygen transport in acceptor doped oxides, *Solid State Ionics*, 2000. **129**, p. 13

102. Pérez-Coll, D., Núñez, P., Ruiz-Morales, J.C., Peña-Martínez, J., Frade, J.R. Re-examination of bulk and grain boundary conductivities of $Ce_{1-x}Gd_xO_{2-\delta}$ ceramics, *Electrochim. Acta*, 2007. **52**, p. 2001

103. Pérez-Coll, D., Marrero-López, D., Núñez, P., Piñol, S., Frade, J.R. Grain boundary conductivity of $Ce_{0.8}Ln_{0.2}O_{2-\delta}$ ceramics (Ln = Y, La, Gd, Sm) with and without Co-doping, *Electrochim. Acta*, 2006. **51**, p. 6463

104. Avila-Paredes, H., Shvareva, T., Chen, W., Navrotsky, A., Kim, S. A correlation between the ionic conductivities and the formation enthalpies of trivalent-doped ceria at relatively low temperatures, *Phys. Chem. Chem. Phys*., 2009. **11**, p. 8580.

105. Pérez-Coll, D., Sánchez-López, E., Mather, G.C. Influence of porosity on the bulk and grain-boundary electrical properties of Gd-doped ceria, *Solid State Ionics*. 2010. **181**. 1033–1042

106. Wang, Z., Kale, G.M., Tang, X. Sintering behaviour and ac conductivity of dense $Ce_{0.8}Gd_{0.2}O_{1.9}$ solid electrolyte prepared employing single-step and two-step sintering process *Journal of Materials Science*, 2004, **49 (8)**, 3010-3015.

107. Rahman, M.N., *Ceramic Processing and Sintering*. 2nd ed. New York: Marcel Dekker, 2003.

108. Brinker, C.J. and G.W. *Scherer, Sol-Gel Science the Physics and Chemistry of Sol-Gel Processing*. London: Academic Press, 1990

109. Wang, Z., Kale, G.M., Yuan, Q., Mojtaba, G. X-Ray micro-tomography of freeze dried nickel alginate beads and transformation into NiO nanopowders. *RSC Advances*, 2012. **2**(26): p. 9993-9997.

110. Sikorski, P., Mo, F., Skjåk-Bræk, G., Stokke, B.T. Evidence for Egg-Box-Compatible Interactions in Calcium-Alginate Gels from Fiber X-ray Diffraction. *Biomacromolecules*, 2007. **8**: p. 2098-2103.

111. Pawar, S.N. and K.J. Edgar, Alginate derivatization: A review of chemistry, properties and applications. *Biomaterials*, 2012. *33*: p. 327 - 3305.

112. Liew, C.V., et al., Evaluation of sodium alginate as drug release modifier in matrix tablets. *International Journal of Pharmaceutics*, 2006. **309**(1–2): p. 25-37.

113. Silvia Vicini, et al., Gelling process for sodium alginate: New technical approach by using calcium rich micro-spheres. *Carbohydrate Polymers* 2015. **134** p. 767–774.

114. Stewart, M.B., et al., The role of poly-M and poly-GM sequences in the metal-mediated assembly of alginate gels. *Carbohydrate Polymers*, 2014. **112**: p. 486-493.

115. Mandal, S., Basu, S.K., and Sa, B. Ca^{2+} ion cross-linked interpenetrating network matrix tablets of polyacrylamide-grafted-sodium alginate and sodium alginate for sustained release of diltiazem hydrochloride. *Carbohydrate Polymers*, 2010. **82**(3): p. 867-873.

116. Rajkumar, M., Meenakshisundaram, N., and Rajendran, V. Development of nanocomposites based on hydroxyapatite/sodium alginate: Synthesis and characterisation. *Materials Characterization*, 2011. **62**(5): p. 469-479.

117. Zhang, S.M., Cui, F.Z., Liau, S.S., Zhu, Y., Han, L. Synthesis and biocompatibility of porous nano-hydroxyapatite/collagen/alginate composite. *Journal of Materials Science: Materials in Medicine,* 2003. **14**(7): p. 641-645.

118. Ueyama, Y., Ishikawa, K. Mano, T., Koyama, T., Nagatsuka, H., Suzuki, K., Ryoke, K. Usefulness as guided bone regeneration membrane of the alginate membrane. *Biomaterials,* 2002. **23**(9): p. 2027-2033.

119. Bottom, R., Thermogravimetric Analysis. In: Gabbott, P. ed. *Principles and Applications of Thermal Analysis*. Oxford: Blackwell Publishing, 2008, pp. 87-118.

120. Gabbott, P. ed. *Principles and Applications of Thermal Analysis*. Oxford: Blackwell Publishing, 2008.

121. West, A.R., *Basic Solid State Chemistry*. West Sussex: John Wiley & Sons, 1984.

122. Cullity, B.D., and Stock, S.R. *Elements of X-Ray Diffraction*. 3rd ed. 2001: Prentice Hall.

123. William D. Callister, J., *Materials Science and Engineering an Introduction*. Fifth ed. 2000: John Wiley & Sons.

124. Hammond, C., *The Basics of Crystallography and Diffraction*. Fourth ed. 2015: Oxford Science Publications.

125. Larson, A. C.; Von Dreele, R.B. GSAS. Report LAUR 86-748. Los Alamos National Laboratory, New Mexico, USA (2004).

126. Zhao, Z., *Pulsed Laser Deposition and Characterisation of Rare Earth Doped Glass-polymer Optical Materials*. Ph.D. thesis, University of Leeds, 2012.

127. Luo, T., *Spectrometer Attachments for The Scanning Electron Microscope*. Ph.D. thesis, National University of Singapore, 2009.

128. Goodhew, P.J., Humphreys, J., and Beanland, R. *Electron Microscopy and Analysis*. Third ed. 2001: Taylor & Francis.

129. Dumont, M.F., *Nanostructures of Metallophosphates and Cyanometallates for Applications and Physical Studies*. Ph.D. thesis, University of Florida. 2011.

130. Fultz, B. and Howe, J. *Transmission Electron Microscopy and Diffractometry of Materials*.: Springer, 2001.

131. Smith, E., Dent, G. *Modern Raman Spectroscopy – A Practical Approach*. West Sussex: John Wiley & Sons, 2005.

132. McCreery, R.L. *Raman Spectroscopy for Chemica1 Analysis*. New York: John Wiley & Sons, 2000.

133. Szymanski, H.A. ed. *Raman Spectroscopy Theory and Practice*. New York: Plenum Press, 1966.

134. Macdonald, J.R. and W.B. Johnson, *Impedance Theory, Experiment, and Applications*. 2005: John Wiley & Sons.

135. Archer, W.I., Armstrong, R.D., The application of AC impedance methods to solid electrolytes. In: Thirsk, H.R. ed. *Electrochemistry*. London: Royal Society of Chemistry, 1980, pp. 157-202.

136. Sinclair, D.C., Characterization of Electro-materials using ac Impedance Spectroscopy, *Bol. Soc Esp. Cerám. Vidrio*, 1995. **34**: p. 55-65.

137. Macdonald, J.R., Impedance Spectroscopy. *Annals of Biomedical Engineering*, 1992. **20**: pp. 289-305.

138. Rahayu. S., Forester, J., Kale, G.M., Ghadiri, M. Promising solid electrolyte material for an IT-SOFC: crystal structure of the cerium gadolinium holmium oxide $Ce_{0.8}Gd_{0.1}Ho_{0.1}O_{1.9}$ between 295 and 1023 K. *Acta Crystallographica Section C: Structural Chemistry*, 2018, **74 (2)**, 236-239.

139. Sardar, S., Kale G., and Ghadiri, M. Structural study of holmium zirconate nanoparticles obtained through carbon neutral sol-gel process. *Thermochim. Acta*, 2019, **676**, 120-129.

140. Sardar, S., Kale, G., Ghadiri, M. Influence of processing conditions on the ionic conductivity of holmium zirconate ($Ho_2Zr_2O_7$). *Ceramics International.* 2020. **46**. 11508-11514.

141. Wang, Z., Kale, G.M., Ghadiri, M. Novel Ion-Exchange Process for the Preparation of Metal Oxide Nanopowders from Sodium Alginate. *Journal of the American Ceramic Society*, 2012. **95** (10), pp 3124-3129.

142. Hume-Rothery, W. Researches on the nature properties and conditions of formation of intermetallic compounds, with special reference to certain compounds of tin. *J. Inst. Met.*, 1926, **35**: p. 295

143. Artini, C., Pani, M., Lausi, A., Masini, R., & Costa, G.A. High Temperature Structural Study of Gd-Doped Ceria by Synchrotron X-ray Diffraction (673 K $\leq$ T $\leq$ 1073 K). *Inorg. Chem*. 2014. **53**, 10140-10149.

144. Tianshu, Z., Hing, P., Huang, H. & Kilner, J. Ionic conductivity in the CeO_2–Gd_2O_3 system ($0.05 \leq Gd/Ce \leq 0.4$) prepared by oxalate coprecipitation *Solid State Ionics*, 2002. **148**, 567−573.

145. Pezeshkpour, S., Abdullah, A.Z., Salamatinia, B., Horri, B.A. Ionic–gelation synthesis of gadolinium doped ceria ($Ce_{0.8}Gd_{0.2}O_{1.90}$) nanocomposite powder using sodium-alginate, *Ceramics International,* 2017, **43**: 7123-7135.

146. Pezeshkpour, S., Salamatinia, B., Horri, B.A. Synthesis and characterization of nanocrystalline NiO-GDC via sodium alginate-mediated ionic sol-gel method, *Ceramics International*, 2018, **44**: 3201-3210.

147. Bloom, R. *Development and Optimisation of Novel Fibrous Oxygen Carriers for Chemical Looping Reforming Processes*, Ph.D. thesis, University of Leeds, 2018.

148. Williams, D.B. and Carter, C.B. *Transmission Electron Microscopy: A Textbook for Materials Science.* New York: Springer, 1996.

149. Williams, D.B. and Carter, C.B. *Transmission Electron Microscopy: A Textbook for Materials Science.* New York: Springer, 2009.

150. Chen, Y.-F., et al., The effect of calcination temperature on crystallinity TiO_2 nanopowders. *Journal of Crystal Growth*, 2003. **247**: p. 363-370.

151. Grätz, H., Ostwald ripening: New relations between particle growth and particle size distribution. *Scripta Materialia*, 1997. 37: p. 9-16.

152. Gladman, T., *Grain Size Control*. London: Maney Publishing, 2004

153. Kang, S-J. L. *Sintering: Densification, Grain Growth, and Microstructure*, 1st edn, Oxford: Butterworth-Heinemann, 2004.

154. Denton, A.R., Ashcroft, N.W. Vegards law, *Phys. Rev.*, 1991, **A 43**, 3161-3164.

155. Aboud, A.A., Al-Kelesh, H., El Rouby, W.M.A., Farghali, A.A., Hamdedein, A., Khedr, M.H. CO_2 responses based on pure and doped CeO_2 nano-pellets. *J Mater Res Technol*, 2018, **7**,14-20.

156. Taniguchi, T., Watanabe, T., Sugiyama, N., Subramani, A. K., Wagata, H., Matsushita, N.; Yoshimura, M. Identifying defects in ceria-based nanocrystals by UV resonance Raman spectroscopy. *J. Phys. Chem. C*, 2009, **113**, 19789-19793.

157. Spanier, J.E. Robinson, R.D. Zhang, F. Chan, S-W. Herman, I. P. Size-dependent properties of CeO_{2-y} nanoparticles as studied by Raman scattering. *Phys. Rev. B*, 2001, **64**, 245407-8.

158. Kosacki, I., Petrovsky, V., Anderson, H.U., Colomban, P. Raman spectroscopy of nanocrystalline ceria and zirconia thin films. *J. Am. Ceram. Soc.*, 2002, **85**, 2646-2650.

159. Zhang, J., Ke,C., Wu, H., Yu, J., Wang, J., Wang, Y. Solubility limits, crystal structure and lattice thermal expansion of Ln_2O_3 (Ln=Sm, Eu, Gd) doped CeO_2, *Journal of Alloys and Compounds*, 2017, **718**: 85-91.

160. Chavan, S.V., and Tyagi, A.K. Phase relations and lattice thermal expansion studies in the $Ce_{0.50}RE_{0.50}O_{1.75}$ (RE = rare-earths), *Mater. Sci. Eng.* A. 2005, **404**, 57−63

161. Zheng, Y., Zhou, M., Ge, L., Li, S., Chen, H., Guo, L., Effect of Dy on the properties of Sm-doped ceria electrolyte for IT-SOFCs, *Journal of Alloys and Compounds*, 2011, **509**: 1244-1248.

162. Kumar, V.P., Reddy, Y.S., Kristaiah, P., Prasad, G., Reddy, C.V. Thermal and electrical properties of rare-earth co-doped ceria ceramics, *Mater. Chem. Phys.*, 2008, **112**: pp. 711-718.

163. Kostogloudis, G.Ch., Vasilakos, N. and Ftikos, Ch. Crystal structure, thermal and electrical properties of $Pr_{1-x}Sr_xCoO_{3-\delta}$ (x=0, 0.15, 0.3, 0.4, 0.5) perovskite oxides, *Solid State Ionics*, 1988, **106**: pp. 207-218, G.C.

164. Kostogloudis, G.Ch., and Ftikos, Ch. Crystal structure, thermal expansion and electrical conductivity of $Pr_{1-x}Sr_xCo_{0.2}Fe_{0.8}O_{3-\delta}$ ($0 \leq x \leq 0.5$), *Solid State Ionics,* 2000, **135**: pp. 537-541.

165. Sha, X., Lü, Z., Xiqiang, H., Miao, J., Xin, X., Su, W. Preparation and properties of rare earth co-doped $Ce_{0.8}Sm_{0.2-x}Y_xO_{1.9}$ electrolyte materials for SOFC, *Journal of Alloys and Compounds*, 2006, **424**: p.315-321.

166. Mogensen, M., Lindegaard, T., Hansen, U.R., Mogensen, G. Physical Properties of Mixed Conductor Solid Oxide Fuel Cell Anodes of Doped CeO_2. *J. Electrochem. Soc*. 1994, **141**, 2122–2128.

167. Khakpour, Z., Youzbashi, A.A., Maghsoudipour, A. Influence of Gd^{3+} and Dy^{3+} co-doping and sintering regime on enhancement of electrical conductivity of ceria-based solid electrolyte, *Ionics*, 2014, **20**:1407–1417

168. Irvine, J.T.; Sinclair, D.C.; West, A.R. Electroceramics: Characterization by Impedance Spectroscopy. *Adv. Mater.*, 1990, 2, 132-138.

169. Macdonald, J.R, Impedance Spectroscopy Emphasizing Solid Materials and Systems. New York: John Wiley & Sons, 1987.

170. Coles-Aldridge, A.V., Baker, R.T. Oxygen ion conductivity in ceria-based electrolytes co-doped with samarium and gadolinium, *Solid State Ionics*, 2020, **347**:115255.

171. Shirbhate, S., Yadav, A.K., Acharya, S. Investigation of in-situ oxygen vacancies dissociation mechanism and associated atomic scale reshuffling during oxy-ion migration in nanostructured co-doped ceria, *Solid State Ionics*, 2020, **345**,115157.

172. Torun H. O., Cakar S., Thermal characterization of Er-doped and Er–Gd co-doped ceria-based electrolyte materials for SOFC, *Journal of Thermal Analysis and Calorimetry*, 2018, **133**:1233–1239

173. Mahato, N., Amitava, B., Alka, G., Shobit, O., Kantesh, B. Progress in materials science progress in material selection for solid oxide fuel cell technology: a review. *Prog Mater Sci*. 2015, **72**:141–337.

174. Kim, G., Lee, N., Kim, KB., Chang, H., Song, S.J., Park, J.Y. Various synthesis methods of aliovalent-doped ceria and their electrical properties for intermediate temperature solid oxide electrolytes. *Int J Hydrog Energy*. 2013, **38**(3):1571–87.

175. Kilner, J.A. Fast oxygen transport in acceptor doped oxides, *Solid State Ionics*, 2000, **129**: p. 13

176. Ali, A., Rafique, A., Kaleemullah, M., Abbas, G., Khan, M.A., Ahmad, M.A., Raza, R. Effect of Alkali Carbonates (Single, Binary, and Ternary) on Doped Ceria: A Composite Electrolyte for Low-Temperature Solid Oxide Fuel Cells, *ACS Appl. Mater. Interfaces*, 2018, **10**, 806−818.

177. Dikmen, S. Effect of co-doping with Sm^{3+}, Bi^{3+}, La^{3+}, and Nd^{3+} on the electrochemical properties of hydrothermally prepared gadolinium-doped ceria ceramics, *J. Alloys Compd.* 2010, **491**: 106–112.

178. Zhang, T.S., Ma, J., Kong, L.B. et al. Preparation and electrical properties of dense submicron-grained $Ce_{0.8}Gd_{0.2}O_{2-\delta}$ ceramics. *Journal of Materials Science Letters*, 2003, **22**: 1809–1811.

179. Acharya, S. A. The effect of processing route on sinterability and electrical properties of nano-sized dysprosium-doped ceria, *J. Power Sources*, 2012, **198**, 105–111.

180. Winck, L.B., Ferreira, J.L. de A., Martinez, J.M.G., Araujo, J.A., Rodrigues, A.C.M., da Silva, C.R.M. Synthesis, sintering and characterization of ceria-based solid electrolytes codoped with samaria and gadolinium using the Pechini method. *Ceramics International*, 2017, **43**:16408–16415.

181. Pikalova, E.Yu., Murashkina, A.A., Maragou, V.I., Demin, A.K., Strekalovsky, V.N., Tsiakaras, P.E. CeO_2 based materials doped with lanthanides for applicationsin intermediate temperature electrochemical devices. *International Journal of Hydrogen Energy*, 2011. **36**: p.6175-6183

182. Duran, P., Moure, C., Jurado, J. R. Sintering and microstructural development of ceria-gadolinia dispersed powders. *J. Mater. Sci.* 1994, **29**, 1940-1948.

183. Kim, S. G., Park, Y. B. Grain boundary segregation, solute drag and abnormal grain growth. *Acta Mater*. 2008, **56** (15), 3739-3753.

184. Daza, P.C.C., Meneses, R.A.M., Rodrigues, A.C.M., Silva, C.R.M. Ionic conductivities and high resolution microscopic evaluation of grain and grain boundaries of cerium-based codoped solid electrolytes. *Ceram. Int*. 2018, **44**, 13699-13705.

185. Chen, I. W. Grain boundary kinetics in oxide ceramics with the cubic fluorite crystal structure and its derivatives. *Interface Sci*. 2000, **8**, 147-156.

186. Aoki, M., Chiang, Y.M., Kosachi, I., Lee, L.I.R., Tuller, H., Liu, Y.P. Solute segregation and grain-boundary impedance in high-purity stabilized zirconia. *J Am Ceram Soc*, 1996, **79**:1169–1180.

187. Baral, A.K., Sankaranarayanan, V. Ion transport and dielectric relaxation studies in nanocrystalline $Ce_{0.8}$Ho0.2$O_{2-\delta}$ material, *Physica B: Condensed Matter*, 2009, **404**: 1674–1678.

188. Baral, A.K., Sankaranarayanan, V. Ionic Transport Properties in Nanocrystalline $Ce_{0.8}A_{0.2}O_{2-\delta}$ (with A = Eu, Gd, Dy, and Ho) Materials, *Nanoscale Res Let,* 2010, **5**:637–643

189. Ou, D.R., Mori, T., Ye, F., Zou, J., Drennan, J. Comparison between Y-doped ceria and Ho-doped ceria: Electrical conduction and microstructures, *Renewable Energy*, 2008, **33**: p. 197

190. Subbarao, E.C. *Solid Electrolytes and Their Applications*, New York: Plenum Press, 1980.

191. Chandra, S. *Superionic Solids Principles and Aplications*, 3ª ed., New York: North Holland Publishing, 1981.

192. Stojmenović, M., Bošković, S., Žunić, M., Babić, B., Bajuk-Bogdanović, D. Mentus, S. Studies on structural, morphological and electrical properties of $Ce_{1x}Er_{x}O_{2-\delta}$ (x=0.05-0.20) as solid electrolyte for IT-SOFC. *Materials Chemistry and Physics*, 2015, **153**: p. 422-431.

193. Cui J., Hope G. A., Raman and fluorescence spectroscopy of CeO_2, Er_2O_3, Nd_2O_3, Tm_2O_3, Yb_2O_3, La_2O_3, and Tb_4O_7, *Journal of spectroscopy*, 2015, p. 1-8

194. Schmitt et al. A review of defect structure and chemistry in ceria and its solid solution, *Chem. Soc. Rev.*, 2020, **49**, 554

195. Artini, C. Rare-Earth-Doped Ceria Systems and Their Performance as Solid Electrolytes: A Puzzling Tangle of Structural Issues at the Average and Local Scale, *Inorg. Chem*. 2018, **57**: 13047−13062

196. Artini, A., Carnasciali, M.M., Plaisier, J.R., Costa, G.A., Pani, M. A novel method for the evaluation of the Rare Earth (RE) coordination number in RE-doped ceria through Raman spectroscopy, *Solid State Ionics*, 2017, **311**: p. 90-97

197. Mandal, B. P., Roy, M., Grover, V., Tyagi, A. K. X-ray diffraction, μ-Raman spectroscopic studies on CeO_2-RE_2O_3 (RE = Ho, Er) systems: observation of parasitic phases. *J. Appl. Phys.* 2008, **103**, 033506.

198. Kuharuangrong, S. Ionic conductivity of Sm, Gd, Dy and Er-doped ceria. *Journal of power sources*, 2007, **171**: 506-510.

Appendix A

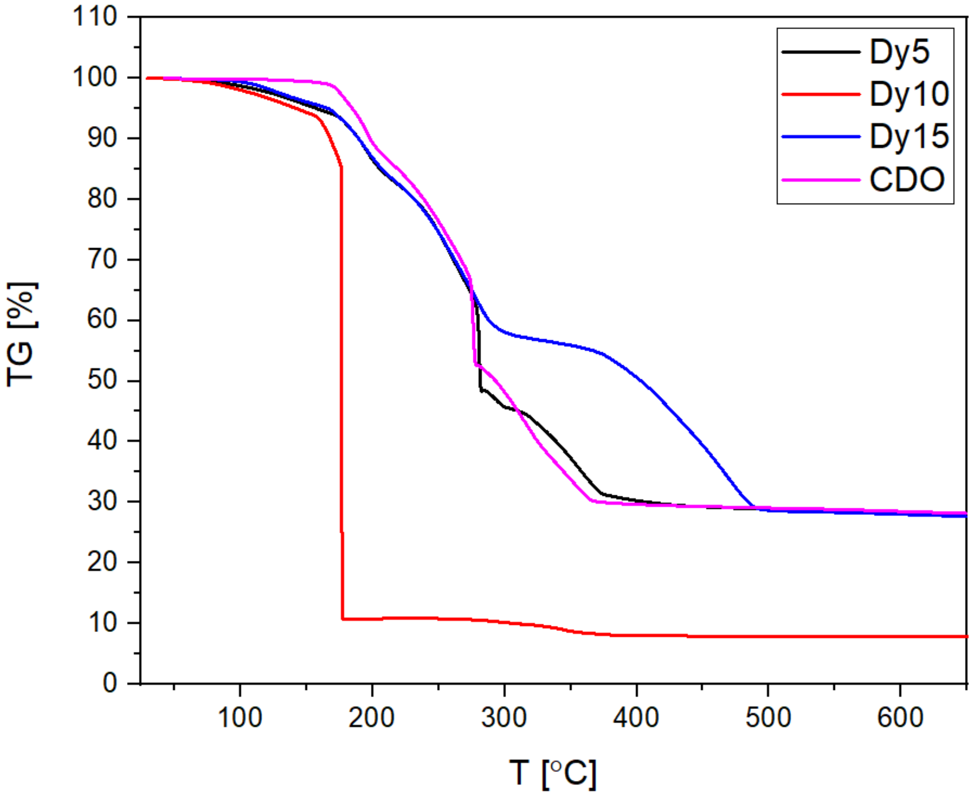
TG [%]
T [°C]
Dy5
Dy10
Dy15
CDO
0
10
20
30
40
50
60
70
80
90
100
110
100
200
300
400
500
600

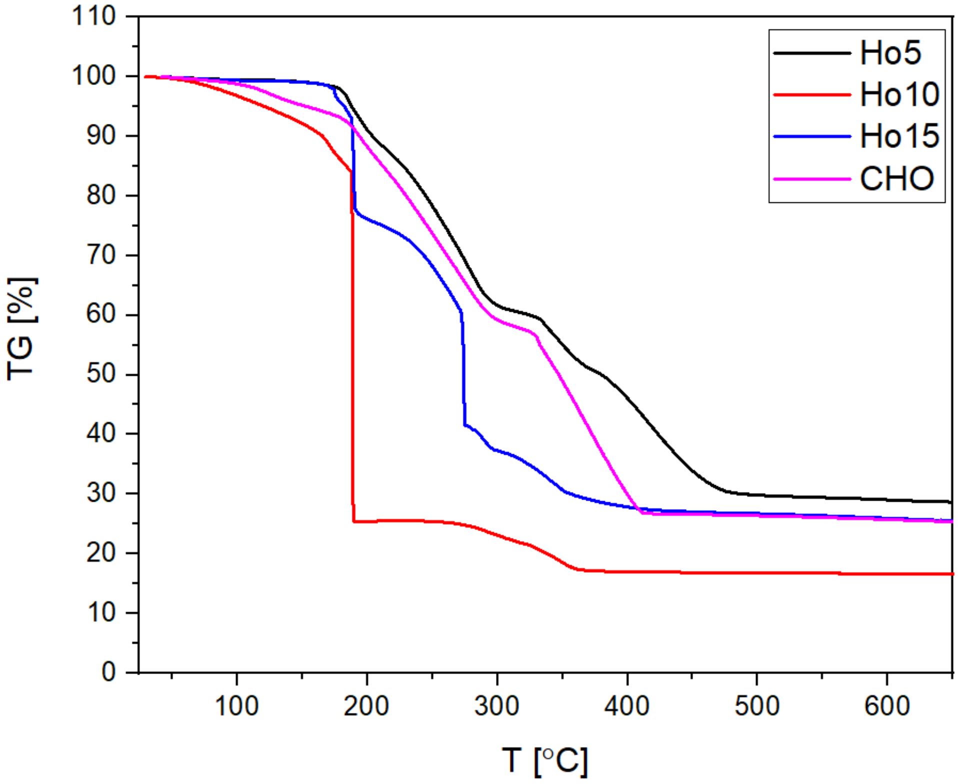
TG [%]
T [°C]
Ho5
Ho10
Ho15
CHO
0
10
20
30
40
50
60
70
80
90
100
110
100
200
300
400
500
600

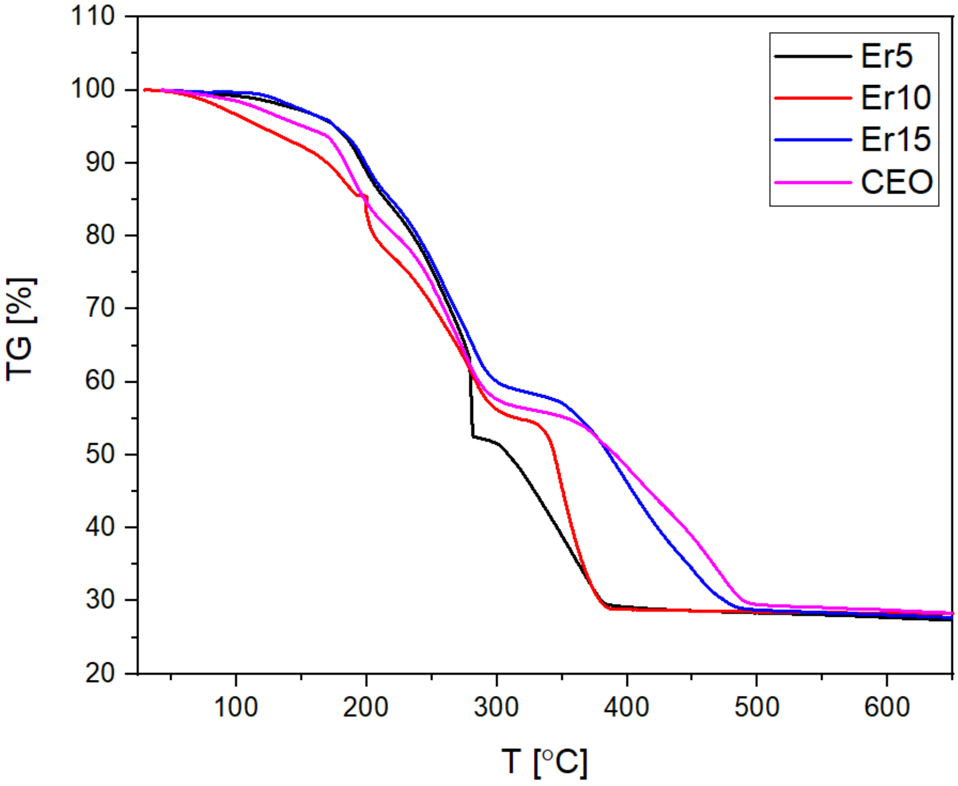

Figure A.1 TGA of metal complex $Ce_{0.8}Dy_xGd_{0.2-x}O_{1.9}$, $Ce_{0.8}Ho_xGd_{0.2-x}O_{1.9}$, $Ce_{0.8}Er_xGd_{0.2-x}O_{1.9}$ ($0 \leqslant x \leqslant 0.2$) dried beads in controlled atmosphere of air.